UNIVERSITY OF CALIFORNIA, SAN DIEGO

Optimization of the Dynamic Behavior of Strongly Nonlinear Heterogeneous Materials

A dissertation submitted in partial satisfaction of the requirements for the degree Doctor of Philosophy

in

Engineering Sciences (Mechanical Engineering)

by

Eric B. Herbold

Committee in charge:

Professor Vitali F. Nesterenko, Co-Chair
Professor David J. Benson, Co-Chair
Professor Katja Lindenberg
Professor Yu-Hwa Lo
Professor Vlado A. Lubarda

2008

The dissertation of Eric B. Herbold is approved, and it is acceptable in quality and form for publication on microfilm and electronically:

Co-Chair

Co-Chair

University of California, San Diego

2008

DEDICATION

This work is lovingly dedicated to my family.

Anfangen zu spinnen und Gott gibt das Gewinde.
(Begin to weave and God gives the thread.)

TABLE OF CONTENTS

LIST OF FIGURES

LIST OF TABLES

ACKNOWLEDGEMENTS

This work was performed under the direction of Professor V. F. Nesterenko and Professor D.J. Benson at the University of California, San Diego from 2003-2008. I feel very fortunate and thankful that I have had the opportunity to work with Professor Nesterenko and Professor Benson who have been encouraging advisors as I have made my way through the doctoral program. I would also like to thank Professor V.A. Lubarda, Professor K. Lindenberg, and Professor Y.-H. Lo for their questions and suggestions in regards to my work.

I am also grateful for the Powell fellowships and supplemental support from the M&AE department that supported me through my first year of studies. The main financial support for the remaining years of my studies was provided by the National Science Foundation (NSF Grant No. DCMS03013220), the Office of Naval Research (ONR Grant No. N00014-06-1-0263) and the Multi-University Research Initiative (MURI ONR Grant No. N00014-07-1-0740).

I would like to thank Chiara Daraio, with whom I had the pleasure of working with through the first three years of my graduate studies. A good portion of my numerical calculations in these years were performed in parallel with her experiments with one-dimensional granular chains. Professor S. Jin also made a significant contribution to the granular chain experiments by suggesting a novel method of 'tuning' the behavior of the propagating waves.

While working on the characterization of W-Al-PTFE composite materials I had the opportunity to work with Professor D. Benson using *Raven*[1] for the finite element calculations. I appreciate his help while I learned how to use the program and our discussions throughout this project. It was also a pleasure working with

[1]Raven is a two dimensional, multi-material Eulerian hydrocode with heat transfer written by D. Benson. [Benson (1992)]

Jing Cai on this project.

In the summer of 2005 I met with Professor S. Gavrilyuk while he was visiting UCSD to give a seminar. I would like to thank him for taking time to talk with me and propose two new ideas for joint papers with Professor V. F. Nesterenko and I.

I would also like to thank Mason A. Porter, Chiara Daraio, Ivan Szelengowicz and Panos G. Kevrekidis for including me in fruitful discussions on diatomic chains that resulted in two subsequent publications. I would also like to mention that David Kim and Sofia Wang provided excellent experimental work in regards to the diatomic chain studies performed at UCSD. It was interesting to be involved in similar projects with two separate groups with two different approaches to the same topic.

Last but certainly not least I would like to thank my family and friends. My wife Nicole "Cole" has been a true inspiration in my life and her patience and support of me throughout my graduate studies shall be repaid as we grow old together. I would also like to thank my parents and their seemingly infinite support.

Some of the Chapters are, in whole or part, published or submitted for publication. The first section of Chapter 2 has been published in *Physical Review E*, **72**, art. 016603, pp. 1-9 with C. Daraio, V.F. Nesterenko, E.B. Herbold, and S. Jin in 2005. The second section of Chapter 2 has been published in *Physical Review E*, **73**, art. 026610, pp. 1-10 with C. Daraio, V.F. Nesterenko, E.B. Herbold and S. Jin. The contributions made by the dissertation author to these works consisted of developing a discrete nonlinear dynamics code for comparison with the experiments and providing text and figures for the discussion and conclusions.

Sections 1 and 2 of Chapter 3 have been published in *Physical Review Letters*, **95**, art. 158702, pp. 1-4 with V.F. Nesterenko, C. Daraio, E.B. Herbold and

S. Jin and *Physical Review Letters*, **96**, art. 058002, pp. 1-4 with C. Daraio, V.F. Nesterenko, E.B. Herbold and S. Jin. The contributions made by the dissertation author to these works consisted of further development of a discrete nonlinear dynamics code for comparison with the experiments and providing text and figures for the discussion and conclusions.

Sections 1 through 5 in Chapter 4 have, in part, been submitted to *Physical Review E* by E.B. Herbold, J. Kim, V.F. Nesterenko, S. Wang and C. Daraio. The dissertation author was the primary investigator and author of this paper. Part of section 6 in Chapter 4 is a derivation omitted in an article published in *Physical Review E Rapid Comm.*, **77**, art. 015601(R), pp. 1-4 by M.A. Porter, C. Daraio, E.B. Herbold, I. Szelengowicz and P.G. Kevrekidis.

Section 1 in Chapter 5 has been published in *AIP Conference Proceedings*, **845** (1), pp. 1523-1526 by E.B. Herbold, V.F. Nesterenko, and C. Daraio. Section 2 in Chapter 5 has been published in *Physical Review E*, **75**, art. 021304, pp. 1-8 by E.B. Herbold, and V.F. Nesterenko. The dissertation author was the primary investigator and author of these papers.

Chapter 6 has been published in *Applied Physics Letters*, **90**, art. 261902 by E.B. Herbold and V.F. Nesterenko. The dissertation author was the primary investigator and author of this paper. Chapter 7 has been submitted to the *Journal of Applied Physics*, E.B. Herbold, V.F. Nesterenko, D.J. Benson, J. Cai, K.S. Vecchio, F. Jiang, J.W. Addiss, S.M. Walley, and W.G. Proud. The dissertation author was the primary investigator and author of this paper.

VITA

Personal Information

Born in Sacramento, California

Citizenship: United States of America

Education

2003	B.S. *cum laude*, California State University, Sacramento
2005	M.S., University of California, San Diego
2008	Ph.D. University of California, San Diego

Honors and Awards

APS/SCCM travel award recipient, August 2005.

Powell Fellowship, UCSD (2003)

JSOE Powell Supplement, UCSD (2003)

Research Experience

UCSD - University of California, San Diego (September 2003 to present) - Research Assistant to Professor V. F. Nesterenko.

Teaching Experience

Teaching Assistant, Dept. of Mechanical and Aerospace Engineering, U.C. San Diego (2005-2008).

"*Fundamentals of Solid Mechanics I*" MAE 131A (undergraduate level, 1 quarter).

"*Fundamentals of Solid Mechanics II*" MAE 131B (undergraduate level, 1 quarter).

"*Mechanics III: Vibrations*" MAE 130C (undergraduate level, 1 quarter).

PUBLICATIONS

Refereed Journal

Herbold, E.B., Kim, J., Nesterenko, V.F., Wang, S., Daraio, C. (2008) Tunable frequency band-gap and pulse propagation in a strongly nonlinear diatomic periodic chain, *Physical Review E*, (41 pages) submitted.

Herbold, E.B., Nesterenko, V.F., Benson, D.J., Cai J., Vecchio, K.S., Jiang, F., Addiss, J.W., Walley, S.M., Proud, W.G. (2008) Particle size effect on strength, failure and shock behavior in Polytetrafluoroethylene-Al-W granular composites, *Journal of Applied Physics*, (35 pages) (accepted August 2008).

Porter, M.A., Daraio, C., Szelengowicz, I., Herbold, E.B., Kevrekidis, P.G. (2008) Highly nonlinear solitary waves in heterogeneous periodic granular media, *Physica D*, (17 pages) (accepted July 2008).

Porter, M.A., Daraio, C., Herbold, E.B., Szelengowicz, I., Kevrekidis, P.G. (2008) Highly nonlinear solitary waves in periodic dimer granular chains, *Physical Review E Rapid Comm.*, **77**, art. 015601(R), pp. 1-4.

Cai, J., Nesterenko, V.F., Vecchio, K.S., Herbold, E.B., Benson, D.J., Jiang, F., Addiss, J.W., Walley, S.M., Proud, W.G. (2008) The influence of metallic particle size on the mechanical properties of PTFE-Al-W powder composites, *Applied Physics Letters*, **92**, art. 031903, pp. 1-3.

Herbold, E.B., Nesterenko, V.F. (2007) Solitary and shock waves in discrete strongly nonlinear double power-law materials, *Applied Physics Letters*, **90**, art. 261902, pp. 1-3.

Herbold, E.B., Nesterenko, V.F. (2007) Shock wave structure in a strongly nonlinear lattice with viscous dissipation, *Physical Review E*, **75**, art. 021304, pp. 1-8.

Daraio, C., Nesterenko, V.F., Herbold, E.B. and Jin, S. (2006) Pulse mitigation by a composite discrete medium. *Journal De Physique IV*, **134**, pp. 473-479.

Daraio, C., Nesterenko, V.F., Herbold, E.B., Jin, S. (2006) Energy trapping and shock disintegration in a composite granular medium. *Physical Review Letters*, **96**, art. 058002, pp. 1-4.

Daraio, C., Nesterenko, V.F., Herbold, E.B., Jin, S. (2006) Tunability of solitary wave properties in one-dimensional strongly nonlinear phononic crystals. *Physical Review E*, **73**, art. 026610, pp. 1-10.

Daraio, C., Nesterenko, V.F., Herbold, E.B., Jin, S. (2005) Strongly nonlinear waves in a chain of Teflon beads. *Physical Review E*, **72**, art. 016603, pp. 1-9.

Nesterenko, V.F., Daraio, C., Herbold, E.B., Jin, S. (2005) Anomalous wave reflection at the interface of two strongly nonlinear granular media. *Physical Review Letters*, **95**, art. 158702, pp. 1-4.

Refereed Conference Proceedings

Herbold, E.B. and Nesterenko, V.F. (2007). Solitary and shock waves in strongly nonlinear metamaterials. *AIP Conference Proceedings*, **955**, pp.231-234.

Herbold, E.B., Cai, J., Benson D.J. and Nesterenko, V.F. (2007). Simulation of particle size effect on dynamic properties and fracture of PTFE-W-Al composites. *AIP Conference Proceedings*, **955**, pp.785-788, [arXiv: cond-mat/0708.1205v1].

Daraio, C., Nesterenko, V.F., Herbold, E.B. and Jin, S. (2005) Strongly nonlinear waves in polymer based phononic crystals. *AIP Conference Proceedings*, **845** (1), pp. 1507-1510.

Herbold, E.B., Nesterenko, V.F. and Daraio, C. (2005) Influence of controlled viscous dissipation on the propagation of strongly nonlinear waves in stainless steel based phononic crystals. *AIP Conference Proceedings*, **845** (1), pp. 1523-1526, [arXiv: cond-mat/0512367v2].

Grant Reports

Nesterenko, V.F., Benson, D.J., Meyers, M.A., Vecchio, K., Cai, J., Herbold, E.B., Hunt, R.J.A., Addiss, J.W. and Jiang, F. (2007) Initiation of high density dense polymer/metal energetic materials under mechanical stimulus. United States Office of Naval Research, contract number: N00014-026-1-0263.

Invited Talks

Dynamic Properties of Heterogeneous Media (09/17/07), One-hour talk at the High Explosives Research and Development (HERD) facility handled by the University of Florida Research Engineering Education Facility (REEF).

Optimization of Dynamic Behavior in Heterogeneous Materials (01/30/08), One-hour talk at the Univ. of Florida Research and Engineering Education Facility (REEF) for the Particulate Mechanics in Extreme Environments workshop.

Conference Presentations

APS - Shock Compression of Condensed Matter, Kona, HI (June, 2007) *Solitary and shock waves in discrete double power law materials.* Herbold, E.B., Nesterenko, V.F.

APS - Shock Compression of Condensed Matter, Kona HI (June, 2007) *Simulation of particle size effect on dynamic properties and fracture of PTFE-W-Al composites.* Herbold, E.B., Cai, J., Benson, D.J. and Nesterenko, V.F.

ARO - 17^{th} U.S. Army Solid Mechanics Symposium, Baltimore, MD (April, 2007) *The role of porosity in PTFE-W-Al composites under dynamic loading.* Herbold, E.B., Cai, J., Addiss, J.W., Benson, D.J. and Nesterenko, V.F.

UCSD - Research Expo, San Diego, CA (February, 2007) *Force chain effect on the dynamic compressive strength of W-Al-PTFE composites.*

UCSD - Research Expo, San Diego, CA (February, 2007) *Wave propagation in strongly nonlinear dissipative systems.*

Dymat - 8^{th} International Conference on Mechanical and Physical Behaviour of Materials Under Dynamic Loading, Dijon, France (September, 2006) *Pulse mitigation in a composite granular medium*, Daraio, C., Nesterenko, V.F., Herbold, E.B. and Jin, S.

APS - Shock Compression of Condensed Matter, Baltimore, MD (August, 2005) *Influence of controlled viscous dissipation on the propagation of strongly nonlinear waves in stainless steel based phononic crystals.* Herbold, E.B., Nesterenko, V.F., Daraio, C.

APS - Shock Compression of Condensed Matter, Baltimore, MD (August, 2005) *Strongly nonlinear waves in polymer based phononic crystals.* Daraio, C., Nesterenko, V.F., Herbold, E.B. and Jin, S.

UCSD - Research Expo, San Diego, CA (March, 2005) *Experimental and numerical analysis of interfacial wave reflections in sonic vacua.*

UCSD - Research Expo, San Diego, CA (February, 2004) *Tunability of contact interaction in strongly nonlinear phononic materials.*

Professional Memberships

APS - Applied Physics Society, Topical Group of Shock Compression and Condensed Matter (SCCM).

TBP - Tau Beta Pi engineering honor society

ABSTRACT OF THE DISSERTATION

Optimization of the Dynamic Behavior of
Strongly Nonlinear Heterogeneous Materials

by

Eric B. Herbold
Doctor of Philosophy in Engineering Sciences (Mechanical Engineering)
University of California, San Diego, 2008
Professor Vitali F. Nesterenko, Co-Chair
Professor David J. Benson, Co-Chair

New aspects of strongly nonlinear wave and structural phenomena in granular media are developed numerically, theoretically and experimentally. One-dimensional chains of particles and compressed powder composites are the two main types of materials considered here. Typical granular assemblies consist of linearly elastic spheres or layers of masses and effective nonlinear springs in one-dimensional columns for dynamic testing. These materials are highly sensitive to initial and boundary conditions, making them useful for acoustic and shock-mitigating applications.

One-dimensional assemblies of spherical particles are examples of strongly nonlinear systems with unique properties. For example, if initially uncompressed,

these materials have a sound speed equal to zero (sonic vacuum), supporting strongly nonlinear compression solitary waves with a finite width. Different types of assembled metamaterials will be presented with a discussion of the material's response to static compression. The acoustic diode effect will be presented, which may be useful in shock mitigation applications. Systems with controlled dissipation will also be discussed from an experimental and theoretical standpoint emphasizing the critical viscosity that defines the transition from an oscillatory to monotonous shock profile.

The dynamic compression of compressed powder composites may lead to self-organizing mesoscale structures in two and three dimensions. A reactive granular material composed of a compressed mixture of polytetrafluoroethylene (PTFE), tungsten (W) and aluminum (Al) fine-grain powders exhibit this behavior. Quasistatic, Hopkinson bar, and drop-weight experiments show that composite materials with a high porosity and fine metallic particles exhibit a higher strength than less porous mixtures with larger particles, given the same mass fraction of constituents. A two-dimensional Eulerian hydrocode is implemented to investigate the mechanical deformation and failure of the compressed powder samples in simulated drop-weight tests. The calculations indicate that the dynamic formation of mesoscale force chains increase the strength of the sample. This is also apparent in three-dimensional finite element calculations of drop-weight test simulations using LS-Dyna despite a higher granular bulk coordination number, and an increased mobility of individual grains.

1

Introduction

There is a continuing need to describe the complex dynamic behavior of heterogeneous materials for engineering applications. The state of the art is constantly changing in the design and use of meta-materials as advances in experimental, theoretical and numerical investigations reveal new and exciting (and sometimes unexpected) properties that may be of practical use. For example, recent investigations have proposed the design of strongly nonlinear granular meta-materials for practical applications ranging from shock or sound protection devices [Nesterenko (2001)] to novel designs of ink-jet printers [Sen et al. (1999)]. Two types of heterogeneous materials are investigated here: idealized one-dimensional materials where a purely nonlinear interaction between masses describes the local deformations, and two and three dimensional compressed powder composites.

This work focuses on the strongly nonlinear dynamic behavior of these materials and their potential use in phononic applications requiring a robust and easily tunable material response and energetic materials where the response of the compressed powder composite must be tailored to meet specific strength and failure criteria. The mathematical treatment of strongly nonlinear dynamic behavior dif-

fers from weakly nonlinear or linear dynamic behavior in that the nonlinear terms encountered in the physically based models are comparable to the dispersive (and dissipative) terms. Also, the overall response of compressed powder composites to dynamic loading are not fully characterized by bulk or local responses due to self organizing meso-scale structures, such as force chains, which have a dramatic effect on the material response (e.g. stress induced anisotropy [Majmudar and Behringer (2005)]) and may be considered strongly nonlinear. The materials in each chapter are considered heterogeneous in terms of their microstructure, material composition or geometrical configuration.

Current theoretical and numerical investigations regarding the meso-scale of randomized granular materials use approaches such as fabric tensors to describe the granular microstructure, which reveals hyperbolic stress equations that predict the emergence of force chains spanning multiple scales in the material [Ball and Blumenfeld (2002), Blumenfeld (2004), Gerritsen et al. (2008)]. Investigations of the static or bulk mechanical properties include those using effective medium approximations of granular materials [Sahimi (2003a), Makse et al. (2004)], though various observations of static properties at different scales have led to various limitations to these approximations [Goddard (1990), Makse et al. (1999), Sahimi (2003b), Goldenberg and Goldhirsch (2005)]. Dynamic investigations have revealed an abundance of new phenomena, reviewed in Jaeger and Nagel (1992) and Jaeger et al. (1996), due to the ability of a granular material to behave as either a gas, liquid or solid [Roessig et al. (2002), Corwin et al. (2005), Viningland et al. (2007)].

Many important dynamic properties of idealized one-dimensional granular materials are being discovered that would be difficult to find in random assemblies of particles. Namely, the existence of strongly nonlinear solitary waves [Nesterenko (1983), Lazaridi and Nesterenko (1985), Nesterenko (2001)], the "acoustic diode ef-

fect" Nesterenko et al. (2005), and granular protectors for impulse mitigation [Hong (2005)] to name a few. Therefore, it is important to contribute to the current understanding of granular materials in one dimension for the creation of new types of metamaterials with tailored dynamic behaviors and to make connections to more complex systems.

The terms *heterogeneous* and *granular* are used to describe the types of materials used in this document, though the term *granular* is usually reserved for materials where energy losses are significant. Heterogeneous materials encompass a more general description of materials including idealized assemblies of grains. These idealized materials have a simple structure providing the means to theoretically and experimentally glean behavioral information from them for direct comparison. For example, the dawn of the optics and phonon branches of physics primarily dealt with photon-particle or particle-particle interactions at a basic level as a means to determine material response or character. In doing so, seemingly pathological material constructs were devised in order to make these physical predictions. Of course, real materials do not behave as perfect lattice structures, but the investigations of idealized materials enlighten one to, perhaps, new and unexpected results.

The first part of this work (Chapters 1-6) is concerned with pulse propagation in strongly nonlinear granular materials in one dimension. In Chapter 2, properties of Polytetrafluoroethylene (PTFE) and the effect of static compression by an externally applied force are investigated. In Fig. 1.1 (a), these two chains of sphers are shown as vertical columns, which are typically contained in a cylindrical guide in experiments. In the experiments and numerical calculations described in the text, the one-dimensional chains are usually impacted by a *striker* and the wave profiles are observed at an observation point within the chain, which is recorded by

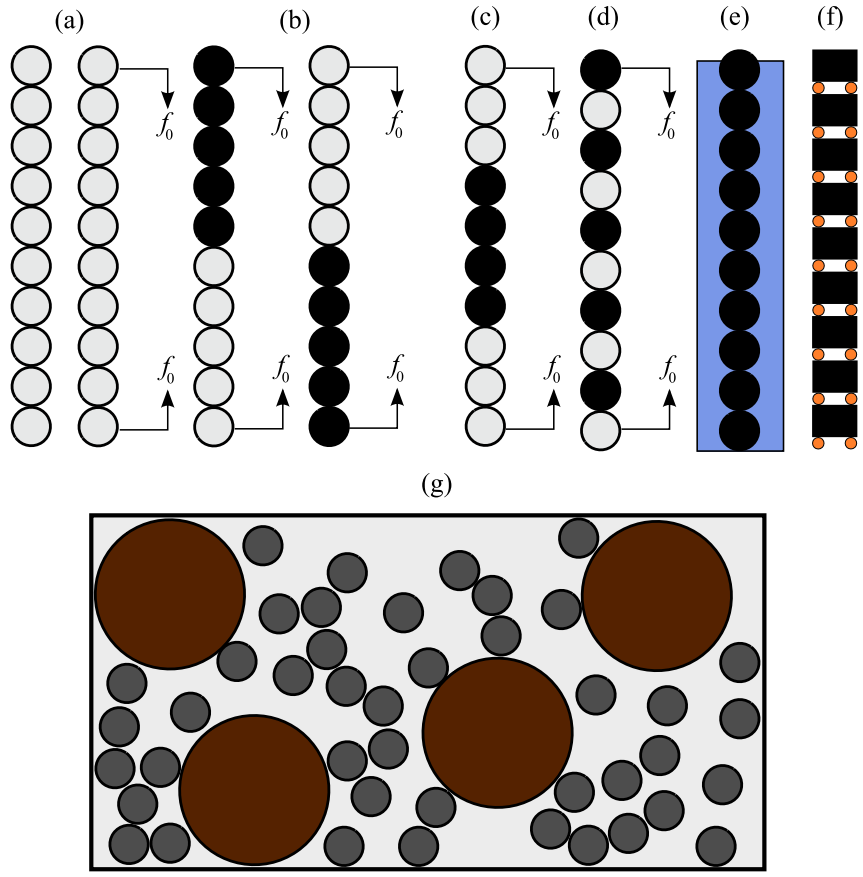

Figure 1.1: Material configurations in each chapter. (a) 1D chain of PTFE spheres without (left) and with (right) initial static compression f_0 (Ch. 2). (b) Stainless steel (black) and PTFE (gray) in two distinct cases for interface experiments including static compression (Ch. 3). (c) Stainless steel and PTFE in 'granular container' experiments (Ch. 3). (d) 1D 'diatomic' chain of stainless steel and PTFE for the investigation of frequency band-gaps that depend on f_0 (Ch. 4). (e) Stainless steel spheres immersed in different liquids (blue rectangle) for the investigation of dissipation in strongly nonlinear pulse propagation (Ch. 5). (f) Stainless steel cylinders and toroidal rubber 'o-rings' (orange circles) representing a chain with a double-power-law force-displacement relationship (Ch. 6). (g) Pressed powder composites. A PTFE (gray background) matrix contains tungsten (large brown circles) and aluminum (dark gray circles) for dynamic testing of a reactive material (Ch. 7).

a piezoelectric gauge and oscilloscope.

The materials investigated in Chapter 3 have an impedance mismatch at the interface of two disparate chains of particles. In Fig. 1.1 (b) two different configurations are shown where a chain of stainless steel (black) particles are on the top or bottom of a PTFE chain. The effects of initial static compression (f_0) are also investigated. In the second part of Chapter 3 sections of stainless steel or PTFE particles are inserted to observe the effects of the impedance mismatch as a propagating wave travels through two interfaces. This configuration is shown in Fig. 1.1 (c). Diatomic chains are investigated in Chapter 4 and can be seen in Fig. 1.1 (d). The effects of viscous dissipation on the propagation of solitary waves in stainless steel spheres is investigated in Chapter 5 (the fluid surrounding the chain is shown in Fig. 1.1 (e)). An example of a strongly nonlinear meta-material is investigated in Chapter 6 where o-rings are used to compose the first example of a double power-law material (Fig. 1.1 (f)).

In the second part of this work (Chapter 7) the dynamic behavior of compressed powder composites is investigated. An example of the microstructure of these compressed powders is shown in Fig. 1.1 (g). The motivation for these types of investigations comes from the use of these materials in defense applications [see Gourdin (1983), Gourdin (1986) for a review] in the form of plastic bonded explosives, energetic and reactive materials. Here, the investigations focus on reactive compressed powder composites, which differ from energetic and explosive materials by having a metastable chemical composition that will not react without continuous dynamic deformation (i.e. the release of chemical energy is not self-sustaining). A strongly nonlinear stress-strain behavior may be observed in reactive compressed powder composites due to the self-organization of force chains, which provide the majority of the resistance to external loading. However, the structural and chemical

performance requirements of these materials often contradict one another. For example, material failure may preclude chemical reaction wasting much of the chemical potential. Therefore, it is important to be able to predict the dynamic mechanical behavior of these materials, including any dependence on strain-rate or modes of failure, for potential applications.

1.1 One-dimensional Strongly Nonlinear Chains of Elastic Spheres

1.1.1 Elastic Contact: Using a Quasi-Static Law for Dynamic Problems

Strongly nonlinear granular materials are defined as any material that has a completely nonlinear interaction potential between adjacent particles. For example, Hertz law predicts a nonlinear force-displacement relationship for the behavior of two solid elastic bodies in contact [Hertz (1881), Hertz (1896)]. The nonlinear force-displacement relationship for two spheres in contact follows the relationship, $F \propto \delta^{3/2}$, which is a purely geometrical nonlinearity. This law is derived for the quasi-static loading of two elastic (and convex) bodies. Hertz (1896) also derived expressions for the duration of impact, which were experimentally verified soon after Hertz published his original work by Schneebeli (1885), Hamburger (1887) and Tait (1900), where materials from metals to tree sap were used to verify the predicted collision times and define coefficients of restitution depending on impact velocity, temperature, etc. An account of the progression of this work may be found in Chapter 8 of Love (1944).

Not more than 10 years later, Rayleigh (1906) extended Hertz work by considering the effects of vibrations resulting from the collision of spheres at differ-

ent impact velocities. The experiments performed by Schneebeli (1885), Hamburger (1887) and Tait (1900) provided the result that the rebounding velocities of two spheres appeared to decrease proportional to the increase of the impact velocity (i.e. the coefficient of restitution). However, it was found that the vibrations of the colliding spheres did not appreciably account for energy dissipation. This was also pointed out by C.V. Raman commenting that "*The energy thus lost* [due to oscillation] ... *can be made as small as desired by sufficiently reducing the* [atmospheric] *pressure.* [Thus] *the dissipation of energy has to be ascribed entirely to failure of perfect elasticity during impact.*" (Raman (1918)). Therefore, the use of Hertz' theory for the elastic impact of two spheres in dynamics problems is restricted by three conditions: the characteristic time of collision must be less that the oscillation period of the bodies in contact, the maximum shear stresses in the region of contact must be less that the elastic limit, and the radius of the contact surface must be much less than the radii of curvature of either contacting body.

Additional to the above mentioned modes of energy loss between contacting bodies, inter-particle friction has also been investigated in numerous recent investigations in the literature on colloids [Davis et al. (1985), Campbell (1990), Zhang et al. (1999)] and graunular chains [Reigada et al. (2003), Rosas et al. (2005), Job et al. (2005)]. Viscous dissipation has also been considered in granular chains [Duvall et al. (1969), Herbold et al. (2006), Herbold and Nesterenko (2007), Rosas et al. (2007)] in Chapter 5 resulting in a new type of wave resembling a combination of a shock and solitary wave. A nonlinear, viscoelastic dissipation is derived in the kinetic theory of granular gases in the context of binary collisions of particles where Hertz law may also be used [Brilliantov and Pöschel (2004)].

1.1.2 Waves: From Linear to Strongly Nonlinear

Each chapter in this dissertation deals with dynamic loading of materials, which invariably results in the propagation of energy in the form of waves. The nature of these waves depend on the loading conditions and may range from a short duration impact resulting in one large leading pulse or an impact of relatively long duration that may form a series of pulses or a shock wave. The mathematical descriptions of these waves in granular materials have many mathematical similarities to the descriptions of waves in fluids and gases. Among the different types of waves just mentioned, their character may also be classified by the degree of nonlinearity in the system. This is a relatively recent notion that has been developing for more than 230 years.

Linear Waves

In terms of a modern mathematical treatment of waves le Rond d'Alembert (1747) is known to be the first to publish the 'wave equation' for disturbances propagating on a stretched string. From this point on, many developments in mathematics (e.g. partial differential equations), physics and mechanics were developed in tandem, fueled by disagreements between the likes of L. Euler, D. Bernoulli, and J. Le Rond d'Alembert [Manacorda (1991)]. The original linear wave equation is applied in the classic monographs by Tyndall, Rayleigh, and Helmholtz on the theory of sound [Tyndall (1884), Helmholtz (1954), Rayleigh (1976a), Rayleigh (1976b)] that are some of the fundamentals found in physics and acoustics literature today.

More recent literature on acoustics deals with many aspects of sound propagation in linear elastic materials such as periodic elastic composites where frequency band gaps may be utilized to design properties of phononic materials for frequency

filters, or sound/vibration devices or wave-guides. For a comprehensive review of band structures in periodic elastic composites Kushwaha (1996) discusses band-gap 'crystals' in photonic and phononic materials. Sigmund and Jensen (2003) investigate the systematic design of solid materials with band-gap structures to either maximize (waveguiding) or minimize (wave damping) the structural response at the material boundaries. Fabrication of sonic crystals have been shown to reduce or completely eliminate certain frequencies passing through the material [Liu et al. (2000)]. These crystals may be fabricated to target specific frequency ranges and may be used in applications where *in-situ* tunability of the material is not necessary. Linear acoustic materials with the ability to tune the location of the band gap in the frequency spectrum has been considered by Goffaux and Vigneron (2001) where the angle of rotation of an array of solid prismatic rods in a air-filled cavity were shown to have this ability.

Weakly Nonlinear Waves

In 1834, a young Scottish engineer named John Scott Russell observed a heap of water formed at the prow of a horse drawn barge in the Union Canal at Hermiston while conducting experiments on the efficiency of canal boat designs. The wave that he observed appeared to translate without a noticeable change in speed or shape, which he called the "wave of translation" and is now known as the solitary wave [Russell (1845)]. Russell was convinced that this formation was something truly unique compared to any type of wave that had ever been observed in fluids and prompted him to initiate a series of experiments to prove it. Russell's discovery was met with much opposition from Stokes and Airy who adamantly refuted his subsequent experimental observations as misinterpretations of their linear theory. An

account of this apparent dispute is detailed in Darrigol (2005). What is surprising, however, is that even when the mathematical description of Russel's solitary wave was reported in 1895 by Korteweg and deVries (1895), Russell's discovery is never mentioned. The Korteweg deVries (KdV) is used to describe weakly nonlinear wave behavior in dispersive media (i.e. finite amplitude shallow water waves or low amplitude strain waves in precompressed granular chains). Zabusky and Kruskal (1965) investigated collisionless plasmas using the KdV equation and reported an unusual behavior of the 'solitons'. It was shown that the soliton is a nonlinear physical process where "interacting localized pulses do not scatter irreversibly" [Zabusky and Kruskal (1965)]. This stationary nature of the waves in space and time allowed an interpretation of the recurrence phenomena reported by Fermi et al. (1965) and their numerical experiments on weakly nonlinear effects in a discrete chain of masses connected by nonlinear springs.

The soliton solution of the KdV equation has implications that extend all the way back to Russell's discovery of the wave of translation describing large amplitude waves in shallow water. Russell's observation of the wave of translation and the latent mathematical and numerical investigations captured the attention of researchers in numerous branches of the physical sciences who began looking for solitons and nonlinear phenomena in their respective fields. Weakly nonlinear waves appear in numerous branches of mechanical engineering including fluids and solids (granular and microstructural [Kunin (1982)]). They also appear in electrical networks and biological systems [Remoissenet (1996)] and chemical processes [Heimburg and Jackson (2005)].

In the context of this work, weakly nonlinear waves propagate in compressed chains of spheres when the displacement due to the propagating disturbance is much less than the static displacement between masses (δ_0). The discrete equations of

motion for spherical particles (masses) in a weakly nonlinear chain is,

$$\ddot{u}_i = A\left(u_{i-1} - u_i + \delta_0\right)^{3/2} - A\left(u_i - u_{i+1} + \delta_0\right)^{3/2} \tag{1.1}$$

where u_i denotes the displacement of the particle center from its equilibrium position, $A = E\sqrt{2R}/[3m(1-\nu^2)]$, and $m = 4/3\pi\rho_0 R^3$ is the mass of the particles. In Eq. (1.1) the chain is assumed to be composed of identical particles. The displacements of the particle centers were assumed to be much smaller than the initial displacement of the particles at the outset. Equation (1.1) may be expanded using $|u_{i-1} - u_i|/\delta_0 \ll 1$ as a small parameter [Nesterenko (2001)],

$$\ddot{u}_i = \frac{3}{2}A\delta_0^{1/2}\left(u_{i-1} - 2u_i + u_{i+1}\right) + \frac{3}{8}A\delta_0^{-1/2}\left(u_{i-1} - 2u_i + u_{i+1}\right)\left(u_{i-1} - u_{i+1}\right). \tag{1.2}$$

Notice that the le Rond d'Alembert (1747) wave equation may be easily obtained from Eq. (1.2) and (1.5) when the nonlinear term (the second term on the right hand side) is negligible.[1] The continuum variable replacements are,

$$u_i = u(x,t) \tag{1.3}$$

$$\begin{aligned} u_{i-1} &= e^{-a\partial/\partial x}u(x,t) \\ u_{i+1} &= e^{a\partial/\partial x}u(x,t) \end{aligned} \tag{1.4}$$

The discrete approximation in Eq. (1.2) may be expressed as an equation for a long-wave in a continuous medium if the length of the propagating disturbance is much larger than the particle diameter $a = 2R$,

$$u_{tt} = c_0^2 u_{xx} + 2c_0\gamma u_{xxxx} - \sigma\left(u_x^2\right)_x \tag{1.5}$$

[1] Eq. (1.2) is also similar to the discrete equations used by Fermi et al. (1965) where the discrete nonlinear terms (quadradic and/or cubic) were considered a small perturbation to the linear wave equation.

where $c_0^2 = 6A\delta_0^{1/2}R^2$, $\gamma = c_0R^2/6$ and $\sigma = c_0^2R/\delta_0$. Higher order terms were neglected in Eq. (1.5) including the convective derivative, which may be negligible when the particle velocity is much less than the speed of the propagating pulse (and is close the the sound speed c_0). The KdV equation may be obtained by transformation of Eq. (1.5) [Karpman (1975)],

$$\xi_t + c_0\xi_x + \gamma\xi_{xxx} + \frac{\sigma}{2c_0}\left(\xi^2\right)_x \tag{1.6}$$

where $\xi = -u_x$. The solutions to Eq. (1.6) for stationary solitary waves (where $u(x,t) = u(x - Vt)$ and V is the pulse speed) are well known [Sander and Hunter (1991)] and have been experimentally verified in fluids and electrical, optical, and granular materials [Remoissenet (1996), Nesterenko (2001)]. The solution to Eq. (1.6) for stationary solitary waves is,

$$\xi - \xi_0 = \Delta\xi = \Delta\xi_m \mathrm{sech}^2\left[\frac{\sigma\Delta\xi_m}{24c_0\gamma}\left(x - Vt\right)\right], \tag{1.7}$$

where $V = c_0 + (\sigma/6c_0)\Delta\xi_m$ and the characteristic width of the soliton is $L = \sqrt{24c_0\gamma/\sigma\Delta\xi_m}$. At this point, one may wonder what type of behavior should be expected when the amplitude of the propagating disturbance is comparable to the initial state. For example, from Eq. (1.7) one might expect that a large amplitude wave ($\Delta\xi_m \gg \xi_0$) would have a width inversely proprotional to the square root of $\Delta\xi_m$, which would, at some point invalidate the long wave-length approximation used to derive Eq. (1.7). A more general theory exists for strongly nonlinear waves, which includes all of the previously mentioned wave equations, and is central to the optimization of the dynamic properties of strongly nonlinear materials.

Strongly Nonlinear Waves

One-dimensional chains of masses may exhibit dramatically different behavior than a linear or weakly nonlinear elastic medium when the force-displacement

relationship between masses behaves according to a power-law potential ($F \propto \delta^n$, where $n > 1$). The nonlinear dependence of force on displacement is a prerequisite for solitary wave propagation, which is not possible in linear elastic materials. These 'nonlinear' materials allow linear, weakly nonlinear and strongly nonlinear waves, corresponding to the ratio of the force amplitudes of the propagating pulse to any initial static compression force. Thus, these materials are highly sensitive to initial and boundary conditions resulting in the tunability of strongly nonlinear chains (Chapter 2) anomalous reflected compression pulses from the interface of two different chains (Chapter 3, the 'acoustic-diode' effect), enhanced mitigation properties (Chapters 3 and 6) and tunable frequency band-gaps in 'diatomic' mass chains (Chapter 4).

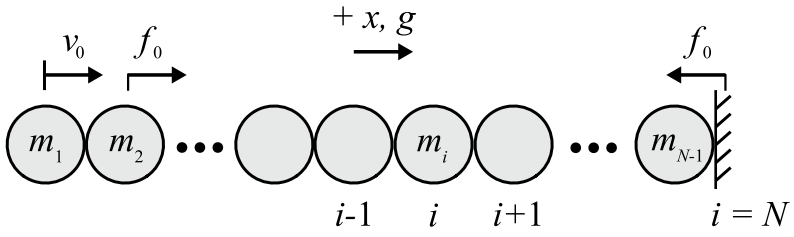

Figure 1.2: Schematic of a typical one-dimensional column (chain) of spheres (particles), which may or may not include an initial static compression force f_0 ($f_i = f_0$ from Eq. (1.8). The left-most sphere (the striker or piston) impacts the particles and the disturbance propagates from left to right. The positive coordinate and direction of the gravitational field (if applicable) are also shown. A stationary boundary or 'wall' is usually defined after the last particle in the chain.

Strongly nonlinear strain waves of finite and fixed size propagate in chains composed of adjacent masses with power law interaction potentials (or any positive

power-law repulsive relationship with an exponent greater than unity). The existence of solitary waves in lattices with power-law repulsive potentials was proven in Friesecke and Wattis (1994). The discrete equations of motion for a chain of contacting particles are,

$$m\ddot{u}_i = A_{i-1,i}\left(u_{i-1} - u_i\right)^n - A_{i,i+1}\left(u_i - u_{i+1}\right)^n + mg + f_i(t, u(x,t), v(x,t)) \quad (1.8)$$

where $u_i = u_i(x,t)$ is the particle displacement, $A_{i-1,i}$ and $A_{i,i+1}$ denote the effective stiffness of the contact, m is the mass of the particle, g is the gravitational constant and f_i may be an applied force (constant or varying), an additional function related in the case of multiple power laws (Chapter 6) or a dissipative function depending on the velocity $v(x,t)$ (Chapter 5). Eq. (1.8) is similar to Eq. (1.1) except the initial displacement of the particles, δ_0, is not included. A typical example of the discrete chain is shown in Fig. 1.2.

Interestingly, the finite width of a strongly nonlinear solitary wave depends only on the exponent n of the interaction potential [Nesterenko (1983), Nesterenko (2001)]. In Hertzian systems (where $n = 3/2$) the width is about five times the width of the particles in the chain. Larger values of the power law exponent correspond to shorter wave lengths [Rosas and Lindenberg (2004)]. It is quite remarkable that the exact solution of the long-wave approximation of Eq. (1.8) adequately describes the strain waves found in experiments using one-dimensional granular systems despite the fact the wavelength is so close to the spatial size of the particles in the system. In this sense, the wave equations derived for the discrete chain of particles first given by Nesterenko (1983) may be thought of as the limiting case for continuum wave equations. To illustrate this point consider, for example, the chain of particles shown in Fig. 1.2 for $f_0 > 0$. Under conditions of impact by the first particle, this system will propagate an impulse according to different nonlinear regimes, which

depend on the ratio of the amplitudes of the propagating impulse (in units of force, for example) to the level of static compression f_0. Therefore, the absence of static compression corresponds to a strongly nonlinear system where the aforementioned ratio is infinite. For moderate levels of static compression the wave amplitude may be considered as a small parameter for expansion in the long wave approximation of Eq. (1.8). It has been shown Nesterenko (2001) and in the previous section that this second small parameter results in equations for weakly nonlinear waves; the Korteweg-De Vries (Eq. (1.6)) and Boussinesq (Eq. (1.5)) equations.

1.1.3 Statics in a Chain of Contacting Elastic Spheres

In the numerical calculations of one-dimensional chains of nonlinearly interacting elements, using some form of the discrete Eq. (1.8), the static configuration needs to be determined. Often times in two and three dimensional systems (especially if there is any disorder) the boundary conditions are applied and a calculation is commenced with an artificial viscosity to quickly equilibrate the system of particles. However, this method consumes a significant portion of the total simulation time as the number of particles increases. For calculations of chains similar to Fig. 1.2 the boundary conditions in one-dimension are given for a chain of particles interacting with an arbitrary single power-law interaction (see Chapters 1-5) and the double power-law interaction given in Chapter 6 (using $n_1 = 3/2$ and $n_2 = 6$). The equilibrium positions of the particle centers for two different cases are presented here.

Compressed Chain of Spheres with an Arbitrary Power Law Interaction

The chain of spheres compressed by an initial compressive force is statically determinate when there is a fixed boundary at one end. To find the positions of the

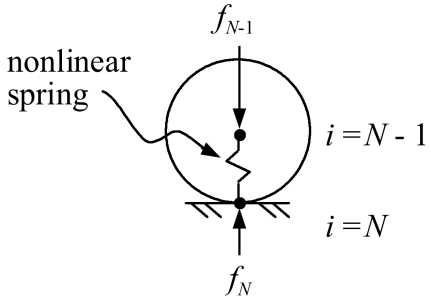

Figure 1.3: Schematic of the equivalent static forces at the boundary of a granular chain.

sphere centers under gravitational and/or a constant compressive force the problem may be solved iteratively from this fixed boundary using the displacement u_{i+1} to find u_i. From the bottom, f_{N-1} is defined as the sum of all forces above the solid boundary (where $u_N = 0$). Thus, f_N is the reaction force at this boundary (see Fig. 1.3). The problem is then equivalent to finding the change in length of a nonlinear spring, which is depicted in Fig. 1.3. The expression for f_{N-1} in this figure is

$$f_{N-1} = \sum_{k=1}^{N-1} \left(m_k g + f_k \right), \tag{1.9}$$

which may include any number of applied forces above the boundary. The equation for f_N is

$$f_N = m_{N-1} A_{N-1,N} \left(u_{N-1} - u_N \right)^n \tag{1.10}$$

For the statics problem $f_{N-1} = f_N$ for equilibrium. Thus,

$$u_{N-1} = \left[\frac{1}{A_{N-1,N}} \sum_{k=1}^{N-1} \left(m_k g + f_k \right) \right]^{1/n} + u_N \tag{1.11}$$

Once u_N is known, the general form of Eq. (1.11) is

$$u_i = \left[\frac{1}{A_{i,i+1}} \sum_{k=1}^{i} \left(m_k g + f_k \right) \right]^{1/n} + u_{i+1}, \tag{1.12}$$

which may be applied to find the displacements of particles u_{N-1} to u_2 or u_1 depending on whether the first particle needs to be considered as a part of the compressed chain.

Compressed Chain of Elements with a Double Power-Law Interaction

In Chapter 6 the discrete equations of motion for a double power-law interaction is [Lindley (1966a), Lindley (1966b), Freakley and Payne (1978)]

$$\begin{aligned} m_k\ddot{u}_k &= A_{k-1,i}\left(u_{k-1}-u_k\right)^{3/2} \\ &+ B_{k-1,k}\left(u_{k-1}-u_k\right)^{6} \\ &+ A_{k,k+1}\left(u_k-u_{k+1}\right)^{3/2} \\ &+ B_{k,k+1}\left(u_k-u_{k+1}\right)^{6} \\ &+ m_k g + f_{c,k}. \end{aligned} \tag{1.13}$$

For a chain with N masses in equilibrium, Eq. (1.13) becomes,

$$A_{N-1,N}\left(u_{N-1}-u_N\right)^{3/2} + B_{N-1,N}\left(u_{N-1}-u_N\right)^{6} + \sum_{k=0}^{N-1}(m_k g + f_{c,k}) = 0, \tag{1.14}$$

where $u_N = 0$ is the displacement of the boundary and is kept for convenience. Since u_N is known, Eq. (1.14) is the template for an iterative scheme to find the displacements from mass N to 1. Equation (1.14) may be simplified:

$$AU^{3/2} + BU^6 + \gamma = 0, \tag{1.15}$$

where $U = u_{i-1} - u_i$, $A = A_{i-1,i}$, $B = B_{i-1,i}$ and $\gamma = 1/A_{i-1,i}\sum_{k=0}^{i-1}(m_k g + f_{c,k})$. This can be solved for U with the quartic formula

$$U = \frac{1}{24}^{1/3}\left(\sqrt{4\gamma\left(\frac{144}{r}\right)^{1/3} + 72\left(\frac{A}{B\sqrt{s}}\right) - (12r)^{1/3}/B} - \sqrt{\frac{s}{6}}\right)^{2/3} \tag{1.16}$$

where

$$r = \sqrt{3}B\left(3\sqrt{3}A^2 + \sqrt{256\gamma^3 B + 27A^4}\right) \tag{1.17}$$

and

$$s = 6\,(12)^{1/3}\left(r^{1/3}/B - 4\gamma\,(12/r)^{1/3}\right). \tag{1.18}$$

Since the displacement at the boundary is always zero (i.e. $u_N(t) = 0$), u_{N-1} may be computed with Eq. (1.16). Once u_{N-1} is computed, u_{N-2} can be calculated. This procedure continues until u_1 is found. Note that the displacement of each mass is dependent upon the gravitational field and compressive (or tensile) forces above itself.

1.2 Dynamic Mechanical Properties of Pressed Powder Composites

In the previous sections the elastic and dynamic contact of 'grains' were introduced with the intent of investigating different configurations of ordered metamaterials for acoustic or shock mitigating applications. These sections are also pertinent for investigating compressed powder composites, but the focus is shifted from wave dynamics to dynamic mechanical properties. The mechanical properties of these composites are highly dependent on the morphology, material composition, size distribution, and composite material synthesis (e.g. pressing pressure, temperature, mass/volume fractions, etc.).

In Chapter 7 the investigated pressed powder composites are reactive materials, where the chemical reaction between the constituent materials takes place during compression at high strain-rates. These materials are relatively new, in concept, dating back to 1971 [Office of Naval Research (2005)] when W. H. Holt and

W. Mock, Jr. conceived these materials, which had the potential to be "500 percent more effective than current U.S. weapons." (Office of Naval Research (2005)). One of the distinguishing features of reactive materials is that the stored chemical potential is released upon material deformation and is not self-propagating in contrast to energetic materials, which may support detonation waves depending on the initiation energy threshold.

The complexity of the microstructure of these composite materials make it difficult to estimate its overall strength and the material's response *a priori*. The material structure may be optimized at the meso-scale in order to facilitate the desirable release of mechanical and subsequent chemical energy in hot spots (e.g. shear bands) to optimize the amount and/or rate of energy release by the material. For example, varying particle size and morphology in pressed explosives (Setchell (1984), Bardenhagen and Brackbill (1998), J.C. Foster et al. (2000), Roessig et al. (2002)) or layer thicknesses in laminates Mann et al. (1997) significantly alter the shock-sensitivity and the rate of energy release. Ignition sites within composite energetic materials under compressive load have been ascribed to the stress or force-chain formation in granular energetic materials [Balzer et al. (2004), Siviour et al. (2004)].

2

Characterization of Viable Materials for Strongly Nonlinear Wave Propagation

This chapter will extend the overview by including mathematical descriptions of the one-dimensional chains as well as experimental apparatus used (some of which will appear in the appendix). I will discuss the characterization of PTFE as a viable material for strongly nonlinear wave propagation as well as point out other candidate materials. Some experimental and numerical results will be provided and proper reference to the appendices will be indicated throughout.

2.1 Strongly Nonlinear Waves in a Chain of Teflon Beads

One of the distinguished properties of strongly nonlinear materials is the existence of a qualitatively new solitary wave with a finite width that is independent of amplitude. This solitary wave was first discovered in 1983 analytically and numerically by Nesterenko (1983) and later in 1985 it was observed in experiments [Lazaridi and Nesterenko (1985)]. Strongly nonlinear wave dynamics is a relatively new area of interest, which is a natural extension of weakly nonlinear wave dynam-

ics described by the Korteweg-de Vries equation (Eq. (1.7)) [Nesterenko (1992a)]. Statically compressed, strongly nonlinear granular chains may behave as weakly nonlinear systems similar to the one considered in Fermi et al. (1965). In contrast to weakly nonlinear systems, the behavior of strongly nonlinear uncompressed granular chains exhibit qualitatively new features [Nesterenko (1992a), Hascoët and Herrmann (2000), Nesterenko (2001), Sen and Manciu (2001), Reigada et al. (2003), Musienko and Manevich (2004), Kastner (2004b), Kastner (2004a)]. Novel applications might arise from understanding the basic physics of these one-dimensional systems. Sound focusing devices (tunable acoustic lenses and delay lines), sound absorption layers and sound scramblers are among the most promising engineering applications.

Non-classical, strongly nonlinear wave behavior appears if the granular material is weakly compressed [Nesterenko (1983), Lazaridi and Nesterenko (1985), Nesterenko (2001)]. In this case, the amplitude in a wave is significantly higher than the forces caused by initial precompression. The anharmonic approximation based on the small parameter (ratio of wave amplitude to initial precompression) is not valid. The principal difference between the strongly nonlinear case and the "strongly" compressed weakly nonlinear chain is due to the lack of a small parameter with respect to the wave amplitude in the former case. The long wave equation for particle displacement u for strongly nonlinear waves [Nesterenko (1983), Nesterenko (2001)] is,

$$u_{tt} = -c^2 \left((-u_x)^{3/2} + \frac{a^2}{10} \left\{ (-u_x)^{1/4} \left[(-u_x)^{5/4} \right]_{xx} \right\} \right)_x , \tag{2.1}$$

where,

$$-u_x > 0, \quad c^2 = \frac{2E}{\pi\rho\left(1-\nu^2\right)}, \quad c_0 = (3/2)^{1/2} c\xi_0^{1/4}. \tag{2.2}$$

Here E, ρ, and ν are the bulk elastic modulus, density, and Poisson ratio of the

particles in the chain. The particle diameter is denoted by a and ξ_0 is the initial strain in the system (phononic crystal). It should be mentioned that constant c is the same order of magnitude as the bulk sound speed in the particle material and not the sound speed in the phononic crystal. Instead, the parameter c_0 corresponds to the long wave sound speed, which is related to the initial strain ξ_0. This equation for high amplitude pulses (or for negligible precompression) has no characteristic wave speed and its solution is independent of amplitude. The regularized equation and the equation for a general interaction law can be found in Nesterenko (2001). Despite its complex nature Eq. (2.1) has simple stationary solutions with unique properties that are similar to the stationary solutions for the discrete chain even though some differences due to the relatively short width of solitary wave exist [Nesterenko (1983), Chatterjee (1999), Hascoët and Herrmann (2000), Nesterenko (2001), Sen and Manciu (2001), Manciu and Sen (2002), Rosas and Lindenberg (2004)]. The solitary wave speed V_s in a sonic vacuum can be closely approximated by one hump of a periodic solution with finite length L equal to only five particle diameters [Nesterenko (1983), Nesterenko (2001)]:

$$\xi = \left(\frac{5V_s^2}{4c^2}\right)\cos^4\left(\frac{\sqrt{10}}{5a}x\right) \tag{2.3}$$

The concept of a sonic vacuum was introduced in Nesterenko (1992c), Gavrilyuk and Nesterenko (1993), Nesterenko (1993), Nesterenko (1994) to emphasize the fact that in an uncompressed chain (ξ_0=0) the characteristic sound speed is equal to zero. The solitary wave speed V_s has a nonlinear dependence on the maximum

strain ξ_m, the particle velocity ξ_m and the force between particles F_m:

$$\begin{aligned} V_s &= \frac{2}{\sqrt{5}} c \xi_m^{1/4} \\ &= \left(\frac{16}{25}\right)^{1/5} c^{4/5} v_m^{1/5} \\ &= 0.68 \left(\frac{2E}{a\rho^{3/2}\left(1-\nu^2\right)}\right)^{1/3} F_m^{1/6} \end{aligned} \tag{2.4}$$

In a weakly compressed chain a supersonic solitary wave ($V_s > c_0$) with an amplitude much higher than the initial precompression propagates with a speed V_s, which can also be closely approximated by one hump of the periodic solution corresponding to zero prestress [Nesterenko (1983), Nesterenko (2001)].

The speed of a wave in a sonic vacuum can be infinitesimally small if the amplitude of the wave is also small. It is interesting that a strongly nonlinear system supports solitary waves that are composed from a constant strain and only two harmonics (with a wavelength approximately equal to $2.5a$ and $5a$ respectively) (see Eq. (2.3)). The existence of this unique wave was verified analytically, numerically and in experiments [Nesterenko (1983), Lazaridi and Nesterenko (1985), Nesterenko (1992a), Shukla et al. (1993), Zhu et al. (1997), Coste et al. (1997), Manciu et al. (1999b), Hinch and Saint-Jean (1999), Coste and Gilles (1999), Chatterjee (1999), Hascoët and Herrmann (2000), Nesterenko (2001), Manciu and Sen (2002)]. This solitary wave can be considered as a soliton in a physically reasonable approximation [Nesterenko (1983), Nesterenko (1992a), Nesterenko (2001)], though small amplitude secondary solitary waves were observed in numerical calculations after the collision of two identical solitary waves. The ratio of the largest amplitude of the secondary wave to the amplitude of the original wave is about 0.02 [Manciu et al. (2001)]. This solitary wave is of a fundamental interest because Eq. (2.1) is more general than the weakly nonlinear KdV equation, which describes the behavior of various physical

systems [Remoissenet (1996)] and the former includes the latter.

The solitary wave speed V_s in a chain with an initial finite strain ξ_0 due to an applied static compression for, which may be used to 'tune' the wave speeds, can be written in terms of the normalized maximum strain $\xi_r = \xi_m/\xi_0$ or force $f_r = F_m/F_0$ [Nesterenko (2001)]:

$$\begin{aligned} V_s &= \frac{c_0}{\xi_r - 1}\left\{\frac{4}{15}\left[3 + 2\xi_r^{5/2} - 5\xi_r\right]\right\}^{1/2} \\ &= \frac{0.9314}{f_r^{2/3} - 1}\left(\frac{4E^2F_0}{a^2\rho^3\left(1-\nu^2\right)^2}\right)^{1/6}\left\{\frac{4}{15}\left[3 + 2f_r^{5/3} - 5f_r^{2/3}\right]\right\}^{1/2} \end{aligned} \tag{2.5}$$

For simplicity only the leading approximation was used to connect the strains in the continuum limit and the forces in a discrete chain in Eqs. (2.4) and (2.5).

It is important to mention that V_s can be significantly smaller than the bulk sound speed in the material composing the beads and can be considered approximately constant at any narrow interval of its relative amplitude f_r. The described properties of strongly nonlinear waves might allow the use of sonic vacuum based materials as effective delay lines with exceptionally low speed of signal propagation. The estimation based on Eq.(2.4) with Youngs modulus $E = 600$ MPa, Poissons ratio $\nu = 0.46$ and density $\rho = 2.210^3$ kg/m^3 [DuPont product information] of PTFE shows that it is possible to create materials with an impulse speed below 100 m/s, which corresponds to a particle velocity of 0.2 m/s or smaller. This signal speed in condensed soft matter is below the level of the sound speed in gases at normal conditions. In this chapter the experimental results for pulse propagation in chains of PTFE spheres are explained in accord with the main conclusions of the outlined strongly nonlinear theory. The speed of the signals is in the range of 88 m/s to 168 m/s. Uniformly compressed discrete chains are considered in numerical analysis and in experiments [Nesterenko (1992a), Nesterenko (2001), Arancibia-Bulnes and Ruiz-

Suárez (2002)]. It was shown that the solitary wave speed generated by an impact of a piston with the same velocity increases with precompression. Also, the tendency of the impulse to split into a train of solitary waves decreases and the solitary wave width increases. Gravitationally loaded discrete chains are considered in numerical calculations in Hong et al. (1999), Sen et al. (2001), Hong and Xu (2001).

It should be noticed that particles with Hertzian contacts serving as strongly nonlinear springs are not the only way of discovering a sonic vacuum type system. Any power law interaction between particles ($n > 1$) results in a similar behavior [Nesterenko (1992c), Hascoët and Herrmann (2000), Nesterenko (2001)]. Also, any general strongly nonlinear interaction laws support solitary waves with a finite length for the long wave approximation [Nesterenko (2001)]. Different physical systems can be designed with properties suitable for the realization of sonic vacuum type behavior. For example, a forest of vertically aligned carbon nanotubes exhibits strongly nonlinear but non Hertzian type force interaction with spherical particles which can be used for assembling strongly nonlinear phononic crystals [Daraio et al. (2004a)].

The solitary wave width for general strongly nonlinear interaction law is proportional to the bead diameter (or distance between particles) and the speed has a nonlinear dependence on amplitude [Nesterenko (2001)]. It is interesting that a power-law interaction with $n = 3$, corresponding to a physical system of particles on an unstretched string in transverse vibrations [Nesterenko (1992c),Nesterenko (2001)] supports periodic harmonic waves and solitary waves with a linear dependence of maximum strain on speed.

2.1.1 Experimental Procedures and Results

One-dimensional phononic crystals were assembled filling a PTFE hollow cylinder (with inner diameter 5 mm) with chains of 11 and 21 PTFE spheres (McMaster-Carr catalogue) with a diameter equal to $a = 4.76$ mm and a mass equal to $m = 0.1226$ g (standard deviation 0.0008 g) (Fig. 2.1). Different numbers of particles were used to clarify the stages of impulse transformation and interaction with the wall. A chain assembled from 18 PTFE particles with smaller diameter a=2.38 mm and mass equal to 0.0157 g (standard deviation 0.0003 g) in a PTFE tube with an inner diameter equal to 2.5 mm was also tested. Using two different sizes of beads helps to understand the behavior of the investigated polymeric material in the contact area at different stresses, strains and strain rates, which are dependent on the particle size. Scaling down the particle sizes is important for future applications in different devices (i.e. biomedical application, imaging, sound scrambling, etc.). Waves of different amplitudes and durations were excited by impacting the top of the chain with strikers of different masses and velocities.

The experimental set-up for measurements of solitary wave speed, duration and force amplitude together with the measurements of the reflected pulse from the wall is presented in Fig. 2.1. It includes three calibrated piezo-sensors (RC 103 μs) connected to a Tektronix 2014 oscilloscope. Two lead zirconate titanate based piezo-gauges (3 mm side plates with thickness 0.5 mm) with nickel plated electrodes and custom microminiature wiring, supplied by Piezo Systems, Inc., were embedded inside two PTFE particles similar to [Nesterenko (2001),Nesterenko et al. (1995),Job et al. (2005)]. The particles with embedded sensors consisted of two PTFE caps with a total mass $2M = 0.093$ g and a sensor with a mass $m = 0.023$ g glued between these caps. Including glue, the total mass of the sensor was equal to 0.116 g (Fig.

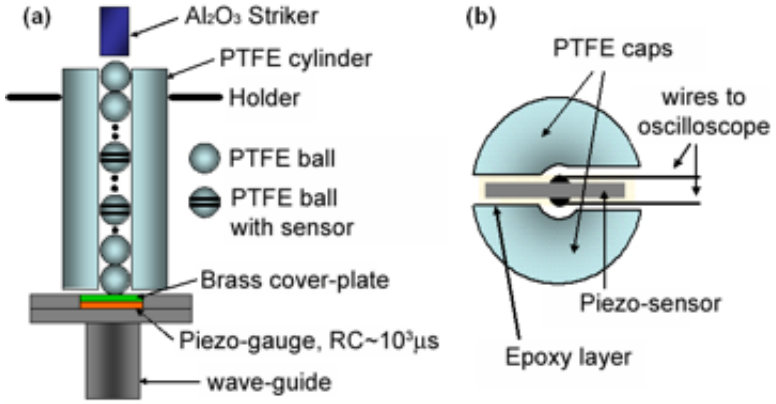

Figure 2.1: (a) Experimental setup for testing of one-dimensional phononic crystals with PTFE spheres; (b) schematic drawing of a particle with an embedded piezosensor.

2.1(b)), which was very close to the mass of the PTFE particle 0.123 g. This design allows a calculation of the speed of solitary wave simultaneously with measurement of the forces acting inside the particles.

A third piezo-gauge, supplied by Kinetic Ceramics, Inc., was bonded with epoxy on electrode foils for contacts and reinforced by a 1 mm brass plate on the top surface. The sensor assembly was then placed on the top surface of a long vertical steel rod (wave-guide) embedded at the other end into a steel block to avoid possible wave reverberation in the system (Fig. 2.1(a)). This sensor was calibrated by using the impact of a single steel sphere, which provides similar conditions of loading as in the experimental measurements. The initial velocity of the steel sphere and the linear momentum conservation law were used for calibration. The area under the force-time curve measured by the gauge was integrated from the beginning of impact up to the point of maximum force and compared with linear momentum of particle at the beginning of impact. The sensors in the two particles were calibrated by

comparison with the signal from the sensor at the wall. This was done using a controlled, relatively long, simultaneous loading of the particle with the sensor and the sensor in the wall by an impact of a massive piston.

The introduction of a particle with a different mass (particle with a sensor) in the chain of particle of equal masses results in wave reflections investigated in Manciu et al. (2000), Hascoët and Herrmann (2000), Sen et al. (2001). It was suggested to use reflected signals for the detection of buried inclusions [Manciu et al. (2001)]. In numerical calculations, a slightly lighter particle with mass 0.116 g was introduced into the chain of particles with mass 0.123 g producing wave reflections that would be too small to detect experimentally. Attenuating soliton like pulse in a chain of random particles was considered in Nesterenko (1983), Nesterenko (1992a), Nesterenko (2001), Manciu et al. (2001).

To interpret the signal measured in the experiments the particle with an embedded sensor was considered as a rigid body (Fig. 2.2(a)). The forces on the sides of the contacts of the particle (F_1 and F_2) can be easily related to the forces acting on both sides of the sensor (F_3 and F_4):

$$\begin{aligned} F_3 &= \frac{F_1+F_2}{2} + \frac{F_1-F_2}{2}\frac{m}{2M+m}, \\ F_4 &= \frac{F_1+F_2}{2} - \frac{F_1-F_2}{2}\frac{m}{2M+m} \end{aligned} \tag{2.6}$$

From Eq. (2.6) the average of the compression forces, F_3 and F_4, (considered positive) is equal to the average value of forces F_1 and F_2, $F \equiv (F_1+F_2)/2$ acting on the particle contacts. It should be mentioned that in the numerical modeling of the system the particles are considered rigid bodies and only contact forces F_1 and F_2 are taken into consideration. The time dependence of forces on the particle contacts were calculated numerically and their average values are presented in Fig. 2.2(b).

In the case of $m \ll M$, the forces on each side of the sensor (Eq. (2.6))

are very close to the average forces on the particle contacts [Nesterenko (2001), Nesterenko et al. (1995)]. In this case the forces F_3 and F_4 deviate from their average value by less than 20% in the vicinity of signal shoulders, and are seen from the time dependence of contact forces in Fig. 2.2(b). It should be noted that at the moment when the averaged force F is maximum it is equal to the corresponding forces F_3 and F_4 (Fig. 2.2(b), Eq. (2.6)). A comparison of averaged force and contact forces (Fig. 2.2(b)) reveals that averaging reduces the maximum amplitude of the force and increases the duration of the pulse. This averaged curve is used for the comparison with experimental results based on the sensors embedded in the particles.

To relate the maximum value of average compression force $F_{m,e}$ measured by the embedded sensor to the value of the maximum force at the contact between neighboring particles (Fig. 2.2(a)), a coefficient β was determined in numerical calculations. It represents the ratio of the dynamic force on the particle contacts to the maximum average of dynamic forces $F_{m,n}$ acting on the two contacts of the given particle in the solitary wave. Relating the two forces facilitates the use of Eqs. (2.4) and (2.5) with experimental data. The dependence of β on the normalized force amplitude of a solitary wave is presented in Fig. 2.2 (c). This coefficient has negligible dependence on elastic moduli of PTFE particles ($< 1\%$ in investigated range of a solitary wave amplitude and relevant range of elastic modulus from 600 MPa to 1460 MPa). It should be mentioned that the investigated range of relative amplitudes of the dynamic force and static compression represents a strongly nonlinear regime of the system behavior resulting in relatively short wavelength solitary waves. The coefficient β is approximately equal to 1 in the linear regime when the amplitude of the dynamic force is much smaller than the initial precompression and the solitary

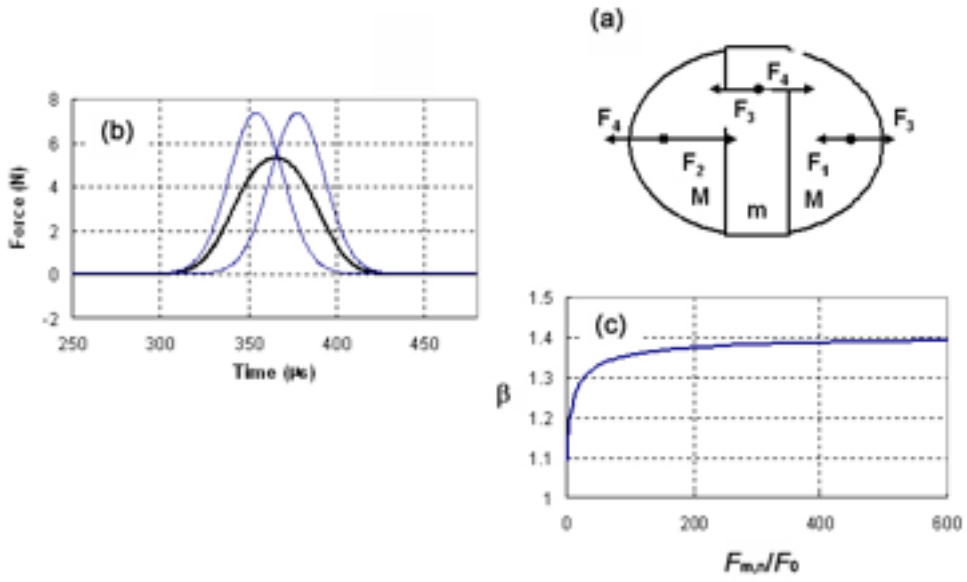

Figure 2.2: (a) Schematic drawing showing the forces acting on the different parts of particle with embedded sensor; (b) Force vs. time plot obtained in numerical calculations for the two contacts of the particle with embedded sensor (left and right curves corresponding to F_1 and F_2) and the average of the previous two (central curve); (c) Dependence of the coefficient β on the amplitude of the normalized dynamic average force ($F_{m,n}/F_0$) in the solitary wave ($F_{m,n}$ is the maximum of the central curve in (b)), found in numerical calculations.

waves are very long in comparison with a particle diameter.

The maximum compression force on the contact between two particles (F_m) adjacent to the particle with the sensor was calculated using the equation:

$$F_m = \beta F_{m,e} + F_0, \tag{2.7}$$

where $F_{m,e}$ is the maximum averaged dynamic compression force measured experimentally by the gauge embedded in the particle (it is represented by $F_{m,n}$ in numerical calculations) and F_0 is the gravitational compression.

Pulses of different durations and amplitudes in the one-dimensional phononic crystals were generated by an impact of an alumina (Al_2O_3) cylinder (0.47 g), a PTFE sphere with a diameter of 4.76 mm (mass 0.123 g) or a stainless steel bead with a diameter of 2 mm (mass 0.036 g) onto the top particle of the chain. Single solitary waves can be generated by an striker with a mass equal to the mass of the spheres in the system which is physically equivalent to the application of a δ-function force [Nesterenko (1983), Nesterenko (1992a), Nesterenko (2001)]. To generate a single solitary wave in a chain of 21 PTFE spheres, the mass of the striker was equal to m=0.123 g. Sensors were placed in the 9^{th} and 5^{th} ball from the bottom and in the wall at the bottom of the vertical chain.

The theoretically predicted speed of solitary waves in strongly nonlinear phononic crystals has a strong dependence on the amplitude represented by Eqs. (2.4) and (2.5) for sonic vacuums and for statically compressed chains, respectively. This is shown in Fig. 2.3(a) together with the corresponding numerical calculations of the solitary wave speed for discrete chains. The curves based on the long wave approximation (Eqs. (2.4) and (2.5)) and the numerically calculated values practically coincide. In experiments (solid dots in Fig. 2.3(b)), the solitary wave speeds

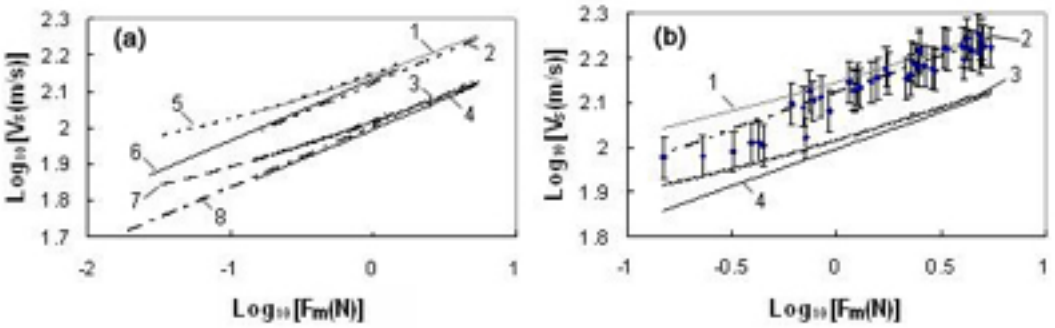

Figure 2.3: Dependence of the solitary wave speed on its amplitude. (a) Comparison of numerical results for a discrete chain and analytical data obtained from the long wave approximation. Curves 1 and 3 represent the long wave approximation for gravitationally pre-compressed systems (Eq.(2.5)) at E=1460 MPa and E=600 MPa respectively; curves 5 and 7 represent the corresponding numerical calculations for a discrete chain. Curves 2 and 4 are the theoretical curves based on Eq.(2.4) for a sonic vacuum with a Youngs modulus equal to 1460 MPa and 600 MPa respectively. Curves 6 and 8 represent the corresponding numerical calculations for these cases. (b) Comparison of the experimental values (shown by solid dots) with the curves obtained from the long wave approximation. Curves 1-4 in (b) are the same as in (a).

for different amplitudes were obtained by dividing the distance between the sensors by the measured peak-to-peak time interval. The corresponding force amplitude in the solitary wave was found based on the measurements of gauges embedded inside the particles. The $\log_{10} F_m - \log_{10} V_s$ curves presented in Fig. 2.3(b) are based on these measurements. The accuracy of the measurements of the amplitude of solitary waves was in the range of 15% to 30 % for large and small amplitudes. The larger errors are due to the higher signal to noise ratio at low amplitudes. In experiments the accuracy of the speed measurement can be estimated within 10 % due to the uncertainty in the sensors alignment (approximately 1 mm for each sensor).

After measuring the speed and duration of the propagating pulse, the widths of solitary waves were calculated for the corresponding force amplitudes (Table 2.1). The same data obtained from the numerical analysis of discrete chains with the elastic modulus of PTFE euqal to 1.46 GPa, which based on the averaged forces on the particle contacts, are also shown along with the solitary wave width truncated at the level 0.2% and 4% of the solitary wave amplitude.

Experimental results for forces measured by sensors embedded into the particles and into the wall corresponding to a 2.0 m/s impact velocity are shown in Fig. 2.4(a). The zero time in all experiments corresponds to the start of the recording triggered by the signal. In the numerical calculations presented in all figures the zero time corresponds to the moment of impact.

One of the distinguished features of strongly nonlinear sonic vacuum type system is the fast decomposition of a shock type pulse caused by an impact on a short distance from the impacted side [Nesterenko (1983), Nesterenko (1992a), Nesterenko (2001)]. To check if the PTFE based strongly nonlinear phononic crystal exhibits this property, the impact by striker with a larger mass (Al_2O_3 cylinder 0.47 g) was

Table 2.1: Experimental data for amplitude, speed, duration and normalized width of solitary wave in the PTFE chain composed of particles with diameter 2R=4.76 mm. Numerical data for discrete chains are also presented for comparison.

	Experimental Data			Numerical Results		
F_m	Duration	V_s	$L/2R$	V_s	L/2R	L/2R
[N]	[μs]	[m/s]		[m/s]	(at 0.2%)	(at 4%)
5	153	168	5.4	190	5.4	4.0
2	164	152	5.2	164	5.7	4.1
0.6	233	106	5.2	137	6.2	4.3
0.1	326	97	6.6	109	7.8	5.3
0.06	360	88	6.7	103	8.6	5.7

employed to create a longer initial shock pulse in chains of different lengths. This impact results in an incoming pulse shape at the entrance of the system with the rise time equaling 50 μs and an initial decay with the characteristic exponential behavior $A\exp(-0.0185t)$, where the time (t) is measured in microseconds, starting from the peak of the signal with amplitude A. The total duration of the incident signal is equal to 370 μs. The result for the short chain composed of 11 PTFE particles is presented in Fig. 2.5(a).

It is important to note that if the exponential curves are drawn through the solitons maxima, corresponding to the force history at a given point (in Fig. 2.5 this point corresponds to the wall), they will depend on the position of the sensor due to the dependence of solitary wave speeds on amplitude. Exponential decays corresponding to experimental data and numerical calculations at the wall

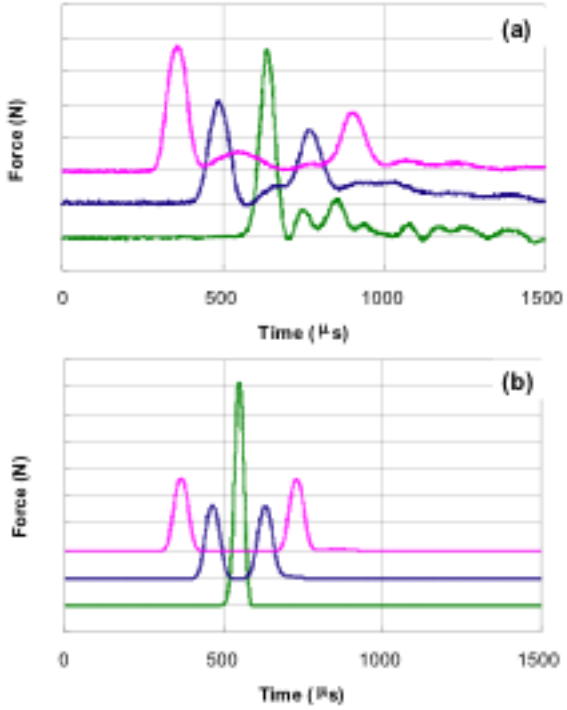

Figure 2.4: Solitary waves in a PTFE chain generated by PTFE ball-striker with a velocity of 2 m/s: (a) incident, reflected solitary waves and force on the wall detected experimentally in the chain of 21 PTFE beads with diameter 4.76 mm. The curves represent force vs. time detected by the sensor embedded into the 9th ball from the wall (top curve), and by the sensor in the 5th ball from the wall (middle curve) and at the wall (the vertical scale is equal to 0.5 N); (b) numerical calculations for a discrete chain under conditions corresponding to experimental conditions in (a). Curves represent the average value of the forces acting on the top and bottom contact of each sensor. Grid scaling on the vertical axes is 2 N.

are $A_e \exp(-0.0067t)$ and $A_n \exp(-0.0059t)$ (the time is measured in microseconds). The absolute values of the coefficients in these exponents are about three times smaller than in the incident pulse (0.0185) due to the dependence of solitary wave speeds on amplitude. Despite the evident attenuation in experiments ($A_e < A_n$) the corresponding exponents for enveloping curves in experimental data and numerical calculations are close to each other. This suggests that the attenuation of the solitary waves is not strongly dependent on their amplitudes at the investigated range of amplitudes.

A chain of smaller diameter PTFE particles (2.38 mm) was also investigated to determine the diameter-dependence of strongly nonlinear behavior of PTFE-sphere-based sonic vacuum and dissipative properties. It should be mentioned that based on Hertz law the radius of the contact area is decreasing with particle radius under the same force. The experimental results are presented in Fig. 2.6 (a) for a short duration of shock loading (impact by a 2 mm diameter steel ball with a mass about 2.3 times that of the PTFE particle) and for relatively long duration of impact induced by a PTFE ball with a diameter 4.76 mm and mass 0.123 g (Fig. 2.6(c)).

2.1.2 Numerical Calculations

It was shown previously [Nesterenko (1983),Lazaridi and Nesterenko (1985), Nesterenko (1992a), Coste et al. (1997), Coste and Gilles (1999), Nesterenko (2001)] that wave propagation in one-dimensional system of linear elastic beads can be described considering particles as rigid bodies connected by nonlinear springs according to Hertz law (Eq. 2.8) for contact interaction of spheres [Hertz (1881), Timoshenko

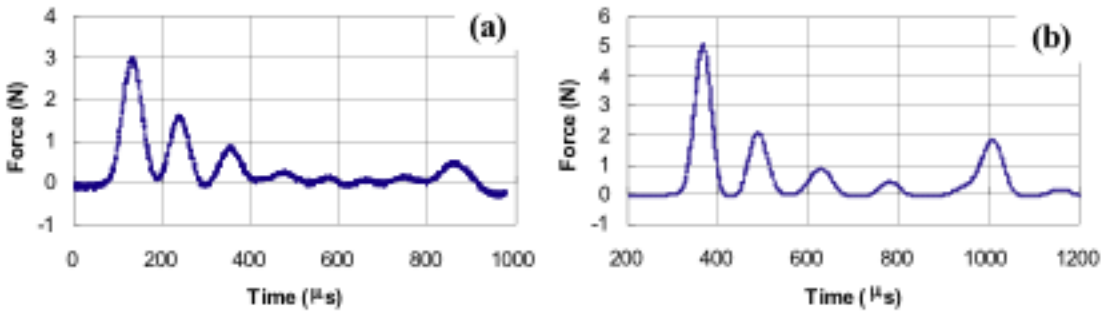

Figure 2.5: Experimental and theoretical results demonstrating that a short chain of PTFE beads with a diameter 4.76 mm supports a train of solitary waves induced by the alumina striker with a mass equal four times the mass of the particle. (a) Force detected in experiment by the sensor mounted at the wall supporting an 11 PTFE particle chain, striker velocity 0.44 m/s, vertical scale is 1 N. (b) Numerical calculations corresponding to experimental conditions in (a), including gravitational precompression; vertical scale is 1 N, elastic modulus 1.46 GPa.

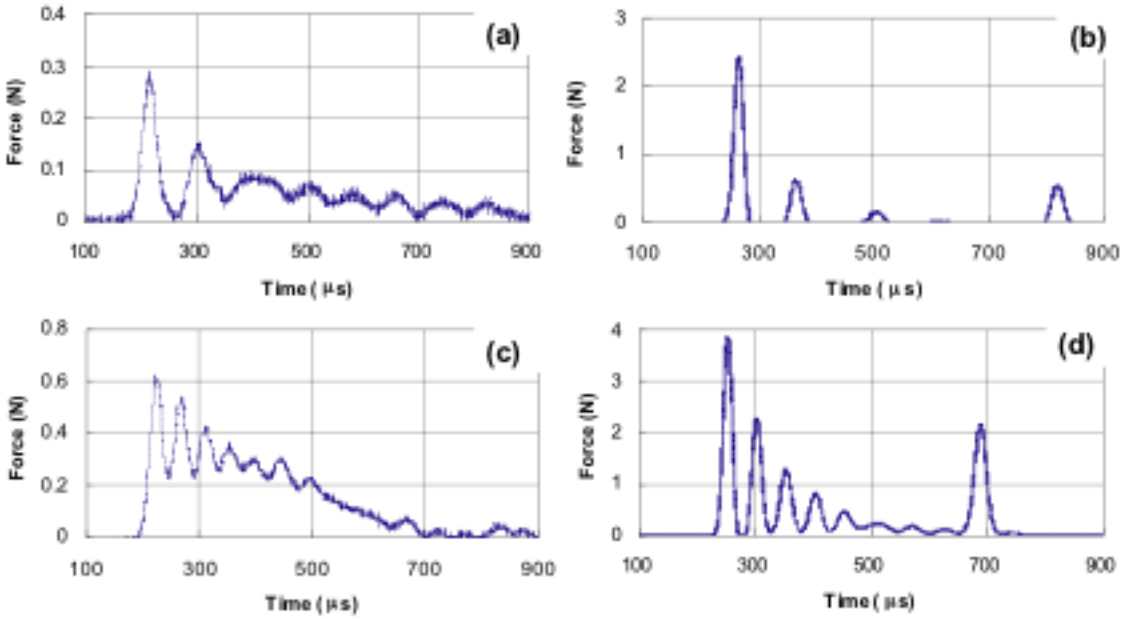

Figure 2.6: The experimental and theoretical results demonstrating that a PTFE chain of smaller particles with 2.38 mm diameter supports the solitary waves and oscillatory shock waves modified by dissipation in experiments. (a) The leading solitary wave with an oscillatory tail detected at the wall generated in a chain of 18 smaller PTFE balls (0.016 g) (the velocity of 2 mm diameter steel ball impactor (0.036 g) was 0.89 m/s); (b) Numerical calculations corresponding to experimental conditions in (a), including gravitational precompression, elastic modulus 1.46 GPa; (c) Oscillatory shock wave detected at the wall generated in a chain of 18 PTFE balls, impacted at velocity 0.89 m/s with a 5 mm diameter PTFE ball (0.123 g); (d) Train of solitary waves detected in numerical calculations corresponding to experimental conditions in (c), including gravitational precompression, elastic modulus 1.46 GPa.

and Goodier (1987),p.414].

$$F = \frac{2E}{3\left(1-\nu^2\right)}\left(\frac{R_1 R_2}{R_1+R_2}\right)^{1/2}\left[R_1+R_2-(x_1-x_2)\right]^{3/2} \tag{2.8}$$

A system of second order differential equations was reduced to the first order equations [Nesterenko (1983), Nesterenko (1992a), Nesterenko (2001)] and numerical calculations were performed using Matlab.

For comparison with experiments an average compression force $F = (F_1 + F_2)/2$ was calculated for solitary waves based on the compression forces on the particle contacts (F_1, F_2). Both of these plots are shown in Figure 2.2(b). Hertz law was used in the calculations for the interaction of the PTFE particle interaction. Due to the strain rate sensitivity, different values of the elastic modulus are used for PTFE and the value of Poisson's ratio for the material is equal to 0.46 [DuPont,Ehrenstein (2001)]. The interaction between the flat wall and last particle was also described by Hertz law with an elastic modulus of 115 GPa and Poisson's ratio of 0.307 for red brass (Cu_{85}-Zn_{15}). Hertz law was also used for the interaction between the alumina impactor (E=416 GPa, ν=0.231) and the first PTFE particle. No dissipation was included in numerical analysis. A gravitational force acting on the particles causing an initial nonuniform precompression in the chain (increasing toward the wall) was included in the calculations. The linear momentum (before the reflection from the wall) and energy were conserved with a relative error of 10^{-12}% and 10^{-8}%. Results of the numerical calculations correspond to the experimental set-up and conditions are shown in Figs. 2.2 (b), (c), Fig. 2.3, see corresponding curves, Fig. 2.4(b), Fig. 2.5(b), and Fig. 2.6(b) and (d).

2.1.3 Discussion

PTFE is a polymeric viscoelastic material with a strong strain rate sensitivity [Zerilli and Armstrong (2001)] and exceptionally low elastic modulus [Ehrenstein (2001)]. At normal conditions Youngs and flexural moduli for PTFE are in the range of 400 750 MPa and Poissons ratio is 0.46 [Ehrenstein (2001), Gondret et al. (2001)]. This property can be very attractive for ensuring a very low speed of soliton propagation and tunability of the system. But it is not evident that a chain formed from this type of beads will support strongly nonlinear solitary waves as for chains made from typical linear elastic materials like stainless steel [Lazaridi and Nesterenko (1985), Coste et al. (1997), Coste and Gilles (1999)]. In particular, the role of dissipation and deviation from linear elastic law [Zerilli and Armstrong (2001)] for PTFE under high strain and high strain rate deformation in the contact area with high gradients of strain is the primary concern. In the present study, the strains obtained were up to 0.06 based on estimation of maximum compressive stresses in the center of contact on the order of 80 MPa at a maximum force approximately equal to 5 N. The typical strain rates were approximately 400 s^{-1} and the compressive strains at the center of contact were about 0.06 decreasing to zero at a distance about 170 micrometers.

Beads made from Nylon with an elastic modulus that is six times larger than for PTFE demonstrated a Hertz type interaction law [Coste and Gilles (1999)]. Chains made of these beads supported the propagation of strongly nonlinear solitary waves with amplitudes in the range 1 to 33 N. In the experiments the range of amplitudes was extended for solitary waves toward far smaller values by more than order of magnitude, down to 0.03 N. The dynamic behavior of sonic vacuum type systems at such low amplitudes is very interesting especially in view of potential

practical applications related to noise reduction in the audible acoustic range, acoustic lenses and delay lines, and for investigation of validity of Hertz law at very low displacements.

Furthermore, one of the distinguished features of sonic vacuum systems is a strongly nonlinear dependence of solitary wave speed on amplitude and precompression (Eqs. (2.4) and (2.5)), which are the important factors in imparting the tunability of various properties of these systems, for example in delay lines or acoustical lenses. The dependence of the solitary wave speed on the force amplitude (F_m), based on Eqs. (2.5) and (2.4), is shown in Fig. 2.3(a) and (b) (curves 3 and 4 respectively) with an elastic modulus equal to 600 MPa [AcraBall Mfg. Catalog]. Results of the numerical calculations for a discrete chain are also shown in Fig. 2.3(a) at the same value of elastic modulus (see curves 7 and 8). It is clear that theoretical and numerical approaches result in very close values of speeds at the given interval of amplitudes. A noticeable deviation of experimental data from curve 1 in Fig. 2.3(b) was observed for the low amplitude solitary waves. Comparison of the solitary wave profiles and speeds in a discrete chain and in the continuum approximation for different nonlinear interaction laws are considered in Hascoët and Herrmann (2000),Rosas and Lindenberg (2004).

It is evident that there is a large difference between experimental values of soliton speed obtained in numerical calculations and in long wave theory for large amplitudes of force if the value of Youngs modulus was taken as 600 MPa [AcraBall Mfg. Catalog]. If 400 MPa is used for the PTFE elastic modulus [Gondret et al. (2001)], the difference between experimental speeds at high amplitude and predicted values based on the long wave approximation (or on numerical calculations) will be even more dramatic.

It should me mentioned that the dependence of the shock wave speed u_s on

particle velocity u_p in polymers (Hugoniots in $u_s(u_p)$ coordinates) extrapolated to bulk sound speed results in significantly higher values than the sound speed at normal conditions measured using an ultrasonic technique. This well known discrepancy indicates a rapidly varying change of compressibility at low values of shock amplitudes [Carter and Marsh (1995)]. For PTFE, the extrapolated value of bulk speed c_b from Hugoniot gives a value of 1.68 km/s in comparison with 1.139 km/s from ultrasonic measurements. Using c_b=1.68 km/s from extrapolated Hugoniot measurements and Poisson's ratio 0.46, the corresponding Youngs modulus is equal to 1.46 GPa and is obtained based on relations for elastic solids [Fung (1965)]. Ultrasonic data for the same material gives a value of the elastic modulus equal to 704 MPa [Fung (1965)]. The calculated theoretical and numerical data for solitary wave speed versus amplitude using an elastic modulus of 1.46 GPa are presented in Fig. 2.3(a) (see curves 1, 2, 5 and 6). When comparing the analytical data (curves 1-2 in Fig. 2.3(a) and (b) at $E = 1.46$ GPa) with the experimental data (in Fig. 2.3(b)) there is a better agreement between the experimental results and the calculated speed of solitary waves at high amplitude.

Calculations with an elastic modulus of 1000 MPa results in a reasonable correspondence between experimental data and calculations at the lower range of investigated force amplitudes of solitary waves. This suggests that the elastic modulus of PTFE is likely to be stress and strain rate dependent.

In a sonic vacuum, the solitary wavelength does not depend on amplitude; it depends on the behavior of the interaction force [Hascoët and Herrmann (2000),Nesterenko (2001)]. In the case of a Hertzian interaction ($n = 3/2$, Eq. (2.7)) this length is equal to five particles. The properties of solitary waves were used to establish validity of Hertz law for different materials [Coste and Gilles (1999)]. Measuring solitary wave speeds and durations in the experiments allows a straight-

forward calculation of the solitary wave widths corresponding to different amplitudes (see Table 2.1).

In the experiment corresponding to Fig. 2.4(a), for example, the speed of the leading solitary wave (with an amplitude equal to 2 N) was measured using the 5^{th} and 9^{th} particles from the wall and was found to be 152 m/s. The estimation based on the peak to peak measurements between the sensor in 5^{th} particle and the wall gave a similar value. The duration of solitary wave was about 164 μs resulting in the length of solitary wave equal to 5.2 times the diameter of the PTFE particle (Table 2.1). This is very close to the predicted length of solitary wave in long wave approximation equal to 5 particle diameters [Nesterenko (2001), Nesterenko (1992a), Nesterenko (2001)]. The measurements of the averaged force using sensors embedded in the particle results in a slightly longer pulse in comparison to the pulse duration based on the contact forces (Fig. 2.2(b)).

It is clear from the experimental data that the widths of solitary waves with relatively large amplitude are close to the predicted value of 5 particle diameters based on Hertz interaction law. Numerical analysis of a solitary wave in a sonic vacuum demonstrated that the energy contained in 5 particles is equal to 99.999996% of the total energy of the solitary wave. The distribution of velocities of particles in a solitary wave including more than 5 particles was analyzed in Chatterjee (1999), Sokolow et al. (2007). It should be mentioned that these widths do not depend on the elastic modulus. The widths of the solitary waves tend to be wider at lower amplitudes of propagating signals (Table 2.1). This may be due to the influence of gravitational precompression being closer to the impulse amplitude which drives the system away from the strongly nonlinear limit, producing broader solitary pulses tending to the weakly nonlinear regime described by solitary waves of Korteweg deVries (KdV) equation (Eq. (1.5)) [Nesterenko (1992a), Nesterenko

(2001), Arancibia-Bulnes and Ruiz-Suárez (2002)]. Numerical calculations performed in this work demonstrated a similar dependence of solitary widths with the amplitudes seen in Table 2.1.

It is evident from the comparison between Fig. 2.4(a) and (b) that numerical calculations of the behavior of a discrete system and experimental results are in close agreement with respect to the signal amplitudes and time durations between corresponding pulses. It is noted, however, that the amplitude of the reflected solitary wave recorded by the sensor inside the 9^{th} bead is significantly smaller than the amplitude of the incident wave. This is apparently due to the presence of dissipation in experiments, which was not taken into account in numerical calculations and will be addressed in future research.

From the preceding discussions it is apparent that a chain of low modulus PTFE beads also supports the propagation of strongly nonlinear solitary waves, which is yet another realization of the sonic vacuum type phononic crystals with an exceptionally low speed of the signal.

Another remarkable feature of a sonic vacuum type system is the very fast decomposition of longer initial pulse into a train of solitary waves [Nesterenko (1983), Lazaridi and Nesterenko (1985), Nesterenko (1992a), Hascoët and Herrmann (2000), Nesterenko (2001)]. Apparently this phenomenon can be obscured by the strong dissipation in the system. To check if this property is also demonstrated by a chain of PTFE particles, a striker mass equal to $m_s = 0.47$ g that was higher than the mass of the particles in the chain created a longer incident pulse. Usually the number of solitary waves with significant amplitude is comparable to the ratio of the striker mass to the mass of the beads in the chain Nesterenko (1983), Nesterenko (1992a), Hascoët and Herrmann (2000), Nesterenko (2001), Daraio et al. (2004b).

The results of this experiment are shown in Fig. 2.5. It is evident that

this Teflon-based "sonic vacuum" also demonstrates a very fast decomposition of the initial impulse on a distance comparable with the soliton width (Fig. 2.5(a) and (b)) and a clear tendency of signal splitting is very noticeable already after only 10 particles. The mass of the striker was chosen to be about four times that of the particles in the chain, expecting a decomposition of the initial triangular pulse into a train of four solitary waves. It should be mentioned that the number of solitary waves may be significantly larger if smaller amplitudes are included [Hascoët and Herrmann (2000),Sokolow et al. (2007)]. This example also demonstrates that a short duration impact on a highly nonlinear sonic vacuum type ordered periodic systems results in a train of solitary waves instead of a shock wave, which is intuitively expected. An increase of the duration of impact results in a shock wave impulse with an oscillatory structure where the leading pulse can be of the KdV type solitary wave for a weakly nonlinear chain or strongly nonlinear solitary wave with a finite width for the strongly nonlinear case [Nesterenko (1983), Nesterenko (1992a), Nesterenko (2001)]. Similar qualitative agreement of the experimental results and numerical calculations was found for all investigated conditions of impacts.

Previous experimental work [Lazaridi and Nesterenko (1985), Shukla et al. (1993), Zhu et al. (1997), Coste et al. (1997), Coste and Gilles (1999)] with chains of steel beads, acrylic disks and spheres, glass, brass and nylon beads validated the prediction of strongly nonlinear solitary wave as stationary solutions of strongly nonlinear wave equation (Eq. (2.1)). In those cases, the amplitude of the maximum force in the solitary wave was at least 3 times greater (1 N for Nylon beads) than the one obtained in this section for PTFE beads (0.03 N). This and the higher elastic modulus of Nylon resulted in higher speeds of signal propagation (the minimum reported speed was 235 m/s for Nylon beads [Coste and Gilles (1999)]). Furthermore, PTFE is a very versatile visco-elastic material. It is widely biocompatible, has a

very low coefficient of friction, and a very low elastic modulus which ensures its applicability in a large variety of engineering solutions. As a result, the speed of signal propagation in experiments were equal to 88 m/s for a force amplitude of 0.06 N (Table 2.1), which is more than two times smaller than the speed of solitary waves detected for nylon beads [Coste and Gilles (1999)] and more than 3 times smaller than the sound speed in the air at normal conditions. In principle, a sonic vacuum type media of different structure (Hertzian and non Hertzian) can support solitary waves with infinitesimally small amplitude and speed of propagation. In the future, it is not unreasonable to expect that a sonic vacuum type system which supports detectable solitary waves with force amplitudes similar to the one investigated in this chapter with a speed of the order of magnitude of 10 m/s or lower could be designed using new materials with tailored elastic properties.

Finally, it is important to investigate the influence of particle size on the system behavior for application purposes. In fact, a smaller size of particles composing the PTFE based strongly nonlinear system results in different stresses and strain-rate conditions in the contact area which may affect the system behavior. Experiments were conducted with smaller diameter PTFE spheres (2.38 mm) to check the validity of the strongly nonlinear theory. Experimental and numerical results are presented in Fig. 2.6. In the experiments, pulses were generated by an impact of a 2 mm diameter steel sphere (0.036 g, Fig. 2.6(a), (b) and a 5 mm diameter PTFE ball (0.123 g, Fig. 2.6 (c), (d)) at velocity 0.89 m/s. Numerical calculations did not account for the effects of dissipation. It is evident that the smaller diameter PTFE particles do support the sonic vacuum type behavior, although in this case the effect of dissipation appears to be more significant. The influence of dissipation on the dynamics of solitary waves in strongly nonlinear discrete systems was considered in Manciu et al. (2001), Rosas and Lindenberg (2003). The effect of dissipation is

likely to be responsible for the tail present after the 2^{nd} solitary waves formed in experiments (Fig. 2.6(a)), and delays the solitary wave splitting in experiments in comparison with numerical results (compare Fig. 2.6 (a) to (b) and Fig. 2.6 (c) to (d)).

2.1.4 Conclusions

The propagation of impulses in one-dimensional strongly nonlinear phononic crystals assembled from PTFE spheres was investigated for different conditions of loading and geometrical parameters. It was demonstrated, for the first time, that the chains of PTFE beads with different diameters support the Hertzian behavior with very low signal propagation speed due to its exceptionally low Youngs modulus and despite viscoelastic nature of PTFE. Single solitary waves and decomposition of the signal into trains of solitary waves with amplitude more than one order of magnitude smaller than previously reported were observed. Small amplitude solitons broke the sound barrier having a speed of propagation well below sound speed in air. Single solitary waves and trains of strongly nonlinear solitary waves were excited by impact were investigated experimentally and were found to be in reasonable agreement with numerical calculations based on Hertz interaction law with Young modulus 1000 MPa for the lower amplitudes and 1460 MPa for higher amplitudes of signals, both being significantly higher than its value at normal conditions.

2.2 Tunability of Solitary Wave Properties in One-Dimensional Strongly Nonlinear Phononic Crystals

One-dimensional strongly nonlinear chains of spheres are presently a very active area of research because they provide a natural step from weakly nonlinear

to strongly nonlinear wave dynamics [Nesterenko (2001)]. Their versatility stems from the Hertzian contact interaction governing the forces between the spheres as was shown in the previous section. These systems permit the unique possibility of tuning the wave propagation behavior from linear to weakly nonlinear and further to strongly nonlinear regimes.

Through simple noncontact magnetically induced static compression it is possible to tune the wave propagation response of the system from the strongly nonlinear to the weakly nonlinear regime. This allows a fine control of the propagating signal shape and speed with an adjustable static compressive force. Novel applications in different areas may arise from understanding the basic physics of these tunable strongly nonlinear one-dimensional systems, especially at a low magnitude range of stresses corresponding to signals used in ultrasonic diagnostics or in the audible range. For example, tunable sound focusing devices (acoustic lenses), tunable acoustic impedance materials, sound absorption layers and sound scramblers are among the most promising engineering applications.

The non-classical, strongly nonlinear wave behavior appears in the chain if the system is weakly compressed with a force F_0 [Nesterenko (1983), Lazaridi and Nesterenko (1985), Nesterenko (1992c)]. The term weakly is used when the static compressive force (F_0) is very small with respect to the maximum force in a wave. A supersonic solitary wave that propagates with a speed V_s with a force magnitude much higher than F_0 can be closely approximated by one single positive pulse of the periodic solution corresponding to a zero static force (or $\xi_0 = 0$). This exact solution has a finite length equal to only five particle diameters for a Hertzian contact interaction [Nesterenko (1983), Chatterjee (1999), Nesterenko (1992c)]. In the continuum approximation the solitary wave speed V_s has a nonlinear dependence on the maximum strain ξ_m, which translates to a nonlinear dependence on the maximum force

F_m on the contacts between the particles in discrete chains. The speed of a solitary wave V_s has a nonlinear dependence on the normalized maximum strain $\xi_r = \xi_m/\xi_0$ in the continuum approximation or, equivalently, the normalized force $f_r = F_m/F_0$ in the discrete chain with beads of diameter a, bulk density ρ, Poisson's ratio ν and Youngs modulus E (Eq. (2.9), [Nesterenko (1992c), Daraio et al. (2005)]):

$$\begin{aligned} V_s &= \frac{c_0}{\xi_r - 1}\left[\frac{4}{15}\left(3 + 2\xi_r^{5/2} - 5\xi_r\right)\right]^{1/2} \\ &= 0.9314\left(\frac{4E^2F_0}{a^2\rho^3\left(1-\nu^2\right)^2}\right)^{1/6}\frac{1}{f_r^{2/3}-1}\left[\frac{4}{15}\left(3 + 2f_r^{5/3} - 5f_r^{2/3}\right)\right]^{1/2}. \end{aligned} \tag{2.9}$$

The sound speed c_0 in a chain statically compressed with a force F_0 can be deduced from Eq. (2.9) at the limit for $f_r = 1$:

$$\begin{aligned} c_0 &= \left(\frac{3}{2}\right)^{1/2} c\xi_0^{1/4} \\ &= 0.9314\left[\frac{2E}{a\rho^{3/2}\left(1-\nu^2\right)}\right]^{1/3} F_0^{1/6}, \end{aligned} \tag{2.10}$$

where the constant c is

$$c = \sqrt{\frac{2E}{\pi\rho\left(1-\nu^2\right)}}. \tag{2.11}$$

Equation (2.9) also allows the calculation of the speed of weakly nonlinear solitary waves (f_r is slightly larger than 1) which is the solution of the Korteweg-de Vries (KdV) equation [Nesterenko (2001)].

When f_r or ξ_r are very large (i.e. F_0 (ξ_0) is approaching 0) Eq. (2.9) reduces to the Eq. (2.12) for solitary wave speed V_s in a "sonic vacuum" [Nesterenko (1992c), Gavrilyuk and Nesterenko (1993)] for continuum approximation and discrete chains respectively

$$\begin{aligned} V_s &= \frac{2}{\sqrt{5}} c\xi_m^{1/4} \\ &= 0.6802\left[\frac{2E}{a\rho^{3/2}\left(1-\nu^2\right)}\right]^{1/3} F_m^{1/6}. \end{aligned} \tag{2.12}$$

The term sonic vacuum is used for strongly nonlinear systems without a linear part in the force displacement relation between particles in which no characteristic sound speed is present [Nesterenko (1992a), Nesterenko (2001)]. For simplicity only the leading approximation was used to connect strains in the continuum limit and forces in discrete chain in Eqs. (2.9) and (2.12). The apparent similarity between Eq. (2.10) and Eq. (2.12) is striking and can be misleading because these equations describe qualitatively different types of wave disturbances. Equation (2.10) represents the speed of a sound wave with an infinitely small dynamic force magnitude in comparison with the initial precompressive force and with a long wavelength. This wave is the solution of the classical linear d'Alambert wave equation [le Rond d'Alembert (1747)]. Equation (2.12) corresponds to the speed of a strongly nonlinear solitary wave with a finite width of 5 particle diameters where the ratio of the magnitude of the dynamic force of the solitary wave to the initial static compression is equal to infinity. This solitary wave is the solution of the strongly nonlinear wave equation first derived in Nesterenko (1983). A strongly nonlinear compression solitary wave exists for any general power-law interaction between particles with an exponent in the force dependence on displacement $n > 1$ (Hertz law is a special case when $n = 3/2$) [Nesterenko (1992c), Nesterenko (1993), Nesterenko (1994), Hascoët and Herrmann (2000), Nesterenko (2001)]. The exponent n determines the width of the solitary wave and the dependence of its speed on the maximum strain. The corresponding equations for the speed and width of these solitary waves in the continuum approximation were first derived in Nesterenko (1993). The results of numerical calculations for discrete chains can be found in Rosas and Lindenberg (2004). A general type of strongly nonlinear interaction law also supports the strongly nonlinear compression or rarefaction solitary waves depending on an elastic hardening or softening behavior [Nesterenko (1993), Nesterenko (2001)].

It is possible to find from Eqs. (2.9)-(2.12) that the speed V_s of a solitary wave propagating in a one-dimensional granular chain can be significantly smaller than the sound speed in the material composing the beads and can be considered approximately constant in any narrow interval of its relative magnitude f_r due to the small exponent in the power law dependence. The signal speed of strongly nonlinear and linear compression waves in this condensed soft matter can be below the level of sound speed in gases at normal conditions as was experimentally demonstrated for PTFE (polytetrafluoroethylene) based sonic vacuum [section 2.2, Daraio et al. (2005)]. The described properties of strongly nonlinear waves may permit the use of these materials as effective delay lines with an exceptionally low speed of the signal.

In stainless steel based chains, previous experimental and numerical data regarding the dependence of the solitary wave speed on the force magnitude exists only for relatively large magnitudes of dynamic forces (20 N 1200 N) [Coste et al. (1997),Hong et al. (1999),Coste and Gilles (1999)] and 2 N 100 N [Job et al. (2005)] and for large diameters of the stainless steel beads 8 mm and 26 mm respectively. To characterize the behavior of stainless steel based strongly nonlinear systems at force magnitudes closer to the magnitude of the signals used in ultrasonic diagnostics the range of experimental data was extended to a lower force magnitude range down to 0.1 N in a chain of beads with a smaller diameter of 4.76 mm. Scaling down of the size of the beads is important for the assembling of practical devices.

2.2.1 Experimental Setup

The speed, duration and dynamic force magnitude in propagating and reflected pulses from the wall were measured using the experimental set-up presented in Fig. 2.7. One-dimensional PTFE based phononic crystals were assembled in a

PTFE cylinder, with an inner diameter of 5 mm and outer diameter equal to 10 mm. The cylinder was filled vertically with chains of either 20 stainless steel or 52 PTFE balls (McMaster-Carr) with diameter a=4.76 mm and mass 0.1226 g (standard deviation 0.0008 g) (Fig. 2.7 (a)). PTFE has a high strain rate sensitivity [Zerilli and Armstrong (2001)] and an exceptionally low elastic modulus in comparison with metals [Ehrenstein (2001),http://www.dupont.com/teflon/chemical], which ensures a very low speed of soliton propagation (Eqs. (2.9), (2.12)). To compare the properties of the system (signal speed, tunability) 20 stainless steel beads (316 steel, McMaster-Carr catalogue) with diameter a=4.76 mm and mass 0.4501 g (standard deviation 0.0008 g) were assembled in the same PTFE cylinder.

A magnetic steel ball, with diameter a=5.0 mm and mass 0.5115 ± 0.0001 g, was then placed on top of the PTFE or stainless steel chain to magnetically induce a precompression equal to the weight of the magnet (Fig.2.7 (a)). This experimental set up allows the tunability of interfacial properties, as for example in laminar composite systems made from chains of different materials [Nesterenko et al. (2005)].

Three calibrated piezo-sensors (RC 103 μs) were connected to a Tektronix oscilloscope to detect force-time curves. Two piezo-gauges made from lead zirconate titanate (square plates with thickness 0.5 mm and 3 mm side) with Nickel plated electrodes and custom microminiature wiring supplied by Piezo Systems, Inc. were embedded inside two of the PTFE and two steel particles in the chains similar to [Nesterenko et al. (1995), Nesterenko (2001), Job et al. (2005), Daraio et al. (2005)]. The wired piezo-elements were glued between two top parts cut from original beads (Fig. 2.7 (b)). The calculation of the signal speed is based on the time interval between the maxima of the signals detected by the two gauges separated by a known distance (in most cases equal to 5 particle diameters) simultaneously with the mea-

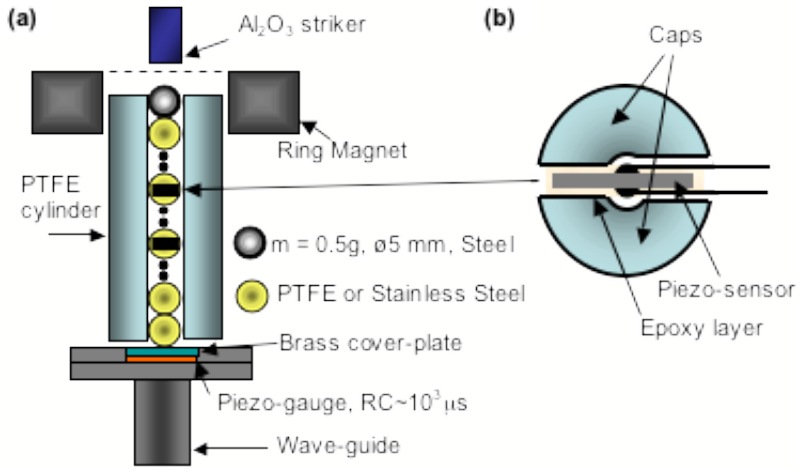

Figure 2.7: (a) Experimental set-up for testing of strongly nonlinear one-dimensional chains, the magnetic particle on the top is used for the tuning of the system behavior through exerting a compressive force on the chain equal to the mass of the magnet. The smaller black circles identify a continuation of the similar particles. (b) Schematic drawing of a particle with embedded piezo-sensor.

surement of the force acting inside the particles. The speed of the pulse was related to the averaged force magnitude between the two gauges representing the magnitude of the contact force.

A typical PTFE particle with an embedded sensor consisted of two similar caps (total mass $2M = 0.093$ g) and a sensor with a mass $m = 0.023$ g glued to them. The total mass of these particles was equal to 0.116 g, which is close to the mass of the original PTFE particle (0.123 g). In theory, the introduction of a particle with a different mass in a chain of particles of equal masses results in weak wave reflections, as observed in Manciu et al. (1999b), Hascoët and Herrmann (2000), Manciu et al. (2001). Numerical calculations with a single particle in the chain with a mass 0.116 g embedded into the chain of particles with mass 0.123 g created negligible effects of wave reflections [Daraio et al. (2005)]. Therefore such small deviation of the sensor mass from the particle mass (<6%) in both the PTFE and stainless steel chains was neglected in the following numerical calculations and thus, the chains were considered uniform for simplicity.

The third piezo-gauge, supplied by Kinetic Ceramics, Inc., was bonded with epoxy on two electrode foils for contacts and reinforced by a 1 mm brass plate on the top surface. This sensor was then placed on the top of a long vertical steel rod (wave-guide) embedded at the other end into a steel block to avoid possible wave reverberation in the system (Fig. 2.7 (a)). The sensor embedded in the wall was calibrated using the conservation of linear momentum during a single impact by a steel ball as in Daraio et al. (2005). Sensors in the particles were calibrated by comparing their signal with the signal from the sensor at the wall under a controlled, relatively long, simultaneous impact loading.

Considering the particles with an embedded sensor as rigid bodies, the forces on the top and bottom of the piezoelectric plate can be easily related to the

forces acting on the corresponding contacts of the sensor [Daraio et al. (2005)]. This simplification allowed a direct comparison of the force-time curves obtained in experiments with the average of the contact forces derived in the numerical calculations. The forces acting on both sides of the sensor deviate symmetrically from the average value of the contact forces if attenuation is negligible. When the measured force reaches its maximum ($F_{m,e}$) it is equal to the corresponding forces on the contacts of the particle and on both sides of the piezoelement [Daraio et al. (2005)].

To relate the maximum value of the dynamic force measured by the embedded sensor $F_{m,e}$ and the value of the maximum contact force between neighboring particles F_m, which is present in the equations for solitary wave speed (Eq. (2.9)-(2.11)), the coefficient β was found numerically as explained in the next section:

$$F_m = \beta F_{m,e} + F_0. \tag{2.13}$$

Strongly nonlinear sonic vacuum type materials allow a significant change of speed of propagation using an initial static compressive force, which make them qualitatively different from the linear systems. The tunability of the signal propagating through the chains was achieved by adding a magnetically induced preload. In contrast, previous investigations used a preloading of the system through the mechanical application of the load using a wire with attached weights or contact interaction between the last particle and the frame [Nesterenko (1993), Coste et al. (1997)]. The former type of preloading allows application of a constant external force to the end magnetic particle independently from its displacement. This was difficult to achieve in the previous attempts especially if the dynamic displacement of the end particle was comparable to its initial displacement due to the preloading. This case would change boundary conditions in an uncontrollable way. The proposed magnetically induced static precompression ensures fixed boundary conditions which are used in

numerical calculations and even allows the additional possibility of a fine tuning of the preload which can be time dependent. A Neodymium-Iron-Boron ring magnet (internal and external diameters 11.43 mm, 53.34 mm respectively, with mass 242.2 g ($\pm$ 0.1 g) from Dexter Magnetics Technologies) was placed around the PTFE cylinder containing the chain and held in place by the magnetic interaction with the magnetic steel particle placed on the top of the chain (Fig. 2.7 (a)). Throughout the whole chain the static compressive force induced by the weight of the magnet was 2.38 N in addition to the nonuniform gravitational preload. This particular set-up was chosen to allow an easy noncontact control over the variation of the static preload by slight axial movements of the magnetic ring or by the use of ring magnets of different masses. A higher level of magnetically induced precompression in experiments (4.25 N) was achieved by adding mass to the magnet.

Nonmagnetic alumina (Al_2O_3) cylinders (0.47 g and 1.2 g) were used in experiments to generate pulses of different durations and force magnitudes in the one-dimensional phononic crystals, by controlled impacts on the top particle of the chain. Waves of different magnitudes were excited with different velocities of the striker impacts.

2.2.2 Numerical Calculations

For a comparison with experiments, numerical calculations were performed using Matlab. Particles were treated as rigid bodies connected by nonlinear springs according to Hertz law as in previous investigations [Nesterenko (1983), Lazaridi and Nesterenko (1985), Nesterenko (1992a), Hinch and Saint-Jean (1999), Nesterenko (2001)]. The validity of the Hertzian interaction for a system composed of PTFE beads was extensively studied and demonstrated in Daraio et al. (2005). As men-

tioned earlier, to compare numerical results and experimental data, an average compression force was calculated for solitary waves based on the corresponding compression forces on the particle contacts. The parameters used in numerical calculations to represent the materials properties are listed in Table 2.2.

Table 2.2: Parameters used in numerical calculations to represent the properties of the materials composing the strongly nonlinear media tested experimentally.

	Elastic Modulus [GPa] [g/cm^3]	Poisson's Ratio [g/cm^3]	Density [kg/m^3] %
PTFE [1]	1.46	0.46	2200
Stainless Steel [2]	193	0.3	8000
Red-brass [3]	115	0.31	8750
Alumina [4]	416	0.23	3900

[1] Daraio et al. (2005), Carter and Marsh (1995) [2] ASM (1983) [3] AISI Type 316L, http://www.efunda.com [4] Munro (1997)

The coefficient β in Eq. (2.13) is determined numerically as $\beta = F_{d,n}/F_{m,n}$, where $F_{m,n}$ is the maximum value of the force obtained numerically by averaging, at each time step, the dynamic forces on the contacts between adjacent particles and $F_{d,n}$ is the magnitude of these dynamic contact forces. $F_{m,n}$ is analogous to $F_{m,e}$ in experiments as described in the section 2.1.1.

The dependence of the coefficient β as a function of the normalized force magnitude in a solitary wave $F_{m,n}$ ($F_{m,n}/F_0$) is shown in Fig. (2.8). The coefficient β is independent of the elastic modulus, but varies with respect to the force magnitude

of the solitary wave approaching a value of unity when $F_{m,n}$ is close to zero. This dependence was taken into account when calculating the value of dynamic contact force from measured values by the gauges inside the particles for both PTFE and stainless steel particles.

The nonuniform static precompression resulting from the gravitational loading of the particles in the vertical chains was included in calculations and added to the magnetically induced prestress. The numerical calculations included the presence of the magnetic bead at the top of the chain in all cases. Energy and linear momentum (before interaction with a wall) were conserved with a relative error of $10^{-8}\%$ and $10^{-12}\%$ similarly as in Daraio et al. (2005). Dissipation was not included in the current numerical analysis.

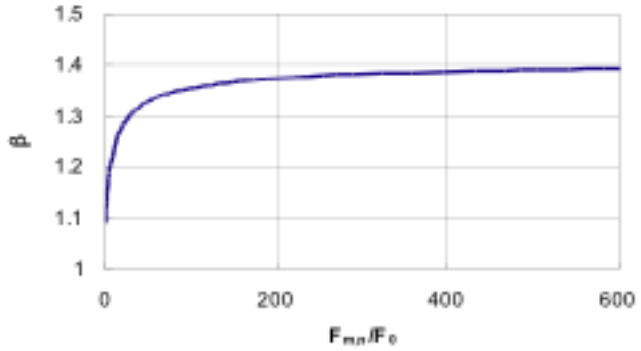

Figure 2.8: Plot representing the β-coefficient for solitary waves found in numerical calculations for the stainless steel case, as a function of the normalized maximum averaged dynamic force on the contacts ($F_{m,n}$ corresponds to $F_{m,e}$ measured by the embedded gauges in experiments).

The force magnitude of the solitary waves was measured with accuracy in

the range of 15% to 30%. The larger error at lower magnitudes is attributed to the higher signal to noise ratio. The accuracy of the speed measurements can be estimated within 10% due to the uncertainty in the sensors alignment (about 1 mm for each sensor).

2.2.3 Results and Discussion

Typical results of the experiments for a chain of 52 PTFE beads capped by the magnetic steel particle are shown in Fig. 2.9 (a), (c). In these experiments, the impulse loading was generated using a 0.47g Al_2O_3 cylinder with a velocity of 0.89 m/s impacting the top of a magnetic particle. Internal sensors were placed in the 20^{th} and 29^{th} beads from the top magnetic particle and the third piezo-gauge was embedded in the wall. The zero time in experiments corresponding to Fig. 2.9 (a), (c) is arbitrary chosen, and the zero time in numerical calculations (Fig. 2.9 (b), (d)) corresponds to the moment of impact.

The obtained experimental profiles and corresponding numerical results for a gravitationally loaded chain are presented in Fig. 2.9 (a), (b). In this weakly compressed state, the Teflon-based "sonic vacuum" demonstrates the typical fast decomposition of an initial impulse over a distance comparable to the soliton width similar to the trains observed in a shorter 21 particle chain (Fig. 2.5). In Fig. 2.9 (a) the duration of the leading solitary wave pulse was equal to 170 μs. The speed of its propagation, based on the time interval between the signals maxima measured by the two embedded sensors, was 129 m/s. These values result in a solitary wave width equal to 4.6 particles diameters. This agrees reasonably well with the solitary wave width predicted in long wave theory for a chain of particles interacting according to Hertz law (5 particles diameter) [Nesterenko (1983), Nesterenko (2001)]. These

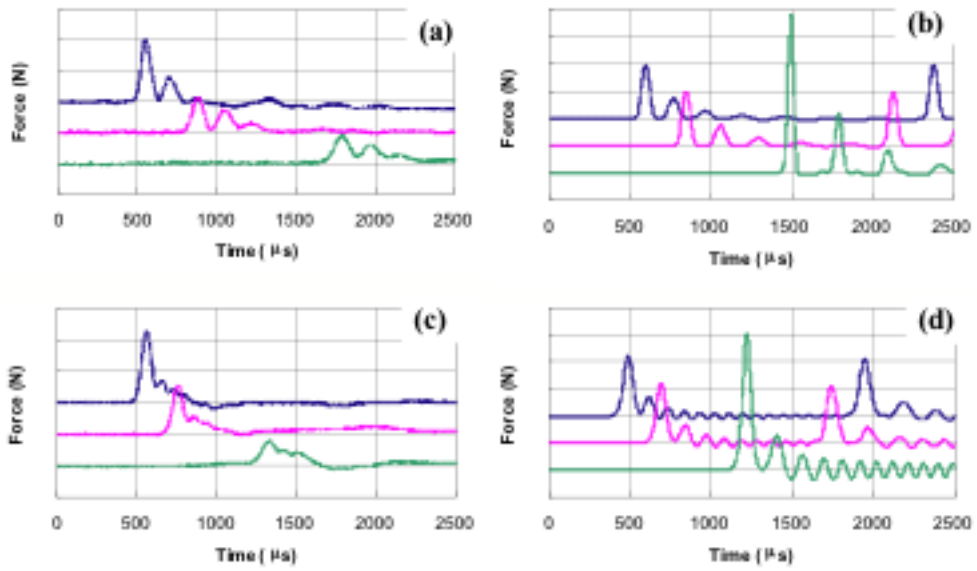

Figure 2.9: Experimental and numerical results corresponding to a chain of PTFE beads with and without magnetically induced precompression. (a) Forces detected in experiment by the sensor in the 20^{th} ball from the impacted side (top curve), by the sensor in the 29^{th} ball (middle curve) and at the wall (bottom curve) without magnetic pre-compression, vertical scale is 0.5 N per division; (b) Numerical calculations of averaged dynamic contact forces between particles and at the wall corresponding to the signals detected by the sensors in (a), without magnetic precompression but including gravitational preload, vertical scale is 2 N per division; (c) Forces detected in experiment with static magnetically induced precompressive force equal 2.38 N, vertical scale is 1 N per division; (d) Numerical calculations corresponding to experimental conditions in (c) including forces due to gravitation and magnetic precompression, vertical scale is 2 N per division.

parameters allow one to evaluate the characteristic strain rates for PTFE at the contact area equal to 400 s^{-1} [Daraio et al. (2005)]. The experimental results (Fig. 2.9 (a), (c)) agreed reasonably well with the numerical calculations under the same testing conditions (Fig. 2.9 (b), (d)) as well as other investigated impact conditions although dissipation is apparent especially at the bottom of the chain (Fig. 2.9).

Results of numerical calculations demonstrated that magnetically induced static compressive force under a similar type of impact caused a qualitative change of the signal shape from a train of solitary waves in a weakly compressed case (Fig. 2.9 (b)) to a few solitary waves with a periodically oscillating tail (Fig. 2.9 (d)). In experiments (Fig. 2.9 (c)) the periodic oscillatory tail was not observed, which may be due to the dissipation caused by the interaction between the wall of the holder and the particles as well as dissipation on the contacts.

One of the most interesting consequences of the noncontact magnetically induced static force applied to the chain is a significant change in the speed of the signal propagation. In Fig. 2.9 (a-d) the pulse excited by the same impact resulted in an increased speed from a value of 129 m/s for the gravitationally loaded chain to 222 m/s for the magnetically preloaded system. This means a 70% control over the initial natural signal speed of the investigated strongly nonlinear system. The solitary wave speed in only gravitationally loaded PTFE chains is about two times smaller than the speed of a solitary wave in the chain of nylon beads [Coste and Gilles (1999)] with magnitude 1 N due to a smaller elastic modulus of Teflon in comparison with Nylon. This is in agreement with theoretical dependence of speed on elastic modulus (Eq. (2.9)).

Interestingly, in numerical calculations the dynamic force magnitudes of the incident pulses in the magnetically precompressed chains are close to the one observed in the only gravitationally loaded chains (compare corresponding curves in

Fig. 2.9 (b) and (d)). Meanwhile, the dynamic force magnitude on the wall in the magnetically precompressed chains in numerical calculations is noticeably smaller than the one in the former case (see bottom curves in Fig. 2.9 (b) and (d)). This shows that the static compressive force can significantly reduce the maximum of the dynamic force acting on the wall though this phenomenon was not observed in the experiments probably due to the decrease of dissipation in the magnetically precompressed chain.

In experiments an impact by the same striker with the same velocity on the gravitationally and magnetically preloaded PTFE chains resulted in an increase of force magnitude by 2 times in the incident pulses (compare corresponding curves in Fig. 2.9 (a) and (c)). This is probably due to the significant decrease of dissipation related to the increase of the stiffness and to the reduction of the relative displacement between the particles under similar conditions of loading at higher precompression. The delayed splitting observed in Fig. 2.9 (c) also contributes to the larger amplitude of the leading pulse.

The low magnitude precursor under magnetic precompression was noticeable especially in the wall gauge (the bottom curve in Fig. 2.9 (c)). This may be due to the propagation in front of the leading solitary wave of a high speed disturbance with the speed of sound in solid PTFE through the central cylindrical column created when the initial precompression flattens the contact area between spherical particles. This phenomenon is not included in the numerical approach and requires further investigation.

Table 2.3 shows a summary of the typical results for the magnitude of the dynamic contact forces F_d and corresponding velocities V_s obtained in experiments. A comparison of 5 representative values obtained experimentally with the corresponding values obtained in numerical calculation and with the theory of long wave

approximation for given values of F_d are included for clarity.

The force data presented in the experimental part of the table (F_d) represents the average of the maximum value of the force at the two contact points ($F_{d,e}$) extracted from the magnitudes of the corresponding signals of the two embedded gauges with force magnitudes $F_{m,e}$, (where $F_{d,e} = \beta F_{m,e}$). The solitary wave speeds related to F_d were obtained by dividing the distance between the sensors (placed in integer intervals of 5 particle diameters) by the measured peak-to-peak time interval. To calculate the speed of a solitary wave corresponding to the given contact force magnitude F_d in the long wave approximation Eq. (2.9) was used, where the total force F_m is the sum of F_d plus F_0 caused by initial precompression (gravitational or gravitational plus magnetic, though gravitational preload is not uniform).

The speed of a solitary wave in the long-wave-approximation is slightly lower than in the numerical calculations for a gravitationally loaded discrete chain at the same magnitude of dynamic force F_d (see left side of Table 2.3). The opposite tendency is characteristic for the case where additional magnetically induced loading is applied (see right side of Table 2.3). In both cases the difference between the long wave approximation and a discrete chain is actually very small, which agrees with the results of [Rosas and Lindenberg (2004)].

It should be noted that the speeds of the solitary wave at the investigated range of dynamic force magnitudes (which is about 2 times higher than the initial precompression force) in the magnetically precompressed chain is slightly higher than the speed of the sound in the system c_0 =211.2 m/s evaluated from Eq. (2.11).

The comparison of the shapes of the leading pulses detected experimentally and the stationary solitary waves obtained in separate numerical calculations

Table 2.3: Comparison of experimental values of the solitary wave speeds V_s with the corresponding values obtained in numerical calculation and with the theoretical values from long wave approximation.

Experimental data		Numerical results		Long-wave approximation	
F_d [N]	V_s [m/s]	$F_{d,n}$ [N]	V_s [m/s]	F_d [N]	V_s [m/s]
Only gravitational precompression					
5.5	168	5.7	184	5.7	182
4.3	166	4.3	177	4.3	174
3.3	167	3.3	170	3.3	167
2.5	163	2.6	163	2.6	161
2.1	143	2.0	159	2.0	155
Magnetic and gravitational precompression					
5.7	241	5.8	228	5.8	230
4.5	235	4.5	224	4.5	227
3.4	230	3.2	220	3.2	223
2.6	221	2.6	218	2.5	221
2.0	223	2.0	215	2.0	220

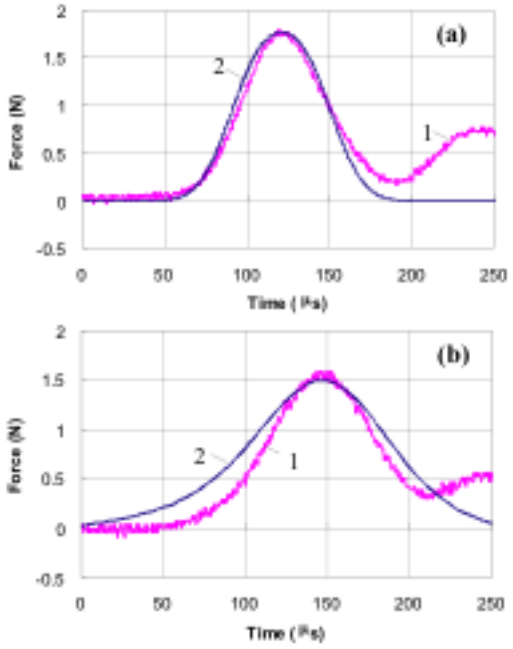

Figure 2.10: The leading pulses obtained in experiments (curves (1)) and stationary solitary waves found in numerical calculations (curves (2)) with the same force magnitude. (a) PTFE chain under gravitational precompression and the stationary solitary wave calculated in a sonic vacuum, (b) Magnetically precompressed PTFE chain and the stationary solitary wave calculated in a uniformly precompressed chain with force 2.38 N. In both cases the PTFE chain was composed of 52 particles and a sensor was embedded into the 21^{st} particle from the top, a magnetic steel particle was positioned on the top and the impactor was the 0.47 g Al_2O_3 cylinder.

including a larger number of particles is shown in Fig. 2.10.

From Fig. 2.10 the shape of the leading pulses in experiments is close to the shape of the stationary solitary waves in the numerical calculations despite that in experiments these pulses were not completely separated from the oscillatory tail at the given distances of the sensors from the impacted end of the chain.

In the magnetically precompressed chains the splitting of the incident pulse into a train of solitary waves is delayed especially when the dynamic force magnitude of the pulse is smaller than or comparable to the initial static compressive force [Nesterenko (1992a), Nesterenko (2001), Arancibia-Bulnes and Ruiz-Suárez (2002)]. At a relatively small value of their ratio the strongly nonlinear solitary wave becomes close to the soliton solution of the Korteweg-de Vries wave equation with a width infinitely increasing with dynamic force magnitude decreasing to zero [Nesterenko (1992a), Nesterenko (2001)]. Detailed analysis of the depth for solitary wave stabilization depending on the relative magnitude of the solitary wave force and the initial precompressive force can be found in Arancibia-Bulnes and Ruiz-Suárez (2002). In the numerical calculations, the leading solitary pulse was formed being completely separated from the oscillatory tail in the vicinity of the 950^{th} particle from the impacted end (curve 2 in Fig. 2.10 (b) corresponds to the 980^{th} particle in the chain included in the numerical calculations). This may explain why the stationary solitary pulse in numerical calculations is wider than the width of the nonstationary leading pulse in the magnetically precompressed chain experimentally detected at the 20^{th} particle (Fig. 2.10 (b)). The corresponding increase of the width of the leading pulse when it propagates inside the magnetically precompressed chain was observed in the numerical calculations.

Figure 2.11 shows the comparison of the experimental results with the theoretical values obtained from the long wave approximation, and the numerical data

for discrete chains of both gravitationally (lower curves and experimental points) and magnetically precompressed (2.38 N) systems (upper curves and corresponding experimental points). It is known that the theoretically predicted speed of solitary waves in strongly nonlinear chains has a strong dependence on the magnitude represented by Eq. (2.9) for precompressed chains. The curves based on the long wave approximation (curves 2 and 4) are very close to the one obtained in numerical calculations (curves 3 and 5). It should be mentioned that this agreement is obtained when only the leading approximation was used to connect strains in the continuum limit and forces in discrete chain in Eqs. (2.9) and (2.12). Experimental data obtained with an increased precompression (4.25 N, not shown in Fig. 2.11) also followed the general trend prescribed by long wave approximation.

At higher force magnitudes in the solitary wave the agreement between the theoretical data and experiments is better than at lower magnitude for the weakly (gravitationally) precompressed chain. This behavior is attributed to the dependence of the elastic modulus of the dynamically deformed PTFE on strain (and strain rate) on the particle contact [Daraio et al. (2005)].

The solution obtained with the long wave approximation (Eq. (2.9)) for a solitary wave refers to a uniformly compressed chain with a static force F_0. The gravitational force, though, results in a nonuniform chain compression. To apply the solution from the long wave approximation to the gravitationally preloaded and magnetically tuned chains to calculate V_s, a constant value of F_0 equal to the value of compressive force at the midpoint between the sensors was used. In the numerical results the local wave speed was calculated taking into account the nonuniform gravitational compression. The small difference observed when comparing the two approaches (compare curves 2 to 3 and 4 to 5 in Fig. 2.11) demonstrated that

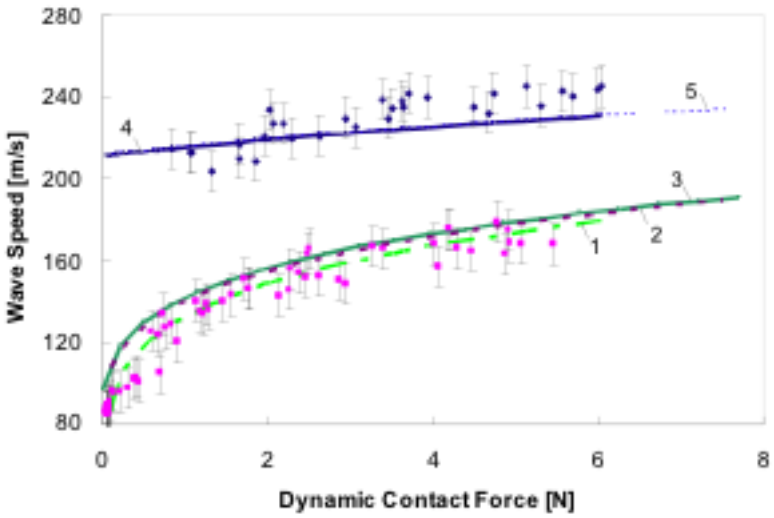

Figure 2.11: Dependence of the solitary wave speed on the magnitude of the contact dynamic force for gravitationally loaded and for magnetically tuned chains composed of PTFE beads. The experimental values for corresponding curves are shown by solid squares and dots. Curve 1 represents the long wave approximation for the sonic vacuum using an elastic modulus for PTFE equal to 1.46 GPa. Curves 2 and 4 are the theoretical curves based on Eq. (2.9), and the corresponding numerical calculations for the discrete chains are represented by curves 3 and 5.

they are in a very good agreement in this range of static and dynamic forces. Even the sonic vacuum approximation (where the gravitational preload is excluded, Eq. (2.12)) agrees reasonably well with the cases where gravitational compressive forces were taken into account (compare curve 1 with 2 and 3) for larger magnitudes of dynamic contact force. At magnitude of dynamic contact forces close to zero, there is a significant difference between the sonic vacuum and the gravitationally precompressed chains. The speed of the wave in sonic vacuum tends to zero at very low magnitude of dynamic contact forces, while in the gravitationally loaded chains it tends to the value of the corresponding sound speed $c_0 = 92.6$ m/s with a dynamic elastic modulus for PTFE taken equal to 1.46 GPa (Eq. (2.10)). The numerical data also demonstrated the same limit for c_0. In the low magnitude range the experimental data is below the long wave approximation and numerical curves. This may be due to the less than 1.46 GPa dynamic elastic modulus of PTFE at smaller strains (and strain rates) [Daraio et al. (2005)].

The increase of the sound speed c_0 in the PTFE chain under the added magnetically induced precompression (2.38 N) in comparison with only gravitational preload (0.017 N, $c_0 = 92.6$ m/s) is about 128% at practically the same density. This results in a corresponding change of acoustic impedances.

The agreement between the speeds in the magnetically tuned system and the estimated theoretical values means that the equations for the dependence of the solitary wave speed based on the nonlinear continuum approximation can be a reasonable foundation for the design of sonic vacuum type devices based on PTFE beads. The speed of the solitary wave at the minimum investigated dynamic force magnitude in the magnetically precompressed chain (limit at F_d approaching zero for curves 4 and 5 for long wave approximation and numerical calculations respectively) is very close to the speed of the sound in the system $c_0 = 211.2$ m/s (estimated based

on long wave approximation Eq. (2.10)).

In the experiments with magnetically induced static precompression the maximum total force (8.4 N) was larger than in the gravitationally precompressed chain. Additionally PTFE was loaded differently in comparison with the weakly compressed chain even when the maximum forces were the same. As mentioned, the elastic modulus of PTFE chains was selected to have a constant value of 1.46 GPa from the extrapolation of the Hugoniot data [Carter and Marsh (1995)]. Despite a difference in the loading conditions at this large strain the higher value of the elastic modulus (compared to the ultrasonically measured elastic modulus at normal conditions) is able to describe the experimental data. Further research on the value of elastic modulus of PTFE under conditions of dynamic deformation and the application of Hertz law is necessary to clarify the observed behavior. The dependence of PTFEs elastic modulus on contact strain may cause a deviation of the contact law from a Hertzian type behavior.

To compare the predictions of the long wave theory for the tunability of strongly nonlinear systems and relate it with the variation of the elastic modulus of the beads, the parameters of the solitary waves were measured in a stainless steel based system under the same magnetically induced precompression. Stainless steel particles have more than two orders of magnitude difference in the elastic modulus (193 GPa) with respect to PTFE (1.46 GPa). The experimental results of previous research [Lazaridi and Nesterenko (1985),Coste et al. (1997),Coste and Gilles (1999), Job et al. (2005)] are in excellent agreement with the predictions of the long wave theory and with the results of numerical calculations for chains composed of stainless steel beads. The addition of a prestress in chains composed of steel beads was also examined in Coste et al. (1997) but for a range of force magnitudes much higher than the one presented in this study. This chapter extends the investigation to multiple

solitary waves in contrast to single solitary wave in Coste et al. (1997).

Experimental and numerical results for chains composed of stainless steel beads are shown in Figs. 2.12 and 2.13. Solitary waves in the chain of stainless steel beads also demonstrated a significant increase of speed with added magnetically induced prestress of 2.38 N. For example, in experiments the leading solitary pulse presented in Fig. 2.12 (a) had a speed of 580 m/s in the gravitationally precompressed chain then increased to 688 m/s with the addition of magnetic precompression in Fig. 2.12 (c). This behavior was also observed in the numerical calculations (Fig. 2.12 (b) and (d)).

Similar to the PTFE based chains, the numerical calculations in the stainless steel based system did not show any change of the dynamic force magnitudes of the incident solitary pulses with the application of the initial magnetically induced precompression (see Fig. 2.13 (b), (d)). This behavior is different than the one observed in experiments, where the added precompression did change the magnitude of the incident pulse (compare Fig. 2.12 (a) and (c)). This difference can be explained by the reduction of dissipation in the precompressed chain in experiments.

It is interesting that a tendency toward a delay of the splitting into a solitary wave train in experiments was observed when the force magnitude of the incident pulse was increased which may be due to the dissipation increase with magnitude of the pulse.

A slight change of the propagating pulse shape was observed in the magnetically precompressed stainless steel chain. The reduced time interval between the maxima of the incident solitary waves in experiments and in numerical calculations (Figs. 2.12 (c) and (d) respectively) demonstrates a significant delay of the pulse splitting. This effect in stainless steel based chains is less noticeable than in PTFE (see Fig. 2.9 (c) and (d)) which may be due to the smaller speed of signal propagation

in the PTFE chains. Also, in the stainless steel case, no increase of the walls pulse magnitude was detected, contrary to the PTFE based chains. The larger difference between the elastic constant of the wall and that of the PTFE chain can be the cause of this phenomenon.

Figure 2.13 shows the comparison of the experimental results with the theoretical values for solitary wave speed versus dynamic force magnitude obtained from the long wave approximation (Eq. (2.9)), of both gravitationally (curve 1 and experimental points) and magnetically precompressed systems (curve 2 and corresponding experimental points). The curves corresponding to the stainless steel system extend to a wider range of magnitudes and velocity and the scale is therefore wider than in Fig. 2.11 for PTFE chains. The curves based on the long wave approximation and the numerical results coincide for both gravitationally and magnetically precompressed chains. When the dynamic force magnitude approaches zero in the magnetically plus gravitationally precompressed chain (F_0=2.44 N), the pulse speed is seen to approach the sound speed (c_0= 539.6 m/s) derived from the long wave approximation (Eq. (2.10)). The change of the sound speed c_0 in the stainless steel chain under the added magnetically induced precompression (2.38 N) in comparison with the system under only the gravitational preload (0.062 N, c_0=292.6 m/s) is about 84% at practically the same density, resulting in the corresponding change of acoustic impedances.

These results show that stainless steel particles under the same static precompressive force demonstrate a higher absolute increase of the solitary wave speed when compared to the PTFE system (compare Fig. 2.11 and 2.13) both in experiments, theory and in numerical calculations. Because the PTFE system is elastically

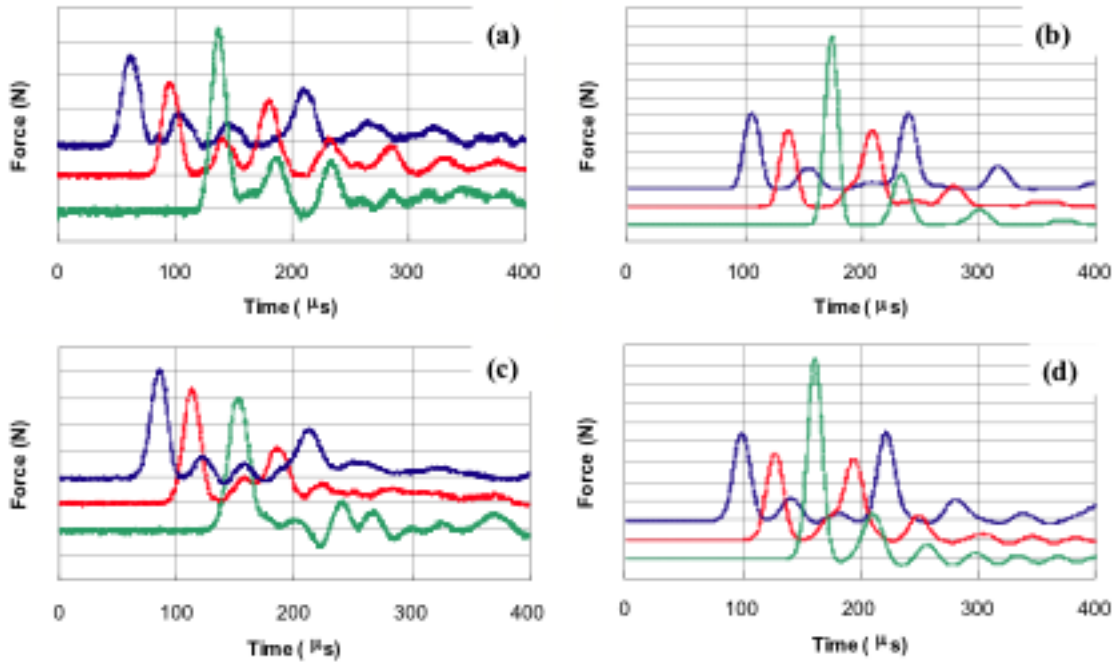

Figure 2.12: Experimental and numerical results on a chain of 21 stainless steel (316) beads with and without magnetic precompression impacted by an alumina striker with a mass equal to 1.2 g and initial velocity equal to 0.44 m/s. (a) Force detected in experiment by the sensor in the 9^{th} ball from the wall (top curve), by the sensor in the 5^{th} ball (middle curve) and at the wall (bottom curve) without magnetic pre-compression; (b) Numerical calculations corresponding to experimental conditions in (a), including gravitational precompression; (c) Force detected in experiment with magnetic pre-compression equal 2.38 N; (d) Numerical calculations corresponding to experimental conditions in (c), including gravitational and magnetic precompression. Vertical scale is 5 N per division for all figures (a-d).

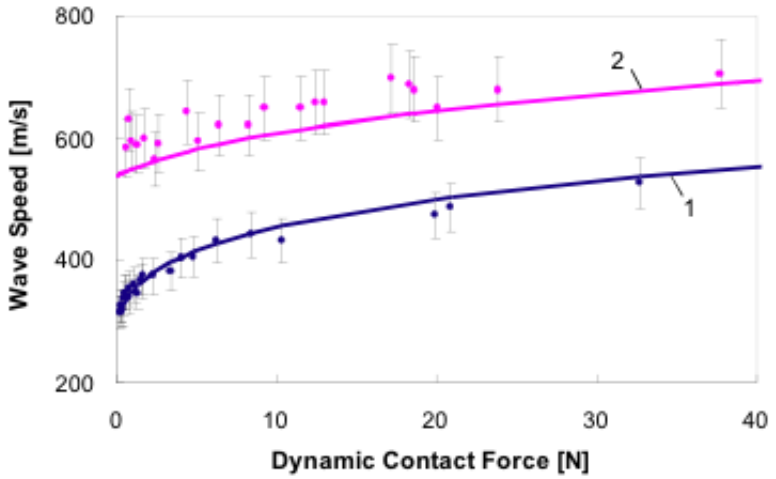

Figure 2.13: Dependence of the velocity of a solitary wave on the magnitude of the dynamic force for both a gravitationally loaded and magnetically tuned stainless steel chain. Experimental values for corresponding curves are shown by solid dots. Curves 1 and 2 are the theoretical curves based on Eq.(2.9), corresponding numerical calculations for discrete chain practically coincide with curves 1 and 2 based on the long wave approximation.

much softer, this result can appear counterintuitive. This behavior of the solitary wave speed with static preloading is due to the fact that, in general, a smaller displacement under the same precompression is outweighed by the larger elastic modulus of stainless steel. These properties of strongly nonlinear phononic crystal can be used for controlled impulse transformation in relatively short transmission lines as well as in tunable acoustic focusing lenses.

2.2.4 Conclusions

A new method of preloading phononic crystals via magnetic precompression was successfully demonstrated for one-dimensional strongly nonlinear systems based on two qualitatively different materials elastic (stainless steel) and viscoelastic (PTFE) beads having more than two orders of magnitude difference in their elastic moduli. This novel method of precompression ensured well controlled boundary conditions and the possibility of a time-dependent fine tuning of the signal speed. The change of the sound speed in these systems under the magnetically induced precompression in comparison with the gravitational preload only is 84% and 128% for stainless steel and PTFE chains respectively at practically the same density. They result in the corresponding change of acoustic impedances.

Both systems were investigated for different conditions of loading under the tunable magnetic prestress. A significant tunability of the speed of the signal was achieved over the natural uncompressed strongly nonlinear system. The change of the solitary wave speed with prestress in experiments is described very well by the results of the long wave approximation and the numerical data, which can be used as a reliable tool in the design of sonic vacuum based devices.

The initial preloading significantly reduced dissipation in the experiments

in both PTFE and stainless steel based systems. A decrease of the reflected wave force magnitude on the wall was observed in numerical calculations for PTFE system. A delay of the splitting of the solitary waves under prestress was observed in experiments and in numerical calculations.

The first section of Chapter 2 has been published in *Physical Review E*, **72**, art. 016603, pp. 1-9 with C. Daraio, V.F. Nesterenko, E.B. Herbold, and S. Jin in 2005. The second section of Chapter 2 has been published in *Physical Review E*, **73**, art. 026610, pp. 1-10 with C. Daraio, V.F. Nesterenko, E.B. Herbold and S. Jin. The contributions made by the dissertation author to these works consisted of developing a discrete nonlinear dynamics code for comparison with the experiments and providing text and figures for the discussion and conclusions.

3

Energy Distribution at the interface of Two Different Granular Chains: Anomalies and Applications

This chapter investigates the distribution of energy within a nonlinear chain of particles. The discussion will extend to impedence mismatching at the interface of two disparate chains and discuss the effects that the gravitational or externally applied precompressive forces have on the dynamic behavior of the collective and individual particle motion(s). The second part of this chapter describes experiments for proposed applications of the described phenomena.

3.1 Anomalous Wave Reflection at the Interface of Two Strongly Nonlinear Granular Media

Strongly nonlinear granular chains are sonic vacuum (SV) type systems that support a new type of solitary wave with parameters determined by the interaction force [Nesterenko (1983), Lazaridi and Nesterenko (1985), Nesterenko (2001)].

These solitary waves are qualitatively different from the well known weakly nonlinear solitary waves of the Korteweg-de Vries equation (Eq. (1.7)) Korteweg and deVries (1895), Remoissenet (1996)] which were first discovered experimentally by Russel [Russell (1845)] in 1834. The concept of a SV was proposed to emphasize the uniqueness of the types of materials that do not support sound waves without initial prestress [Nesterenko (2001), Nesterenko (1994)]. The unique property of these materials is that a single parameter (initial prestress) is able to tune the response from a linear to a strongly nonlinear regime. One of the main features of strongly nonlinear solitary waves is that the speed is strongly influenced by inter-related potential and kinetic energies [Nesterenko (2001)]. A granular chain with particles interacting according to Hertz law [Hertz (1881)] is just one example of strongly nonlinear behaviour which can support the new type of solitary wave [Nesterenko (2001)]. Different groups investigated numerically and experimentally the properties of these waves [Nesterenko (1983), Lazaridi and Nesterenko (1985), Coste et al. (1997), Manciu et al. (1999b), Manciu et al. (1999a), Hinch and Saint-Jean (1999), Coste and Gilles (1999), Manciu et al. (2000), Hascoët and Herrmann (2000), Sen and Manciu (2001), Manciu and Sen (2002), Sen et al. (2003), Job et al. (2005), Vergara (2005)] and found a good agreement with the theoretical predictions based upon a long wave approximation. Nonlinear dynamic properties can be extended to other designed metamaterials including the propagation of electrical or other types of signals. Interesting applications of this new area of wave dynamics have been proposed for the creation of nano-droplets for potential use in novel designs of printers [Sen et al. (1999)].

Another intriguing property of these materials is the reflection of the solitary waves at the interface of two SV materials [Nesterenko (2001), Nesterenko (1994), Vergara (2005), Nesterenko et al. (1995)], from imperfections [Manciu et al. (1999a)]

or from a wall [Job et al. (2005), Vergara (2005)]. Based on the former, the novel concept of impulse trapping inside a protecting granular laminar layer has been proposed [Hong and Xu (2002), Hong (2005)].

In this section the experimental and numerical observation of strongly nonlinear wave interactions at the interface of two SV-type systems resulting in anomalous reflected compression and transmitted rarefaction waves when the magnetically induced prestress is applied.

A new method of noncontact precompression based on the magnetic interaction of the first magnetic particle in the chain with a Nd-Fe-B ring magnet placed outside the chain [Daraio et al. (2006)]. The magnetic force (2.38 N) is practically independent of the motion of the magnetic particle.

In experiments, a chain of 20 nonmagnetic stainless steel (316 type) particles (plus a magnetic particle on the top) with diameter a=4.76 mm and mass 0.4501 g above 21 PTFE (polytetrafluoroethylene) beads with diameter a=4.76 mm and mass 0.1226 g. The elastic moduli and Poisson ratios for PTFE and stainless steel were equal to 1.46 GPa [Daraio et al. (2005)] and 193 GPa, 0.46 and 0.3 respectively. Piezogauges measuring the compression force [Daraio et al. (2005)] were placed in the 8^{th} and 4^{th} particle above the interface and in the 4^{th} and 8^{th} particle below the interface.

The equations of motion used in numerical calculations are similar to those in Nesterenko (1983), Nesterenko (2001). The intrinsic MATLAB ODE45 solver was used with a time step of 0.8 microseconds. No restitutional losses were taken into account. The linear momentum and energy were conserved with a relative error of 10^{-12}% and 10^{-8}%. The curves obtained in numerical calculations represent the averaged compression forces on the contacts of each particle [Daraio et al. (2005)], except curves in Fig. 3.3(a) and (c) where the contact forces between particles are

shown. The displacement (δ) of each particle is calculated from the equilibrium positions with no external load.

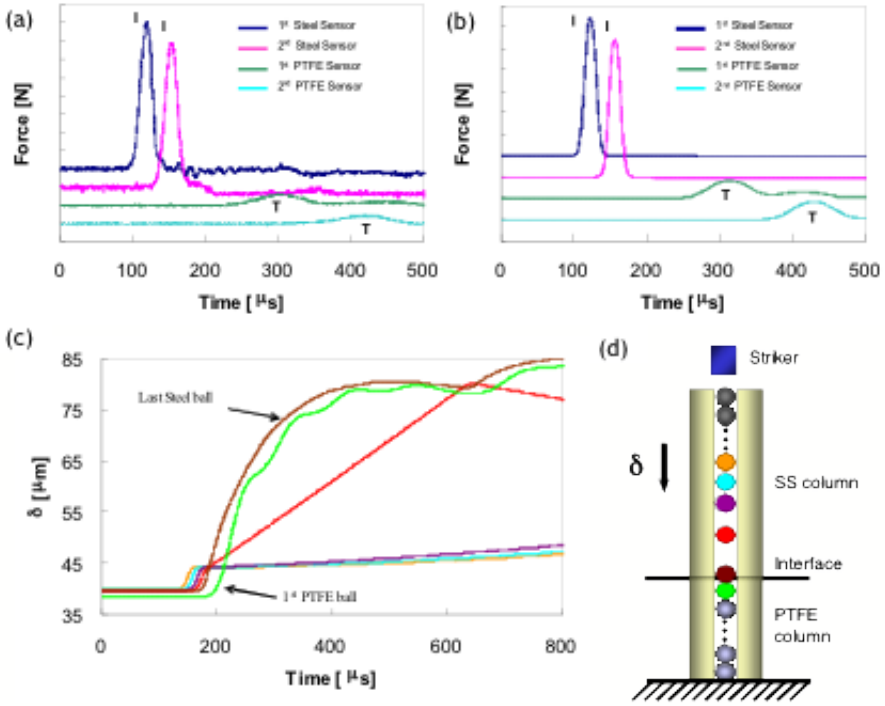

Figure 3.1: Incident pulse (I) interaction with the interface of the two SVs composed of 20 stainless steel and 21 PTFE beads. (a) Experimental data. (b) Numerical simulation of (a), vertical scales 1N (a) 2 N (b) per division. (c) Displacements (δ) of beads adjacent to the interface. (d) The relative positions of particles 600 μs after the impact.

The results without magnetic precompression are presented in Fig. 3.1. A solitary wave (I) was excited in the system by an impact of an alumina cylinder with a mass of 0.47 g and velocity of 0.44 m/s. This single solitary wave generates multiple

pulses (T) in the PTFE chain after the interaction with the interface. No reflected compression wave is detected in experiments or numerical calculations (Fig. 3.1(a) and (b)) as in Nesterenko (2001), Nesterenko (1994), Nesterenko et al. (1995), Hong and Xu (2001), Hong (2005).

The mechanism explaining the practically complete energy transfer into the PTFE chain and the absence of a reflected compression wave is illustrated by the numerical results in Fig. 3.1(c). The slopes of the displacement-time curves represent the velocity of the corresponding particles. It is evident that a series of gaps (Fig. 3.1(d)) open between the stainless steel particles in the vicinity of the interface. Therefore a fracture wave is propagating into the stainless steel chain similar to the one originating when the solitary wave arrives at the free surface [Hinch and Saint-Jean (1999)] due to high gradients of particle velocities. Gap openings are also observed in: a 1-D granular chain in the process of solitary wave collision, which are related to the generation of secondary solitary waves [Manciu et al. (2000), Manciu and Sen (2002), Sen et al. (2003)], and in 2-D numerical simulations of the transmission of the static force [Goldenberg and Goldhirsch (2005)], and it is related to the subharmonics and noise excitation in the transmission of the acoustic wave in granular media [Tournat et al. (2004)].

The gaps opening and closing introduce an entirely new time scale in the system which is determined by the size of the gaps and particle velocities instead of the time of flight determined by particle diameter or length of the chain and signal speed. The strongly nonlinear particles interaction results in a high gradient of particle velocity in the incident wave that translates into a high gradient of velocity near the interface with the last stainless steel particle absorbing the main part of the energy. The zero tensile strength of the chain ensures the uni-directional energy transfer to the PTFE chain without sending any tensile wave back to the stainless

steel chain. Thus, the observed behaviour is due to a double nonlinearity: a strongly nonlinear compression part of the interacting force and a zero tensile strength of the system.

At the moment when the process of energy and linear momentum transmission into the PTFE chain is practically complete, only a very small portion of the impactors kinetic energy (about 0.16%) is reflected and the second steel particle is rebounding from the interface with a velocity of 0.018 m/s. Without the gravitational precompression this particle rebounds much later with a velocity significantly smaller (0.0009 m/s) than in the previous case. This indicates that the reflected energy can be increased with the initial precompression.

The sequence of pulses in the PTFE chain are generated by the decelerating interfacial stainless steel particle, which is demonstrated by the kinks of decreasing amplitude on the displacement curve of the first PTFE particle in Fig. 3.1(c).

The application of the magnetically induced precompression resulted in a completely different reflection of the strongly nonlinear pulse from the interface (compare Fig. 3.1(a) with Fig. 3.2(a) and Fig. 3.1(b) with Fig. 3.2(b)). In this case the compression pulse is propagating into the steel chain followed by an oscillatory rarefaction wave (Fig. 3.2(a) and (b)). The acoustic impedance of the stainless steel chain is about one order of magnitude higher than that of the PTFE chain. In the linear approach the incident compression solitary wave should result in a rarefaction wave propagating back from the interface into the stainless steel chain, it is indeed noticeable from the coordinated change of sign of the slope in the displacement curves starting from the 4th stainless steel particle from the interface (Fig. 3.2(c)). Additional to the expected reflected rarefaction wave, experimentally and numerically anomalous reflected compression waves (R) (Fig. 3.2(a) and (b)) were observed!

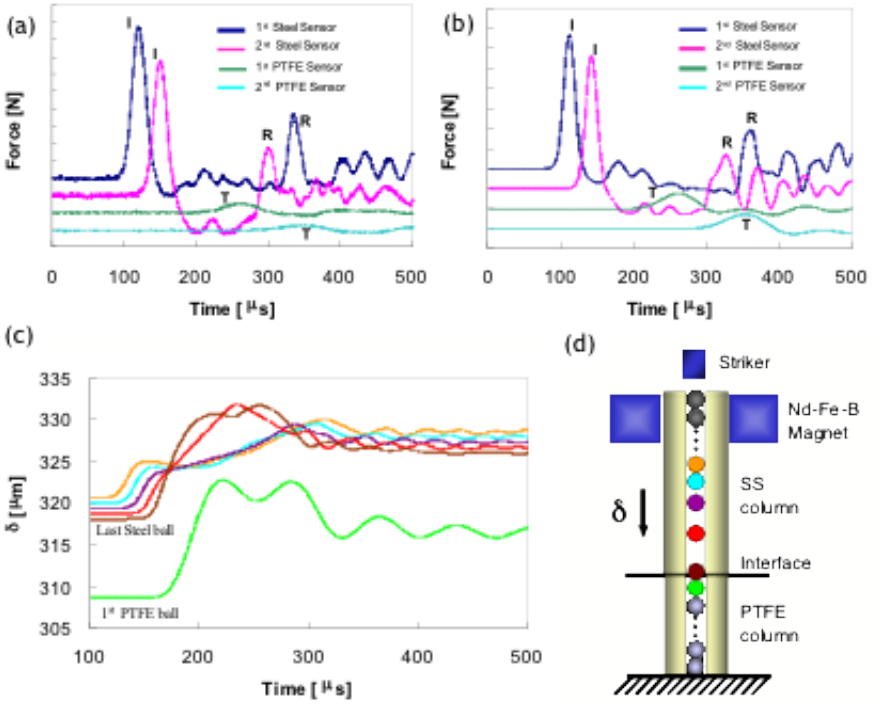

Figure 3.2: Anomalous pulse reflection from magnetically preloaded interface of two sonic vacua in a configuration similar to Fig. 3.1. (a) Experimental data. (b) Numerical simulation of (a); vertical scales 1N (a) and 2 N (b) per division. (c) Displacements (δ) of the stainless steel and PTFE beads adjacent to the interface related to the beginning of the formation of the rarefaction wave and anomalous reflected compression waves. (d) Relative positions of particles about 200 microseconds after the impact.

Based on the measurements of compression force inside particles (Fig. 3.2(a)) the leading reflected pulse in experiments has an amplitude (total contact force F_m including initial preload F_0) of about one half of the amplitude F_m of the incident wave. The relation between measured compression force inside particles and maximum contact force F_m is discussed in Chapter 2. It should be noted that the contribution of the incident rarefaction wave to the reflected compression wave, based on the acoustic impedance ratio, can not bring the force above the initial precompression. Also, the leading transmitted (T) compression pulse in PTFE chain is followed by unexpected rarefaction pulses (Fig. 3.2(a) and (b)).

The superimposed static precompression on the interface of two sonic vacua made this interface visible based on the reflected signal in contrast to the uncompressed case. A peculiar characteristic of the leading reflected compression wave is related to its delayed time of arrival (about 90 microseconds) at the gauges in experiments and calculations based on the distance from the interface and the speed of the incident and reflected compression pulses (Fig. 3.2(a) and (b)).

When the leading reflected compression wave is formed, at 500 microseconds after the impact, the energy transferred to the PTFE chain is about 86% of the combined kinetic energy of the striker and the energy supplied by the magnetic force at the early stage of the motion of the first particle (about 25 microseconds). This contrasts with the previous case where almost all of the kinetic energy of the striker (over 99%) was transferred into the PTFE chain. It may be appropriate to name this dramatic change of reflectivity triggered by the initial precompression (zero and 14% reflected energy respectively) the acoustic diode effect.

The reflected compression waves were formed mainly by the rebounding motion of the last stainless steel particle due to the resistance of the PTFE beads. This phenomenon is a clear manifestation of the discrete nature of the system and can

not be captured in a continuum approximation similar to the fracture of a chain in the vicinity of impacted end [Nesterenko (1983), Nesterenko (2001)] or the formation of secondary solitary waves [Manciu et al. (2000), Manciu and Sen (2002), Sen et al. (2003)]. The particles in the vicinity of the interface are self organizing into a state close to the original precompressed state (Fig. 3.2(c)).

As in the previous case (Fig. 3.1(c)), the stainless steel interfacial particle serves as the main energy transformer from the stainless steel chain to the PTFE chain (Fig. 3.2(c)). Again, a fracture-wave follows the rarefaction wave that is propagating from the interface back into the stainless steel chain. In the case of stronger precompression the gaps are closed rather quickly assisting the formation of reflected compression pulses. The opening and closing of gaps introduce a new time scale which is much shorter than in the previous case due to the significantly smaller size of the opened gaps and larger velocities of the particles moving into the gaps (compare Figs. 3.1(c) and 3.2(c)). Initial precompression in a counterintuitive manner triggers the generation of a reflected compression wave and does not suppress the process of gaps opening and closing but instead makes it faster. Their characteristic opening and closing also participate in the process of wave reflection in this case (Fig. 3.2(c) and (d)). This indicates that the response of the interface between two SVs can be qualitatively tuned by the applied static preloading.

The gap openings between the stainless steel particles in the vicinity of the interface in the investigated set-up has a threshold on the amplitude of the incident wave detected in numerical calculations. This threshold amplitude of contact force Fm is approximately equal to 4.3 N, which is larger than the static preload at the interface 2.473 N. The anomalous reflected compression wave was generated at this amplitude even when no gap openings were detected. This shows that the anomalous reflected compression wave is due to the changing direction of the velocity of the last

stainless steel particle.

To identify the possible influence of the incident rarefaction wave on the reflected compression pulse in experiments, the interaction of a single solitary wave (I) with similarly preloaded (2.38 N) sonic vacua was simulated. It was formed in a stainless steel chain with larger number of particles (1900) (Fig. 3.3(a)) after the impact by an alumina striker with a mass equal to the mass of the stainless steel particle and a velocity of 0.44 m/s. The incident rarefaction wave followed far behind the solitary wave and did not participate in the considered soliton interaction with the interface.

After the interaction, an expected reflected rarefaction wave formed close to the interface in the stainless steel chain and was followed by a compression pulse and an oscillatory tail (Fig. 3.3(b) and (c)). The amplitude of the first reflected compression pulse (Fig. 3.3(b)) and the behaviour of the displacements of the particles adjacent to the interface (Fig. 3.3(d)) were very similar to the experiments and numerical calculations for a smaller number of particles where the incident rarefaction wave was present (Figs. 3.2(b), 3.2(c)). This clearly indicates that the observed anomalous reflected compression pulse and trailing oscillatory tail are caused by the incident solitary wave.

The reflected compression solitary wave is a nonlinear wave with a speed apparently higher than the speed of the head of the reflected rarefaction wave and oscillating tail. It becomes the leading reflected pulse about 1000 particles from the interface as was found in separate numerical calculations with 25000 stainless steel and 1000 PTFE particles. It is interesting that only one anomalous reflected compression solitary pulse was able to overcome the head of the reflected rarefaction wave, with amplitude F_m decreasing by about 40% during this process. As a result,

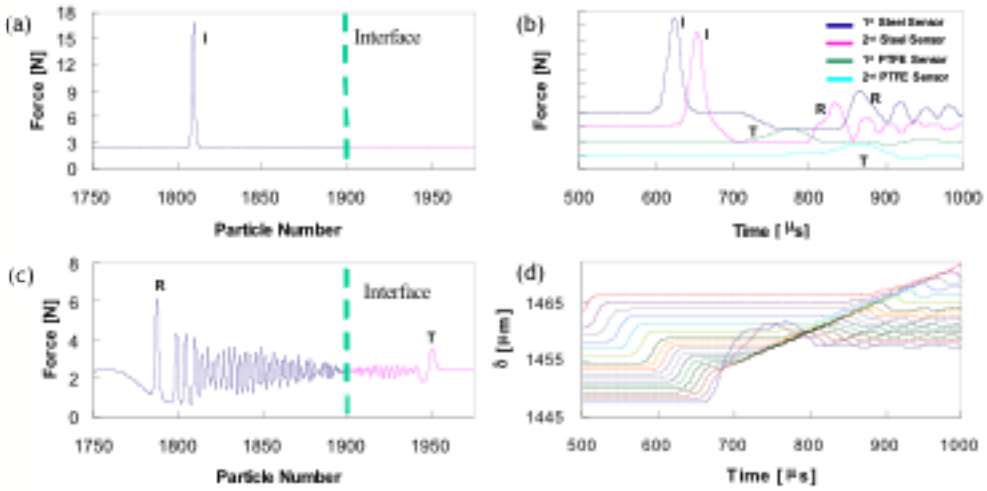

Figure 3.3: (a) Incident solitary wave (I). (b) The forces inside the stainless steel particles corresponding to the positions of the gauges in experiments close to the interface, vertical scale is 2 N per division (compare Fig. 3.3(b) with Fig. 3.2(a),(b)). (c) The reflected rarefaction wave, anomalous compression solitary wave (R) and trailing pulses in the stainless steel chain and transmitted compression pulse (T) with the rarefaction pulse and oscillatory tail in the PTFE chain. (d) Displacements of the stainless steel beads adjacent to the interface.

the reflected signal at a relatively large distance from the interface (larger than 1000 particles) is composed of three essential elements in the following order: leading anomalous reflected compression solitary wave, a rarefaction wave and an oscillatory tail. On later stages the oscillatory tail overcomes the head of the rarefaction wave leaving only a leading reflected compression solitary wave and an oscillatory tail. The leading transmitted compression pulse in the PTFE chain is followed by an unexpected rarefaction wave and an oscillatory tail (Fig. 3.3(c) and (d)), also evolving into a leading transmitted compression solitary wave and an oscillatory tail.

A qualitative change of the reflectivity under the applied precompression was not observed when the wave approached the interface from the PTFE side.

In summary a strong sensitivity to the initial precompression of the reflected and transmitted energy from the interface of the two granular media was observed. This phenomenon can be named the acoustic diode effect. It can be employed for designing tunable information transportation lines with the unique possibility to manipulate the signals delay and reflection at will, and decompositions/scrambling of security-related information. It can also be used for identification of such interfaces (e.g. geological multilayer structure consisting of dissimilar granular materials) and for optimization of shock protection layers composed of uniquely combined composite granular media with layers of different particle sizes (masses) and elastic constants.

3.2 Energy Trapping and Shock Disintegration in a Composite Granular Medium

Strongly nonlinear systems, e.g. one-dimensional chains of beads, exhibit unique wave dynamics [Nesterenko (2001)] especially at the interface of two different granular systems [Nesterenko (2001), Nesterenko et al. (1995), Hong and Xu (2002),

Hong (2005), Nesterenko et al. (2005), Vergara (2005)] or at the interface of granular media and solid matter [Job et al. (2005)]. The strongly nonlinear wave behavior in a chain of elastic spherical beads arises from the nonlinearity of the Hertzian contact interactions between the particles composing the system resulting in a power-law type dependence of the compressive force (F) on the displacement (δ) (where $F \propto \delta^{3/2}$) combined with zero tensile strength. In the case of zero or very weak precompression (resulting in zero or very small sound speed, i.e. sonic vacuum (SV) type systems) the corresponding wave equation supports a qualitatively new solitary wave [Nesterenko (2001)]. A peculiar property of the granular media derives from the possibility of tuning the type of stationary solution produced by the system by varying the precompression acting on the chains [Nesterenko (2001), Coste et al. (1997), Daraio et al. (2006)]. This allows choosing the regime of wave propagation from strongly to weakly nonlinear or the reflection from the interfaces of two granular systems according to the needs of each specific application. Real granular beds composed of iron shot (the waste from metallurgical plants) have been successfully used as shock-mitigating protectors in the design of explosive chambers that reduce the amplitude of shock waves or spall generated by a contact explosion [Nesterenko (2001)].

Granular matter has many known applications but it is difficult to understand its intrinsic dynamic properties due to the strong nonlinearity of forces between particles and complex contact-force distributions between grains [Nesterenko (2001), Goldenberg and Goldhirsch (2005), Corwin et al. (2005), Majmudar and Behringer (2005)]. The understanding of their fundamental behavior may help to create a new class of functional composite materials with novel dynamic properties. In the past, the design of shock protectors focused mainly on the wave transformation provided by layered systems or the enhanced energy dissipation in porous media

[Nesterenko (2001), Benson and Nesterenko (2001), Nesterenko (2003)]. Yet an entirely different way of protecting materials is through the confinement of an impulse in a particular region of the shielding medium called a granular container as predicted by theoretical analysis [Hong and Xu (2002), Hong (2005)], but not experimentally demonstrated. It was observed that soliton confinement occurs within a section composed of low mass particles embedded in a chain of beads with higher mass with the same elastic modulus and contact interaction law [Hong and Xu (2002)]. A more efficient granular container can be designed using a series of sections with particles interacting according to different contact forces and masses [Hong (2005)].

The idea of the impulse confinement in this case is based on the anomalous features of an incident wave interacting with an interface between the two different granular media (stainless steel and PTFE) [Nesterenko et al. (2005)]. It was shown that a solitary wave passing through the interface between a stainless steel and PTFE chain from the stainless steel side transmits all of its energy through the interface into the PTFE section. Furthermore the transmitted signal disintegrates into a sequence of solitary waves (see Fig. 3.4(c) in Nesterenko et al. (2005)). On the other hand, when a solitary wave approaches the same interface from the PTFE side, numerical calculations and experiments have shown that a significant part of the incident pulses energy is reflected back into the PTFE side. The amplitude of the reflected solitary wave is 75% of the incident waves amplitude and the pulse transmitted to the stainless steel chain decomposes into a train of three solitary waves. In this study a granular system composed of sections of stainless steel and PTFE beads with a constant overall number of particles and a fixed ratio between them were tested experimentally and numerically. Multiple interfaces between sections were introduced to enhance the walls protection efficiency. A chain with a similar dynamic behavior can also be made from a different combination of structural elements with strongly

nonlinear interactions.

To create the granular system for pulse trapping and protection of the wall, a constant total number of 32 beads were used. Twenty two of them were the high-modulus, large mass stainless steel beads (non-magnetic, 316 type) and 10 were the low-modulus, small mass PTFE (polytetrafluoroethylene) beads. It was shown that a chain composed of PTFE particles support strongly nonlinear solitary waves [Daraio et al. (2005)]. The diameter of the beads was uniform, 4.76 mm, and the bead arrangements in different configurations were investigated. The mass of the 316 stainless steel bead was 0.45 g, with a density of 8000 kg/m3, Youngs Modulus of 193 GPa and the Poisson ratio equal to 0.3 [for Metals (1983),AISI Type 316L www.efunda.com]. The mass of a PTFE bead was 0.123 g, the density 2200 kg/m3, the elastic modulus was 1.46 GPa, and a Poisson ratio 0.46 [Daraio et al. (2005), Carter and Marsh (1995)]. These types of beads were chosen to demonstrate that the pulse trapping effect is sensitive to the geometrical arrangement of the same number of structural elements for the enhanced protection of the bottom wall from the incoming impulse. Three piezo-sensors were embedded inside the particles as described in Nesterenko et al. (2005), Daraio et al. (2005) allowing the calculations of the time-of-flight for determining the pulse speed. A fourth sensor was embedded in the wall at the bottom of the chain as in Daraio et al. (2004a). The particles were assembled in a vertical PTFE holder. Pulses were generated with a 0.47 g Al_2O_3 rod striker for the single solitary wave type loading and with a 63 g Al_2O_3 rod for the shock-type loading with various velocities. In order to tune the properties of this new granular protector, a magnetically induced non-contact compressive force (2.38 N) was applied as in Nesterenko et al. (2005), Daraio et al. (2006).

First, a granular protector with a single central PTFE section was tested (Fig. 3.4(a)). Here 11 stainless steel beads were placed at the top of the chain, 10

PTFE beads in the middle and 11 steel beads at the bottom, forming a softer central section of the chain. Placing a section of stainless steel particles on the top of the protective layer is important in practical applications to enhance the resistance to the penetration of an impactor and to reduce the effects of a contact explosion in granular beds. The corresponding impulse behavior is presented in Fig. 3.4(b) and 3.4(c) for incident solitary and shock-like waves.

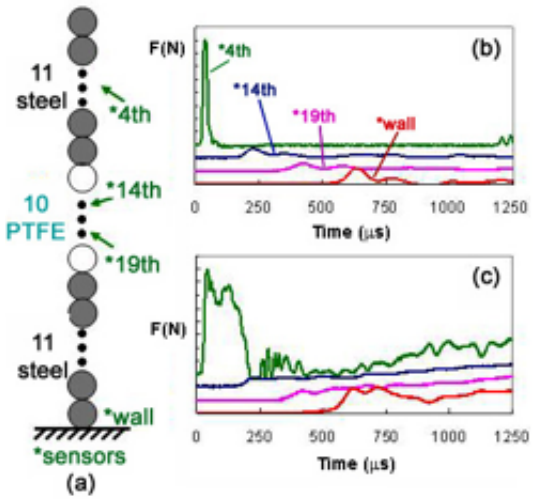

Figure 3.4: Trapping of a solitary- and a shock-pulse in the granular protector with a single central PTFE section. (a) Schematic diagram of the stainless steel and PTFE beads geometrical arrangement used for testing with indicated sensors. (b) Experimental data corresponding to the solitary-type loading. The striker here was an Al_2O_3 cylinder of 0.47 g with an impact velocity of 0.44 m/s. (c) Experimental data corresponding to the shock-like loading with shock amplitude similar to (b) excited by an Al_2O_3 striker (63 g). The y-axes scale is 1 N per division for (b) and (c).

To qualitatively compare the experimental results with the granular containers proposed in Hong (2005), similar tests were conducted exchanging the particles positions. In this case 5 PTFE particles were set on the top and bottom sections of the chain and the 22 stainless steel beads were positioned in the middle (Fig. 3.5(a)). This configuration can be compared to half of the granular container presented in the Fig. 3.5(c) in Hong (2005). The experimental and numerical results are presented in Fig. 3.5 (b) and 3.5(c).

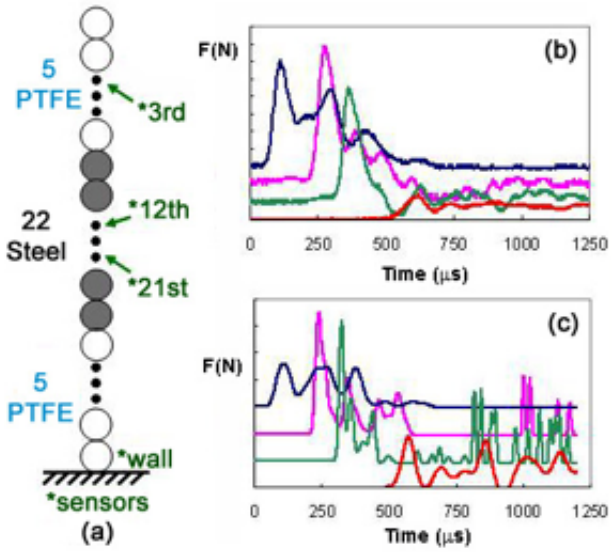

Figure 3.5: Trapping of a solitary pulse in the granular protector with a single stainless steel central section. The striker was an Al_2O_3 cylinder of 0.47g with an impact velocity of 0.44 m/s. (a) Schematic diagram of the stainless steel and PTFE beads geometrical arrangement used for testing with indicated sensors. (b) Experimental data corresponding to the solitary-type loading. The y-axes scale for all curves is 0.2 N per division. (c) Numerical data corresponding to (b). The y-axes scale is 1 N per division.

The granular protector with two PTFE sections (Fig. 3.5(a)) configuration consisted of the same overall number of stainless steel and PTFE beads, but they were divided into two sections of 5 PTFE particles interposed between the stainless steel beads creating a larger number of interfaces in comparison with the Figs. 3.4(a) and 3.5(a).

Numerical analysis of the discrete chains was performed for all the set-ups described to calculate force-time curves as well as the total energy trapped and released by the granular containers. The numerical simulations were run similar to [Daraio et al. (2006),Daraio et al. (2005)] using the equation of motion for the grains with Hertzian contact and identical conditions of impact striker and velocity. The presence of the gravitational precompression (caused by the vertical orientation of the tested chain) was taken into account in the numerical analysis although it has a weak effect at the investigated pulse amplitudes. The effects of dissipation were not included in the calculations and will be addressed in future studies.

In the case of the granular protector with a single PTFE central section, the trapping of the incident solitary pulse in the softer region is clearly evident in experiments (Fig. 3.4(b)) and matched well with the numerical calculations. The experimental data clearly demonstrates that the incident solitary pulse (40 μs long and 8 N in amplitude) is quickly transformed by the PTFE portion of the chain to a much longer signal and it is decomposed into a train of pulses arriving at the wall with a much lower amplitude in experiments.

The processes of impulse transformation and confinement, corresponding to the arrangement represented in Fig. 3.4(a) (Steel-PTFE-Steel), are similar to the one presented in Hong and Xu (2002) (see Fig. 3 there). Specifically, it was observed: (a) a complete transmission of the energy of the incident solitary wave

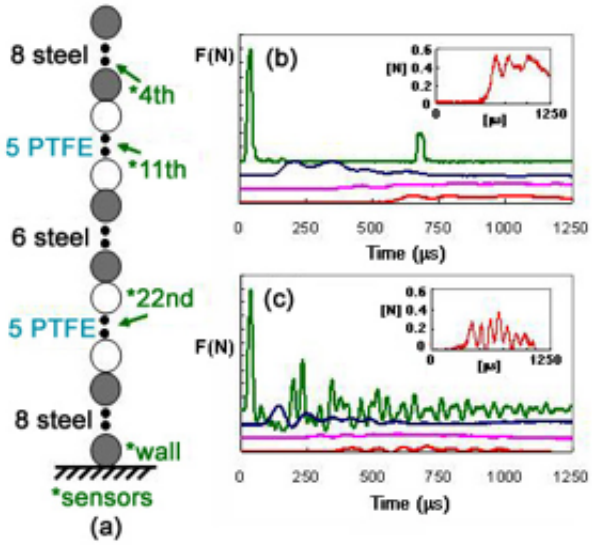

Figure 3.6: Solitary pulse trapping in the composite granular protector with two PTFE sections without and with additional precompresion. (a) Schematic diagram of the arrangement of the stainless steel and PTFE beads with indicated sensors. (b) Experimental results for only gravitationally loaded system obtained with an Al_2O_3 striker (0.47 g) at 0.44 m/s. (c) Experimental results including a magnetically induced precompression; all other conditions as in (b). The y-axes scale is 1 N per division. Insets in (b,c) show the pulse behavior at the wall for the gravitationally loaded and the magnetically tuned system. Note the significantly moderated impulse shape arriving on the wall in (b) and (c): the strong incident impulse (first curve) disintegrates into a very weak series of pulses delivered over a much longer period of time (bottom curve).

into the PTFE section without any wave reflected back in the steel section (see also [Nesterenko et al. (2005)]); (b) a significant reflected pulse propagating back into the PTFE section when the incident pulse arrives from the PTFE side of the interface; (c) the disintegration of the transmitted impulse into a train of solitary waves was observed in both cases.

The solitary wave speed in the steel section of the chain is 357 m/s. The experimental data (Fig. 3.4(b)) shows that the signal speed drops down to 137.4 m/s when the pulse passes through the first interface into the PTFE section. This slowing down can be attributed to the drastically lower elastic modulus of PTFE (1.46 GPa) compared to steel (193 GPa), which enables the pulses to remain mostly trapped in the softer section of the chain for a relatively long time bouncing back and forth between the two interfaces releasing the energy of the impact in both directions very slowly.

The first and largest impulse reaching the wall in Fig. 3.4(b) has an experimentally measured amplitude significantly smaller (about 5 times) than the one measured in independent experiments in a uniform steel chain under identical impact conditions and the same number of particles. In the numerical calculations the reduction is also very significant being 3 times smaller (amplitude 6.7 N) than the wall amplitude of 20 N in a uniform stainless steel chain of beads. The difference between the experimental data and numerical results is most likely due to dissipation not being included in the numerical calculation, which underestimates the total extent of signal amplitude reduction. It also demonstrates that the dissipation present in the experiments can significantly enhance the protection against incident solitary waves. The trapped pulses reflected from the bottom of the central soft section have an amplitude comparable to the incoming pulses in the PTFE section, demonstrating that a significant amount of the total energy remains confined in the softer central

portion of the chain, slowly leaking out only a small amount at each rebound (28% after the first rebound).

The performance of the granular protector with a single PTFE central section against shock wave type loading is shown in Fig. 3.4(c). Trapping in a granular container has not been investigated theoretically or experimentally, though shock-like loading is very important in practical applications. A shock wave is a qualitatively different type of pulse in comparison with solitary wave. It is usually characterized by a longer duration which may affect the reflection and transmission at the interfaces. The results of numerical calculations for both types of incident waves (solitary and shock), showed similar tendencies in the impulse behavior which qualitatively agreed with the experimental results.

To compare this particles arrangement to the one proposed in Hong (2005) the particles position were exchanged as described in Fig. 3.5 (a). This new arrangement, still preserving the total number of beads and the ratio between them, may be qualitatively compared to the design of one half of the granular container presented in the Fig. 3.5(c) in Hong (2005). It is evident from the numerical calculations that this arrangement dramatically improved the efficiency of the walls protection reducing the pulse amplitude reaching the wall from 6.7 N observed in the previous case down to 2 N in Fig. 3.5(c). A similar trend is observed in experiments where the amplitude of the signal reaching the wall drops from 1 N in Fig. 3.4(b) to 0.2 N in Fig. 3.5(b) when impacted with the same striker and velocity.

To investigate the influence of the particle arrangement in this system and to enhance the protection efficiency, the PTFE beads were reorganized as shown in Fig. 3.6(a) increasing the number of interfaces. Here, steel and a PTFE portion of the chains were alternated with a periodicity 8-5-6-5-8, where the two 5-particle sections are composed of PTFE beads only. This geometry resulted in a much better

protection of the bottom wall in comparison to the first case studied (compare Fig. 3.6(b) with Fig. 3.4(b)) by more efficiently trapping most of the incoming pulse and releasing its energy more slowly. In this case the amplitude of the force calculated numerically at the wall was 3.4 times less (2.4 in experiments) than the one detected in the granular protector with a single PTFE section and 10 times less than the one observed in an all-steel chain (not shown). The discrepancy between the numerical and experimental case is probably due to the enhanced effects of dissipation at higher signal amplitudes. However, there exists a qualitative agreement of the wave behavior in experiments and numerical calculation for solitary-type loading.

In this set-up, the first (uppermost) PTFE section works very efficiently trapping a larger amplitude of the pulse and transforming the 40 μs long incoming solitary pulse (from the steel section) into a much longer and delayed train of signals with an overall duration over 1000 μs. Numerical calculations of the energy contained in the PTFE sections confirmed the higher efficiency as a protector: the granular protector with two PTFE sections traps most of the potential energy for a longer time when compared to the single PTFE section and achieves equal wall protection efficiency when compared to the setup presented in Fig. 3.5.

It was previously reported that the wave behavior and the reflection from the interface of two strongly nonlinear systems is strongly affected by an initial precompression causing the phenomenon of anomalous reflection of a compression solitary wave [Nesterenko et al. (2005)]. This is because an anticipated combination of pulses contains a solitary-like reflected rarefaction pulse which is not supported by the equations of motion as a stationary wave [Nesterenko (2001)]. This rarefaction pulse, formed very close to the interface, quickly disintegrates into a complex pattern of waves. This effect of anomalous reflection might be used to control and improve the protecting behavior of the investigated systems.

To explore the influence of the static compression an efficient granular protector was tested with two PTFE sections under a magnetically induced precompression. This resulted in an evident increase of the speed of the signal propagation and in the creation of an anomalous reflected wave [Nesterenko et al. (2005)] on the first steel sensor (uppermost curve) followed by a series of multiple reflected pulses (compare Figs. 3.6(b) and 3.6(c)). The introduction of the preload significantly reduced the force impulse acting on the wall, facilitating the splitting of the signal into a train of low-amplitude waves (see insets in Fig. 3.6(b) and 3.6(c)).

The physical explanation for such an increase in the pulse confinement in the softer region of the chain is related to the self assembly of gaps at the interfaces causing a complex rattling among the interfacial particles combined with the reflection of the pulse from the interfaces of the soft and rigid regions. These gaps allow the two softer regions of the chain to keep the energy trapped longer, therefore enhancing the protection of the wall. Moreover when the signal propagates through the first interface, a fracture wave is formed and propagates back into the stainless steel chain. The presence of these open gaps is counter intuitively enhanced by the static precompression and is responsible for the introduction of a new time-scale in the system as well as the formation of an anomalous reflected wave at the interface under precompression (top curve of Fig. 3.6(c)). As a result, the gaps delay the wave reflection and propagation, and enhance the reflections from the heavy/light interfaces. In this case the total energy trapped in the softer sections remains almost constant within the investigated time. Furthermore the superimposed force transforms the pulse arriving at the wall in a series of well separated pulses, delaying the total momentum reaching the bottom wall. This behavior is very useful as a mean to protect an object from incoming impacts by providing longer distances of pulse traveling within the protector region, thus additionally causing the impact to lose its

energy due to dissipation.

The granular protector with two PTFE sections was also tested for the trapping of shock pulses. To generate such pulses an Al_2O_3 rod (63 g) was used as a striker impacting the first steel bead. The signal reaching the wall was dramatically transformed from an oscillatory, fast-ramping shock loading into a long, slowly increasing series of pulses. This trapped and transformed pulse is likely to be much less damaging to the protected object (the end wall in these experiments). Results of the numerical calculations indicated a similar trend as in the experiments. The data demonstrates that under shock-type loading the softer sections of the chain do not appear to trap energy, thus only acting as pulse transformers, as opposed to the energy trapping of incident solitary waves.

Calculations were also performed for a chain composed of one-by-one alternating stainless steel and PTFE beads to see if the increasing the number of contacts between the two different beads throughout the chain further improves the shock protection. In this case the chain responded as a homogenized two-particle system [Nesterenko (2001)] without the creation of reflected pulses, thus drastically reducing the efficiency of the protector.

In conclusion, the efficiency of soliton-like and shock-like pulse were demonstrated experimentally and numerically trapping and disintegration in a composite granular protector and proved that its efficiency depends on the particles arrangements. The introduction of a magnetically induced precompression divided the signal reaching the wall into a series of subdivided pulses reducing the total force impulse even further.

The shock-disintegrating principles demonstrated here can be utilized for practical three dimensional composite structures. Among the foreseen practical application for such a novel, pulse-disintegrating material are: protection gear for mili-

tary hazards, sound-proof coatings or layers for buildings, protection devices for the human ear from possible exposure to extreme pulses or explosions, and soft-landing of spacecrafts or highly protective shipping box for delicate machineries. Biomedical applications are also conceivable, for example, as a pulse-preventing layer for sensitive regions of human body where the acoustic beam is to be avoided during ultrasonic treatment of brain tumors or deposited stones.

Sections 1 and 2 of Chapter 3 have been published in *Physical Review Letters*, **95**, art. 158702, pp. 1-4 with V.F. Nesterenko, C. Daraio, E.B. Herbold and S. Jin and *Physical Review Letters*, **96**, art. 058002, pp. 1-4 with C. Daraio, V.F. Nesterenko, E.B. Herbold and S. Jin. The contributions made by the dissertation author to these works consisted of further development of a discrete nonlinear dynamics code for comparison with the experiments and providing text and figures for the discussion and conclusions.

4

Pulse Propagation in a Strongly Nonlinear Diatomic Chain of Particles

4.1 Introduction

The two apparent modes are the acoustic and optical modes. The acoustic mode corresponds to the collective motion of the center of mass of the cell. Higher order modes (so-called optical modes) are attributed to the internal degrees of freedom in within the cell (e.g. a cell may translate but the components of the cell may oscillate independently).

The study of pulse propagation in a one dimensional diatomic chain as well as multilayered and periodic samples with a linear interaction law between masses has been a topic of growing interest. This is because the frequency band gaps affect the behavior of the system by prohibiting the propagation of acoustic waves in this part of the frequency spectrum [Kittel (2005)]. Previous theoretical investigations of linear and weakly nonlinear diatomic systems of macroscopic particles have focused on frequency band-gaps [Tasi (1976), Pnevmatikos et al. (1983), Pnevmatikos et al. (1986), Chubykalo et al. (1993), Tchawoua et al. (1993)], localized modes [Parmley

et al. (1995), Franchini et al. (1996)] or discrete gap breathers [Gorbach and Johansson (2003), Manziadis et al. (2003)] in discrete dynamic systems with various interaction laws between particles.

Investigations of band gaps in discrete metamaterials vary widely in experimental applications. For example, band gaps and strongly localized modes are present in transversely loaded strings with masses [Parmley et al. (1995), Lüerßen et al. (2004)] and diatomic chains composed of welded spheres (with band gaps in the frequency range of 55-75 kHz) [Hladky-Hennion et al. (2005)]. Layered structures composed from two disparate materials exhibit acoustic band gaps and pass-bands that may be engineered to be very narrow or broad by introducing multiple periods into the layered structure [Shen and Cao (1999)]. Pass bands are utilized in non-mechanical systems using a slow-wave microelectromechanical delay line in a chain of coupled resonators [Alastalo et al. (2006)]. This capacitively-coupled MEMS delay line structure has a band-pass response and signal group velocity as low as 10 m/s, which can be used as a filter in wireless RF or communication systems.

One dimensional chains of elements interacting according to Hertz contact law are appropriate models to investigate linear, weakly nonlinear and strongly nonlinear wave dynamics [Nesterenko (1983),Coste et al. (1997),Chatterjee (1999),Hinch and Saint-Jean (1999), Coste and Gilles (1999), Nesterenko (2001), Daraio et al. (2005), Job et al. (2005), Nesterenko et al. (2005), Daraio et al. (2006), Sen et al. (2008)]. Their versatility derives from the tunability the wave propagation regime, from linear to strongly nonlinear through an initial static compression. This a priori adjustability of acoustic band gaps in strongly nonlinear diatomic systems [Porter et al. (2008)] allows for the development of various practical applications, ranging from acoustic filters, noise mitigation and absorption layers to vibration insulation and the phonon wave guides.

Strongly nonlinear solitary waves (the main mode of signal propagation in weakly compressed chains) exhibit qualitatively different features than weakly nonlinear systems. They have a finite width [Nesterenko (1983),Coste et al. (1997),Chatterjee (1999),Coste and Gilles (1999),Nesterenko (2001),Daraio et al. (2005)] that is independent of the solitary wave amplitude, and a pulse speed that is much smaller than the bulk sound speed of the spheres composing the chains [Nesterenko (2001)]. The speed of strongly nonlinear solitary waves observed in assembled phononic crystals can be below the range of sound speed of fluids and gases, as it was demonstrated for PTFE and stainless steel based granular systems [Nesterenko (1983), Coste et al. (1997),Chatterjee (1999)]. The strongly nonlinear wave equations derived for uniform and heterogeneous diatomic chains [Nesterenko (1983), Nesterenko (2001), Porter et al. (2008)] represent the most general description of wave dynamics including the weakly nonlinear and linear cases.

It should be mentioned that self-demodulation of nonlinear pulses occur in chains of identical spherical particles as well [Tournat et al. (2004)]. This occurs when the propagating signal contains frequency components above the cutoff frequency, which depends on the static compression force [Coste and Gilles (2008)].

This work investigates the formation and propagation of nonstationary signals (quasiharmonic, solitary and shock waves) in linear, weakly nonlinear and strongly nonlinear diatomic periodic chains of particles. The influence of band gaps on signal propagation and their tunability within the audible frequency range are investigated using chains composed of PTFE spheres and stainless steel cylinders.

4.2 Experimental Procedures

In these experiments the diatomic chain consisted of a periodic arrangement of PTFE spheres and stainless steel cylinders where the masses were placed vertically in a PTFE cylinder with an inner diameter of 5 mm (shown in Fig. 4.1 (a)). The chain consisted of 19 PTFE spheres (McMaster-Carr) with diameter ds = 2R = 4.76 mm and mass m = 0.1226 g and 18 stainless steel cylinders (McMaster-Carr) with height h = 3.12 mm, diameter dc = 4.96 mm and mass M = 0.485 g. Stainless steel cylinders were used to ensure a planar geometry of the deformed contact, as assumed for Hertz contact. An additional ferromagnetic steel particle was placed on the top of the chain to magnetically induce a compression force $F_0 = 2.38$ N which decreased the distance between the particle centers by $\delta_0 = 7.34\mu$m [Daraio et al. (2006)].

Three calibrated piezoelectric sensors (RC 1 ms) were embedded in two of the PTFE spheres and one stainless steel cylinder and connected to an oscilloscope (Tektronix TDS 2014) to measure the force amplitude and determine the speed of the signals. Each sensor was assembled using lead zirconate-titanate piezoelement (3 mm square plates with thickness 0.5 mm) with nickel-plated electrodes and micro-miniature wiring embedded in the particles (Fig. 4.1 (b)). The particles with these sensors were placed in the 2^{nd}, 14^{th} and 27^{th} positions from the top (see Fig. 4.1 (a)). The total mass of each particle including the sensor was approximately equal to the mass of the PTFE particle and stainless steel cylinder respectively. The small mass difference ($< 6\%$) between the particles and particles with sensors were taken into account in the numerical calculations and created negligible effects on the wave propagation. The sensors were calibrated using linear momentum conservation law in separate impact experiments.

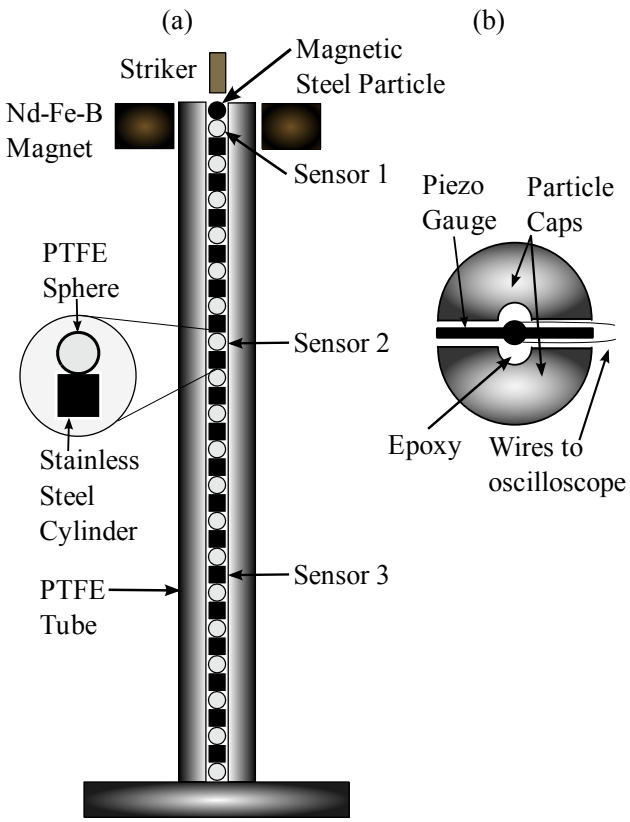

Figure 4.1: Schematic diagram of the experimental setup. (a) The diatomic chain is composed of an alumina striker, stainless steel cylinders, PTFE spheres, embedded sensors (two inside PTFE particles (sensors 1,2) and one (sensor 3) inside stainless steel cylinder) and a Neodymium-Iron-Boron ring magnet for initial static compression. The inset in (a) shows the composition of a unit cell as the basis of the diatomic system. (b) Schematic of a PTFE particle with an embedded piezoelectric sensor.

The pulses were created by impacts of four different strikers made from Al_2O_3 cylinders of different masses, comparable or larger than the mass of one cell in the chain. Each cell consisted of one PTFE sphere and one steel cylinder and had a mass of 0.608 g (see the inset in Fig. 4.1 (a)). The strikers used for the creation of a single and multiple solitary waves were: 0.61 g (about 1 cell mass), 1.22 g (2 cell mass) and 2.75 g (4.5 cell mass) and for shock-like pulses, 17.81 g (about 29 cells mass). The impact velocities used in experiments were 0.44 m/s for the first three masses and 0.20 m/s for the 17.81 g striker.

4.3 Band Gap in a Linear Diatomic Chain

A linear elastic diatomic chain can be assembled from periodic arrangements of elements of different masses and material properties, which are initially compressed by a static force. From an experimental point of view it is convenient to employ the elastic contact of soft spherical particles (PTFE spheres) and elastically rigid cylinders (stainless steel cylinders). The contact between them results in a relatively low elastic modulus of the system leading to a frequency gap within the audible range for possible practical applications.

The diatomic mechanical system studied (PTFE spheres, stainless steel cylinders) is shown in Fig. 4.2. The crosses and black circles represent the initial and current positions of the centers of the corresponding masses in a statically compressed chain, $h/2$ is half of the height of the cylinder, R_P is radius of sphere, δ_0 is the relative displacement of the neighboring particles due to static compression. The static force may be applied using magnetically induced compression [Daraio et al. (2006)]. The linear case presented in Fig. 4.2 (a) shows that the compression due to the static force

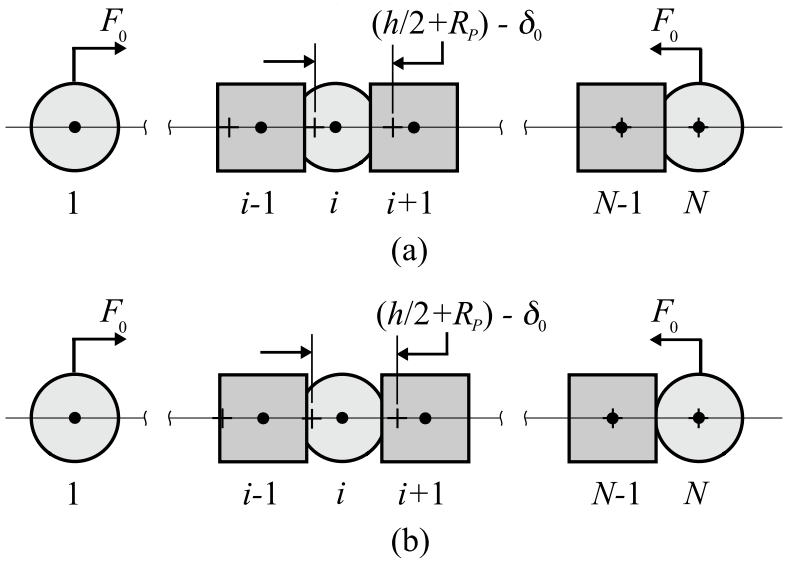

Figure 4.2: Relative positions of particles in diatomic mechanical system corresponding to two wave regimes: (a) strong static compression, (weakly nonlinear case) and (b) weak static compression (strongly nonlinear case). The relative contact area between the particles in the middle of the chain, disturbed by a propagating wave, in comparison with those in undisturbed ends indicate different regimes of behavior.

F_0 is much larger than the perturbed force in the propagating wave. Conversely, the perturbed force in the nonlinear wave is greater than or comparable to the applied force, F_0 (Fig. 4.2 (b)).

The phononic band gap frequencies in an elastic granular chain (Fig. 4.2 (a)) can be found through the linearization of the force displacement relationship between the two particles in the unit cell:

$$F \approx A\left(\delta_0 + \delta_d\right)^{3/2} \tag{4.1}$$

where F is the total compressive force including F_0 created by the static compression and the dynamic part of the force F_d is due to the wave disturbance. The constant A (also given in Eq. (5.6)) depends on the elastic properties and geometry of the contacting particles [Nesterenko (2001)],

$$A = \frac{4E_sE_p\left(1/R_s + 1/R_p\right)^{-1/2}}{3\left[E_s\left(1-\nu_p^2\right) + E_p\left(1-\nu_s^2\right)\right]} \tag{4.2}$$

where E_P and E_S , and ν_P and ν_S are the elastic moduli and Poissons ratio for the PTFE and stainless steel and R_S and R_P are the is radii of contact of the cylinder with a planar contact surface (in this case $1/R_S = 0$) and PTFE sphere. From Eq. (4.2) it is clear that elastic properties of PTFE with very low elastic modulus in comparison with steel dominate the interaction force between particles in the system.

The Taylor expansion may be used to linearize Eq. (4.1) assuming $\delta_0 \gg \delta_d$,

$$F \approx A\delta_0^{3/2} + 3/2A\delta_0^{1/2}\delta_d^{3/2}. \tag{4.3}$$

The first term in Eq. (4.3) is the static force F_0 and the linearized form of dynamic force F_d. The two force components are $F_0 = A\delta_0^{3/2}$ and $F_d = 3/2A\delta_0^{1/2}\delta_d = \beta\delta_d$, where

$$\beta = 3/2A\delta_0^{1/2} = 3/2A^{2/3}F_0^{1/3}. \tag{4.4}$$

The linearized forces between particles result in two linearized equations of motion for the cylinders and spheres with displacements u_{i+1} and v_i from equilibrium positions in compressed chain,

$$M\ddot{u}_{i+1} = \beta\left(v_{i+1} + v_i - 2u_{i+1}\right), \tag{4.5}$$

$$m\ddot{v}_i = \beta\left(u_{i+1} + u_{i-1} - 2v_i\right), \tag{4.6}$$

where $i = 1, 2, , N$, and N is the number of particles (odd indices correspond to spheres and even to cylinders) and M and m denote the masses of the cylinder and sphere. The amplitudes of motion are obtained by substituting the propagating wave solutions represented by $u_{i+1} = ue^{i(kx_{i+1}-\omega t)}$ and $v_i = ve^{i(kx_i-\omega t)}$ into Eqs. (4.5) and (4.6) [Kittel (2005)],

$$M\omega^2 u = 2\beta u - 2\beta v\cos(ka/2) \tag{4.7}$$

$$m\omega^2 v = 2\beta v - 2\beta u\cos(ka/2) \tag{4.8}$$

where $a = 2(h/2 + R_P - \delta_0)$ is the unit cell size. Equations (4.7) and (4.8) have nontrivial solutions for amplitudes of vibrating masses when the determinant is equal zero. The dispersion relation is:

$$\omega^2 = \frac{\beta}{mM}\left(m + M \pm \sqrt{m^2 + M^2 + 2mMcos(ka)}\right). \tag{4.9}$$

This dispersion relation for the linear elastic diatomic chain is shown in Fig. 4.3 for $f = \omega/2\pi$ (the plus and minus sign in Eq. (4.9) correspond to the optical and acoustic branches). The lower and upper bound of the band-gap for this system are expressed by the following equations [Kittel (2005)]:

$$f_1 = \frac{1}{2\pi}\left(\frac{2\beta}{M}\right)^{1/2}, \quad f_2 = \frac{1}{2\pi}\left(\frac{2\beta}{m}\right)^{1/2}. \tag{4.10}$$

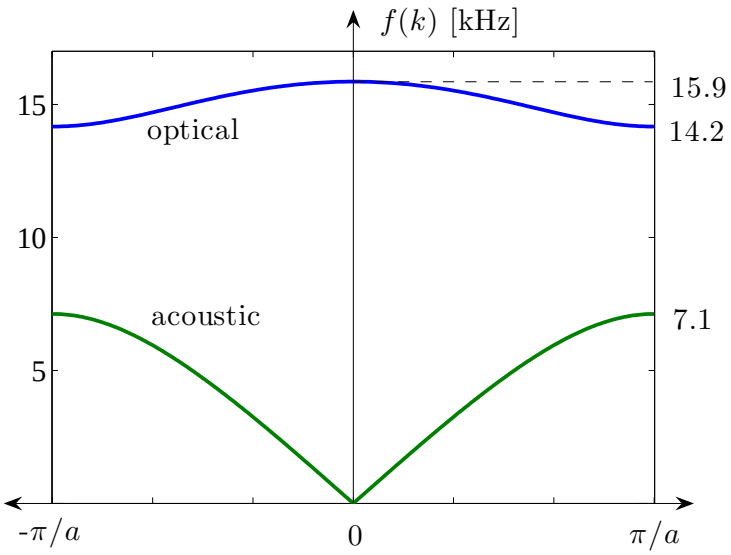

Figure 4.3: Dispersion relation in the first Brillouin zone for linear elastic diatomic chain composed of stainless steel cylinders and PTFE spheres used in the experiments.

The band-gap frequencies may be tuned by changing the value of β that depends on A and the initial compressive force F_0. The band gap is sensitive to the material properties E (Youngs modulus), and ν (Poissons ratio), the particle radii R and the initial static compression (Eqs. (4.2) and (4.3)). Note that the band gap frequencies are nonlinearly dependent on the initial compression force ($f \sim F_0^{1/6}$). The corresponding elastic moduli and Poissons ratio for the diatomic chain are E_P = 1.46 GPa [Daraio et al. (2005)], E_S = 193 GPa, and ν_P = 0.46 and ν_S = 0.3, respectively. These parameters based on Eqs. (4.2), (4.4) and (4.10) with $F_0 = 2.38$ N ($\delta_0 = 7.34\mu$m) result in the limiting frequencies $f_1 = 7,120$ Hz and $f_2 = 14,162$ Hz (Fig. 4.3) that are within the audible range from 20-20,000 Hz.

4.4 Results and Discussion

4.4.1 Signal Transformation in a Tunable Linear Diatomic Chain

Signals with amplitudes much smaller than the magnetically applied static force propagate in the linear regime. It is important to find the transient response of these signals due to initial conditions that are close to a harmonic excitation with frequencies within the band gap to find a characteristic spatial and temporal point where the band gap is able to affect the shape of the propagating pulse. It should be mentioned that the existence of band gap does not answer the question when entering signal will be affected by it. In the linear case the pulses are transformed by dispersion [Nesterenko (2001)] and the role of nonlinearity is not essential. In the following figures the pulses and their corresponding frequency spectrum are plotted for comparison. The abscissa values of the frequency plots are the Fourier coefficients

derived from a fast-Fourier-transform,

$$C_k = \hat{X}(k)/M = \sum_{j=1}^{N} X(j)/M \exp\left[-2\pi i(j-1)(k-1)/N\right], \tag{4.11}$$

where $X(j)$ denotes the vector with length N to be transformed, j and k increment over time and frequency and M is the length of $X(j)$ without padded zeros. For example, C_0 denotes the mean of the transformed function. In each of the following figures, a ratio of $N/M = 5$ was used since the pulses were finite and not exactly periodic. These values were chosen for ease of correlation between the pulse and its spectrum.

In the numerical calculations an oscillatory pulse with a frequency inside the band-gap was created at one end of the periodic diatomic chain (Fig. 4.1) composed of 300 cells, with a PTFE sphere at the top. This PTFE sphere was compressed by a static force of 2.38 N and given an initial velocity of 0.00442 m/s. This resulted in an oscillatory excitation that was approximately harmonic (Fig. 4.4 (a) and (b)). The amplitude of the dynamic force between the top PTFE sphere and the stainless steel cylinder was 0.015 N (160 times smaller than initial compression force) and did not allow the top PTFE particle to separate from the chain. The majority of the frequency spectrum in Fig. 4.4 (b) is between the band-gap frequencies with its largest frequency component at 11 kHz. The Fourier spectrum for all cases were found for propagating pulses up to 15 ms, but the data in Fig. 4.4 (a), (c) and (e) are truncated to clearly show the leading pulse.

The numerical results of the force in the propagating pulse (i.e. the force inside 5^{th} PTFE particle belonging to the third cell and the force inside 11^{th} PTFE particle belonging to the sixth cell) and their frequency spectrums are shown in Fig. 4.4 (c) and (d) and Fig. 4.4 (e) and (f) respectively. The amplitude of the first

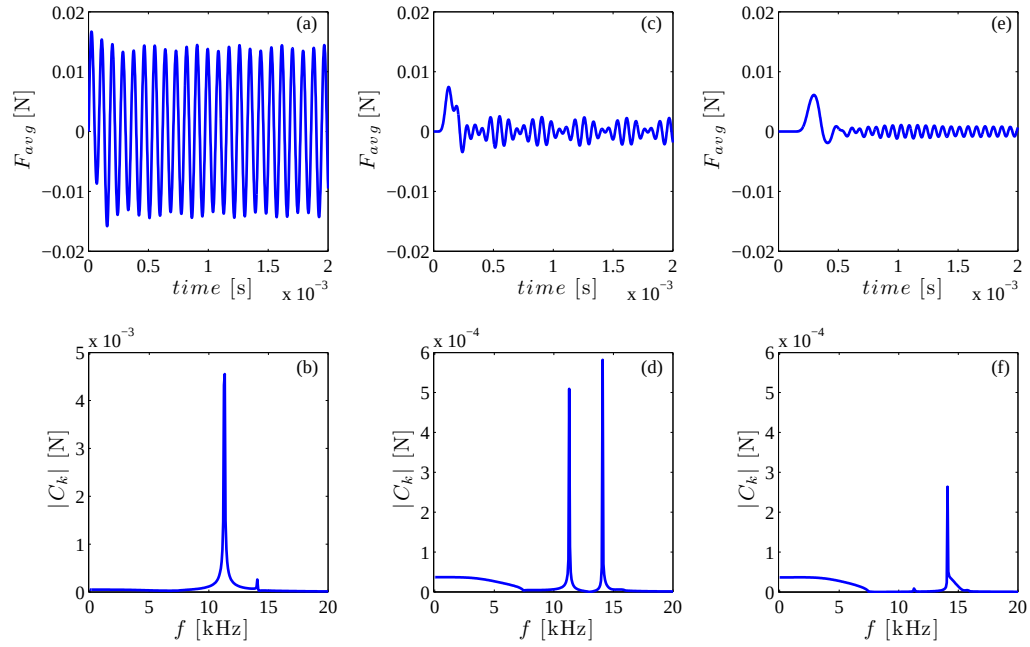

Figure 4.4: Linear chain with a static force $F_0 = 2.38$ N. The top PTFE sphere was given an initial velocity of 0.00442 m/s. (a) Dynamic force between the top PTFE particle and stainless steel cylinder and (b) its Fourier spectrum; (c) Force pulse inside 5^{th} particle (PTFE) (averaged of contact forces between 4^{th} (SS) and 5^{th} (PTFE) and 5^{th} (PTFE) and 6^{th} (stainless steel cylinder) particles) and (d) its Fourier spectrum; (e) Force in transmitted pulse inside 11^{th} (PTFE) particle and (f) its Fourier spectrum.

pulse at the 6^{th} cell is 0.006 N, which is about four hundred times lower than the initial compression force and its width is about nine particles (or 4.6 cells). At the 11^{th} particle the wavelength increases to 4.7 cells. At the 21^{st} particle wavelength of the propagating pulse becomes almost twelve particles (or about 5.9 cells). It is interesting that the initial wavelength is close to 5 cells similar to the pulse width in a strongly nonlinear diatomic chain without initial compression [Nesterenko (2001), Porter et al. (2008)].

It is clear from Fig. 4.4 that this linear chain is able to dramatically change the shape of the initial oscillatory pulse within relatively short distances from the top PTFE particle (within only 6 cells!), which is mainly due to dispersion. As the signal propagates, the frequency spectrums in Fig. 4.4 (b), (d) and (f) show that the pulse preferentially transforms (demodulates) such that the components in the band gap move toward lower and higher frequencies.

The Fourier spectrum of the force in the system very close to the top of the PTFE sphere (inside 5^{th} PTFE particle, Fig. 4.4 (c) and (d)) demonstrates significant frequency components above and below the band gap in addition to the initial signal. This is significantly different than the spectrum of the excited pulse (Fig. 4.4 (a) and (b)). There are two main frequencies in Fig. 4.4 (d): one is the source signal at about 11 kHz and the other is about 14 kHz, which was also present in the input signal at about the same amplitude. These two harmonics are responsible for the beating phenomenon observed in the force signal (Fig. 4.4 (c)). This beating disappears and the trailing oscillations become approximately harmonic at the 11^{th} particle (PTFE) (Fig. 4.4 (e)) due to the complete transformation of the 11 kHz frequency component.

It should be mentioned that the high frequency corresponding to the top

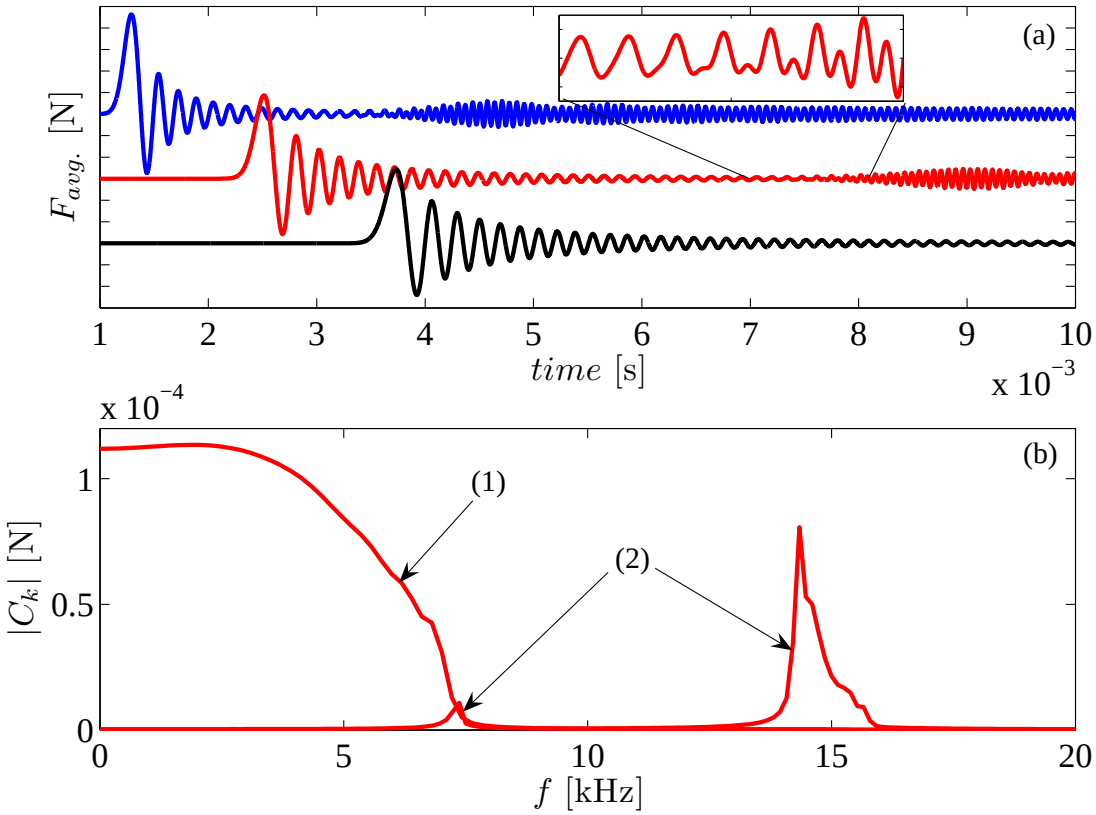

Figure 4.5: Linear chain, static force $F_0 = 2.38$ N, the top PTFE sphere was given an initial velocity of 0.00442 m/s. (a) Forces in the transmitted pulses inside 50^{th} particle (PTFE) (averaged of contact forces between 50^{th} (stainless steel cylinder) and 51^{st} (PTFE) and 51^{st} (PTFE) and 52^{nd} (stainless steel cylinder) particles, inside the 101^{st} particle and inside 151^{st} particles. The vertical scale is 0.001 N/div. The inset in (a) shows the transition from acoustic to optical modes in the 101^{st} particle. (b) Curve (1): The Fourier spectrum for leading pulse for 101^{st} particle up to the time 7 ms with mainly acoustic frequency and curve (2) is the Fourier spectrum for the trailing wave group up from the time 7 to 12 ms containing the optical frequency component.

of the band gap does not disappear during signal propagation. This is due to the oscillatory motion of the light PTFE particle in the cell, which is also a characteristic of nonlinear signals [Nesterenko (2001), Chap. 1, Fig. 1.19]. The relatively small peak around 14 kHz in Fig. 4.4 (b) is present in the initial signal due to the motion of top PTFE particle against the steel cylinder under constant force. The amplitude of this frequency component decays very slowly (compare Figs. 4.4 (b), (d) and (f)) in striking contrast to transformation of the initial 11 kHz component.

It is interesting to investigate pulse transformation at larger distances from the top particle to investigate the behavior of the leading pulse. The shapes of the pulses are presented in Fig. 4.5 (a) for the 51^{st}, 101^{st} and 151^{st} particle. In Fig. 4.5 (a) the pulse continues to change due to linear dispersion; particularly the leading pulse is not of solitary shape at these distances from the top particle as it look closer to the entrance (Fig. 4.4 (c),(e)). The leading part of the propagated signal measured at the 101^{st} particle up to 7 ms has a broad band of frequencies below the band gap (curve 1 in Fig. 4.5 (b)) and after 7 ms the signal is characterized by one peak at the bottom and top of the band gap (curve 2 in Fig. 4.5 (b)). It should be mentioned that the harmonic with frequency about 14 kHz continues to decay with the pulse propagation (compare Figs. 4.4 (d), (f) with Fig. 4.5 (b), curve 2). The wave packet containing frequencies at the top of the band gap (not shown on the bottom wave profile in Fig. 4.5 (a)) propagates with a lower speed in comparison with the leading oscillatory pulse composed of frequencies lower than 7 kHz. It should be mentioned that there is no stationary single pulse in the linear dispersive case and the leading pulse will evolve further during propagation (for example, with decreasing amplitude and increasing width), but the main features of it are already established before it reaches the 100^{th} particle.

4.4.2 Signal Transformation in a Nonlinear Diatomic Chain

The band gap is a property of linear systems (Eqs. (4.7) and (4.8)) and it is not clear if it can influence the signal propagation in the nonlinear regime. Recently, the effects of varying isotropic static compression in the linear and nonlinear regimes for triangular (two-dimensional) lattices of identical steel spheres shows evidence of self-demodulation in the time-frequency plots of acoustic signals [Coste and Gilles (2008)]. Here, the behavior of signals in diatomic chains with amplitudes comparable to the initial compression is investigated numerically.

A nonlinear pulse in the same diatomic chain as the previous section was created when the top PTFE particle was given a higher initial velocity of 0.442 m/s, which is two orders of magnitude larger than in the linear system (Fig. 4.6 (a) and (b)), though the particles in the chain remain in contact. This resulted in a similar oscillatory excitation shown in Fig. 4.4 (a) and (b), but the dynamic force between the top PTFE sphere and stainless steel cylinder have an amplitude comparable to the static compression force (being 1.6 times smaller). The numerical results of the force in the pulse propagating inside the system and their frequency spectrums are shown in Fig. 4.6 (c) and (d) and Fig. 4.6 (e) and (f) respectively. The force inside the 5^{th} PTFE particle belongs to the third cell and the force inside the 11^{th} PTFE particle belong to the sixth cell. The amplitude of the first pulse is at the 6^{th} cell is 0.65 N and is about 3.7 times lower than the initial compression force and its width is about nine particles (or 4.6 cells). This pulse is widening when it propagates in the system. For example at the 21^{st} particle the width is approximately eleven particles (or about 5.7 cells), which is closer to the width of a stationary pulse in strongly nonlinear diatomic chains without static compression [Nesterenko (2001),Porter et al. (2008)].

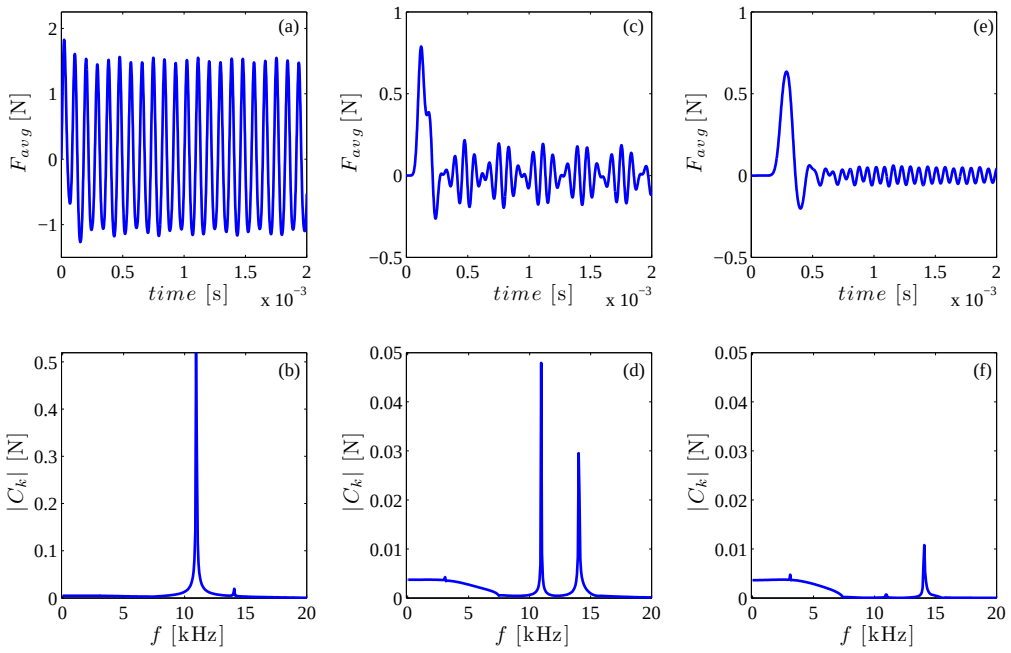

Figure 4.6: Nonlinear chain with a static force of $F_0 = 2.38$ N applied to the top PTFE sphere, which was given an initial velocity of 0.442 m/s. (a) The force between the top PTFE particle and stainless steel cylinder (incoming pulse) and (b) its Fourier spectrum; (c) The force in the transmitted pulse inside the 5^{th} particle (PTFE) (averaged of contact forces between 4^{th} (SS) and 5^{th} (PTFE) and 5^{th} (PTFE) and 6^{th} (stainless steel cylinder) particles and (d) its Fourier spectrum; (e) The force in transmitted pulse inside 11^{th} (PTFE) particle and (f) its Fourier spectrum.

At relatively short distances from impacted end (about 6 cells) it is clear that this nonlinear chain dramatically changes the shape of the pulse as its frequency spectrum shifts toward lower and higher frequencies. The behavior of the signal in this nonlinear chain is similar to the case of linear chain, suggesting that the nonlinearity of the chain does not influence the signal propagation as much as dispersion. This means that, for practical applications, the influence of the band gap is also relevant for finite amplitude nonlinear signals within short distances from the signal source.

The pulse transformation as it propagates into the system at larger distances from the impacted end (up to the 151^{st} particle) is shown in Fig. 4.7. As in the linear case (Fig. 4.5) the leading propagating pulse continues to transform due to dispersion even in the presence of nonlinearity. However, at much larger distances, the leading solitary wave, which is a steady solution in weakly nonlinear case, may separate from the oscillatory part of the signal in contrast with the linear case.

At the 101^{st} particle the leading oscillating pulse (up to 7 ms) has a broad band of frequencies below the band gap (curve 1, Fig. 4.7 (b)) and for the interval from 7 ms to 12 ms it is characterized by two peaks at the vicinity of the bottom (f_1) and one at the top of band gap (f_2) (curve 2, Fig. 4.7 (b)). In contrast to Fig. 4.5 (b) corresponding to linear case there is an additional 3 kHz component, which may be due to the influence of nonlinearity in the system. The wave packet containing frequencies above 14 kHz (not shown on bottom wave profile) propagates with a lower speed than the leading oscillatory pulse composed of frequencies lower than 7 kHz. The oscillations of the first (compressed) particle has a harmonic at 14 kHz (small peak in Fig. 4.6 (b)), which results in signals that propagate into the system with a similar frequency and with a low speed along with the leading pulses

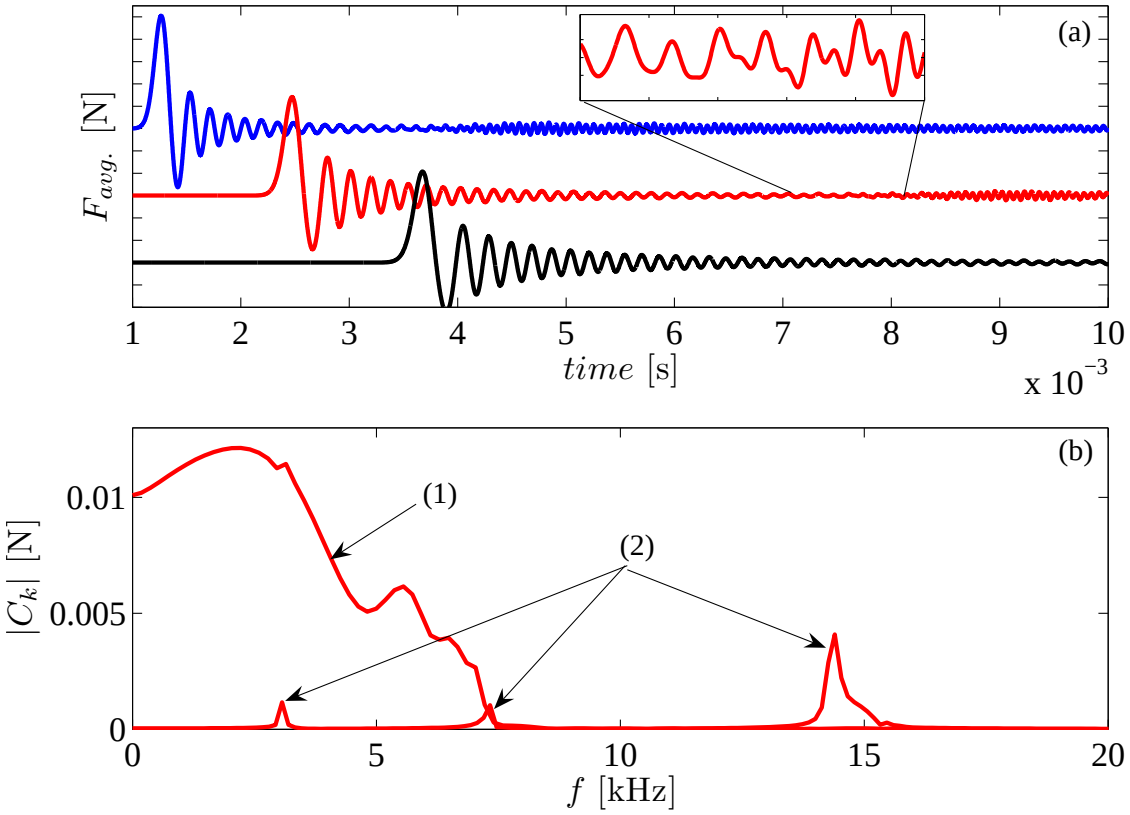

Figure 4.7: Nonlinear chain with a static force of $F_0 = 2.38$ N applied to the top PTFE sphere, which was given an initial velocity of 0.442 m/s. (a) Forces in the transmitted pulses inside the 50^{th} particle (PTFE) (averaged of contact forces between 50^{th} (stainless steel cylinder) and 51^{st} (PTFE) and 51^{th} (PTFE) and 52^{nd} (stainless steel cylinder) particles, inside 101^{st} particle and 151^{st} particles. The vertical scale is 0.1 N/div. The inset in (a) shows the transition from acoustic to optical modes in the 101^{st} particle. (b) Curve (1): Fourier spectrum for the leading pulse for the 101^{st} particle, up to 7 ms containing acoustic frequencies and curve (2) is the Fourier spectrum for the trailing wave group (taken from 7 ms to 12 ms), containing acoustic and optical frequencies.

that travel with speeds corresponding to the acoustic branch.

Since the gap in the frequency spectrum is a property of a linear elastic system it is surprising that in the nonlinear chain, which is a qualitatively different system (for example, it supports solitary wave absent in a linear case), the signal transformation is similar to linear chain. In the trailing wave group there is no component inside band gap, only components at the top of acoustic and bottom of optical bands. The frequency at the top and the bottom are long living in comparison with those inside band gap in both linear and nonlinear chains. So, waves with finite amplitude in a nonlinear material are sensitive to the same range of band gap frequencies as waves with infinitesimally small amplitudes as in linear chains. This allows tunability of the band gap in the nonlinear range of material response based on Eq. (4.10) derived for infinitely small amplitude of signals.

To compare experimental results with the numerical investigation for the nonlinear chain four separate experiments were performed in a diatomic chain composed of 37 elements (including magnetically induced static compression and the gravitational preload) with strikers having different masses and velocities: 0.61 g, 1.22 g, and 2.75 g alumina strikers at $v_0 = 0.44$ m/s and a 17.81 g striker at v_0=0.2 m/s. Each striker generated incoming pulses of different lengths and amplitudes. In each case, the static compression was 2.38 N, applied to the top magnetic spherical particle (in previous numerical calculations force was applied to the top PTFE particle to generate practically harmonic boundary conditions). The experimental set up is shown in Fig. 4.1 and experimental data are presented in the Table 4.1. There is a reasonably good agreement between pulse velocities in experiments and numerical calculations despite dissipation present in experiments.

The results of the impact by the 0.61 g striker are shown in Fig. 4.8. The

Table 4.1: Comparison of average speed V_s of leading pulses taken between particles number 14^{th} and 27^{th} for experiments and numerical results in the nonlinear chain for different masses and velocities of strikers.

	Striker Mass [g]	Pulse Speed [m/s]
Experimental	0.61	175
	1.22	177
	2.75	181
	17.81	179
Numerical	0.61	171
	1.22	173
	2.75	176
	17.81	169

impact resulted in a single pulse at the top of the chain since the striker mass was close to the mass of one cell in the system. The initial signal was quite different (due to the boundary conditions) from Fig. 4.6 (a) although the impulse in experiments also transformed into a single leading pulse (Fig. 4.6 (c) and (e)).

Figure 4.8 shows the experimental results (Fig. 4.8 (a)) and the corresponding numerical calculations (Fig. 4.8 (c)) as well as the Fourier spectrum of each in Figs. 4.8 (b) and (d). It is clear from Fig. 4.8 (b) and (d) that the frequency spectrum of the initial disturbance is inside the band gap (7.1 kHz 14.2 kHz). It is clear that the signal is shifted toward lower frequencies within 7 cells from the impacted end. The dynamic compression of the chain effectively shifts the lower boundary of band gap toward a higher frequency 9 kHz than the predicted lower limit of 7.1 kHz corresponding to static precompression (in situ modification of band gap) explaining higher frequencies in the propagating pulse in comparison with linear case. This fast modification of the signal is similar to previously observed for practically harmonic incoming excitations in linear and nonlinear cases (Figs. 4.4 and 4.6 (b), (d), and (f)). It should be mentioned that similar behavior of Fourier spectrum corresponding to numerical calculations and to experimental data suggests that dissipation (apparently affecting amplitude of signal in experiments) is not the main cause for the observed signal transformation in the frequency domain. A similar behavior of the signals in frequency domain both in experiments and numerical calculations was observed for pulses excited by the impact of an alumina striker (1.22 g at 0.44 m/s) generating a series of pulses.

To increase the duration and amplitude of the incident signal, experiments were conducted using an alumina striker of larger mass (2.75 g at 0.44 m/s). In Fig.

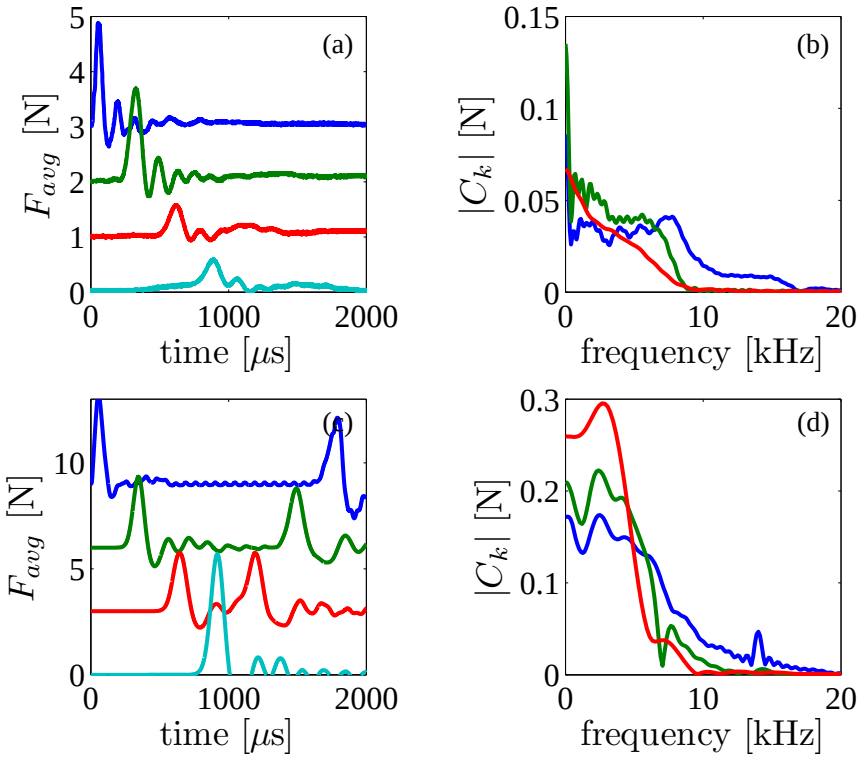

Figure 4.8: Nonlinear chain with a static force of $F_0 = 2.38$ N applied to the top magnetic particles impacted by alumina striker with an initial velocity of 0.44 m/s. (a) Dynamic force in experiments recorded in the first PTFE particle (incoming pulse) and in sensors placed in the PTFE particle in the seventh cell and in the steel cylinder in the 13^{th} cell and in the wall respectively; (b) Fourier spectrum for forces presented in (a) (c) Dynamic force in numerical calculations corresponding to experimental conditions in (a); (d) Fourier spectrum for forces presented in (c).

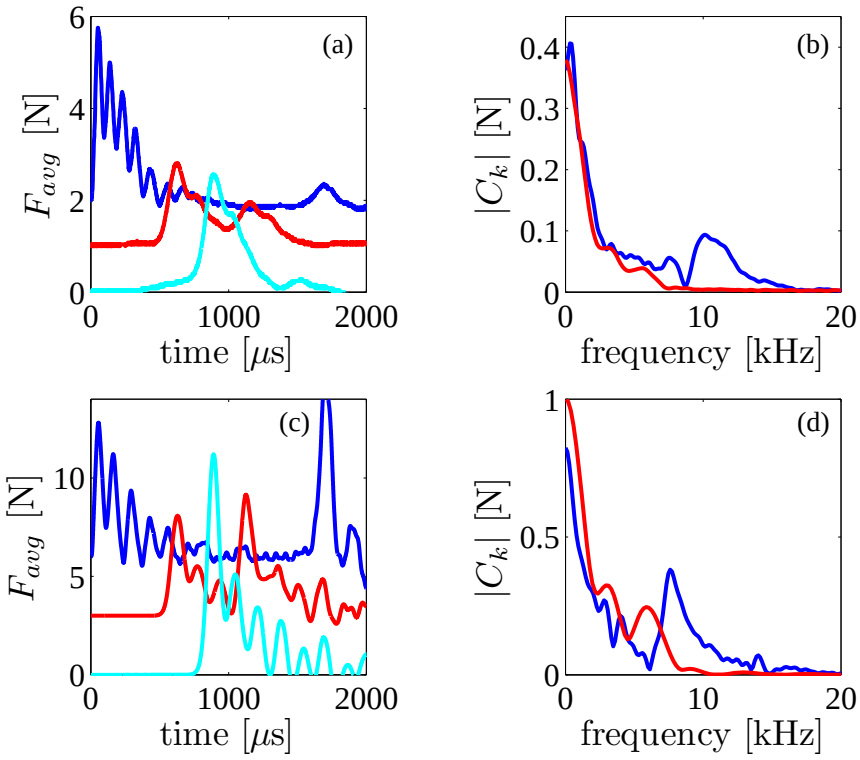

Figure 4.9: Nonlinear case, static force $F_0 = 2.38$ N. The striker had a mass equal to 4.5 cells (2.75 g) and an initial velocity of 0.44 m/s. (a) Dynamic force in experiments between first PTFE particle and stainless steel cylinder (incoming pulse) and between sensors in the steel cylinder in the 13^{th} cell and in the wall respectively; (b) Fourier spectrum for forces presented in (a); (c) Dynamic force in numerical calculations corresponding to experimental conditions in (a); (d) Fourier spectrum for forces presented in (c).

4.9 the experimental and numerical results of the impact of this striker are shown. This impact created a sequence of connected pulses in experiments and numerical calculations and the corresponding frequency spectrum of the incoming pulses are shown in Fig. 4.9 (b) and (d). The frequency spectrum shows that the initial pulse corresponding to the force inside the second (PTFE) particle has a significant portion within the band gap. In comparison with Fig. 4.8 the main portion of the frequency spectrum within the band gap extends to a slightly higher frequency. This may be due to an additional effect of a larger mean effective compression in addition to the static force and thus, increases the lower limit of band gap (in situ modification of band gap). From a comparison of the data for the 2^{nd} and 27^{th} (PTFE) particle it is clear that the spectrum has shifted to lower frequencies, spectrum for the pulse reflected from the wall is not shown for clarity of the graphs. In experiments and numerical calculations the spectrum cut-off observed for the 27^{th} particles is slightly higher than the predicted lower limit of the band gap from the linear approach (7.1 kHz).

A comparison between experimental and numerical data reveal smaller time intervals between peaks in experiments (compare Figs. 4.9 (a) to 4.9 (c)) resulting in a component of Fourier spectrum with higher frequency than in corresponding numerical calculations (compare Figs. 4.9 (b) to 4.9 (d)). This behavior is explained by a delayed separation of solitary pulses in experiments due to dissipation.

To create an oscillatory shock wave in the experiments the impact of an alumina striker was used with a mass of 17.81 g at 0.2 m/s. In Fig. 4.10 the experimental and numerical results corresponding to the impact of this striker and the corresponding frequency spectrum of the pulses are shown in Fig. 4.10 (b) and (d) are shown.

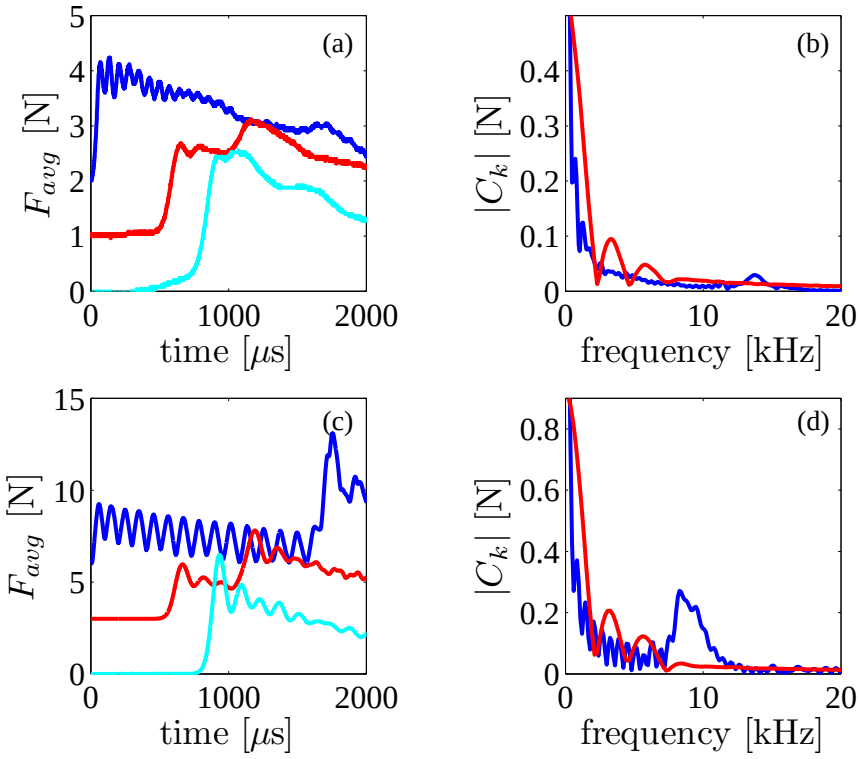

Figure 4.10: Oscillatory shock waves excited in the nonlinear case in a diatomic chain composed of 37 elements, static force $F_0 = 2.38$ N. The striker had a mass equal to 17.81 g (about 29 cells mass) and an initial velocity of 0.2 m/s. (a) Dynamic force in experiments in the first PTFE particle and between sensors in the PTFE particle in the 7^{th} cell and in the steel cylinder in the 13^{th} cell and in the wall respectively; (b) Fourier spectrum for forces presented in (a); (c) Dynamic force in numerical calculations corresponding to experimental conditions in (a); (d) Fourier spectrum for forces presented in (c).

The frequency spectrum shows that the initial pulse in the second (PTFE) particle has a significant portion within the band gap. However, optical modes are not excited in this case. To check if this mode appears as signal propagates the numerical calculations were extended up to 15 ms, but the high frequency component (at about 14 kHz) corresponding to the optical mode trailing the leading shock wave was not observed. This contrasts the linear case with practically harmonic boundary conditions evolving into a leading pulse with an oscillatory tail (Fig. 4.4 (e), (f)). It may be concluded that for all shock loaded cases, the high frequency component is not excited at the boundary.

In comparison to Fig. 4.9 the main portion of the frequency spectrum within the band gap is centered about a slightly higher frequency in numerical calculations (7.7 kHz in Fig. 4.9 (d) and 8.4 kHz in Fig. 4.10 (d) correspondingly). This may be due to the effect of a compressive dynamic force creating a larger mean effective precompression resulting in a higher effective stiffness of the compressed contacts in comparison with initial state.

The oscillations in the initial shock in experiments are significantly damped in the 27^{th} (PTFE) particle and the spectrum shifted to lower frequencies. This can be caused by dissipation if it is larger than some critical value [Herbold and Nesterenko (2007)]. It is interesting and unexpected that this was also the case in the numerical calculations despite the fact that dissipation was not included. The mechanism of the effective smoothing of the oscillating shock profile without dissipation in numerical calculations is explained by the influence of band gap that eliminate the corresponding harmonic in the incoming pulse centered at about 9 kHz within band gap. The effective compression in the shock wave shifts the lower boundary of band gap toward a higher frequency 9 kHz than the predicted lower limit of 7.1 kHz (in situ modification of band gap). Although the initial impact

creates an oscillating shock, as in one mass chain Duvall et al. (1969), Nesterenko (2001), Herbold and Nesterenko (2007), these oscillations cannot propagate due to band gap.

Despite the fact that both experimental and numerical incoming profiles were initially oscillating, the frequencies of oscillations were quite different with a higher frequency being observed in experiments (9 and 12 kHz correspondingly). The mechanism of generating higher frequencies in experiments can be due to slower separation of the pulses in presence of dissipation effectively increasing the observed frequency. To check this hypothesis viscous dissipation was included in numerical calculations (similar to Duvall et al. (1969), Herbold and Nesterenko (2007)) resulting in harmonics with higher frequency (their frequency increasing with viscosity) in comparison to calculations without dissipation. It should be mentioned that magnetorheological liquids allow effective tunability of viscosity with magnetic field [Nahmad-Molinari et al. (1999)], which can be used to tune shock response of granular system immersed in such media.

4.4.3 Signal Transformation in a Strongly Nonlinear Diatomic Chain

If the amplitude of signal is significantly larger than the initial static compression, qualitatively new features can be expected in diatomic chains than in linear and nonlinear pulses. It should be mentioned that in an initially uncompressed chain (sonic vacuum) there is no characteristic band gap that is representative of a linear elastic system. At the same time the compressed state behind a relatively long shock wave can exhibit a phenomena caused by in situ band gap where properties depend on the average compression caused by the wave. This was seen in the previous section for nonlinear impulses (Figs. 4.9 and 4.10).

The propagation of strongly nonlinear waves in diatomic chains is not directly comparable to the previous two cases since the separation of particles is now possible with the absence of initial compression. This also occurs when the initial impact velocity value is large enough for the particle to overcome the static force. The frequency spectrum of the propagating compressive signal should not be affected by the band gap (Eq. (4.10)), since both f_1 and f_2 are very small due to very weak gravitational compression in a vertical chain. In the case of impact by a particle with a mass close to the mass of the cell a single solitary pulse will have a frequency spectrum close to the solution to the long-wave approximation given in Nesterenko (2001), Porter et al. (2008). Higher amplitudes of strongly nonlinear solitary waves result in higher frequencies since the spatial size does not depend on amplitude, but the signal speed increases with wave amplitude. Thus, the allowed frequencies of harmonics composing the single solitary wave are tuned by amplitude of wave.

It is interesting to investigate this case because it will elucidate the effect that the length of the impact has on the resulting frequency spectrum. It was seen in the previous nonlinear case that the additional dynamic compression in the pulse may shift the initial frequency spectrum to higher frequencies.

To compare experimental with numerical results for the strongly nonlinear chain four separate experiments with an identical set up as in the previous sections (Fig. 4.1) were performed with the exception of the magnet used to induce static compression in the previous cases. The only static force in this case is due to gravitational preload in experiments and calculations. Each experiment has incoming pulses of different lengths and amplitudes depending on mass of the striker to excite different Fourier spectrums and observe their evolution. The results of the experiments for a chain of PTFE spheres and steel cylinders in strongly nonlinear regime are shown in Fig. 4.11-4.13 and Table 4.2. There is a reasonably good agreement be-

tween pulse velocities in experiments and numerical calculations despite dissipation present in experiments.

Table 4.2: Comparison of average speed V_s of leading pulses taken between particles number 14^{th} and 27^{th} for experiments and numerical results in a strongly nonlinear diatomic chain.

	Striker Mass [g]	Pulse Speed [m/s]
Experimental	0.61	118
	1.22	121
	2.75	122
	17.81	115
Numerical	0.61	134
	1.22	141
	2.75	146
	17.81	138

The mass of the striker in relation to the mass of the cell roughly corresponds to the number of significant pulses observed in experiments. For example, the impact generated by strikers (Al_2O_3 cylinder) with masses equal to mass of one cell (PTFE sphere and steel cylinder), 2 cells and 4.5 cells generated the one, two and 5 pulses.

In Fig. 4.11 the experimental and numerical results of the impact of a PTFE striker (0.62 g at 0.44 m/s) are shown. This impact created one main pulse in experiments and numerical calculations and the corresponding frequency spectrum

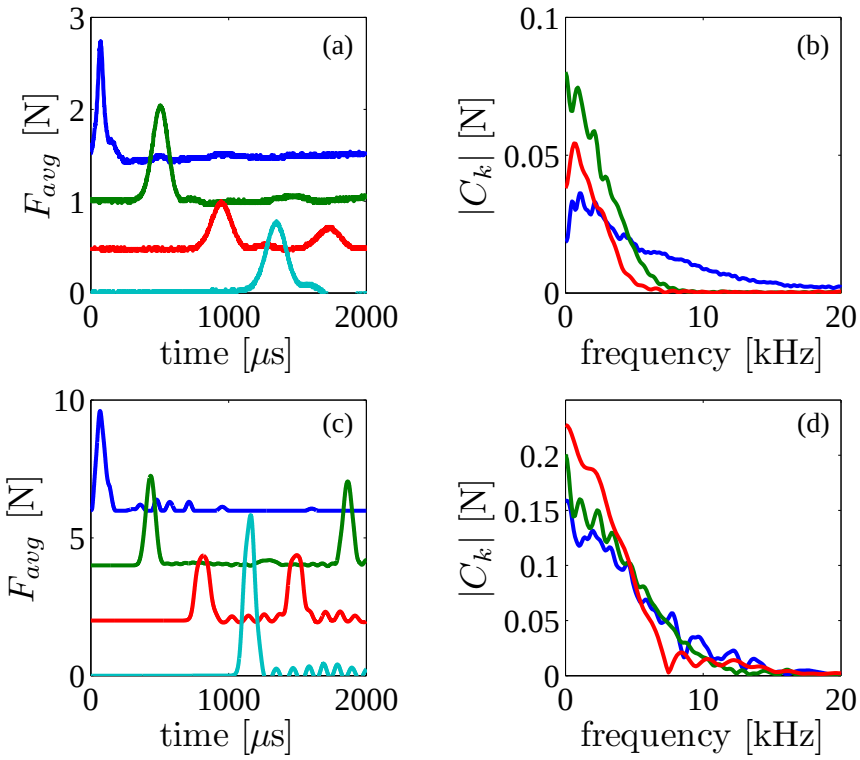

Figure 4.11: Strongly nonlinear case with only a gravitational static load. The striker had a mass equal to one cell (0.61 g) and an initial velocity of 0.44 m/s. Experimental data on the propagation of strongly nonlinear solitary waves in a diatomic chain composed of 37 elements. Curves show the force vs. time behavior detected by the sensors in the 2^{nd} particle (top curve), 14^{th} particle (second curve from top), 27^{th} particle and at the wall (bottom curve). The time begins at the moment of impact and is triggered by the first pulse one the oscilloscope.

of the incoming pulses are shown in Fig. 4.11 (b) and 4.11 (d). In Fig. 4.11 (a), the time duration of the leading solitary wave measured in particle 14 was 330 μs. The average speed of its propagation between particles 14 and 27 was 118 m/s. These values result in a solitary wave width equal to 4.6 cells. This agrees well with the solitary wave width predicted in the long wave approximation for a chain of particles interacting according to Hertzs law, which predicts a wavelength of approximately five cell lengths [Nesterenko (2001),Porter et al. (2008)]. This result corresponds well with numerical results presented in Fig. 4.11 (c) and Table 4.2. There are several smaller solitary waves trailing the main pulse apparent in the top curve of Figs. 4.11 (a) and 4.11 (c). These waves result from multiple impacts of the first PTFE particle from the top magnetic particle and first stainless steel cylinder.

The Fourier spectrum for the strongly solitary wave and the signal in the nonlinear system (compare Figs. 4.8 (b), (d) with 4.11 (b), (d)) are comparable due to the similar durations of the initial pulses. It should be mentioned that the speed of the linear, weakly nonlinear and strongly nonlinear signals in these cases are different but of the same order of magnitude.

The frequency spectrum shifted toward lower frequencies as the pulse propagates into the chain. This is due to the formation of the solitary wave being a stationary solution [Porter et al. (2008)] of the long-wave approximation with a spectrum frequencies being close to the band gap range presented in the previous section for precompressed chain. This coincidence is due to the specific value of the striker velocity creating amplitude of pulses comparable to the initial precompression in previous cases which results in similar sound speed and solitary wave speeds. A more pronounced shift toward lower frequencies in experiments (Fig. 4.11 (b)) with single pulse is attributed to amplitude attenuation resulting in longer pulse duration

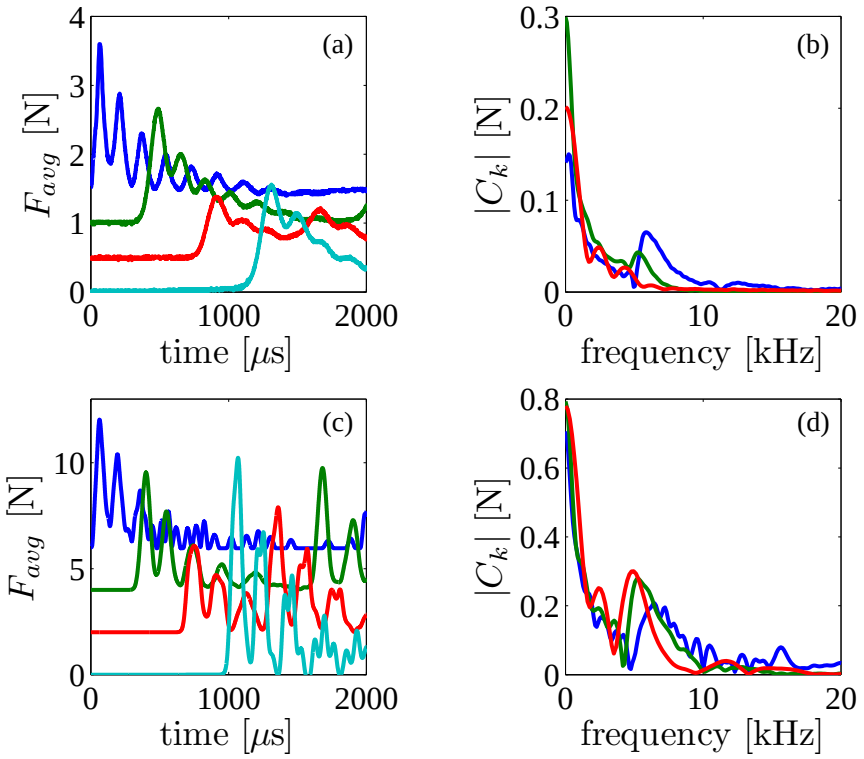

Figure 4.12: Strongly nonlinear case, there is no initial compression and only gravity is included. The striker had a mass equal to 4.5 cells (2.75 g) and an initial velocity of 0.44m/s. Experimental data on the propagation of strongly nonlinear solitary waves in a diatomic chain composed of 37 elements. The curves show the force vs. time behavior detected by the sensors in the 2^{nd} particle (top curve), 14^{th} particle (second from top), 27^{th} particle (third from top) and at the wall (bottom curve).

with the same spatial width.

A similar behavior of signals in frequency domain both in experiments and numerical calculations was observed for pulses excited by the impact of an alumina striker with larger mass (1.22 g at 0.44 m/s) generating a series of pulses.

In Fig. 4.12 the experimental and numerical results of the impact of an alumina striker (2.75 g at 0.44 m/s) are shown. This impact created about 8 pulses in experiments and numerical calculations and the corresponding frequency spectrum of the propagating pulses are shown in Fig. 4.12 (b) and 4.12 (d). At the 27^{th} (stainless steel cylinder) particle it is clear that the spectrum has shifted to lower frequencies.

In Fig. 4.13 the experimental and numerical results of the impact of an alumina striker (17.81 g at 0.2 m/s) are shown. This impact created oscillatory shock waves in experiments and numerical calculations and the corresponding frequency spectrum of the incoming pulses are shown in Figs. 4.13 (b) and 4.13 (d). The incoming oscillatory shock becomes almost monotonic by the 27^{th} (PTFE) particle in experiments and numerical calculations, which was also observed in case of the nonlinear chain (compare Fig. 4.10 (a), 4.10 (c) and Fig. 4.13 (a), 4.13 (c)), despite the fact that dissipation was not included in calculations. The mechanism of changing the oscillatory character of the shock wave without dissipation may be similar to discussed earlier for the case of nonlinear chain. The observed transformation of frequency spectrum is similar to non linear case and may be due to the effects of in situ band gap induced by the dynamic compression behind relatively long shock wave. In one mass chain such transformation of oscillatory shock wave in absence of dissipation was not observed [Herbold and Nesterenko (2007)].

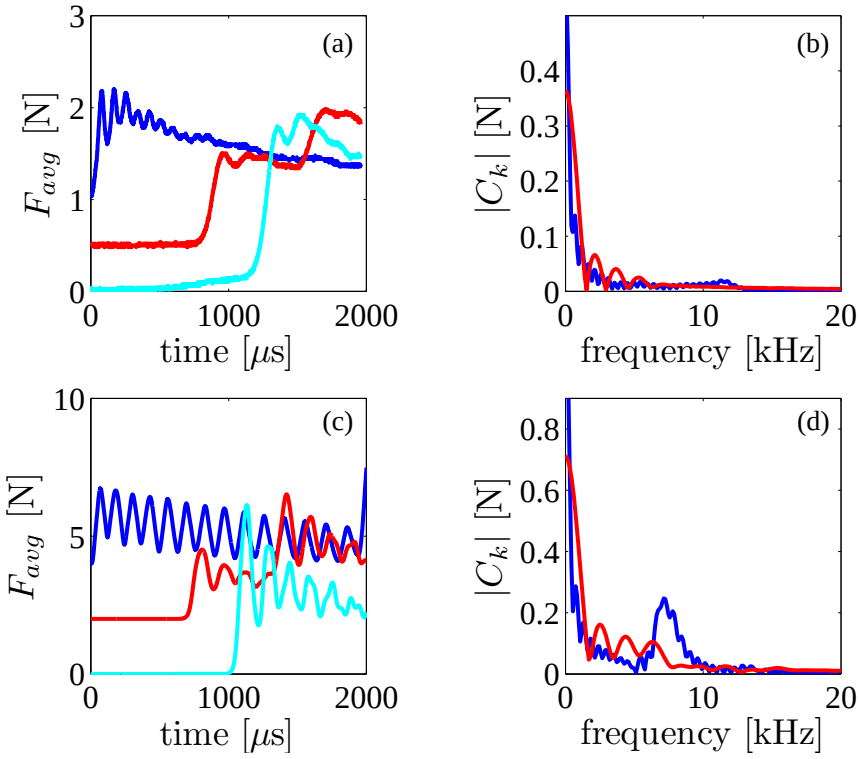

Figure 4.13: Oscillatory shock waves in strongly nonlinear case, there is no initial compression and only gravity is included. The striker had a mass equal to 17.81 g and an initial velocity of 0.2 m/s. (a) Experimental data on the propagation of strongly nonlinear solitary waves in a diatomic chain composed of 37 elements (no precompression other than the gravitational preload is included). The Curves show the force vs. time behavior detected by the sensors in the 2^{nd} particle (top curve), 27^{th} particle (second from the top) and at the wall (bottom curve). (b) Corresponding frequency plots. (c) Numerical calculation corresponding to (a), (d) Frequency plots obtained in the numerical calculations.

4.5 Comparison Between the Analytical Solution and Numerical Calculations of a Strongly Nonlinear Solitary Wave in a Diatomic Chain

In an initially compressed system, a distinct band-gap appears in the frequency spectrum of a nonlinear signal propagating in a diatomic lattice of masses, but when the initial compression is not present the frequency spectrum looks similar to that of a compressed system. In Porter et al. (2008) the expression for the long-wave solution of a solitary pulse with 'sonic-vacuum' initial conditions is provided. With this equation, it is possible to compare not only the pulse shape, but the frequency spectrums of the two pulses (theoretical and numerical). However, experimental data is only available for the force within a particle and this is a difficulty which will be briefly mentioned here. The force measured in experiments is essentially the averaged force of two contact points. This information is readily available in numerical calculations for comparison, but it is probably best to compare the averaged velocities of the theoretical pulse with the velocity profile of the cell-center-of-mass (CCOM) averaged velocities. The cell is defined as one unit containing one of each mass in the dimer chain (one steel and one PTFE particle for example). The CCOM velocity, as will be shown, is readily compared to the exact solution from the long-wave approximation of the dimer chain.

4.5.1 Derivation of the Exact Solution to the LWA in a Diatomic Chain

The strongly nonlinear diatomic chain represents a fundamentally different case from the linear and nonlinear cases where an initial static compression is present. The frequency band gap described by Eqs. (4.10) depends on this compression force

and in its absence the frequency spectrum of the pulse should coincide with the exact solution of the long-wave approximation. The discrete equations of motion for the strongly nonlinear diatomic chain are,

$$\begin{aligned} m_1\ddot{u}_i &= A\left(w_i - u_i\right)^n - A\left(u_i - w_{i-1}\right)^n \\ m_2\ddot{w}_i &= A\left(u_{i+1} - w_i\right)^n - A\left(w_i - u_i\right)^n \end{aligned} \tag{4.12}$$

where

$$A = \frac{4E_1E_2\left(1/R_1 + 1/R_2\right)^{-1/2}}{3\left[E_1\left(1-\nu_2^2\right) + E_2\left(1-\nu_1^2\right)\right]} \tag{4.13}$$

is the stiffness of the contact (similar to Eq. (4.2). The long-wave-approximation begins with the assumption that the propagating pulse is much larger than the unit cell length L ($L >> 2h$ where $h = R_1 + R_2$),

$$\begin{aligned} u_{i\pm1} &= u \pm 2hu_x + 2h^2u_{xx} \pm 4h^3/3u_{xxx} + 2h^4/3u_{4x} + ... \\ w_{i\pm1} &= w \pm 2hw_x + 2h^2w_{xx} \pm 4h^3/3w_{xxx} + 2h^4/3w_{4x} + ... \,. \end{aligned} \tag{4.14}$$

To relate the two displacement fields (u and w), a consistency condition between the two variables is introduced [Büttner and Bilz (1978), Dash and Patnaik (1981), Pnevmatikos et al. (1983), Porter et al. (2008)],

$$w = \lambda\left(u + hb_1u_x + h^2b_2u_{xx} + h^3b_3u_{xxx} + h^4b_4u_{4x} + ...\right). \tag{4.15}$$

with $\lambda = 1$ corresponding to in-phase or 'acoustic' modes and $\lambda = -m_1/m_2$ corresponding to out of phase or 'optical' modes. Here, only acoustic modes will be considered. The term $w_{i\pm1}$ may be expanded

$$\begin{aligned} w_{i\pm1} &= u + h(b_1 \pm 2)u_x + h^2(b_2 \pm 2b_1 + 2)u_{xx} \\ &+ h^3(b_3 \pm 2b_2 + 2b_1 \pm 4/3)u_{xxx} \\ &+ h^4(b_4 \pm 2b_3 + 2b_2 \pm 4/3b_1 + 2/3)u_{4x}. \end{aligned} \tag{4.16}$$

The expansion of Eqs. (4.12) and (4.13) becomes

$$\begin{aligned} m_1 u_{tt} &= A(hb_1 u_x + h^2 b_2 u_{xx} + h^3 b_3 u_{xxx} + h^4 b_4 u_{4x})^n \\ &- A(h(2-b_1)u_x - h^2(b_2 - 2b_1 + 2)u_{xx} \\ &\quad -h^3(b_3 - 2b_2 + 2b_1 - 4/3)u_{xxx} \\ &\quad +h^4(b_4 - 2b_3 + 2b_2 - 4/3b_1 + 2/3)u_{4x})^n \end{aligned} \tag{4.17}$$

and

$$\begin{aligned} m_2 u_{tt} &= A(h(2-b_1)u_x + h^2(2-b_2)u_{xx} + h^3(4/3 - b_3)u_{xxx} \\ &\quad +h^4(2/3 - b_4 u_{4x})^n \\ &\quad -A(hb_1 u_x + h^2 b_2 u_{xx} + h^3 b_3 u_{xxx} + h^4 b_4 u_{4x})^n. \end{aligned} \tag{4.18}$$

Note that the convective derivative (and higher order derivatives in time) in Eqs. (4.17) and (4.18) are negligible since the particle velocity is much smaller than the wave speed Nesterenko (2001) in the granular material. With the definition of the functions

$$\xi = u_x \tag{4.19}$$

$$N(x) = hu_x \tag{4.20}$$

$$\phi_1(x) = h^2 b_2 u_{xx} + h^3 b_3 u_{xxx} + h^4 b_4 u_{4x} \tag{4.21}$$

$$\begin{aligned} \psi_1(x) &= -h^2(b_2 - 2b_1 + 2)u_{xx} \\ &\quad -h^3(b_3 - 2b_2 + 2b_1 - 4/3)u_{xxx} \\ &\quad -h^4(b_4 - 2b_3 + 2b_2 - 4/3b_1 + 2/3)u_{4x} \end{aligned} \tag{4.22}$$

$$\begin{aligned} \phi_2(x) &= h^2(2-b_2)u_{xx} + h^3(4/3 - b_3)u_{xxx} \\ &\quad +h^4(2/3 - b_4 u_{4x} \end{aligned} \tag{4.23}$$

$$\psi_2(x) = h^2 b_2 u_{xx} + h^3 b_3 u_{xxx} + h^4 b_4 u_{4x} \tag{4.24}$$

a small parameter may be defined, $\epsilon \sim \psi_\alpha/N \sim \phi_\alpha/N << 1$ for the series expansion of Eqs. (4.17) and (4.18),

$$\begin{aligned} m_1 u_{tt} &= n\left(hu_x\right)^{n-1}\left[2h^2 b_2 u_{xx} + 2/3h^3\left(3b_3 - 3b_2 + 1\right)u_{xxx}\right. \\ &+ \left. h^4(2b_4 - 2b_3 + 2b_2 - 2/3)u_{4x}\right] \\ &+ n(n-1)h^5\left(hu_x\right)^{n-2}\left\{\left[b_2 b_3 - b_2\left(b_3 - 2b_2 + 2/3\right)\right]u_{xx}u_{xxx}\right\} \\ &+ \frac{n(n-1)(n-2)h^6}{3}\left(hu_x\right)^{n-3}\left(b_2^3 u_{xx}^3\right) + O\left(\epsilon^6\right) \end{aligned} \tag{4.25}$$

and

$$\begin{aligned} m_2 u_{tt} &= n\left(hu_x\right)^{n-1}\left[2h^2(1-b_2)u_{xx} + 2/3h^3\left(4/3 - 3b_3\right)u_{xxx}\right. \\ &+ \left. h^4\left(2/3 - 2b_4\right)u_{4x}\right] \\ &+ n(n-1)h^5\left(hu_x\right)^{n-2}\left\{\left[(2-b_2)(4/3-b_3) - b_2 b_3\right]u_{xx}u_{xxx}\right\} \\ &+ \frac{n(n-1)(n-2)h^6}{3}\left(hu_x\right)^{n-3}\left[\left(2-b_2^3\right)^3 - b_2^3\right]u_{xx}^3 + O\left(\epsilon^6\right) \end{aligned} \tag{4.26}$$

The consistency condition between u and w provided the constants b_1 through b_4, which may be found by equating Eqs. (4.25) and (4.26),

$$b_1 = 1 \tag{4.27}$$

$$b_2 = \frac{m_1}{m_1 + m_2} \tag{4.28}$$

$$b_3 = \frac{2m_1^2 + 4m_1 m_2 - m_2^2}{3\left(m_1 + m_2\right)^2} \tag{4.29}$$

$$b_4 = \frac{m_1\left(m_1^2 + 2m_1 m_2 + 4m_2^2\right)}{3\left(m_1 + m_2\right)^3}. \tag{4.30}$$

The partial differential equation that satisfies both u and w is

$$\begin{aligned} u_{tt} &= \frac{2nc^2}{m_1 + m_2}\left\{\left(u_x\right)^{n-1}u_{xx} + I\left(u_x\right)^{n-1}u_{4x}\right. \\ &\left. + H\left(u_x\right)^{n-2}u_{xx}u_{xxx} + G\left(u_x\right)^{n-3}\left(u_{xx}\right)^3\right\} \end{aligned} \tag{4.31}$$

where $c^2 = Ah^{n+1}$, and

$$\begin{aligned} G &= \frac{(n-1)(n-2)m_1^2h^2}{6\left(m_1+m_2\right)^2} \\ H &= \frac{(n-1)(2m_1-m_2)h^2}{3(m_1+m_2)} \\ I &= \frac{(m_1^2-m_1m_2+m_2^2)h^2}{3(m_1+m_2)^2}. \end{aligned} \tag{4.32}$$

For traveling wave solutions ($u = u(x - V_st)$), Eq. (4.31) may be rewritten in terms of the strain by differentiating it once with respect to x,

$$\begin{aligned} \gamma\xi_{xx} &= \left\{\xi^{n-1}\xi_x + I\xi^{n-1}\xi_{xxx}\right. \\ &\quad \left. +H\xi^{n-2}\xi_x\xi_{xx} + G\xi^{n-3}\left(\xi_x\right)^3\right\}_x \end{aligned} \tag{4.33}$$

where $\gamma = V_s^2(m_1 + m_2)/(2nc^2)$. To get this equation into a tractable form, let $\xi = z^p$,

$$\begin{aligned} \frac{\gamma}{p}\left(z^p\right)_{xx} - \frac{1}{np}\left(z^{np}\right)_{xx} &= \left\{\left[Hp + 3I(p-1)\right]z^{np-2}z_xz_{xx}\right. \\ &\quad \left. +Iz^{np-1}z_{xxx}\right\}_x, \end{aligned} \tag{4.34}$$

provided

$$p = \frac{3I + H \pm \sqrt{I^2 - 2IH + H^2 - 8IG}}{2(G+H+J)}. \tag{4.35}$$

It will be shown that taking the negative value of the radical give the correct wave amplitude scaling. This is done by comparing numerical calculations to the analytical solution being derived.

After integrating Eq. (4.34) once and setting the constant equal to zero, it still needs to integrate once more. Multiplication and division of the right hand side Eq. (4.34) by z^a, (where a will be the integration factor) gives the result:

$$\frac{\gamma}{p}\left(z^p\right)_x - \frac{1}{np}\left(z^{np}\right)_x = Iz^{-a}\left(z^{np+a-1}z_{xx}\right)_x \tag{4.36}$$

provided $a = Hp/I + p(3-n) - 2$. Integrating Eq. (4.36) gives

$$z_{xx} + \sigma z - \mu z^{\eta} + C_2 z^{-(np+a)} = 0, \tag{4.37}$$

where $\sigma = 1/(npI(a+1))$, $\mu = \gamma/(pI(a+1))$, $\eta = 1+p(1-n)$, and C_2 is an integration constant corresponding to an initial strain on the system. Exact solutions may be obtained for $C_2 = 0$,

$$\xi = z^p = B\cos^{2/n-1}\left(\beta(x - V_s t)\right), \tag{4.38}$$

$$v_p = V_s \xi \tag{4.39}$$

where $B = [\mu/\beta^2 s(s-1)]^{1/(k-1)}$, $\beta = \sqrt{\sigma}(1-\eta)/2$, $s = 2/(1-\eta)$ and v_p is the particle velocity. The analytical solution for the particle velocity may be compared to the cell-center-of-mass (CCOM) velocity to a fairly high degree of accuracy.

To begin, a numerical calculation is performed using 600 stainless steel particles and 600 PTFE particles. The material data for the particles is presented in Table 4.3. The initial conditions for the simulations are as follows: $v_0 = 0.44$ m/s, $f_0 = 0$, and $g = 0$ (g is the gravitational constant). The simulation was run (i.e. the equations of motion were integrated in time using the RK45 algorithm) until the leading pulse reached the 'wall' after the 1200^{th} particle. In Fig. 4.14 the particle velocity profiles for the $74^{th} - 76^{th}$ particles is plotted versus time. The main plot shows that behavior in the dimer chain without initial compression is quite different from that of a single species chain of particles: there is substantial oscillation behind the initial pulse. The inset of the figure shows the three pulses. From left to right these pulses are PTFE, stainless steel and PTFE. Note that the PTFE particles undergo two peaks in the time it takes the stainless steel particle to produce one (asymmetric) peak. This is also seen in Fig. 1.19 in Nesterenko (2001).

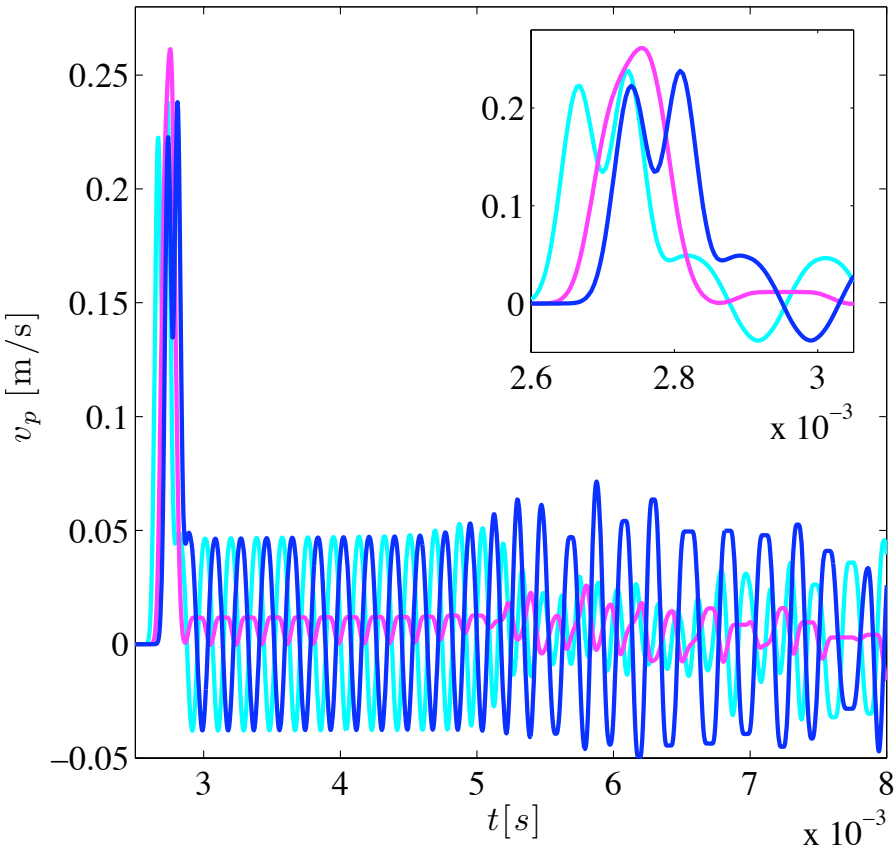

Figure 4.14: Particle velocity profiles of the 74^{th} (light blue), 75^{th} (magenta) and 76^{th} (dark blue) particles.

It would be difficult to compare any one of these particle velocity profiles to the exact solution. It was decided that it would be best to compare the CCOM average velocity with the exact solution. The CCOM average velocities were calculated following:

Table 4.3: Material properties (mass, elastic modulus E, and Poisson's ratio ν) for stainless steel and PTFE. The value of the dynamic elastic modulus of the rubber beads was extrapolated from the experimental data.

Material	Mass	Radius	ρ	E	ν
Steel	0.450 g	2.38 mm	8000 kg/m^3	193 GPa	0.30
PTFE	0.123 g	2.38 mm	2196 kg/m^3	1.46 GPa	0.46

$$\bar{v}_{cm}(t) = \frac{m_1 v_1(t) + m_2 v_2(t)}{m_1 + m_2}, \tag{4.40}$$

where the subscripts 1 and 2 denote the two particles being averaged. It is interesting, still, that there are two different, seemingly stationary, leading pulses in this dimer chain. The velocity profile of the PTFE particle is different from that of the stainless steel chain but is similar to every PTFE's velocity profile (the same is true for the velocity profile of the stainless steel). Also, from Fig. 4.14 it is clear that neither 'stationary' pulse is symmetric. Thus, the CCOM averaged velocity pulses will depend on whether the averages are computed with the steel on the left or right of the PTFE particles. In Fig. 4.15 the cell-center-of-mass averaged velocity is shown for the $74^{th} - 75^{th}$ (steel-PTFE) and the $75^{th} - 76^{th}$ (PTFE-steel) particles. Note that the pulse for the $75^{th} - 76^{th}$ (PTFE-steel) particles is clearly asymmetric but the leading pulse is clearly separated from the trailing oscillations whereas the more

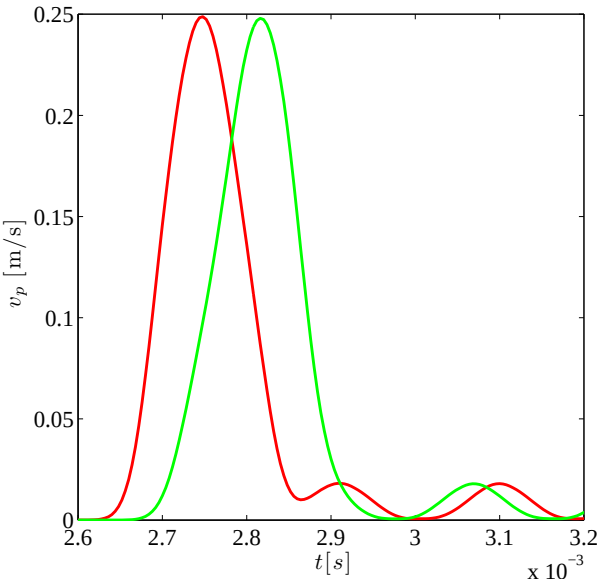

Figure 4.15: Cell-center-of-mass (CCOM) averaged velocity profiles of the $74^{th} - 75^{th}$ and the $75^{th} - 76^{th}$ particles.

symmetric pulse (for the $74^{th} - 75^{th}$ (steel-PTFE) particles is clearly connected to the trailing oscillations. The physical significance of this is not clear to me at this time since these are plots of averaged velocities. However, what is clear is that both pulses have a similar amplitude and speed of $V_s \approx 130$ m/s.

Due to symmetry, it seems that the CCOM averaged velocity profile with the heavy (stainless steel) coming before the light (PTFE) particle is the best candidate to compare to the theoretical prediction of the pulse shape. From Porter et al. (2008) the LWA result for the particle velocity (assuming a Hertzian interaction between particles) is;

$$v_p = BV_s \cos^4(\beta V_s t), \tag{4.41}$$

where m_1 and m_2 are the masses of the steel and PTFE particles, A is the effective stiffness (similar but not equal to that found in Nesterenko's book where $A_n = A/m$ which would not make sense here), $h = R_1 + R_2$ is the distance between particle centers, V_s is the phase speed, B is a constant and β is a constant depending on h, the mass ratio $\omega = m_2/m_1$ and V_s if one wishes to scale the equation in time instead of space. In the paper, instead of t as the independent variable, there is $\xi = x - V_s t$. Also, I will not explain the constant B or β here as they may be found elsewhere.

Using the data from the numerical calculations, the constants for Eq. 4.37 are: $A = 8.444 * 10^7$ kg/m$^{1/2}$s^2, $h = 4.76$ mm, $V_s = 130.1$ m/s, $\beta = 11320$ 1/s and $B = 0.2484$ m/s. The reported value for β here is the same as in Porter et al. (2008) but it is multiplied by V_s to obtain units of 1/s instead of 1/m. In Fig. 4.16 a comparison can be made between the theoretical and numerical calculations of the particle velocity in the dimer chain. The plot shows the cell-center-of-mass (CCOM) averaged velocity profiles of the $74^{th} - 75^{th}$ (stainless steel before PTFE) plotted with the theoretical LWA solution for a dimer chain. Again, the agreement between the shapes (not amplitudes) would be different if the $75^{th} - 76^{th}$ (PTFE before stainless steel) average was shown. Also, the abscissa in this plot is dimensionless to resemble the width of the pulse (approximately 8 particle diameters) and the maxima of each leading pulse were artificially aligned at zero.

The similarities between the two pulses is striking. The amplitudes and the 'loading' side of the pulses are almost identical. However, in numerical calculations, the CCOM averaged velocity shows a connected trailing pulse. I checked at later times (around the 1150^{th} particle) to see if this pulse separated from the leading pulse. It does not. In fact, the difference in the distance between the leading pulse and the first trailing pulse remained unchanged for the duration of 1200 particles!

One might assume that this means that a stationary two-wave structure has

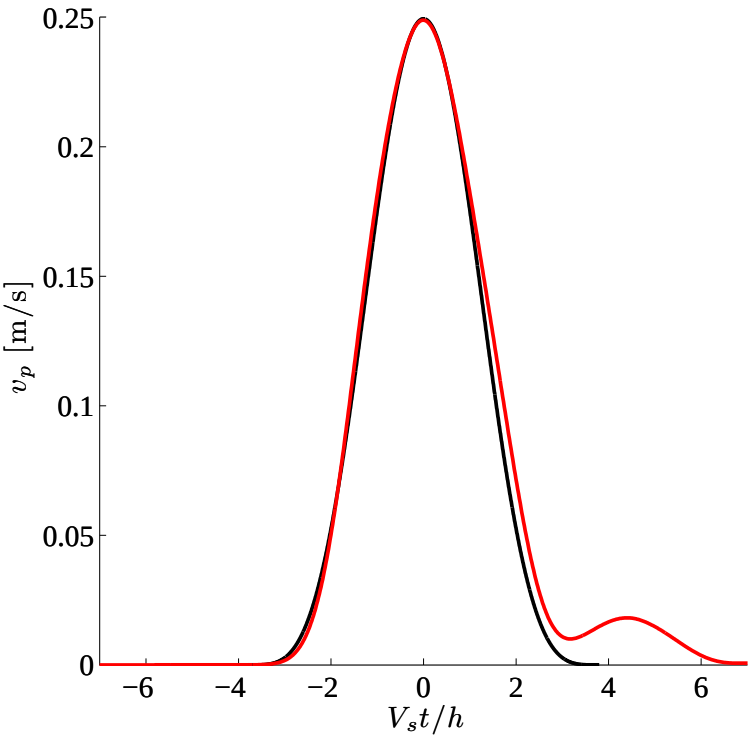

Figure 4.16: Cell-center-of-mass (CCOM) averaged velocity profiles of the $74^{th} - 75^{th}$ (stainless steel before PTFE) plotted with the theoretical LWA solution for a dimer chain.

formed and is propagating in these systems, but I should also mention the amplitude decrease in the leading pulse as it progresses through the chain. The leading pulse amplitude decreases at a constant 0.17% for every 'cell' it traverses (after initially forming after the first 10-20 particles). This means that the leading pulse (the type seen in the stainless steel and the type seen in PTFE) is not stationary, but long-living.

It would be interesting to take the two pulses shown in Fig. 4.16 and compare their frequency spectrums. The analytical result (Eq. (4.37)) represents a

single pulse in an infinite domain as is the leading pulse in the numerical calculations. However, the frequency spectrum of Eq. (4.37) will be discussed first in a periodic time domain.

Transforming Eq. (4.37) yields

$$\hat{v}_p(f) = \frac{B}{8}\left[6\delta(f) + 4\delta(f - \beta/\pi) + \delta(f - 2\beta/\pi)\right], \tag{4.42}$$

where δ is the delta function and the period. Note that there are only 3 fundamental frequencies present since the negative frequency have no physical significance here. There the three frequency components from Eq. (4.38) located at $f = 0$, β/π, and $2\beta/\pi$. The coefficients of the delta functions correspond to the complex coefficients typically obtained in Fourier series expansions. These coefficients will be used to compare theoretical and numerical data since the first value will correspond to the mean of the function, which will provide a rapid check regarding the correctness of the plots. The complex coefficients (in this case they are only real valued) correspond to the three frequency components and are $C = 3B/8, B/4$ and $B/16$.

The transform of a single pulse in an infinite domain will use the piecewise form of Eq. (4.37),

$$v_p = \begin{cases} 0 & t < -\pi/2\beta \\ B\cos^4(\beta t) & -\pi/2\beta \le t \le \pi/2\beta \\ 0 & t > \pi/2\beta \end{cases}, \tag{4.43}$$

which is shown in Fig. 4.16 by the symmetric single pulse. The Fourier transform of Eq. (4.43) is,

$$\hat{v}_p(f) = \frac{3\beta^4 B \sin\left(\pi^2 f/\beta\right)}{2\pi f\left(\pi^2 f^2 - 4\beta^2\right)\left(\pi^2 f^2 - \beta^2\right)}, \tag{4.44}$$

which has the dimensions of v_p multiplied by the period π/β. The (positive) complex coefficients may be obtained by dividing Eq. (4.44) by the period and written in

terms of k by $f \equiv k/T \equiv \beta k/\pi$,

$$C_k = \frac{3B \sin(\pi k)}{2\pi k\,(k-1)\,(k+1)\,(k-2)\,(k+2)}. \tag{4.45}$$

This equation may be verified by passing k to the limit of 0,1 and 2 to obtain the same result as for the periodic function,

$$\begin{aligned} \lim_{k\to 0} C_k &= 3B/8 \\ \lim_{k\to 1} C_k &= B/4 \\ \lim_{k\to 2} C_k &= B/16 \end{aligned} \tag{4.46}$$

and

$$C_k = 0 \quad \forall \quad k > 2 \quad (k \in \mathbb{Z}). \tag{4.47}$$

So, for multiples of the period ($T = \pi/\beta$) the coefficients will be zero. Figure 4.17 shows the frequency spectrum of the two pulses shown in Fig. 4.16. Note that the larger of the two 'zero' values corresponds to $3B/8 = 3 * 0.2484/8 = 0.0932$ m/s. The transformed CCOM pulse from the numerical calculations is similar in shape but the magnitude of the coefficients differs due to the difference in the period. It was assumed that the leading pulse includes the larger and the trailing smaller pulse which make the period longer. Note also that the small rise in the frequency spectrum near $f = 10$kHz is a feature of the function $\cos^4$ and should not be solely attributed to the appearance of the second pulse seen in Fig. 4.16.

The next thing to do is to compare the first zero point of the the frequency spectrum with that of the band-gap formed in the frequency spectrum in dimer chains due to initial compression.

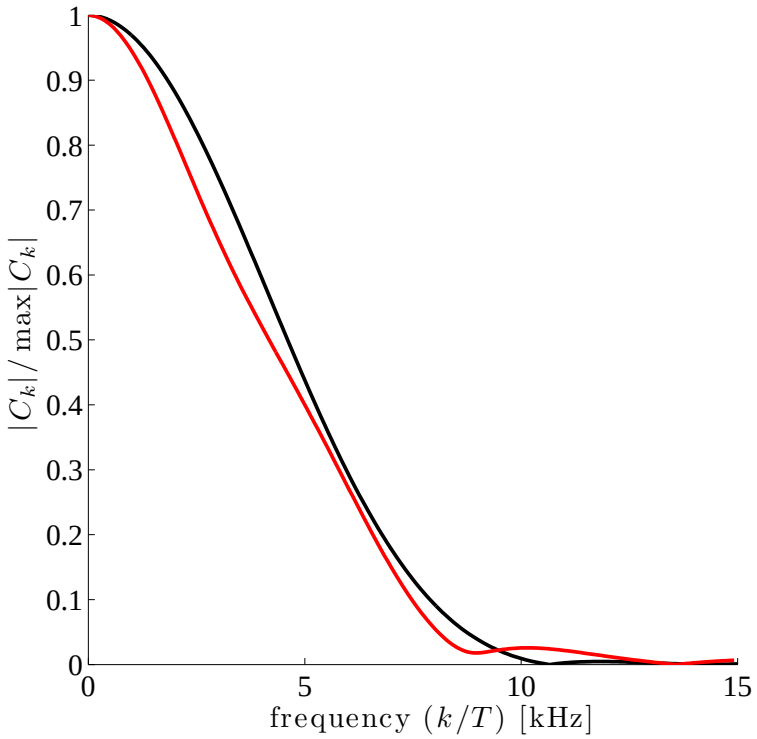

Figure 4.17: Frequency spectrum of the two pulses shown in Fig. 4.16. The C_0 value for the theoretical pulse (black line) corresponds to $3B/8 = 3 * 0.2484/8 = 0.0932$ m/s. The continuous spectrum is shown by taking the pulses in a domain that is 50 times the period (i.e. $N/M = 50$) shown in Fig. 4.16.

4.6 Conclusions

One dimensional diatomic nonlinear phononic crystals have been assembled and tested using PTFE spheres and steel cylinders. The band gap frequencies can be achieved inside the audible range of frequencies and adjusted by the mass of the particles, their elastic modulus and magnetically induced initial static compression. The transformation of pulses with frequencies inside the phononic band gap is observed in numerical calculations in statically compressed chains. It was shown that the band gap rapidly transforms incoming pulses within very short distances from the source in a linear elastic chain.

It was demonstrated that the band gap calculated in the linear approximation is able to transform of practically harmonic signals with large amplitude causing nonlinear behavior of the system. Initial disturbances separated into two groups of waves; pure acoustic and trailing group of signals with optical frequencies.

Strongly nonlinear solitary waves with a width of five cells were observed in experimental and numerical calculations as predicted by the long wave approximation. The experimental results demonstrate a qualitative change of the propagating wave properties under different conditions of static compression. With the magnetically induced compression, the speed of the solitary wave was increased by 50%.

Oscillatory shock waves were excited under the impact of striker in nonlinear and strongly nonlinear systems. They demonstrated a transition to reduced frequency oscillations both in experiments and calculations without dissipation. This may be explained by in situ band gap generated by dynamic compression behind relatively long shock wave. The increased frequency of harmonics in incoming shock profiles in experiments in comparison with numerical calculations may be due to dissipation.

Sections 1 through 5 in Chapter 4 have, in part, been submitted to *Physical Review E* by E.B. Herbold, J. Kim, V.F. Nesterenko, S. Wang and C. Daraio. The dissertation author was the primary investigator and author of this paper. Part of section 6 in Chapter 4 is a derivation omitted in an article published in *Physical Review E Rapid Comm.*, **77**, art. 015601(R), pp. 1-4 by M.A. Porter, C. Daraio, E.B. Herbold, I. Szelengowicz and P.G. Kevrekidis.

5

Hydrodynamic Dissipation and Critical Viscosity in a Strongly Nonlinear Lattice of Deformable Particles

5.1 Hydrodynamic Dissipation in a Granular Assembly of Stainless Steel Spheres

There have been a number of analytical and numerical studies that introduce dissipation in the equations of motion for discrete systems. These losses may be attributed to uncontrolled features in the experimental setup as well as inherent material properties (Job et al. (2005)). In Raman (1918) coefficients of restitution of various materials were ascribed to either plasticity or the production of sound waves in the surrounding medium. He also expressed the desire to "determine in what manner the apparent coefficient of restitution is affected by the density of the surrounding fluid." It is also interesting to investigate (or differentiate) these effects from the viscosity of the surrounding fluid. The energy losses are significant even when the experiments are performed in air (see Fig. 1.25 in Nesterenko (2001)). The be-

havior of a viscous granular gas was investigated [Rosas et al. (2005)] using a viscous drag term depending on the velocity of individual particles. Coefficients of restitution were used to investigate inelastic collisions between two particles [Gondret et al. (2001), Stocchino and Guala (2005)] and viscoelastic interactions were introduced in Ramírez et al. (1999), Brilliantov et al. (1996). Attenuation in a one dimensional particle lattice is analyzed in Manciu et al. (2001), Rosas and Lindenberg (2003). In Duvall et al. (1969), coupled dashpots representing viscous dissipation depending on the relative motion between atoms were introduced for the investigation of steady shock waves in anharmonic spring-mass systems. The influence of Stokes drag force, which is a function of particle velocities, and damping depending on the relative motion of particles considered enveloped solitons in anharmonic discrete lattices was considered in Brunhuber et al. (2006).

To predictably control the dissipation, a chain of spheres may be immersed in viscous fluids. The viscous dissipation of pulses in chains of particles differs from a binary collision in liquid because the compression wave dominates the system's dynamic behavior. This chapter extends current knowledge of a two particle collision in a viscous medium to the case where multiple particle interactions support a solitary wave.

It is well known that one dimensional and ordered two or three dimensional lattices of elastic spherical particles support compressive strongly nonlinear solitary waves for "normal" nonlinear interaction laws between particles [Nesterenko (2001)]. These waves are a natural extension of the well known weakly nonlinear solitary waves such as the Korteweg-de Vries (KdV) solitons. Strongly nonlinear waves exist when the force between particles exhibit a power-law dependence on displacement ($F \propto \delta^n$) for $n > 1$ [Nesterenko (1992c), Nesterenko (1992d), Nesterenko (1992b), Nesterenko (1992a)] and when the dynamic displacement is much greater

than the initial displacements due to gravitational or externally applied loads. The long wave approximations for power-law materials have exact solutions for compressive solitary waves in non-dissipative particle lattices. When lattices are statically compressed they exhibit a dynamic nonlinear behavior that can be tuned [Daraio et al. (2006)] from the strongly to the weakly nonlinear regime. Chains composed of steel, brass, glass, Nylon Nesterenko (2001), Coste et al. (1997), Coste and Gilles (1999) and Polytetraflouroethylene (PTFE) Daraio et al. (2005) particles support solitary waves using Hertz' law for particle interactions. However, dissipation significantly attenuates pulses in most experimental settings [Nesterenko (2001), Daraio et al. (2005), Daraio et al. (2006)] in the strongly and weakly nonlinear regimes and should be included to model real granular systems.

5.1.1 Theoretical Considerations

The analytical model for a one-dimensional Hertzian chain of spheres can be found in Nesterenko (2001). The description of particle interactions in fluids is presented in Gondret et al. (2001), Zhang et al. (1999), Milne-Thomson (1968), Davis et al. (1985), Hocking (1972). One of the complications of using current sphere-fluid models for a chain of spheres is that a developed flow around the sphere is assumed before the particle collision though the duration of the pulse in a chain is relatively short ($\sim$50 μs). In Milne-Thomson (1968) two particles are considered to be traveling towards each other in a surrounding medium. If the spheres are the same size then the total kinetic energy is

$$\frac{1}{4}\left(2m + m' + \frac{3}{8}\frac{m'R^3}{h^3}\right)U^2 = constant, \tag{5.1}$$

where $m = \frac{4}{3}\pi\rho R^3$ is the mass of the particle, $m' = \frac{11}{12}\pi\rho_f R^3$ is the added mass, R is the particle's radius, h is the separation distance between particle centers and

$U = dh/dt$ is the relative particle velocity. Differentiating Eq. (5.1) with respect to h yields the added mass and pressure force terms. The equations of motion for a chain of spheres, with mass m_i, placed vertically in a gravitational field in a fluid becomes

$$\left(m_i + m_i'\right) \frac{d^2 x_i}{dt^2} = F_{c,i}\left(\delta\right) + m_i g + F_{b,i} + F_{D,i} + F_{p,i} + F_{d,i}. \tag{5.2}$$

where $\delta_{i,i+1} = \left(R_i + R_{i+1} + x_i - x_{i+1}\right)$ and the x_i's are the particle positions. The compression force $F_{c,i}$ is based on Hertz law between particle 'i' and the adjacent particles '$i-1$' and '$i+1$';

$$F_{c,i} = \phi\left(\delta_{i-1,i}\right) - \psi\left(\delta_{i,i+1}\right), \tag{5.3}$$

where ϕ and ψ can be expressed as

$$\phi\left(\delta_{i-1,i}\right) = A_{i-1,i}\left(\delta_{i-1,i}\right)^{3/2} \tag{5.4}$$

and

$$\psi\left(\delta_{i,i+1}\right) = A_{i,i+1}\left(\delta_{i,i+1}\right)^{3/2}. \tag{5.5}$$

The coefficients in Eqs. (5.4) and (5.5) are identical except for a shift of indices. The equation for $A_{i-1,i}$ can be inferred from

$$A_{i,i+1} = \frac{4E_i E_{i+1}\left(1/R_i + 1/R_{i+1}\right)^{-1/2}}{3\left[E_{i+1}\left(1-\nu_i^2\right) + E_i\left(1-\nu_{i+1}^2\right)\right]}, \tag{5.6}$$

where E_i and ν_i are the elastic modulus and Poisson's ratio of the particle. For all of the calculations performed with air as the surrounding medium, only the first two terms on the right hand side and the first term on the left side of Eq. (5.2) are used. When liquids surround the chain of spheres the buoyancy, drag, pressure, added mass and dissipative terms are used. The buoyancy force for each particle is

$$F_{b,i} = -\frac{4}{3}\pi R_i^3 \rho_f g, \tag{5.7}$$

where g is the gravitational constant, R_i is the radius of the particle and ρ_f is the density of the fluid. The drag force has a correction factor to account for a Reynold's number Re greater than unity i.e. not in the Stoke's flow regime,

$$F_{D,i} = -6\pi\nu R_i U_i(1 + 0.15Re^{0.687}), \tag{5.8}$$

where ν is the dynamic viscosity and U_i is the particle velocity. The pressure force in Zhang et al. (1999) is written for one sphere moving toward a stationary sphere. In this case, the relative velocity between particles is used,

$$F_{p,i} = \frac{3}{8}\pi R_i^2 \rho_f \left[(U_{i-1} - U_i)^2 - (U_i - U_{i+1})^2\right]. \tag{5.9}$$

An additional dissipative term is introduced based on the relative velocity between particles with a fitting parameter c due to the lack of a qualitative agreement between the experiments and calculations based on the drag force term (Eq. (5.8)). This addition is tantamount to adding a dash-pot between neighboring particles [Duvall et al. (1969)],

$$F_{d,i} = c\left(U_{i-1} - 2U_i + U_{i+1}\right), \tag{5.10}$$

where the coefficient c is a fitting parameter. The physical reason for this term can be due to the radial flow of liquid caused by the change of contact area between particles.

MATLAB's intrinsic ODE45 solver was used to march the explicit calculation forward in time with a time-step of 0.05μs. The error in the energy calculations were found to be less than $10^{-9}\%$ in air and within $10^{-5}\%$ in the fluid. The error in the conservation of linear momentum performed with a chain in air was less than $10^{-12}\%$.

5.1.2 Experimental Procedures and Results

In the experiments, the impulse propagation was investigated in three different media: air, SAE 10W-30 motor oil, and non-aqueous Glycerol GX0185-5. The density and dynamic viscosity used in numerical calculations were $\rho_f = 880$ kg/m^3, $\nu = 0.067$ Ns/m^2 for oil and $\rho_f = 1260$ kg/m^3, $\nu = 0.62$ Ns/m^2 for glycerol. An experiment was performed in each of the three types of media to see how single and multiple solitary waves propagate through the chain. The chain was placed into an adjustable holder, as shown in Fig. 5.1.2 that had four contact points on each sphere. The air or fluid was able to flow freely between the contacts as opposed to the cylindrical holder that had been used in previous experiments.

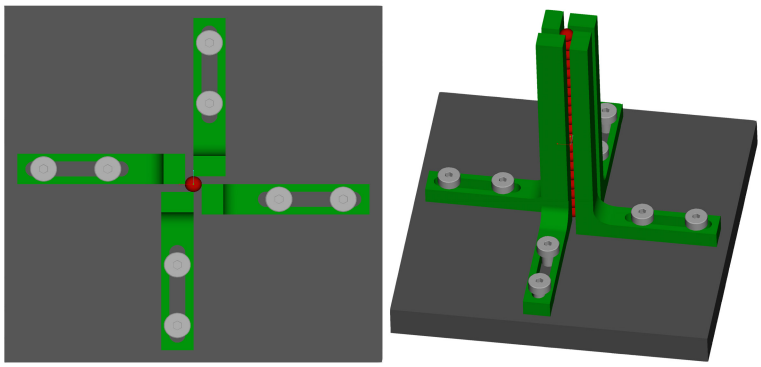

Figure 5.1: Experimental apparatus: The adjustable arms accommodate different sizes and create a four point contact on each particle. The empty space in between the contact allow the fluid to flow unrestricted by the apparatus.

A Tektronix TDS2014 oscilloscope was used to record the voltage values from the particle sensors. A program was written in MATLAB to interface with the oscilloscope and convert the voltages from the piezoelectric gauges to forces in

real-time (this MATLAB code can be found in Appendix C).

To create a single solitary wave, a spherical stainless steel striker with a radius of $R = 4.76$ mm and a mass of $m = 0.4501$ g was used to impact the top of a chain of 19 stainless steel particles (also with $R = 4.76$ mm) with a velocity of $U_0 = 0.44$ m/s. To create multiple solitary waves in the same chain, a cylindrical alumina striker with a larger mass of $m = 1.23$ g impacted the chain at $U_0 = 0.44$ m/s. The elastic modulus and Poisson's ratio of the stainless steel particles were 193 MPa and 0.3, respectively. The experimental results were recorded via piezoelectric gauges imbedded [Daraio et al. (2005)] in the 10^{th} and 15^{th} particles from the top of the chain. The procedures outlined in Daraio et al. (2005) were implemented to compare the calculations to the experimental results using the averaged dynamic force as noted on the vertical axis of Fig. 5.1.2, 5.1.2 and 5.1.2.

In Fig. 5.1.2 the numerical and experimental results are shown for a single solitary wave in a chain surrounded by air (a), (c) and glycerol (b), (d). It is evident that there is a very small difference between the numerical results for the chain in air and glycerol using Eqs. (5.2)-(5.9), which prompted the inclusion of the additional dissipative term (Eq. (5.10)). Without this dissipative term, the numerical results for glycerol shown in Fig. 5.1.2(b) do not exhibit the shape and speed of the pulses in experiments.

In experiments the speeds of the single pulse were $V_s = 520$ m/s in air and increased to $V_s = 541$ m/s in glycerol. It is interesting to note that the calculated signal speed was $V_s = 564$ m/s in air and decreased to $V_s = 540$ m/s in glycerol. In numerical calculations the speed of the single pulses in chains surrounded by both air and glycerol should be higher than the experimental pulse speeds due to the higher amplitude of the waves. Also, one would intuitively think that the pulse speed in

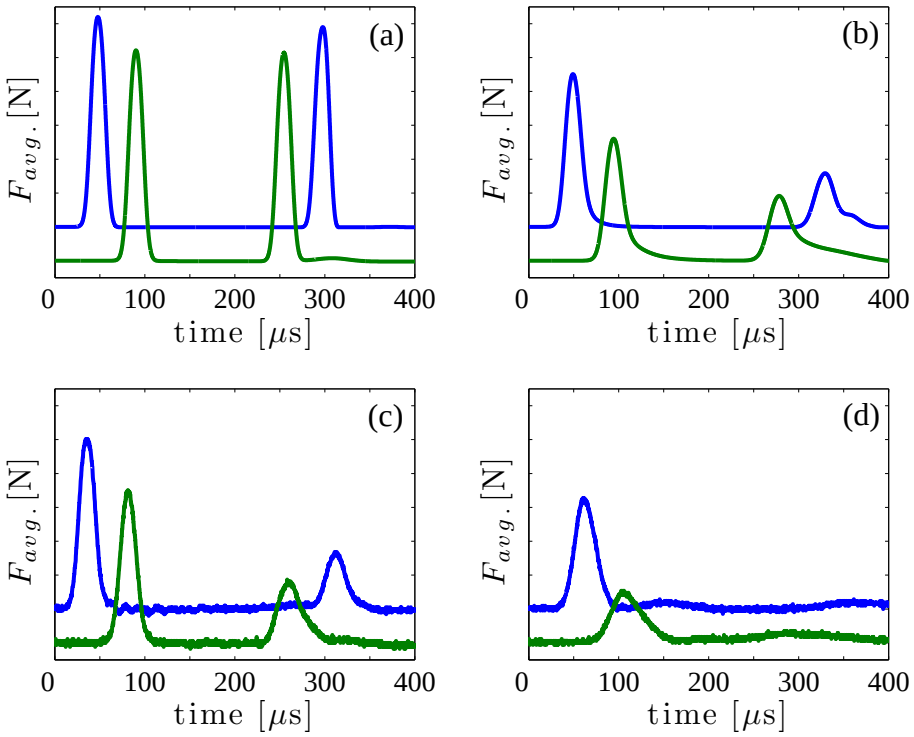

Figure 5.2: Single solitary wave in calculations (a) and experiments (c) in a chain surrounded by air. Results for an identical chain surrounded by glycerol in calculations (b) and experiments (d). Vertical scale is 2 N/div.

air would be higher than in glycerol due to viscous dissipation. This is the case in calculations (even when the additional dissipative term F_d is added) but the opposite is true in experiments (Fig. 5.1.2(c) and (d)).

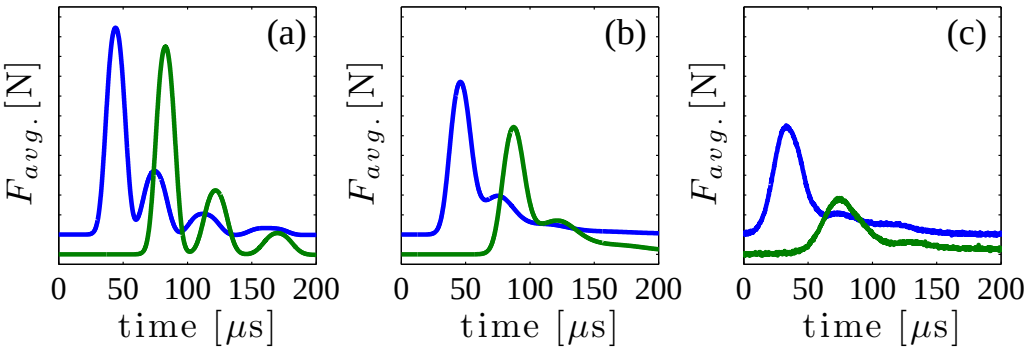

Figure 5.3: (a) Numerical results for multiple solitary waves in a chain of 19 particles surrounded by air. (b) Numerical results for multiple solitary waves in an identical chain surrounded by glycerol. (c) Experimental results related to (b). Vertical scale is 2 N/div.

In Fig. 5.1.2 the numerical results for a train of solitary waves in air and glycerol are presented. The dissipative term F_d was not included in the calculations in (a) and (b) and it is apparent that the amplitudes of the waves are much higher than the experimental results in glycerol (c). Additionally, no signal splitting into a train of solitary waves were present in experiments Fig. 5.1.2(c), which is not reflected by the calculations without the additional dissipative term F_d. Again, the wave speeds in experiments were higher in glycerol than in air.

There is a disparity between the presented analytical formulation using the corrected Stokes drag for dissipation and the experiments. The largest dissipative

term in the calculations (before the addition of the dissipative term F_d) is the drag force term. The reduction of the amplitude of a single pulse was about 3% in oil and about 4% in glycerol when using Eqs. (5.2)-(5.9). These equations, while important for accurately describing a particle trajectory pre and post collision are negligible when their effect on the compression wave are examined.

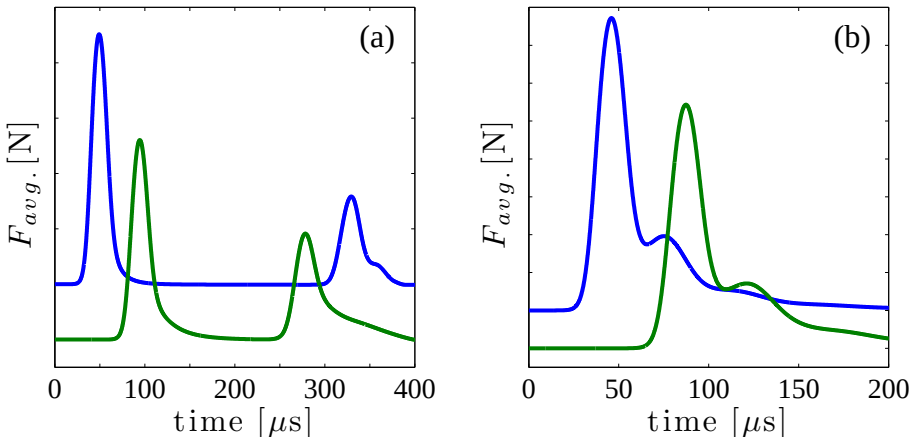

Figure 5.4: (a) Numerical results for a single pulse with additional dissipative term Eq. (5.10) in a chain surrounded by glycerol. (b) Numerical result for an impact by an alumina striker on the same chain. Vertical scale is 2 N/div.

The results of adding the dissipative term Eq. (5.10) are presented in Fig. 5.1.2 for single and multiple pulses traveling in a chain submersed in glycerol. A similar asymmetry and widening of the pulse, apparent in experiments, can also be seen when Fig. 5.1.2 (a) is compared to Fig. 5.1.2 (d). The lower line in Fig. 5.1.2(d) has a noticeable shock-like tail. In calculations the tail of the wave becomes more shock-like as parameter c increases. The qualitative behavior of the pulse in experiments is reproduced in calculations by adding an additional dissipative term

F_d with a coefficient $c = 6.0$ Ns/m for glycerol and $c = 0.648$ Ns/m for oil. These values provided the best comparison between experimental and numerical data and were scaled according to the difference in viscosity. When comparing Fig. 5.1.2(b) and Fig. 5.1.2(b), notice the additional dissipation Eq. (5.10) has also created a shock-like response of the train of solitary waves. In calculations the amplitude and tendency to split decreased by adding this term in accord with experiments.

5.1.3 Conclusions

The experimental results indicate a qualitative change of the propagating shock and solitary waves in a chain immersed in glycerol while only a small change in oil. Without the relative velocity based dissipative term F_d, the equations pertaining to the surrounding fluid could not accurately reproduce the amplitude or the shock like structure of the incident pulse. This term provided the qualitative change needed to match the numerical analysis to the experiments. The numerical analysis predicted a decrease in solitary wave speed as the viscosity of the surrounding fluid increased contrary to experiments. This phenomenon may be explained by an increased effective stiffness modulus between particles in the presence of a viscous fluid.

5.2 Shock Wave Structure in a Strongly Nonlinear Lattice with Viscous Dissipation

In the previous section it was shown that hydrodynamic dissipation significantly attenuates pulse propagation and that an additional term is necessary to account for should be included to model real granular systems. The experimental and numerical work on pulse propagation in lattices immersed in media with different vis-

cosities (air, oil and glycerol) Herbold et al. (2006) demonstrated that a dissipative term based on the relative velocities between particles affect the wave propagation more significantly than Stokes drag. The mechanism of this phenomenon is related to fluid being expelled from and returning to the contact area during dynamic particle interaction on the stages of contact force increase and decrease correspondingly.

The dissipation process influences the behavior of media in the transition area within the shock front and determines the shape of shock profile. For example, in a weakly nonlinear system described by the Korteweg de Vries (KdV) equation, two qualitatively different shock profiles exist depending on the value of the viscosity Karpman (1975); oscillatory if below the critical value and monotonic if above. These two profiles also appear experimentally in strongly nonlinear systems using geometrically identical lattices of lead and steel particles under similar loading conditions Nesterenko (2001). The energy dissipation in the strongly nonlinear lead particle lattice is attributed to the significant plastic deformation in the vicinity of the particle contact, which resulted in a monotonic shock profile.

To the best of my knowledge there is no result for the critical viscosity that ensures a transition from an oscillatory to a monotonic shock profile in strongly nonlinear discrete lattices (e.g. one dimensional granular chains) or in the corresponding long-wave approximations.

This section studies the effects of this dissipative term on the type of shock wave profiles (i.e. monotonic or oscillatory) in a discrete strongly nonlinear system using numerical analysis. A dissipative term based on the relative velocity between neighboring particles is introduced in the discrete equations and a critical viscosity is found using the long wave approximation. The numerical results are compared to the analytical treatment of the same system in the context of the long-wave approximation.

5.2.1 Equations of Motion for a Strongly Nonlinear Dissipative Discrete Lattice

In the general case an interaction law between neighboring particles in a one-dimensional lattice can be described by a function of their relative displacements $f(u_i - u_{i+1})$, where u_i is the displacement of the i-th particle. To account for viscous dissipation, a term based on the relative velocities between particles [Duvall et al. (1969), Herbold et al. (2006), Brunhuber et al. (2006)] is added to the description

$$\begin{aligned} m\ddot{u}_i &= f(u_{i-1} - u_i) - f(u_i - u_{i+1}) \\ &+ \mu(\dot{u}_{i-1} - 2\dot{u}_i + \dot{u}_{i+1}) \end{aligned} \tag{5.11}$$

where m is the mass and μ is the viscosity coefficient and the dots over the displacements (u) denote differentiation with respect to time. A compressive solitary wave exists for Eq. (5.11) in the absence of dissipation and a stationary shock wave exists when dissipation is included for a "normal" interaction law in the continuum approximation. The term "normal" refers to an increasing repulsive potential as the distance between particle centers decreases ($f'' > 0$) [Nesterenko (2001)]. In the case of abnormal interactions ($f'' < 0$) solitary and shock rarefaction waves may exist. The various properties of these two types of waves are discussed in Nesterenko (2001). The existence of solitary waves in a non-dissipative discrete lattice for "normal" interactions is proven in Friesecke and Wattis (1994). As a subset of Eq. (5.11), particles interacting according to a power-law potential represent a relatively broad class of interactions where exact solutions of long-wave approximations can be found for solitary waves [Nesterenko (1983)]. The system of equations using a power law

potential and including a viscous dissipation term is

$$\begin{aligned} \ddot{u}_i &= A_n \left(u_{i-1} - u_i\right)^n - A_n \left(u_i - u_{i+1}\right)^n \\ &+ p \left(\dot{u}_{i-1} - 2\dot{u}_i + \dot{u}_{i+1}\right), \end{aligned} \tag{5.12}$$

where A_n depends on the geometry of the contact region and the material properties and n is the degree of nonlinearity in the system ($n = 3/2$ for Hertzian contact between particles). The damping coefficient p is defined $p = \mu/m$, where μ is analogous to the constant used for a dashpot model, which was found to adequately describe viscous dissipation in the previous section [Duvall et al. (1969), Herbold et al. (2006), Brunhuber et al. (2006)]. Numerical investigations for discrete systems with moderate values of n ($n < 2$) agree well with the results obtained in the long-wave approximation [Rosas and Lindenberg (2004), Manciu et al. (2001), Hascoët and Herrmann (2000)]. The classical Hertzian interaction between perfectly elastic spherical particles is a special case of Eq. (5.12) when $n = 3/2$. In this case, experimental results qualitatively agree with the long-wave approximation and numerical results for a one dimensional discrete particle lattice made from various types of materials [Nesterenko (2001), Daraio et al. (2005)]: though dissipation was noticeable in practically all of the experiments.

5.2.2 The Long Wave Approximation and Critical Viscosity

The long wave approximation can be derived from the strongly nonlinear Eq. (5.12) by assuming that the particle diameter, $a = 2R$, is significantly smaller than the propagating wavelength L so that $\epsilon \equiv a/L << 1$, similar to Nesterenko

(2001), Kunin (1975),

$$\begin{aligned} u_{tt} &= -c_n^2 \left[(-u_x)^n + \frac{na^2}{24} \left((n-1)(-u_x)^{n-2} u_{xx}^2 - 2(-u_x)^{n-1} u_{xxx} \right) \right]_x \\ &+ pa^2 u_{txx} \end{aligned} \tag{5.13}$$

where $c_n^2 = A_n a^{n+1}$. Terms of the order $O(\epsilon^6)$ and higher are omitted in the expansions of Eq. (5.12) as well as the convective derivatives, which is valid for a certain range of wave amplitudes Nesterenko (2001). It should be noted that the expression for the long-wave sound speed c_0 can be obtained based on the linearization of Eq. (5.13), $c_0 = c_n \sqrt{n} \xi_0^{(n-1)/2}$, where ξ_0 is the initial strain due to static compression. In the case of linear media, $n = 1$, Eq. (5.13) is reduced to the well known Boussinesque equation with a linear dispersive and dissipation term. Stationary solutions of Eq. (5.13) without the viscous term have been discussed inNesterenko (2001) and investigated numerically for various values of n [Chatterjee (1999), Hinch and Saint-Jean (1999), Hascoët and Herrmann (2000), Manciu et al. (2001), Arancibia-Bulnes and Ruiz-Suárez (2002), Rosas and Lindenberg (2004)].

Here, the stationary shock solutions of Eq. (5.13) $u(x,t) = u(x - V_{sh}t)$, where V_{sh} is the shock wave velocity will be analyzed. This solution satisfies the following, Eq. (5.14), where the strain is defined as $\xi(x) \equiv -u_x$,

$$\begin{aligned} \frac{V_{sh}^2}{c_n^2} \xi_x &= \left[\xi^n + \frac{na^2}{24} \left((n-1) \xi^{n-2} \xi_x^2 + 2 \xi^{n-1} \xi_{xx} \right) \right]_x \\ &- \frac{pa^2 V_{sh}}{c_n^2} \xi_{xx}. \end{aligned} \tag{5.14}$$

The variable replacement $z = \xi^{(n+1)/2}$ is used to simplify Eq. (5.14), which can be integrated from x to ∞ with the boundary conditions $z(+\infty) = z_0$, $z_x(x = +\infty) =$

$z_{xx}(x=+\infty)=0$,

$$\begin{aligned}\frac{V_{sh}^2}{c_n^2}z^{2/(n+1)} &= z^{2n/(n+1)} \\ &+ \frac{a^2 n}{6(n+1)}z^{(n-1)/(n+1)}z_{xx} \\ &- \frac{2pa^2V_{sh}}{c_n^2(n+1)}\frac{z_x}{z^{(n-1)/(n+1)}}+C_1. \end{aligned} \tag{5.15}$$

Equation (5.15) is simplified further using the variable replacements $z=(V_{sh}/c_n)^{(n+1)/(n-1)}\,y$ and $x=a\eta\sqrt{n/6(n+1)}$,

$$\begin{aligned} y_{\eta\eta} &- \bar{p}y^{-2(n-1)/(n+1)}y_\eta + y - y^{-(n-3)/(n+1)} \\ &+ y^{-(n-1)/(n+1)}C_2 = 0, \end{aligned} \tag{5.16}$$

where $\bar{p}$ represents the dimensionless viscosity:

$$\bar{p} \equiv \frac{2ap}{V_{sh}}\sqrt{6/n(n+1)}. \tag{5.17}$$

Eq. (5.16) can be expressed as a nonlinear oscillator moving in a "potential field" $W(y)$ with a nonlinear "dissipative" term,

$$y_{\eta\eta} = -\frac{\partial W(y)}{\partial y} + \bar{p}y^{-2(n-1)/(n+1)}y_\eta, \tag{5.18}$$

where the function $W(y)$ is defined

$$W(y) = \frac{1}{2}y^2 - \frac{n+1}{4}y^{4/(n+1)} + C_3 y^{2/(n+1)}. \tag{5.19}$$

The relations between the constants C_3, C_2 and C_1 are

$$C_3 = \frac{n+1}{2}C_2 = \frac{n+1}{2}\left(\frac{c_n}{V_{sh}}\right)^{2n/(n-1)}C_1. \tag{5.20}$$

As a representative example of a real system where particles interact according to Hertz law, the potential $W(y)$ is plotted in Fig. 5.5 and five curves are

shown for different values of C_3 using $n = 3/2$. Each of the curves (1)-(4) in Fig. 5.5 has a local minimum at y_2 (indicated by arrows) and a local maximum at y_1. Stationary solitary waves are not permitted in the system represented by curve (5) where there are no local extrema (i.e. there is no potential well).

The motion of a nondissipative oscillator with a total energy equal to the local maximum of $W(y)$ at y_1 corresponds to the solitary wave solution. Nondissipative oscillations corresponding to curve (4) have an initial energy close to the local maximum of $W(y)$, which results in a relatively small range of "displacement" y. This type of behavior is related to weakly nonlinear waves, in which an initial strain is high with respect to the dynamic change in strain caused by the passing wave. Curve (1) corresponds to the strongly nonlinear case of a sonic vacuum where the initial strain is equal to zero and the ratio of the strain in the wave to the initial strain is infinite.

The effective potential energy $W(y)$ has a local extrema if C_3 is positive and smaller than some critical value (5/27 in the case of $n = 3/2$) for $n > 1$ [Nesterenko (2001)]. The local minimum and maximum values of the potential in the presence of dissipation can be interpreted as the initial and final states of the stationary shock wave. The local maximum of $W(y)$ at y_1 is related to the initial strain in front of the shock wave and the local minimum at y_2 corresponds to the final equilibrium state. Each pair of y_1 and y_2 are uniquily defined by the values of n and C_3.

It is possible to express C_3 in terms of V_{sh}, c, and ξ_0 for a solitary or shock wave solutions using the condition at the local maximum at y_1, $\partial W(y)/\partial y|_{y=y_1} = 0$,

$$C_3 = \frac{n+1}{2}\left(\frac{c_n}{V_{sh}}\right)^{2/(n-1)} \xi_0 \left[1 - \left(\frac{c_n}{V_{sh}}\right)^2 \xi_0^{n-1}\right]. \tag{5.21}$$

Weakly and strongly nonlinear regimes can be determined by the values of V_{sh} with

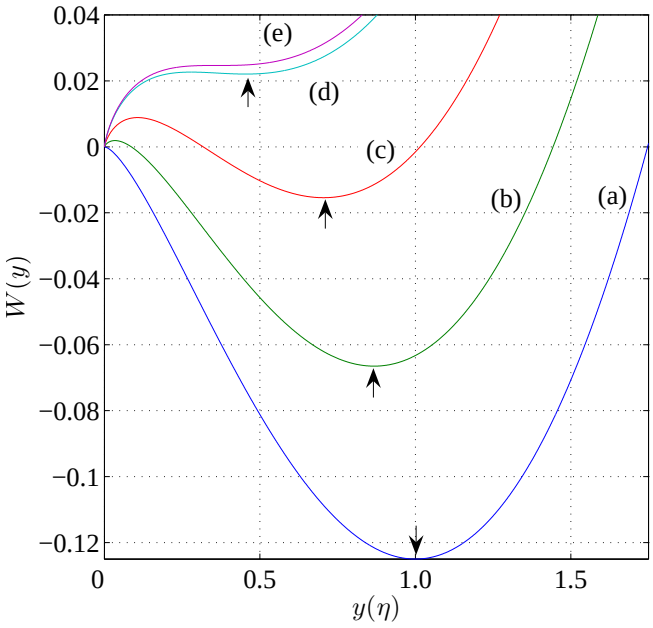

Figure 5.5: Plot of the potential $W(y)$ for the strongly nonlinear wave equation when $n = 3/2$ (Hertzian potential). Curve (1) $C_3 = 0$, curve (2) $C_3 = 5/81$, curve (3) $C_3 = 10/81$, curve (4) $C_3 = 0.18$ and curve (5) $C_3 = 5/27$ (limiting case where there is no local extrema). The local maximum of each curve correspond to the position of y_1, which is the initial state of the shock wave. The arrows indicate the minima of $W(y)$, y_2, which is the final state of the shock wave.

respect to the sound speed c_0, which also determines C_3. For example, when V_{sh} approaches c_0 then C_3 approaches $5/27$ when $n = 3/2$.

The behavior of the strain in a stationary shock profile in the vicinity of the final state of the shock wave can be analyzed by linearizing Eq. (5.16) representing y as a sum of two terms,

$$y(\eta) = y_2 + \Psi(\eta) \tag{5.22}$$

where $\Psi(\eta) \ll y_2$. It is assumed that the transition from an oscillatory to monotonic shock profile can be identified by the behavior of solutions in the vicinity of the final state represented by y_2. Substituting Eq. (5.22) into Eq. (5.16) results in the linear equation,

$$\begin{aligned} \Psi_{\eta\eta} &- \bar{p} y_2^{-2(n-1)/(n+1)} \Psi_\eta \\ &+ \frac{2}{n+1}\left(n - y_2^{-2(n-1)/(n+1)}\right)\Psi = 0. \end{aligned} \tag{5.23}$$

In the derivation of Eq. (5.23) the constant C_3 was expressed as a function of y_2 based on the equation for the derivative of the potential function being equal to zero at $y = y_2$, $\partial W(y)/\partial y|_{y=y_2} = 0$,

$$C_3 = \frac{n+1}{2}\left[y_2^{2/(n+1)} - y_2^{2n/(n+1)}\right]. \tag{5.24}$$

Equation (5.23) is an equation for a linear oscillator with dissipation. It has the solution

$$\Psi(\eta) = b_1 \exp\left[\left(\frac{\bar{p}}{2} y_2^{-2(n-1)/(n+1)} \pm g(y_2)\right)\eta\right] \tag{5.25}$$

where b_1 is a constant and

$$g(y_2) \equiv \frac{1}{2}\left[\bar{p}^2 y_2^{-4(n-1)/(n+1)} - \frac{8}{n+1}\left(n - y_2^{-2(n-1)/(n+1)}\right)\right]^{1/2}. \tag{5.26}$$

Imaginary values of $g(y_2)$ correspond to an oscillatory profile and the transition from an oscillatory to a monotonic shock profile occurs when $g(y_2) = 0$. Thus, the critical

damping coefficient can be derived from Eq. (5.26). It depends on properties of the potential function, including the power law exponent n, and position of the local minimum y_2

$$\bar{p}_c = \sqrt{\frac{8}{n+1}\left(n y_2^{4(n-1)/(n+1)} - y_2^{2(n-1)/(n+1)}\right)}. \tag{5.27}$$

In the case of a sonic vacuum, the local minimum is at $y_2 = 1$ (Fig. 1 curve (1)), which corresponds to $C_2 = 0$ in Eq. (5.16). Using $y_2 = 1$ in Eq. (5.27) gives the expression for the dimensionless critical viscosity corresponding to the transition from and oscillatory to a monotonic shock profile in a sonic vacuum for arbitrary n,

$$\bar{p}_{c,sv} = \sqrt{8(n-1)/(n+1)}. \tag{5.28}$$

Combining Eq. (5.28) with Eq. (5.17) results in a dimensional form of the critical viscosity:

$$p_c = \frac{V_{sh}}{a}\sqrt{n(n-1)/3}. \tag{5.29}$$

This critical viscosity depends on the amplitude of the shock wave through its speed V_{sh}, which is related to the final particle velocity or the strain behind the shock. The critical viscosity can be close to zero for very small amplitudes of the shock in a sonic vacuum since V_{sh} is not restricted by the sound speed.

It is interesting to investigate the validity Eq. (5.28), derived using Eq. (5.23) in the vicinity of y_2 in the entire y domain of the fully nonlinear equation Eq. (5.16). Figure 5.6 shows the different types of shock wave propagating in a sonic vacuum for different values of $\bar{p}$ by solving Eq. (5.16) using Matlab. The critical value $\bar{p}_{c,sv} = 1.265$ was obtained from Eq. (5.28) using $y_2 = 1$ and $n = 3/2$ corresponding to a Hertzian interaction. The value of $y = 0$ at point $\eta = 0$ corresponds to the y_1, the local maximum of $W(y)$ for curve (1) in Fig. 5.5. In the numerical solution to

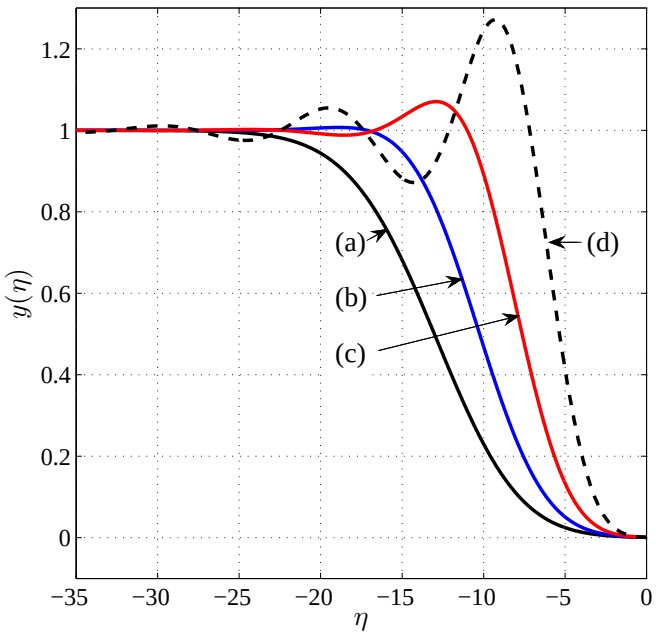

Figure 5.6: Oscillatory and monotonic shock waves in a "sonic-vacuum" ($C_3 = 0$). Each curve is a plof of the numerical solution of Eq. (5.16) for $n = 3/2$ (Hertzian potential) and $\bar{p}_c = 1.265$. The curves (1)-(4) in the figure show the solution at different values of $\bar{p}$: (1) $\bar{p} = \bar{p}_c$ (2) $\bar{p} = 0.75\bar{p}_c$ (3) $\bar{p} = 0.5\bar{p}_c$ (4) $\bar{p} = 0.25\bar{p}_c$.

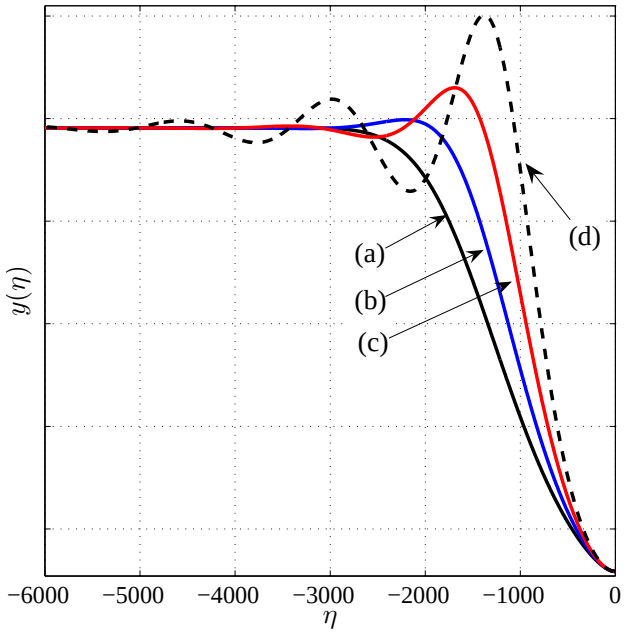

Figure 5.7: Oscillatory and monotonic shock waves in a weakly nonlinear lattice ($C_3 = 49999/270000$). In this plot of the numerical solution of Eq. (5.16) the calculated $\bar{p}_c$ value is 0.074 and curves (1)-(4) in the figure show the solution at different values of $\bar{p}$. Curve (1) corresponds to $\bar{p} = \bar{p}_{c,sv}$ curve (2) to $\bar{p} = 0.75\bar{p}_{c,sv}$ curve (3) to $\bar{p} = 0.5\bar{p}_{c,sv}$ curve (4) to $\bar{p} = 0.25\bar{p}_{c,sv}$.

Eq. (5.16), in the strongly nonlinear regime, an initial displacement of $\Delta y = 0.001$ was given to y to start motion from the point corresponding to $y_1 = 0$ (Δy is equal to 0.1% of the final y_2 value). The shock profile corresponding to the critical viscosity $\bar{p} = \bar{p}_{c,sv}$ is shown in curve (1) in Fig. 5.6. It is apparent that the value of $\bar{p}_{c,sv}$ adequately describes the transition from oscillatory to monotonic profile shown in curves (4)-(1) in Fig. 5.6.

It is clear that even though the expression for $\bar{p}_{c,sv}$ is derived in the vicinity of the final state of the shock wave, Eq. (5.28) expresses the global transition from oscillatory to monotonic shock profiles in the strongly nonlinear regime corresponding to a sonic vacuum quite well.

Remarkably, the reduction of the viscosity resulting in the transition from a monotonic to an oscillatory shock front does not dramatically reduce the shock onset-width (5.6). The term *shock onset width* is used here to describe the distance, in η, from the initial state to the maximum of the first peak of the shock-front. This can be partially explained because the shock onset-width is limited by the half-width of the solitary wave solution in a nondissipative system as $\bar{p} \to 0$. The equation for the width of a strongly nonlinear solitary wave in a sonic vacuum for particles interacting according to a general power law is [Nesterenko (2001)],

$$L_s = \pi a/(n-1)\sqrt{n(n+1)/6}, \tag{5.30}$$

where a is the particle diameter. The width of a strongly nonlinear solitary wave can be expressed in terms of η for comparison with the shock onset-width seen in Fig. 5.6. Dividing this expression by two gives the non-dimensional limit of shock onset-width corresponding to a very low viscosity,

$$\bar{L}_{s,1/2} = \pi/2(n+1)/(n-1), \tag{5.31}$$

Substituting $n = 3/2$ into this expression results in an onset-width of $\bar{L}_{s,1/2} = 7.8$, which is very close to the width shown in curve (4) in Fig. 5.6 for a relatively small dissipation value $\bar{p} = 0.25\bar{p}_{c,sv}$.

It is important to note that the width of the shock front is the distance from the initial state, y_1, to the steady final state, y_2, which is significantly larger than the onset-width for the oscillatory shock profile. The width of the monotonic shock wave corresponding to $\bar{p}_{c,sv}$ is approximately $7a$, which is about 3 times greater than the solitary wave half-width in a non-dissipative strongly nonlinear sonic vacuum type system (see curve (1) in Fig. 5.6). In an over-damped system, where $\bar{p} > \bar{p}_{c,sv}$ the width of the shock front and onset-width are identical and increase with increasing viscosity. For an underdamped system, where $\bar{p} < \bar{p}_{c,sv}$, the shock front width is again longer than in the critically damped case due to the oscillatory tail. For example, compare curve (4) in Fig. 5.6, where $\bar{p} = 0.25\bar{p}_{c,sv}$ to curve (1) in Fig. 5.6, $\bar{p} = \bar{p}_{c,sv}$.

It is interesting that a long shock front width that is significantly larger than distance between particle centers exists in two distinct cases corresponding to qualitatively different paths to the final state. In the case of weak dissipation the final state is attained through multiple, slightly damped, oscillations. In the case of a relatively strong dissipation, where $p > p_c$, the final state is attained very slowly without oscillations. As a result the shock front width is minimal in a critically damped system at $p = p_c$.

5.2.3 Discussion of Weakly Nonlinear Shock Waves with Damping

The critical viscosity given by Eq. (5.27) corresponds to the transition from an oscillatory to a monotonic shock profile in the general case including both strongly and weakly nonlinear regimes. It is interesting to compare this prediction

of the critical viscosity in a weakly nonlinear case with the behavior of solution of Eq. (5.16). Oscillatory and monotonic profiles of y corresponding to Eq. (5.27) in the weakly nonlinear potential $W(y)$ (for values of C_3 close to 5/27) were obtained using Matlab and are shown in Fig. 5.7. In the numerical solution of Eq. (5.27), a value of $C_3 = 49999/270000$ was used, which is slightly smaller than critical value $C_3 = 5/27$. For this value of C_3, the initial and final state in the shock wave are $y_1 = 0.3605474$ and $y_2 = 0.3652323$. An initial displacement of 0.1% of the difference between the starting and final y values ($\Delta y = 4.710^{-6}$) was given to y to start the motion from y_1.

In a strongly precompressed system the behavior of the solution in the vicinity of y_2 is expected to closely match the global behavior of the solution because the change of strain in the wave is small compared to the initial strain of the system. The decrease of viscosity from the critical value $\bar{p}_{c,sv}$ (calculated using Eq. (5.26) to the smaller values $0.75\bar{p}_{c,sv}$, $0.5\bar{p}_{c,sv}$ and $0.25\bar{p}_{c,sv}$ corresponds to the transition from the monotonic profile shown in curve (1) in Fig. 5.7 to the oscillatory shock profiles in curves (2), (3) and (4) in the weakly noninear regime.

The equation for the critical viscosity in a dissipative system that behaves according to the weakly nonlinear KdV equation (which is partial case of Eq. (5.13)) is derived in Karpman (1975), which is valid for shocks in plasmas and fluids. The general equation for the critical viscosity Eq. (5.27) can be related to the known result of the partial weakly nonlinear case using $n = 3/2$ for the Hertzian potential between particles for future comparison with experiments. Also, the KdV equation with dissipation can be easily obtained from Eq. (5.13) to apply results of Karpman (1975) directly.

Relating the strongly nonlinear theory to the weakly nonlinear theory asymptotically is important to assure that the more general strongly nonlinear theory is

consistent (i.e. contains the latter as a special case). Equation (5.13) is the long wave approximation of the one-dimensional system including dissipation and may be related to the KdV equation by adding an additional parameter for expansion. It is assumed that the weakly nonlinear system is initially compressed in initial strain ξ_0 and that any traveling wave in the system will be a small perturbation: $\xi = \xi_0 + \bar{\xi}$, where $\bar{\xi}/\xi_0 \ll 1$. This ratio is the second small parameter needed to derive the weakly nonlinear equation in addition to $R/L \ll 1$ required for the long wave approximation, where L is the characteristic wavelength. Differentiating Eq. (5.13) with respect to x and denoting $\xi = -u_x$ results in a second order partial differential equation in terms of the strain,

$$\xi_{tt} - pa^2\xi_{txx} - c_n^2\left\{\xi^n + \frac{na^2}{24}\left[(n-1)\,\xi^{n-1}\xi_x^2 + 2\xi^{n-1}\xi_{xx}\right]\right\}_{xx}. \tag{5.32}$$

In the following equations the overbar will be omitted for ξ. Including the expansion $\xi = \xi_0 + \bar{\xi}$ in Eq. (5.32) gives the following equation:

$$\begin{aligned} \xi_{tt} \;&-\; c_n^2\left[n(n-1)\xi_0^{n-2}\left(\xi_x^2 + \xi\xi_{xx}\right) + n\xi_0^{n-1}\xi_{xx} + \frac{na^2}{12}\xi_0^{n-1}\xi_{xxxx}\right] \\ &-\; pa^2\xi_{txx} = 0. \end{aligned} \tag{5.33}$$

This equation can be simplified similar to Nesterenko (2001) without the restrictions on the value of n

$$\xi_{tt} - \frac{\hat{p}_w}{2}\xi_{txx} - c_0^2\xi_{xx} - 2c_0\gamma\xi_{xxxx} - \sigma\left(\xi_x^2 + \xi\xi_{xx}\right), \tag{5.34}$$

where $\hat{p}_w = a^2p$, $c_n^2 = Aa^{n+1}$, $c_0^2 = nAa^2\delta_0^{n-1} = nc_n^2\xi_0^{n-1}$, $\delta_0 = a\xi_0$, $\sigma = (n-1)ac_0^2/\delta_0$ and $\gamma = a^2c_0/24$. Terms of the order $O(u^2/L^6)$ were omitted in the expansion (where $\xi \sim u/L$). It is assumed that the KdV equation is contained, as an approximation, to Eq. (5.34) as a wave equation in one direction. The method described by Kunin

(1975) is used here to reduce Eq. (5.34) to the first order with yet undetermined coefficients,

$$\xi_t + B\xi_{xx} + C\xi_x + D\xi_{xxx} + E\xi\xi_x = 0. \tag{5.35}$$

Finding the coefficients requires a rather tedious comparison of Eq. (5.35) with Eq. (5.34). For example, to find B, Eq. (5.35) is multiplied by B and differentiated with respect to x twice,

$$B\xi_{txx} \sim -B^2\xi_{xxxx} - BC\xi_{xxx} + O(u/L^6) + O(u^2/L^5). \tag{5.36}$$

Similarly, to find C, Eq. (5.35) is multiplied by C then differentiated with respect to x,

$$C\xi_{tx} \sim -BC\xi_{xxx} - C^2\xi_{xx} - CD\xi_{xxxx} - CE\left(\xi_x^2 + \xi\xi_{xx}\right). \tag{5.37}$$

Continuing in this way gives

$$\begin{aligned} D\xi_{xxx} &\sim -CD\xi_{xxxx} + O(u/L^6) + O(u^2/L^5) \\ E\xi_t\xi_x &\sim -CE\xi_x^2 + O(u^2/L^5) \\ E\xi\xi_{tx} &\sim -CE\xi\xi_{xx} + O(u^2/L^5) \end{aligned} \tag{5.38}$$

Differentiating Eq. (5.35) and combining Eqs. (5.36)-(5.38) gives,

$$\xi_{tt} - \left(B^2 + 2CD\right)\xi_{xxxx} - 2BC\xi_{xxx} - 2CE\left(\xi_x^2 + \xi\xi_{xx}\right) - C^2\xi_{xx} = 0, \tag{5.39}$$

which can be compared readily to Eq. (5.34) to obtain the coefficients

$$\begin{aligned} B &= -2R^2p \\ C &= c_0 \\ D &= \gamma - \frac{2R^4p^2}{c_0} \\ E &= \frac{\sigma}{2c_0}. \end{aligned} \tag{5.40}$$

Thus, the resulting wave equation, Eq. (5.34), is approximated by the KdV equation including dissipation when written for a wave traveling in one direction,

$$\xi_t - \hat{p}_w \xi_{xx} + c_0 \xi_x + \left(\gamma + \frac{\hat{p}_w^2}{2c_0}\right) \xi_{xxx} + \frac{\sigma}{2c_0} \xi \xi_x = 0. \tag{5.41}$$

where $\hat{p}_w \equiv 2R^2 p$ is the viscosity coefficient for a system that permits weakly nonlinear waves (hence, the subscript w) and has units of dynamic viscosity.

Note Eq. (5.41) contains a second order correction to the dissipative term. This term is neglected because $p_c \to 0$ as y_2, and C_3, approach their critical values (see curves (4) and (5) in Fig 5.5). The equation of critical viscosity for this weakly nonlinear system based on [Karpman (1975)] is

$$p_{c,w} = \frac{c_0}{\sqrt{6}R} \sqrt{\frac{V_{sh}}{c_0} - 1}. \tag{5.42}$$

Equation (5.42) can also be obtained as the limit of the critical viscosity in the general strongly nonlinear case given by Eq. (5.27) as $V_{sh} \to c_0$. For a Hertzian interaction, $n = 3/2$ is placed into Eq. (5.27) along with the definition of $\bar{p}$ from Eq. (5.17),

$$p_c = \frac{V_{sh}}{2\sqrt{2}R} \sqrt{\frac{3}{2} y_2^{4/5} - y_2^{2/5}}. \tag{5.43}$$

To write this equation in terms of the speed of the shock wave V_{sh} and initial sound speed c_0 the relation between y_2 and y_1 are used [Coste et al. (1997)]

$$y_2 = \left[\frac{1}{2}\left(1 - y_1^{2/5} + \sqrt{\left(1 - y_1^{2/5}\right)\left(1 + 3y_1^{2/5}\right)}\right)\right]^{5/2}. \tag{5.44}$$

Using the expression for c_0

$$c_0^2 = 3/2 \xi_0^{1/2} c^2. \tag{5.45}$$

and for y_1 in terms of c_0 and V_{sh},

$$y_1 = (2/3)^{5/2} \Lambda^5 \tag{5.46}$$

where $\Lambda = (c_0/V_{sh})$ is used for brevity. Using the expressions for c_0 and y_1 and substituting Eqs. (5.44)-(5.46) into Eq. (5.43) obtain

$$p_c = \frac{c_0}{4\sqrt{2}R}\left[\frac{4}{3} - \frac{4}{3}\Lambda^2 + \Lambda^{-2} + \left(1 - 2\Lambda^2\right)\sqrt{\Lambda^{-4} + \frac{4}{3}\Lambda^{-2} - \frac{4}{3}}\right]^{1/2}. \tag{5.47}$$

For weakly nonlinear system, $V_{sh} = c_0 + \Delta$ ($\Delta/c_0 \ll 1$), and this small parameter can be used to expand Eq. (5.47. This expansion results in the critical viscosity in the weakly nonlinear system,

$$p_c = \sqrt{\frac{\Delta c_0}{6R^2}}. \tag{5.48}$$

Eq. (5.42) is recovered from Eq. (5.48) with the replacement $\Delta = V_{sh} - c_0$. Thus, Eq. (5.27) describing the transition from oscillatory to monotonic shock profiles in a general nonlinear case is consistent with the known equation for the critical viscosity in a weakly nonlinear system.

5.2.4 Numerical Investigation of the Critical Viscosity in a Discrete System

The numerical analyses of a discrete particle lattice are presented here for comparison with the results based on the long-wave approximation leading to the value of critical viscosity, Eq. (5.27). There are a few key qualitative differences between applied analytical approach in the frame of the long wave approximation and the numerical calculations of discrete particle lattice. First, the analytical approach assumes a stationary profile with a constant shock wave speed but does not account for the transient development of the wave into its steady state. Additionally, the absence of a restoring force in the discrete system distinguishes it from the continuum approach in complex ways even in the absence of dissipation [Nesterenko et al.

(2005)]. Also, it is important to compare the critical viscosity value derived from the long wave approximation to a value characteristic for shock waves in discrete chains because the width of a weakly dissipated shock is comparable to the size of the particles; especially for large values of n. These features may result in significantly disparate behaviors of the shock wave solutions of the long wave approximation and the discrete lattice.

The numerical analyses will test how well Eq. (5.27) and (5.28) predict the transition from an oscillatory to a monotonic shock profile in a discrete system even though the expressions for p_c rely on the behavior of solution in the vicinity of the final state of the shock wave. This numerical investigation will focus on a sonic vacuum type system since the solution based on the long wave approximation is expected to be a better fit to the behavior of a discrete system in the weakly nonlinear regime.

A shock wave is created in the numerical simulation by prescribing a constant velocity v_0 to the first particle of an initially quiescent lattice at $t = 0$. The discrete displacement solution is used to find the strains for comparison with the long-wave approximation. The equation for the strain ξ in a discrete lattice taken between particles i and $i + 1$ is defined as

$$\xi = (u_i - u_{i+1})/2R. \tag{5.49}$$

To compare numerical results for developing and stationary shock waves in a discrete lattice with the stationary solution in the long wave approximation the particle velocity in the final state in the shock wave is assumed to be equal to the velocity of the first particle in the numerical calculations. It should be mentioned that final state of the shock wave in a sonic vacuum in the long wave approximation corresponds to the value of $y = 1$ (see Fig. 5.5) resulting in the following relations between shock

speed V_{sh}, particle velocity v_0 and strain ξ_{sh} in the final state:

$$V_{sh} = c_n^{2/(n+1)} v_0^{(n-1)/(n+1)} = c_n \xi_{sh}^{(n-1)/2}. \tag{5.50}$$

The plots of the numerical calculations and the curves obtained in the long wave approximation are presented in non-dimensional coordinates y and η;

$$\begin{aligned} y &= (c_n/v_0)\xi^{(n+1)/2}, \\ \eta &= -\frac{c_n^{2/(n+1)} v_0^{(n-1)/(n+1)} t}{2R} \sqrt{6(n+1)/n}. \end{aligned} \tag{5.51}$$

Equations (5.49)-(5.51) are used to plot the numerical data in Figs. 5.8-5.10. We compare the numerical solution for oscillatory and monotonic shock waves in a discrete lattice with the long wave approximation in case when $n = 3/2$ for spheres interacting with a Hertzian potential. The data in Table 5.1 were selected to resemble a real system similar to those found in previous experimental work [Daraio et al. (2006),Herbold et al. (2006),Nesterenko et al. (2005)] for the purpose of future comparison with experiments. The expression for A in Eq. (5.12) assumes a homogeneous particle mass and radius throughout the lattice: $A = E\,(2R)^{1/2} \,/\, (3m\,(1-\nu^2))$, where $m = 4/3\pi R^3 \rho_0$. The values of p in the numerical simulation of discrete lattice were $p = 0.1p_c$ and $p = p_c$, the values of p_c were calculated from the combination of Eq. (5.29) and Eq. (5.50) and the parameters from Table 5.1.

Fig. 5.8 depicts the early development of an oscillatory shock wave in a discrete lattice of 1000 particles when $p = 0.1p_c$ at $t \cong 100\mu s$. Fig. 5.8(b) are the discrete $y_{i+1/2,j}$ values of the first sixteen particle contacts at four different time-steps for a short duration (about $5\mu s$). The discrete y values are plotted at four different time-steps to comprise a wave profile for comparison with the long-wave approximation, Fig. 5.8(a). Note the underdevelopment of the oscillations behind

Table 5.1: Parameters Used in Numerical Analysis

	Symbol	Units	Value
Young's Modulus	E	[GPa]	193
Poisson's Ratio	ν		0.3
Density	ρ	$[kg/m^3]$	8000
Particle Radius	R	$[m]$	$2.38\ 10^{-3}$
Mass	m	[kg]	$4.52\ 10^{-4}$
Critical Viscosity	${\mu_c}^1$	$[Ns/m]$	32.15
Number of Particles	N		1000
Initial Velocity	v_0	$[m/s]$	0.5
Time Step	δt	$[\mu s]$	0.875

the first peak and the lag of the shock-front. A phase shift is also noticeable in Fig. 5.8(b), but the stationary profile must be investigated to see if this is a transient artifact of the nonstationary state. Contrasting the slower speed of the shock front and the phase shift, the amplitude of the leading pulse and qualitative structure of the shock wave matches well with the long-wave approximation.

The early development of a monotonic shock profile is shown in Fig. 5.9 using $p = p_c$. The curve in Fig. 5.6(a) is used again in Fig. 5.9(a) for comparison. The first nine $y_{i+1/2,j}$ values are shown at $t \cong 37\mu s$. In the unsteady state, the profile oscillates slightly behind the shock front and the shock front width is less than its final shape. It is interesting that the qualitative shape of the unsteady shock profile closely matches the long-wave approximation. In contrast to the oscillatory profile, there is no noticeable lag of the shock front in comparison to the long-wave approximation.

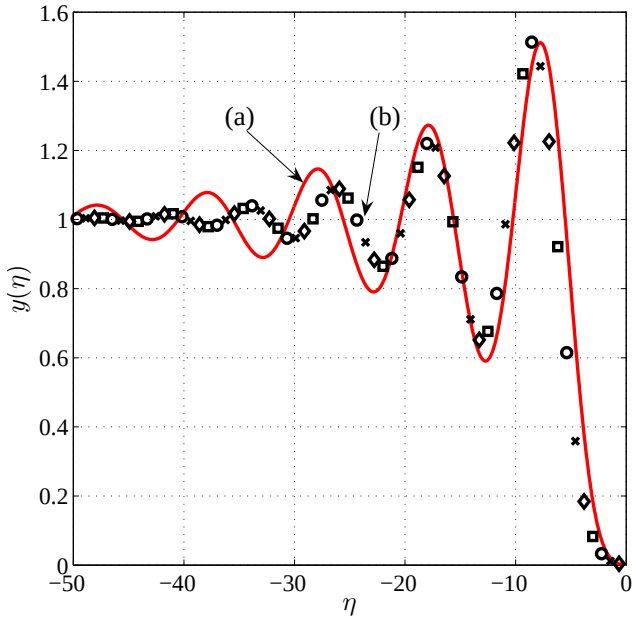

Figure 5.8: An oscillatory shock wave in a strongly nonlinear lattice close to the impacted end. Curve (1) The numerical solution of the long-wave approximation, Eq. (5.16), for $\bar{p} = 0.1\bar{p}_c$. Curve (2) The circles represent the path of y in a discrete particle lattice for the interaction of the 15^{th} and 16^{th} particle from $t = 48.13\mu s$ (far right) to $t = 102.4\mu s$ from the beginning of impact (far left) with the same value of viscosity. For convenience both curves are plotted from the moment of arrival of shock wave at given point.

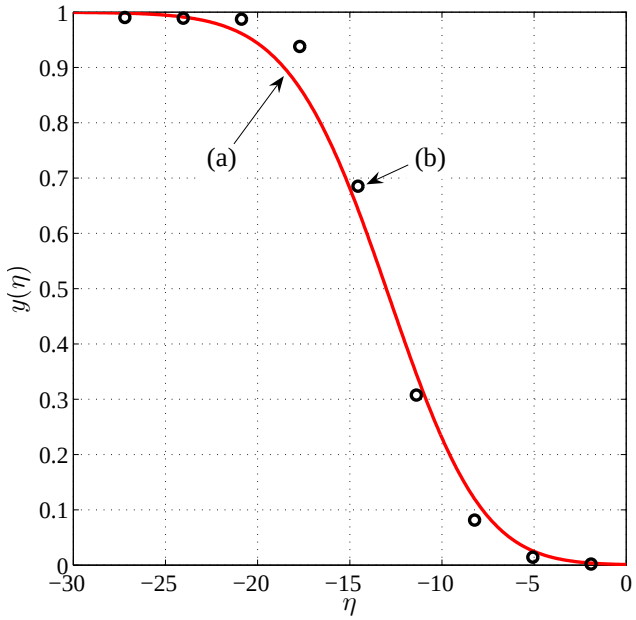

Figure 5.9: Comparison of the early development of a monotonic shock wave in a discrete strongly nonlinear lattice and stationary solution in the long wave approximation. Curve (1), the solid line is a plot of the solution of the long-wave approximation, $y(\eta)$, for $\bar{p} = \bar{p}_c$. Curve (2), the circles represent the path of y in a discrete lattice for the first interaction of the 5^{th} and 6^{th} particle from $t = 5\mu s$ to $t = 35\mu s$. For convenience both curves are plotted from the moment of arrival of shock wave at given point.

Figure 5.8 depicts the early development of an oscillatory shock wave in a discrete lattice in comparison with the results of long wave approximation using $p = 0.1p_c$. Time t is calculated starting from the moment of arrival of shock wave at given point of observation. The points comprising curve (2) in Fig. 5.8 are the discrete y values between the 15^{th} and 16^{th} particles. Note the progressive phase shift between oscillations, slightly larger amplitude of the first peak and the smaller amplitudes of the oscillations behind it in comparison to the analytical solution shown in curve (1). Despite these differences, the qualitative behavior of the oscillatory shock wave matches well with the long-wave approximation in this unsteady regime of propagation close to the impacted end of the lattice.

The early development of a monotonic shock profile at a distance close to the impacted end in a discrete lattice is shown in curve (2) in Fig. 5.9 for the critical viscosity p_c derived from the long wave approximation. Curve (1) in Fig. 5.9 represents the stationary profile of a shock wave in the long wave approximation (it is identical to curve (1) in Fig. 5.6) for comparison to the results for discrete lattice. The y values for the contact between 5^{th} and 6^{th} particles are shown from times $t = 5\mu s$ to $t = 35\mu s$ starting from the moment of impact.

In this unsteady state of shock propagation, curve (2) in Fig. 5.9 oscillates slightly as it approaches $y = 1$ behind the shock front and the shock onset width is less than that of curve (1). It is interesting that, despite this tiny oscillation, the qualitative shape of the shock profile closely resembles the steady state solution for the long-wave approximation. This shows that the critically damped shock profile in a strongly nonlinear discrete system approaches a stationary state after traveling only a few particles after formation.

The corresponding data for both oscillatory and monotonic profiles in the

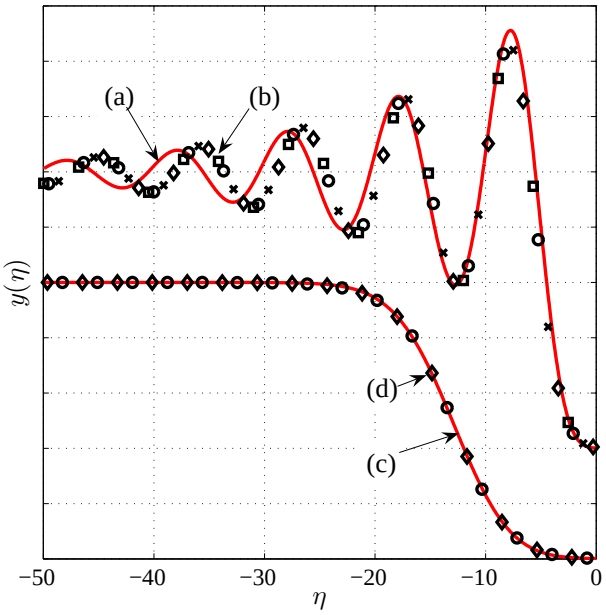

Figure 5.10: Comparison of oscillatory (a) and monotonic (b) steady shock waves in a discrete strongly nonlinear lattice and the results of the long wave approximation. Curve (1) is the stationary solution of the long wave approximation for an oscillatory shock front; curve (2) is a set of discrete points representing the parameter y related to the strain between particles: $\square$ – particle contacts 218-234 at time $t = 1638\mu s$, $\Diamond$ – particle contacts 454-468 at $t = 3278\mu s$, $\times$ – particle contacts 685-701 at t=4918μs, $\bigcirc$ – particle contacts 919-934 at $t = 6557\mu s$; curve (3) is a stationary solution of the long wave approximation for a monotonic shock front; curve (4) is set of discrete points representing the parameter y between particles for comparison with curve (3): $\Diamond$ – particle contacts 455-470 at $t = 3278\mu s$, $\bigcirc$ – particle contacts 921-937 at $t = 6557\mu s$. For convenience all curves are plotted from the moment of arrival of shock wave at given point.

long wave approximation and in the discrete lattice at a few distances from entrance are shown in Fig. 5.10. Curve (1) in Fig. 5.10(a) is identical to curve (1) in Fig. 5.8. Curve (4) in Fig. 5.10(b) closely matches the long-wave approximation curve (3) for the monotonic shock wave. It is assumed that if a profile is not changing qualitatively after traveling through a few hundred particle contacts, it is steady enough for the present discussion.

The difference in shock-front widths in curve (2) (Fig. 5.9) is indistinguishable when compared to curve (2) in Fig. 5.10(b). This means that the critical value of viscosity p_c from Eq. (5.27) captures the transition from oscillatory to monotonic wave profiles in discrete lattice very well on the stationary stages of shock wave propagation.

5.2.5 Conclusions

The long-wave approximation of a strongly nonlinear system with a power law dependence of force on displacement was extended to include viscous dissipation that depends on the relative velocities of neighboring particles. From this approach an equation for a critical viscosity describing the transition from oscillatory to monotonic shock profiles in a strongly nonlinear regime was derived. This equation naturally includes the weakly nonlinear case. Numerical calculations of the discrete system agreed well with the results of long wave approximation. It should be emphasized that the initial disturbance in a discrete chain approaches a stationary shock regime at a distance comparable to the width of the stationary shock front from the boundary particle. This is analogous to the case of a nondissipative system where the initial disturbance forms a single or a train of solitary waves after traveling a short distance that is comparable to the width of the leading pulse of a stationary

shock front. The shock onset width was defined and compared with the width of a solitary wave. The shock front width is minimized when the viscosity is equal to its critical value.

Section 1 in Chapter 5 has been published in *AIP Conference Proceedings*, **845** (1), pp. 1523-1526 by E.B. Herbold, V.F. Nesterenko, and C. Daraio. Section 2 in Chapter 5 has been published in *Physical Review E*, **75**, art. 021304, pp. 1-8 by E.B. Herbold, and V.F. Nesterenko. The dissertation author was the primary investigator and author of these papers.

6

A New Type of Strongly Nonlinear Metamaterial

It is well known that strongly nonlinear compressive solitary waves exist in granular media composed of spheres, which exhibit a Hertzian interaction at the contact point. The solitary wave solution of the long-wave approximation and in numerical calculations was discovered in Nesterenko (1983) and reproduced in various conditions and for different materials in Nesterenko (2001), Friesecke and Wattis (1994), Chatterjee (1999), Hinch and Saint-Jean (1999), Hascoët and Hermann (2000),Hascoët and Hinch (2002),Rosas and Lindenberg (2004),Sokolow et al. (2007),Lazaridi and Nesterenko (1985),Shukla et al. (1993),Zhu et al. (1997),Coste et al. (1997), Daraio et al. (2005), Daraio et al. (2006). Experiments have also shown that these waves exist in various materials under various loading conditions [Lazaridi and Nesterenko (1985),Shukla et al. (1993),Zhu et al. (1997),Coste et al. (1997), Daraio et al. (2005), Daraio et al. (2006)]. The theoretical descriptions of strongly nonlinear compressive solitary waves have focused mainly on power-law potentials between particles where the force-displacement relationship is described by $F \propto \delta^n$. Strongly nonlinear compression solitary waves were shown to exist for

arbitrary normal nonlinear interaction between elements in the long wave approximation [Nesterenko (2001)] and for a discrete chain Friesecke and Wattis (1994). An example of this type of strongly nonlinear material is a Hertzian system where the power-law exponent is $n = 3/2$. The nonlinearity in these systems is due to the changing surface area of the contact plane, which starts as an arbitrarily small circle, for infinitesimally small strains, then increases to a circle of finite dimension.

6.1 Description of Double Power-Law Materials

In this chapter, the geometrical nonlinearity begins with an arbitrarily thin circular line of contact of toroidal o-rings and metal plates that increases in thickness under compression. In a first approximation polymer/rubber o-rings can be considered massless nonlinear springs compared to the mass of rigid intermittent steel cylinders. Polymer or rubber based strongly nonlinear systems are able to absorb larger amount of impact energy in comparison with granular systems based on spherical particles. The quasi-static deformation of o-rings has been experimentally investigated in Lindley (1966a), Lindley (1966b), Freakley and Payne (1978). The empirical form of the equation relating force to displacement is a double power-law where $F \propto \left(\delta^{3/2} + \delta^{6}\right)$. The unique structure of this relationship is represented by two regimes of nonlinear behavior where the Hertzian regime determines the dynamic behavior of small perturbations ($\delta < 0.2$) and the higher order term dominates at larger deformations. The quasi-static force versus displacement relationship presented in Lindley (1966b), Freakley and Payne (1978) is used as the basis for the equations of motion in the following numerical analysis,

$$\begin{aligned} \ddot{u}_i &= A\left[(u_{i-1}-u_i)^{3/2}-(u_i-u_{i+1})^{3/2}\right] \\ &+ B\left[(u_{i-1}-u_i)^{6}-(u_i-u_{i+1})^{6}\right], \end{aligned} \tag{6.1}$$

where $\delta_{i,i+1} = (u_i - u_{i+1})/d$, u_i and u_{i+1} denote the displacement of the cylinder on either side of the o-ring, $A = 1.25\pi DE/md^{1/2}$ and $B = 50\pi DE/md^5$. The other constants in Eq. (6.1) are d, which is the cross-sectional diameter of the toroid (o-ring) and D and E, which are the outside diameter of o-ring and E is the Youngs modulus. Eq. (6.1) describes experimental data reasonably well for $\delta \leq 0.45$ [Lindley (1966a), Lindley (1966b), Freakley and Payne (1978)].

We neglect dissipation in the numerical calculations in this investigation as well as gravitational effects as they are negligible the compared to the loading force. Precompression can be introduced into Eq. (6.1) by application of an external force to the end particle in a chain of these elements [Daraio et al. (2005), Daraio et al. (2006)].

The o-rings used in these experiments have outside and cross-sectional diameters of 8 mm and 1.76 mm respectively. The aspect ratio of these diameters is D/d = 4.55, which is within the experimental range investigated in Lindley (1966a), Lindley (1966b), Freakley and Payne (1978) where data for o-rings with aspect ratios ranging from 3 to 30 are well described by Eq. (6.1).

6.2 The Dependence of Wave Profile on the Solitary Wave Amplitude

A property of single power-law materials is that the pulse shape does not depend on the amplitude of the solitary wave. The amplitude of this wave depends

on the velocity of the striker while the width of the traveling pulse remains constant. In contrast to this property, the shape and width of a solitary pulse depends on the amplitude in double power-law materials.

The dependence of shape and duration on pulse amplitude is shown in Fig. 6.2. The pulses were created by an impact of a single particle with a mass equal to the mass of the cylinder in the chain and with different initial velocities resulting in a single solitary wave. A chain of 40 elements was numerically constructed using the properties of PTFE o-rings (with $E = 1.46$ GPa [Daraio et al. (2006), Carter and Marsh (1995)], $D = 8$ mm and $d = 1.76$ mm) between stainless steel cylinders with a mass of 3.276 g. The diameter and height, h, of the cylinders are 10 mm and 5 mm respectively. The pulse was created by a stainless steel sphere with a diameter of 4.76 mm and a mass of 0.456g. In each of the five curves in Fig. 6.1 a single pulse was generated and half the resulting symmetric single solitary wave is shown between the 20^{th} and 21^{st} elements by plotting the normalized force (where F_{max} is the maximum force in the wave) with non-dimensional time. The value of V_s shown on the abscissa of Fig. 6.1 was calculated from the results of the numerical calculations by dividing the distance between the 15^{th} and 20^{th} elements $5(h + d)$ by the time between the maximum strains in the wave. The dotted lines in Fig. 6.1 show the shape of the pulse using only the Hertzian interaction in curve 1 and the result for second term in Eq. (6.1) with $n = 6$ in curve 5. Curve 2 is created with a relatively large velocity $v_0 = 300$ m/s but the shape and duration of the pulse closely match that of curve 1. In curves 3 and 4 the pulse is more compact than curve 1 and the duration of the pulse is about 3 elements.

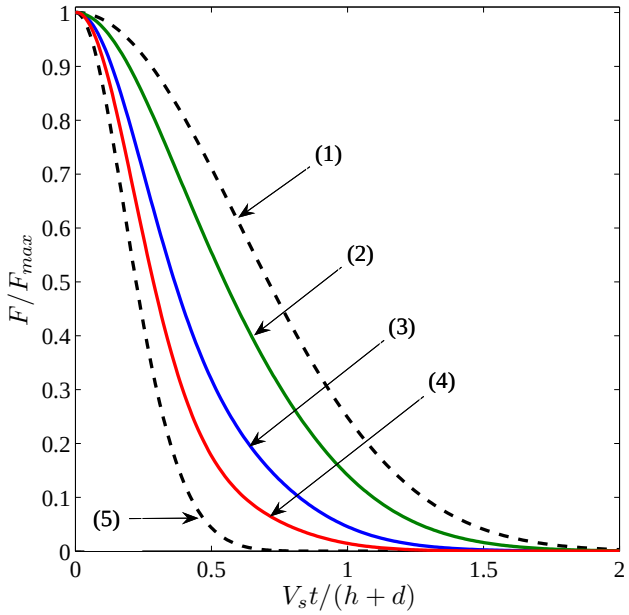

Figure 6.1: Plot of normalized force vs. dimensionless time in a chain of 40 elements. The half-curves are the forces between the 20^{th} and 21^{st} particles for six different calculations. Curve 1: Force for a system impacted by a striker with a velocity $v_0 = 1$ m/s using only the Hertz law ($n = 3/2$) term. Curve 2: System using both power-law terms with $v_0 = 300$ m/s. Curve 3: System using both power-law terms $v_0 = 500$ m/s. Curve 4: System using both power-law terms with $v_0 = 800$ m/s. Curve 5: System using only the higher order power-law relationship ($n = 6$) and $v_0 = 1$m/s.

6.2.1 Strong Dependence of Wave Speed on its Amplitude

It is clear that the shape of double power-law pulses depends on the amplitude and this elucidates an important characteristic of these waves. In single power-law materials the pulse speed is related to the initial and maximum strain (or maximum particle velocity) by a single power-law relationship in the long-wave approximation [Nesterenko (2001)]. Recent experimental and numerical investigations show that the pulse speed can be effectively tuned by initially compressing a Hertzian chain of particles [Daraio et al. (2005), Daraio et al. (2006)].

In a precompressed double power-law system an additive combination of two parts is used to calculate the sound speed c_0,

$$c_0^2 = a^2 \left[\frac{3}{2} A \left(a\xi_0 \right)^{1/2} + 6B \left(a\xi_0 \right)^5 \right], \tag{6.2}$$

where $a = d + h$ and h is the height of the cylinder. It is evident from Eq. (6.2) that the term with an exponent of 5 (corresponding to the $n = 6$ term) allows the sound speed to be tuned, with precompression, to a larger degree. For example, for small initial strains, the long-wave sound speed is changing with exponent 1/4 and at larger precompression it follows exponent 5/2.

The change of exponent (from 1/4 to 1/6) characterizing the dependence of speed of small amplitude signals (sound waves) on initial confinement pressure P was reported for randomized three-dimensional granular packings [Jia et al. (1999)]. Double power-law materials are qualitatively different because the change of the exponent is due to contact interaction alone and not to the change of the coordination number with preload in the latter case. Also, there is an increasing dependence of sound speed on preload in double power-law materials in contrast to the decreasing rate seen in granular packings.

Figure 6.2 shows the dependence of pulse speed on the maximum strain in

the wave. It should be noted that the pulse speed converges to a single power-law relationship in the low and high regions of strain and that there is an intermediate region where the pulse speed is transitional. Each of the curves in Fig. 6.2 are the result of 26 calculations using 50 elements (cylinders and PTFE o-rings) and a 5 mm diameter spherical stainless steel particle for various striker impact velocities. Each of the simulations estimated the pulse speed and maximum strain in the pulse between the 25^{th} and 30^{th} particle. Curve 1 shows the pulse speed, V_s, dependence on maximum strain, ξ_{max}, for the double power-law materials. Curves 2 and 3 are the result of running the calculations using a single power law with $n = 6$ and to $n = 3/2$. Also, curves 2 and 3 have the power law dependence identical to a long wave approximation with slight difference in the constant before exponent. The agreement is better for $n = 3/2$ than for $n = 6$ due to a smaller width of the solitary wave, similar to observed in [Rosas and Lindenberg (2004)]. Note that curve 1 diverges from curve 3 into an intermediate region before it converges to curve 2. This suggests that additive use of the equations for V_s in Nesterenko (1983), Nesterenko (2001) for double power law material cannot be used to construct curve 1 as a combination of two parts in contrast that sound speed at some initial precompression.

It is evident that the power law exponent $n = 6$ represents a qualitatively different case in comparison with Hertzian law (where $n = 3/2$) with respect to much stronger tunability of sound speed due to precompresion and dependence of solitary wave speed on amplitude. This will also facilitate the splitting of initial pulse into train of solitary waves already very fast in Hertzian systems [Nesterenko (2001)].

In double power-law materials there is a dramatically greater capability to tune pulse speeds due to the fact that pulses behave according to the higher order power-law in an experimentally attainable range using polymer and soft rubber o-

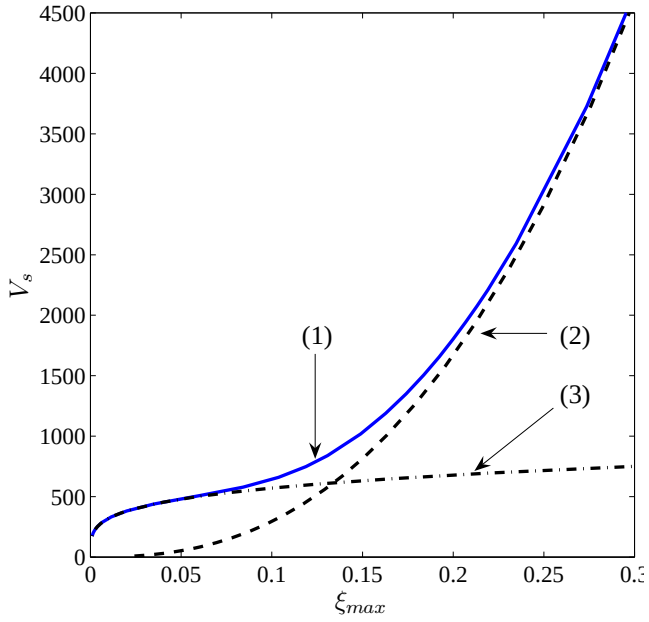

Figure 6.2: This plot contains three separate sets of calculations that show the dependence of pulse speed on the maximum strain in the pulse. Curve 1 is the result of 26 calculations using 50 elements and a 5 mm diameter spherical stainless steel particle. Each of the simulations used estimated the pulse speed and maximum strain in the pulse between the 25^{th} and 30^{th} particle. Curves 2 and 3 plot similar results to curve 1 except that only the higher (curve 2) and lower order Hertzian (curve 3) power law is used.

rings. It will also allow greater tunability of band gaps in two mass chains.

It is natural to expect that a larger exponent in a single power law exponent will facilitate the splitting of an initial impulse into a train of solitary waves due to shorter duration of solitary wave at larger exponents. This is a fundamental characteristic of strongly nonlinear systems and their tendency to partition energy into waves whose width depends only on the value of the power-law exponent. For example, the width of a solitary wave in an arbitrary single power-law material is,

$$L_n = \frac{\pi a}{n-1}\sqrt{\frac{n\,(n+1)}{6}} \tag{6.3}$$

where a is the diameter of spherical particles (or center to center distance between cylinders) and n is the value of the exponent. For Hertzian systems ($n = 3/2$) the width of the wave is approximately 5 particles. For a value of $n = 6$ the width of the wave less than 2 particles. The duration of an impact and the value of the exponent determine the number of waves created. In the case of a double-power law material the magnitude, duration and both power-law exponents determine the number of pulses created, the pulse shape and strongly nonlinear regime in which they travel.

Two numerical calculations were conducted to show how an initial impulse splits into a train of solitary waves in single power-law Hertzian chains and double power-law chains. A column of 400 elements (stainless steel cylinders and PTFE o-rings) was impacted by a striker with a mass five times greater than the elements in the chain. In Fig. 6.3(a) the strain of the resulting wavetrain is shown for the case using the double power law and Fig. 6.3(b) shows the case of a Hertzian wavetrain. It is clear that the enveloping shape of the two wave trains shown in Fig. 6.3(a) and 6.3(b) are quite different in shape. In Fig. 6.3(a) the amplitude of the pulses decreases gradually in contrast to the Hertzian system.

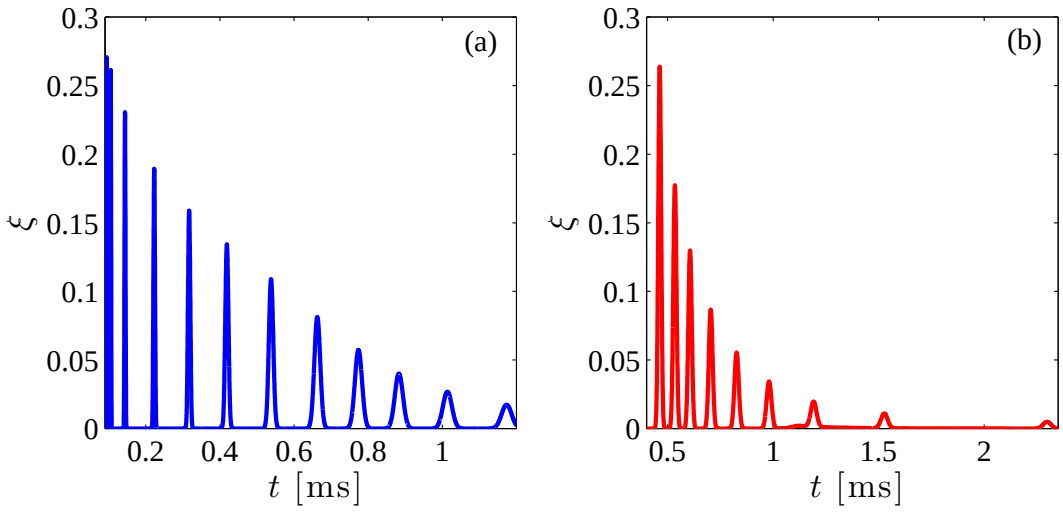

Figure 6.3: A train of solitary waves was created in a chain of 400 elements. The strain is plotted as a function of time for a (a) double power law system and a (b) Hertzian ($n = 3/2$) system.

In Table 6.1 the maximum strains and the wave speeds are given for the first nine pulses in double power-law materials and Hertzian systems for comparison. The train of solitary waves in Hertzian systems shows that pulse speed depends on the maximum strain in each wave corresponding to curve 3 in Fig. 6.2. In the system using both power laws the velocity and maximum strain of the waves (given in Table 6.1) correspond to points on curve 1 in Fig. 6.2. The last wave in the train is completely in the Hertzian regime based on these values.

6.3 Experimental Results

Experiments were performed for comparison with numerical data using 35 stainless steel cylinders ($h = 5$ mm and a diameter of 10 mm) and 34 PTFE o-rings ($d = 1.76$ mm, $D = 8$mm and $E = 1.46$ GPa and mass $m = 0.103$ g). The set up for the experiments is shown in Fig. 6.4. The column of cylinders and o-rings are placed in a hollow PTFE cylinder and two gauges composed of cylinders with imbedded piezo sensors are placed within the column (see Fig. 6.4(a)). Two sensors were constructed by using an epoxy to secure a piezo gauge between two halves of a cut cylinder to create a sensor with similar mass and height to the other cylinders in the column (see Fig. 6.4 (b)). It was determined that placing the sensors in the 3^{rd} and 8^{th} cylinder position from the top of the chain resulted in the best data. The positions of the sensors are the same for each experiment presented here and the numerical calculations also reflect this placement.

A single pulse was observed in experiments by impacting the top of the assembly shown in Fig. 6.4 (a) with a stainless steel sphere whose radius and mass were 2.38 mm and 0.455 g respectively. The initial velocity of the impacting sphere

Table 6.1: A train of solitary waves was created in a column of 400 elements in a numerical calculation (corresponding to Fig. 6.3(a) and 6.3(b)). The pulse speed and maximum strain in the first nine pulses were calculated to find if a train of solitary waves could be present in different nonlinear regimes. The second and third column shows that the train of pulses spans two separate regions; namely the transitional and higher order regimes when both power laws are used. The last two columns show that a single power law, using only the Hertzian, result in a train of solitary waves following curve 3 in Fig. 6.2.

Pulse	Double Power Law		Hertzian Law	
Number	ξ_{max}	V_s [m/s]	ξ_{max}	V_s [m/s]
1	0.2707	2596	0.2638	726.8
2	0.2612	3380	0.1775	656.3
3	0.2306	2485	0.1298	609.0
4	0.1894	1610	0.0867	554.1
5	0.1588	1134	0.0554	493.4
6	0.1343	871.1	0.0344	436.1
7	0.1090	689.8	0.0197	400.0
8	0.0814	569.0	0.0110	334.7
9	0.0573	501.5	0.0050	271.5

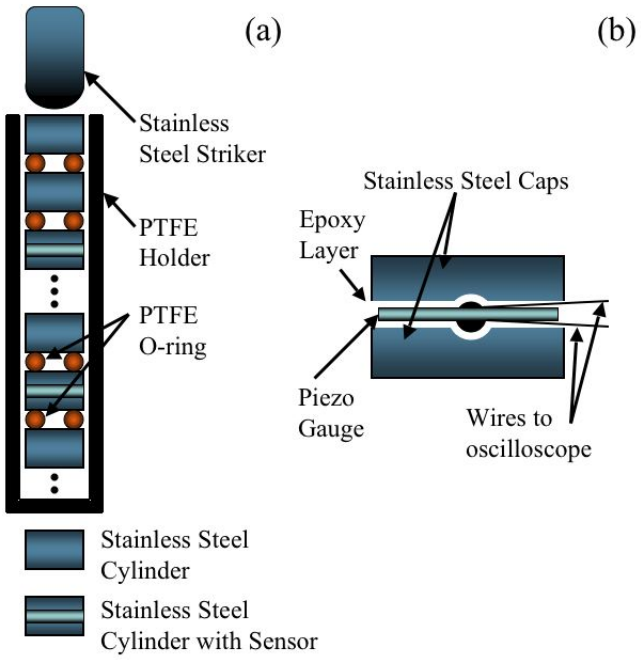

Figure 6.4: (a) Experimental setup of o-rings placed in between stainless steel cylinders and a striker with a hemispherical end. (b) A schematic diagram of the sensor construction.

was $v_0 = 2.08$ m/s. The experimental and numerical results are shown in Fig. 6.5. It is remarkable that the amplitude of the pulses at the 3^{rd} cylinder match so well. The wave amplitude and pulse speed correspond to the Hertzian regime and it is interesting that the quasistatic theory for point contact works so well for the contact of toroids with planes.

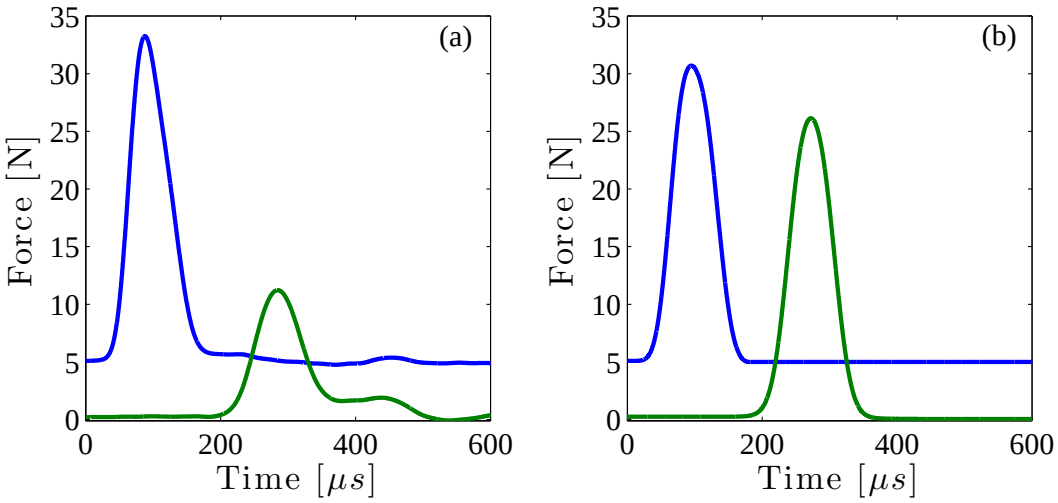

Figure 6.5: (a) Single pulse generated in experiment in a double power law chain using PTFE o-rings. (b) Numerical results using a 5mm dia. steel striker (0.454g) with a velocity of $v_0 = 2.08$ m/s.

The average pulse speed between the two cylinders in Fig. 6.5(a) is 172 m/s and the second pulse is highly attenuated. The pulse speed in Fig. 6.5(b) is 208 m/s in the calculations. In a separate calculation, an identical pulse to the one shown in Fig. 6.5(b) is created in a chain of 400 elements. The force amplitude of the wave at the 8^{th} cylinder was $F_8 = 26.699$N and the amplitude was $F_{50} = 26.693$N at the 50^{th} particle. Such a small difference in force suggests an almost fully developed solitary

wave at a very short distance from the end of the chain. It is also assumed that the solitary wave in experiments is attenuated as well.

In separate calculations the behavior of two identical solitary waves in a head-on collision was investigated. The leading solitary waves emerge with practically the same amplitudes after the collision followed by secondary solitary waves with 10^6 times smaller amplitudes than the primary waves similar to the results in Manciu et al. (2000).

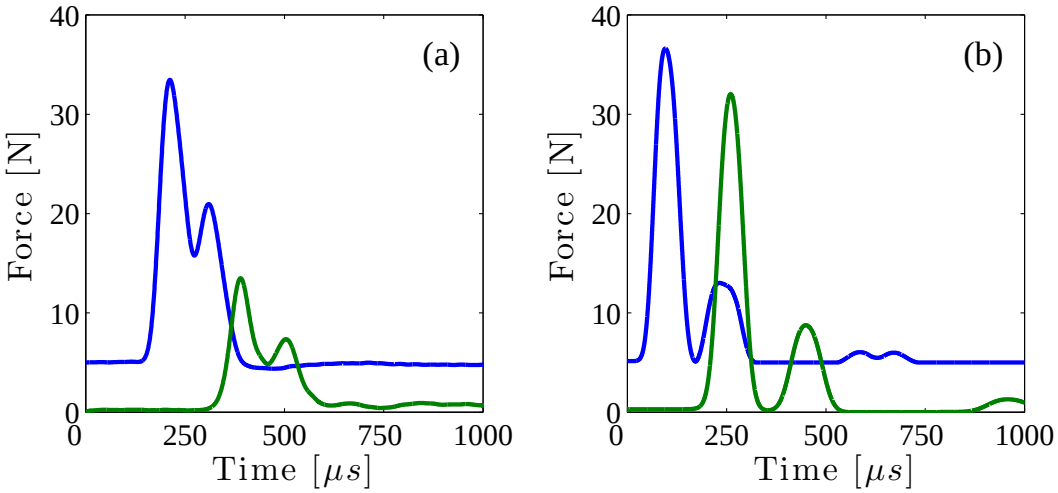

Figure 6.6: Two pulses generated in a double power law chain using PTFE o-rings. (a) experimental results using a stainless steel impacting rod with a 10 mm hemispherical tip (6.236g) with a velocity of $v_0 = 0.44$ m/s. (b) Numerical results using similar impact conditions.

To show that the waves in experiments act as strongly nonlinear solitary waves it is important to show that there is a tendency of a relatively long impulse to split into a train of solitary waves. The experimental results of an impact of a

striker with a mass equal to $m = 6.236$g on a chain of 40 elements is shown in Fig. 6.6. It is apparent from Fig. 6.6(a) that there is a tendency for two pulses to form in experiments although attenuation prohibits the complete separation seen in Fig. 6.6(b). The attenuation is known to prohibit the splitting of solitary waves in other cases as well [Herbold et al. (2006)]. Despite the difference in the splitting of the pulses the speeds of the pulses are reasonably close when comparing the experiments to the numerical calculations. The speed of the first pulse is 190 m/s and the second is 173 m/s in Fig. 6.6(a) and the speed of the first pulse and second pulses are 208 m/s and 161 m/s in Fig. 6.6(b).

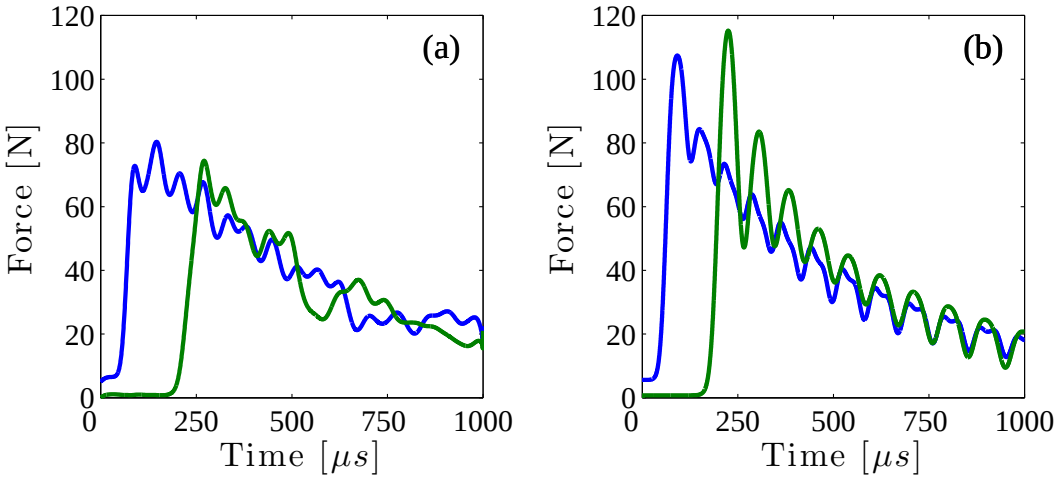

Figure 6.7: Oscillatory shock like waves are generated in a double power law chain using PTFE o-rings and a stainless steel impacting rod with a 10 mm hemispherical tip (53.84g) with a velocity of $v_0 = 0.767$ m/s. (a) Experimental results show an oscillatory profile. (b) numerical results.

Pulses excited by an impactor with mass equal to $m = 53.84$g (15 times the

the mass of cylinders) were investigated to investigate the type of shock wave present in double-power law systems. It is especially important for this system because the level of dissipation may dramatically change the shock profile from oscillatory to monotonic [Herbold and Nesterenko (2007)]. The results of experiments and numerical data are shown in Fig. 6.7 (a) and 6.7(b). The amplitude of the pulse was inside Hertzian range of interaction law. The shock wave speed is 204 m/s in experiments despite the evident dissipation (see Fig. 6.7 (a)). The shock wave speed in numerical calculations was 264 m/s (see Fig. 6.7(b)). The profile of the shock wave is oscillatory, which means that the effective viscosity (if dissipation is linearly dependent on the relative velocities of the cylinders) is below the critical value, $mV_{sh}/2a$, where $a = (h + d)$ is the distance between centers of the cylinders. An application of this equation gives a critical viscosity of about 50 Ns/m.

6.4 Conclusions

A new strongly nonlinear system was proposed and experimentally realized based on toroidal o-rings as strongly nonlinear springs. Numerical calculations demonstrated the existence of solitary waves in double power-law materials, which are qualitatively different from monomial power-law materials in the shape of solitary wave depending on the amplitude. A qualitatively new behavior of splitting of an initial pulse, and oscillatory shock waves was observed. Despite dissipation the numerical calculations give a correct estimate of pulse speed based on the quasistatic behavior of o-rings.

Chapter 6 has been published in *Applied Physics Letters*, **90**, art. 261902 by E.B. Herbold and V.F. Nesterenko. The dissertation author was the primary investigator and author of this paper.

7

Metallic Particle Size Influence On the Dynamic Mechanical Properties of Polytetraflouroethylene-Al-W Powder Composite Materials

7.1 Introduction

Mixtures containing polytetrafluoroethylene (PTFE) and aluminum (Al) are known to be energetic under dynamic and/or thermal loading Davis et al. (1998), Holt et al. (2000), McGregor and Sutherland (2004), Dolgoborodov et al. (2005), Ames (2006), Denisaev et al. (2007). These materials are formulated to generate a large quantity of heat during the reaction driven by bulk mechanical deformation as in thermites Walley et al. (2000). This chapter considers the mechanical behavior of PTFE-Al-W composites where tungsten (W) with varying particle size was used to increase density Cai et al. (2008a) keeping the composition of PTFE-Al mixture close to the stoichiometric value.

Tailoring the mechanical and chemical properties of reactive materials is im-

portant for various applications. For example, varying particle size and morphology in pressed explosives (Setchell (1984), Bardenhagen and Brackbill (1998), J.C. Foster et al. (2000), Roessig et al. (2002)) or layer thicknesses in laminates Mann et al. (1997) can significantly alter the shock-sensitivity and the rate of energy release. Ignition sites within composite energetic materials under a compressive load have been ascribed to the stress or force-chain formation in granular energetic materials Balzer et al. (2004), Siviour et al. (2004).

Considering a moving coordinate system that is coincident with a moving shock front in a PTFE-Al-W mixture the large, high strength heavy particles (W in this case) may transform their kinetic energy, which they had ahead of the shock front, into the thermal energy of small, soft particles behind the shock front [Nesterenko (1986), Nesterenko (2001)]. Thus, this mixture under shock loading works like a natural transformer of the kinetic energy of one component (W) into the internal energy of another, in this case of PTFE and Al particles, thus promoting the ignition of the chemical reaction between them.

One of the distinguishing features of reactive materials is that the stored chemical potential is released upon material deformation and is not self-propagating in contrast to energetic materials, which may support detonation waves depending on the initiation energy threshold. The material structure may be optimized at the mesoscale in order to facilitate the desirable release of mechanical and subsequent chemical energy in hot spots (e.g. shear bands) to optimize the amount and/or rate of energy release by the material.

In this chapter the modes of dynamic failure and overall strength of PTFE-Al-W granular composites are the primary points of investigation. The experimental samples were prepared to understand how these properties are affected by varying the metallic particle size, which also determines the inherent porosity for a given

densification pressure. Quasistatic, Hopkinson bar, and drop-weight experiments were performed on composite material samples. Two and three-dimensional multi-material Eulerian hydrocode simulations of drop-weight tests with the different types of samples are used to elucidate the observed experimental results. The behavior of these granular composites under shock loading conditions is also examined in two-dimensional numerical calculations.

7.2 Experimental Procedures and Results

7.2.1 Sample Preparation

Three main types of composite materials had identical mass ratios and were prepared by cold isostatic pressing (CIPing) of powder mixtures (17.5 % PTFE, 5.5 % Al, and 77 % W, by weight). The density and porosity of the two the materials with large W particles, with respect to the third type (see Table 7.1), varied only in the pressing conditions. Note that under the same CIPing conditions (pressing pressure, time and sample size) the density of the porous PTFE-Al-W with fine W particles was 6 g/cm^3 while the density of dense PTFE-Al-W with coarse W particles was 7.1 g/cm^3, which is close to the theoretical density. At the same pressing condition, the mixture of PTFE and Al powders can be fully densified Cai and Nesterenko (2006). It is important to emphasize that although the dense sample with coarse W particles is relatively free of pores and cracks, the average spacing between metallic grains is expected to be greater than in the sample with fine W particles with the same constituent material volume ratios.

The metallic powder granules had an approximate spherical shape with the following sizes: 2 μm Al powder (Valimet H-2), coarse W powder sieved to less than 44 μm (Teledyne, -325 mesh) and fine W powder sieved to less than 1

μm (Alfa-Aesar). The size of the PTFE powder grains was approximately 100 nm (DuPont, PTFE 9002-84-0, type MP 1500J). The mixed powders were ball milled in a SPEX 800 mill for 2-10 minutes using alumina balls to reduce agglomeration. The typical dimensions of the solid cylindrical samples were 10 mm high and 10.44 mm in diameter and the masses were equal to 4 to 5 grams. Three to six samples of each type of composite material were tested in each type of experiment.

Table 7.1: Quasistatic and dynamic properties of the sample materials.

Sample Materials		Dense PTFE-Al-coarse W	Porous PTFE-Al-fine W	Porous PTFE-Al-coarse W	Pure Dense PTFE
Size of W Particles (μm)		< 44	< 1	< 44	...
CIP Pressure (MPa)		350	350	20	350
Density (g/cm^3)		7.1 ± 0.4	6.0 ± 0.3	6.0 ± 0.3	2.1 ± 0.1
Porosity (%)		1.6	14.3	14.3	4.5
Ultimate Comp. Strength (MPa)	Quasistatic (10^{-3}s^{-1})	18 ± 1	22 ± 6	5.8 ± 0.2	2.3 ± 0.3
	Hopkinson bar (500 s^{-1})	30 ± 1	45 ± 7	10 ± 3	21 ± 3
	Drop-weight (300 s^{-1})	32 ± 2	55 ± 6	11 ± 2 (40 ± 11)	...

Porous PTFE-Al-W samples containing coarse W particles (termed porous PTFE-Al-coarse W) were processed with a significantly reduced CIPing pressure (20 MPa) to investigate the behavior of materials with different porosity and different

particle sizes of the W powder. This resulted in a similar porosity to samples with fine W particles (compare the porous PTFE-Al-fine W sample with the porous PTFE-Al-coarse W sample in Table 7.1). Samples of CIPed PTFE with a density of 2.1 g/cm^3 were also manufactured for the measurements of properties (e.g. the failure strain) of the PTFE material used in the numerical analysis of the composite behaviors.

7.2.2 Quasistatic Tests

Quasistatic compression tests were performed using the SATEC^{TM} Universal Materials Testing Machine (Instron; Canton, MA). The load was applied at a nominal deformation strain rate of 0.001 s^{-1} and was terminated when the sample was fractured. The ultimate compressive engineering stresses for the composite and densified PTFE materials are listed in Table 7.1.

In Fig. 7.1 the mode(s) of failure for the investigated materials are compared. Both shear and axial cracks were observed in the porous samples with small W particles (see Fig. 7.1 (a) and (b)) and the porous samples with large W particles (see Fig. 7.1 (c) and (d)). The higher density samples with coarse W powder show failure patterns in a unique combination of axial and circumferential cracks (Fig. 7.1 (e) and (f)).

Figure 7.2 shows typical stress strain curves for the three different types of samples shown in Fig. 7.1. These tests consistently demonstrated that porous PTFE-Al-W materials with fine W particles exhibit the highest compressive strength (see curve (1)). It is natural to expect that porous materials in compression tests fail due to axial cracks caused by tensile stress concentration at the vicinity of pores [Timoshenko and Goodier (1987)]. However, it is interesting that the observed fracture pattern in the porous PTFE-Al-W containing fine W particles consisted mainly of

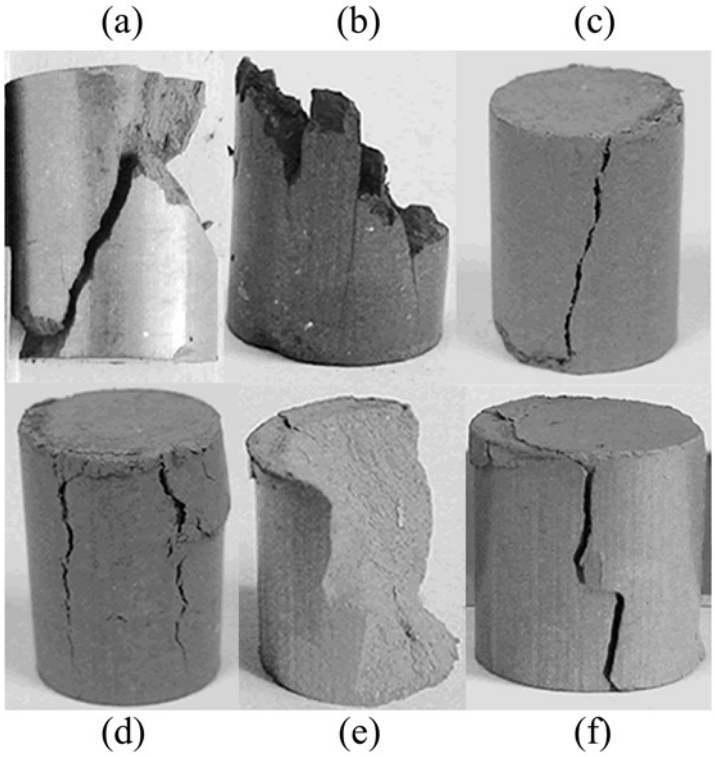

Figure 7.1: Fracture detail of various samples after quasistatic testing. (a) Shear crack and (b) axial and shear cracks in the porous PTFE-Al-fine W composite sample; (c) Axial/shear and (d) axial cracks in the porous PTFE-Al-coarse W composite sample; (e), (f) kinked axial cracks in the dense PTFE-Al-coarse W composite sample. All samples had identical initial dimensions of 10.44 mm diameter and 10 mm height.

shear cracks (see Fig. 7.1 (a) and (b)). It is also important to mention that the sample strength is proportional to the slope of the stress strain curve indicating an effective modulus at the initial stage of deformation.

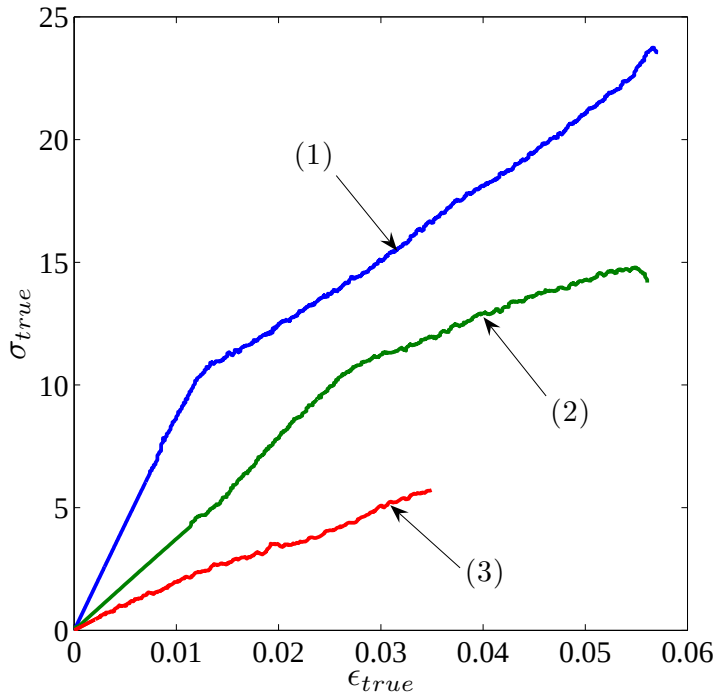

Figure 7.2: Quasistatic stress-strain curve of PTFE-W-Al composite materials with variation of density and particle size of W. Curve (1) shows the results of the sample with fine W particles and porosity above 14%. Curve (2) shows the results of the sample with large W particles, which was almost fully densified. Curve (3) shows the results of the sample with large W particles CIPed at a lower pressure to induce about 14% porosity.

7.2.3 Hopkinson Bar Tests

Dynamic testing was performed using a Hopkinson bar which comprises three 19 mm diameter bars: a 457 mm long C350 maraging steel striker bar, a 1828 mm long C350 maraging steel incident bar and a 1828 long magnesium alloy transmitting bar. Since the investigated materials are generally of lower strength, a linear elastic, low modulus magnesium alloy transmission bar was used to obtain a high signal to noise ratio in the transmitted signals. The Hopkinson Bar testing usually generated about 5% strain in the samples for the investigated materials. Samples of CIPed monolithic PTFE were also tested (see Table 7.1) to obtain the ultimate compressive strength of the PTFE matrix and the failure strain (about 0.05). The equations for calculating stress, strain and strain rate, in the sample in the Hopkinson bar experiment are,

$$\begin{aligned} \sigma(t) &= \frac{\varepsilon_T(t) A_0 \left(E_{MS} + E_M\right)}{2A} \\ \varepsilon(t) &= \frac{1}{L}\int_0^t \left[C_{MS}\left(\varepsilon_T(t) - 2\varepsilon_R(t)\right) - C_M \varepsilon_T(t)\right] dt \\ \dot{\varepsilon}(t) &= \frac{C_{MS}\left[\varepsilon_T(t) - 2\varepsilon_R(t)\right] - C_M \varepsilon_T(t)}{L}. \end{aligned} \tag{7.1}$$

In Eqs. (7.1), C_{MS} and C_M denote the sound speed in the maraging steel incident bar (5000 m/s), and the magnesium transmitted bar (5000 m/s) and A_0 denotes the areas of the bars and A denotes the area of the sample with length L. The constants E_{MS} and E_M denote the elastic moduli of the maraging steel (200 GPa) and the magnesium bar (45 GPa).

Each type of sample microstructure is shown in Fig. 7.3 prior to Hopkinson bar testing. These micrographs are typical of each sample type prepared for all three experiments. In the dense sample with large W particles it is clear that there is very little porosity (Fig. 7.3 (a)). However, in the other two types of samples, porosity is

present and agglomerated groups of metallic particles within the matrix are present (Fig. 7.3 (b)-(d)).

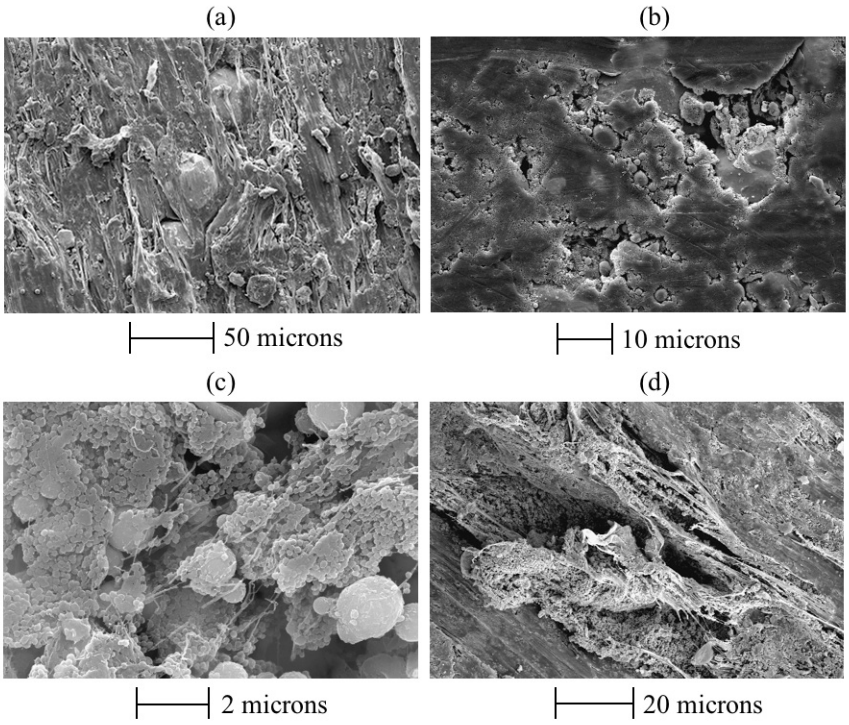

Figure 7.3: Micrographs of the sample microstructure before Hopkinson bar tests. (a) Dense sample with coarse W particles. (b) and (c) Porous sample with coarse W particles. (d) Porous sample with fine W particles.

It is important to emphasize that although the dense sample with coarse W particles shown in Fig. 7.3 (a) is relatively free of pores and cracks the average spacing between grains is much greater than the microstructure of the sample with fine W particles (Fig. 7.3 (d). In fact, the microstructure shown in Fig. 7.3 (d) is relatively insensitive to pressing pressures above the reported value of 350 MPa due

to the self-organized metallic grain structure, which prohibited further dilatational changes at pressures reasonably above this pressure. Thus, the metallic particles in this case may be considered fully compacted without full sample densification.

The Hopkinson bar results for the three composite materials and the pure PTFE samples are shown in Fig. 7.4 and listed in Table 7.1. In Fig. 7.4 (a) three stress versus strain plots and three corresponding strain rate versus strain plots are shown for the porous sample with small W particles. The striking differences between the three experiments may be attributed to the samples' ultimate strength and final strain value strong dependence on the *in situ* state of the metallic particles. In other words, the mesostructure of the metallic particles may or may not be conducive to resisting load at any point during dynamic deformation. However, compared to the other samples, the ultimate strength of this sample is the largest.

There is also a noticeable variation in the results for the porous sample with large W particles shown in Fig. 7.4 (b). In one of the tests, the sample shows a relatively higher strength throughout. This may be due to the gradual densification of the sample, which is possible when the CIPing pressure is too low to densify the composite material. Even with densification, the ultimate strength of this sample is very low compared to the pure PTFE sample shown in Fig. 7.4 (d).

The most consistent tests result from the dense sample with large W particles. Compared to the Fig. 7.4 (b), this sample may not easily densify any further. Also, the metallic particles are sparsely distributed throughout the PTFE matrix with respect to the porous sample with small W particles (Fig. 7.4 (a)). This may, in effect, produce a cushioning effect between the metallic particles and explain why the sample has a relatively lower average strength than the sample with small W particles.

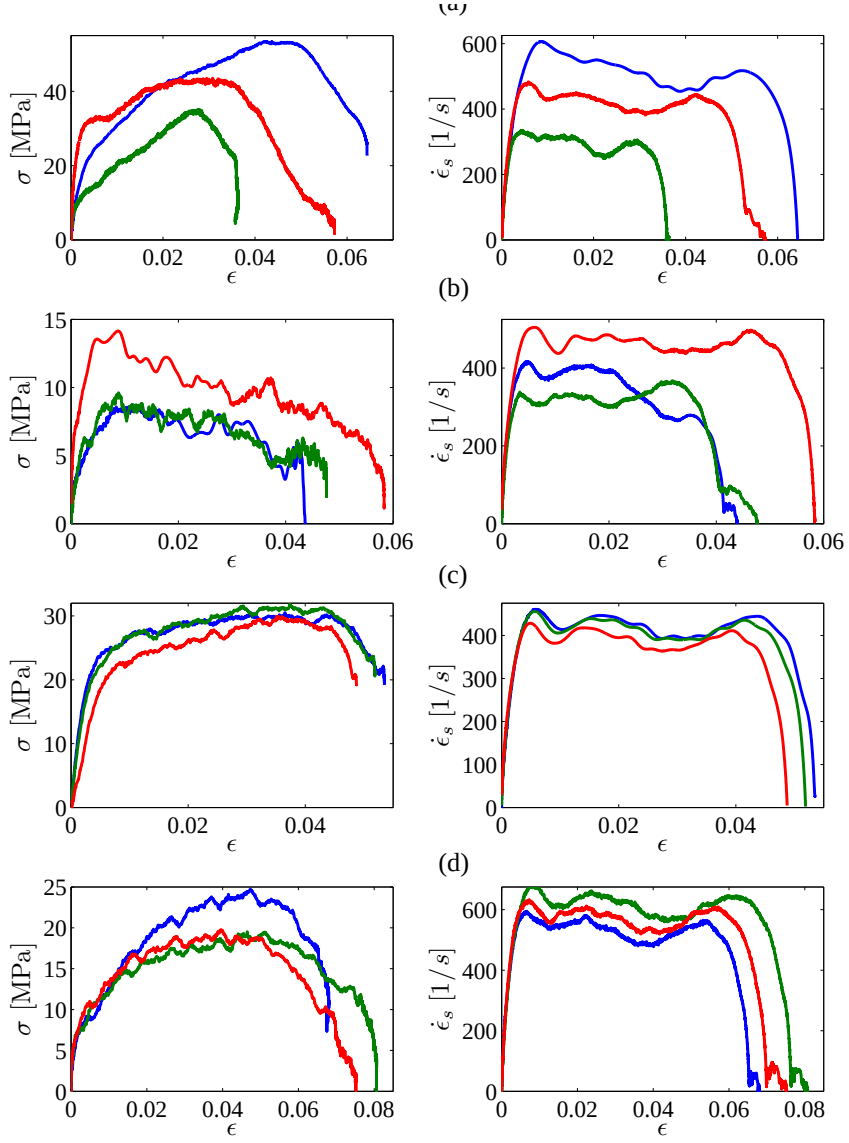

Figure 7.4: Hopkinson bar stress-strain and strain-rate-strain curves of a (a) porous PTFE-Al-W composite sample containing fine W particles, (b) porous PTFE-Al-W composite samples containing coarse W particles, (c) dense PTFE-Al-W composite samples containing coarse W particles and (d) cold isostatically pressed PTFE samples.

To investigate the modes of failure in each sample the micrographs of the initial sample mictrostructure, Fig. 7.3, are compared to similar micrographs of the composites after Hopkinson bar tests (Fig. 7.5). The dense sample with large W particles is shown in Fig. 7.5 (a) and (b) and it is clear that PTFE fibers span the crack openings between large particles or groups of particles. PTFE microfibers ($\sim$ 1 μm) were observed and discussed by Brown et al. (2005) above 30 °C. The PTFE fiber shown in Fig. 7.5 (b) has a diameter of about 60-90 nm and the bulk temperature of the sample was initially 22 °C although localized heating may have augmented the formation of such small fibers.

The microstructure of the porous sample with large W particles is shown in Fig. 7.5 (c) where melting is apparent around groups of particles. Small PTFE fibers are also visible between the crack openings. The porous sample with small W particles (Fig. 7.5 (d)) shows that the crack surface has many clusters of agglomerated particles along with a dense network of larger PTFE fibers spanning the crack opening and between these clusters. The difference between the size of the PTFE fibers between the samples with large and small W particles may be due to the matrix having a larger surface area to adhere to when larger W particles are present. This may allow the matrix to hyperextend a single fiber through crack surfaces instead of tangling networks of larger fibers as was seen when smaller metallic particles were dispersed through the matrix (compare Fig. 7.5 (a) with (d)).

7.2.4 Drop-Weight Tests

The investigated samples have a relatively low strength as evident from Table 7.1. Because of this, the signal in standard drop weight test is obscured by inevitable noise due to oscillations in the drop weight device. A soft drop-weight test

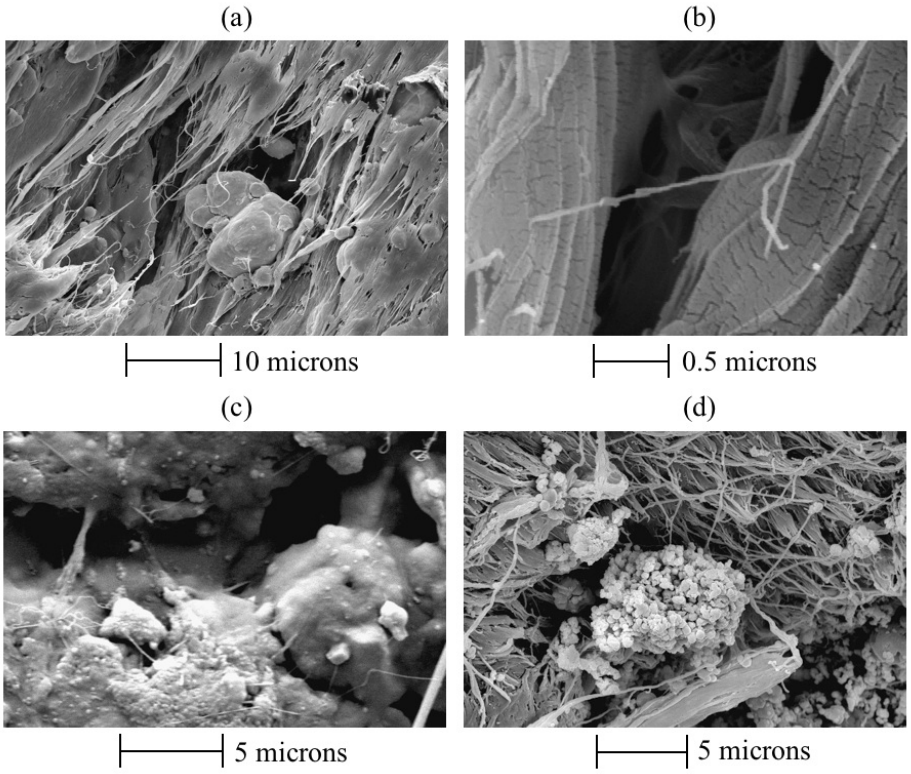

Figure 7.5: Micrographs of the sample microstructure after Hopkinson bar tests. (a) Dense sample with coarse W particles after Hopkinson bar. The PTFE was fractured and is attached to the large W particles. (b) Higher magnification of the dense sample with coarse W particles showing PTFE nanofibers. The diameter of the fibers ranged from 60-100 nm and networks of these formed between crack openings in the sample. (c) Porous sample with coarse W particles. Melting of the PTFE has occurred around groups of metallic particles and stretched PTFE fibers are noticeable between these groups. (d) Porous sample with fine W particles. Agglomeration of the metallic particles appears to be held together by PTFE.

(Cai et al. (2008a), Addiss et al. (2007)) was developed to allow effective testing of low strength samples. An o-ring was placed on the top of the upper anvil of the drop-weight apparatus to reduce the mechanical oscillations in the system caused by the impact of the mass. This method effectively reduced high amplitude parasitic oscillations. The results of the dynamic measurements of the ultimate engineering compressive stresses are presented in Table 7.1. Comparing the strengths of the porous PTFE-Al-fine W and the porous PTFE-Al-coarse W, it is clear that porosity itself does not contribute to the higher strength of the porous composite filled with fine W particles.

The porous samples with coarse W particles also demonstrated an unusual behavior. Figure 7.6 shows the engineering stress for each sample plotted versus time. In each case an copper ring surrounded the sample to arrest the deformation at different strains (0.03-0.27) in the vertical direction. In Fig. 7.6 (a) some of the porous samples with large W particles exhibited a very low strength and failed in shear at approximately 11 MPa (curve 1) while others exhibited considerably higher strength above 50 MPa (curve 2). The higher ultimate compressive strength may be attributed to the gradual densification during the initial stage of deformation, which leads to a considerably increased strength relative to those samples that appear to fail almost immediately upon impact.

The ultimate compressive strength of the *in situ* densified samples is greater than the pressing pressure (20 MPa) and comparable to that of the dense samples with coarse W. Such behavior can be expected when the ultimate compressive strength is comparable to the densification pressure used to prepare samples and was not observed for porous samples with fine metallic particles or denser samples with coarse W particles (Table 7.1). It is uncertain why some samples fail by shearing at low strain while others are densified during the test leading to an increased

strength. There is clearly some competition occurring between the compaction of the soft visco-elastic matrix and fracture during the deformation process.

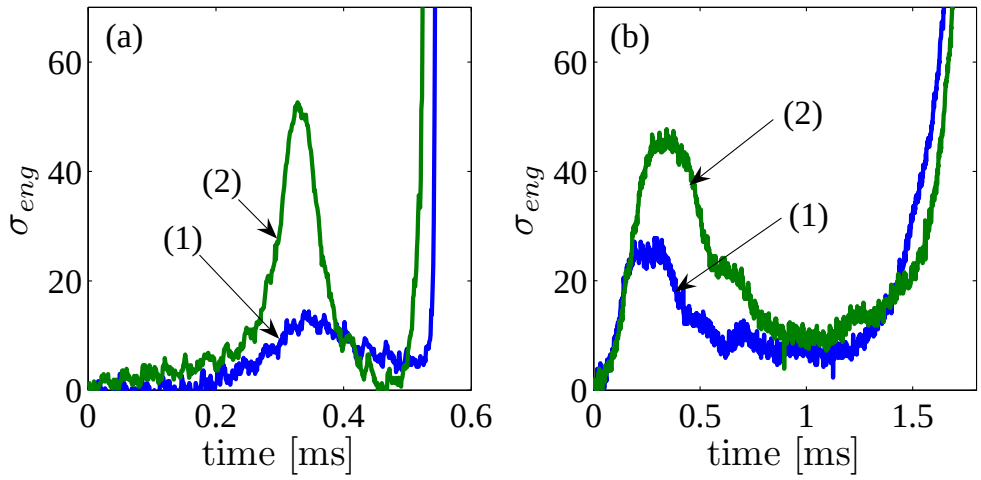

Figure 7.6: Stress vs. time curves obtained in drop weight experiments. (a) Curves (1) and (2) correspond to the porous sample with coarse W particles. The remarkable difference between the two curves is due to the densification of the sample, shown in curve (2), before fracture. (b) Curve (1) corresponds to the densified sample with coarse W particles. Curve (2) corresponds to the porous sample with fine W particles.

In Fig. 7.6 (b) typical experimental results of the engineering stress versus time are shown for the dense sample with coarse tungsten particles (curve 1) and the sample with fine tungsten particles. Again, the sample with fine tungsten particles exhibits higher strength. However, there is no indication of densification as a preconditioning or strength enhancing mechanism in either of these samples.

Figure 7.7 shows recovered samples where the deformation was interrupted

at corresponding engineering strains. The stress-strain curve associated with this sample is similar to curve 1 shown in Fig. 7.7. The sample has failed by shear localization. A symmetrical pattern of cracks can be seen in the fractured samples (Fig. 7.7), though the samples microstructure is inherently random.

Debonding of the metal particles from the matrix and the fracture of the matrix were two major mesoscale mechanisms resulting in the failure of the sample (Cai et al. (2008b)). The relevant mesoscale mechanism of shear localization at low levels of strain is considered in Cai and Nesterenko (2006) and examples of shear localization due to micro-fracture mechanisms leading to reaction in granular materials can be found in Dey and Johnson (1998), Shih et al. (1998), Nesterenko (2001).

7.3 Numerical Modeling of a Drop-Weight Test and Discussion

Results of quasistatic and dynamic tests are consistent with each other with respect to the influence of particle size on sample strength. Drop weight tests were selected for numerical analysis due to well defined boundary conditions determined by the approximate constant velocity of the dropped weight. A two-dimensional numerical simulation using Raven [Benson (1992)], which is a Multi-Material Arbitrary Lagrangian Eulerian (MM-ALE) hydrocode, was used to explain the unusual dependence of increased ultimate compressive strength with the decreased of size of metallic particles (high porosity, low density samples) in drop-weight tests. Two dimensional granular packings were used for the modeling of shock compaction and determination of microkinetic energy (Benson et al. (1997)) as photoelastic polymer

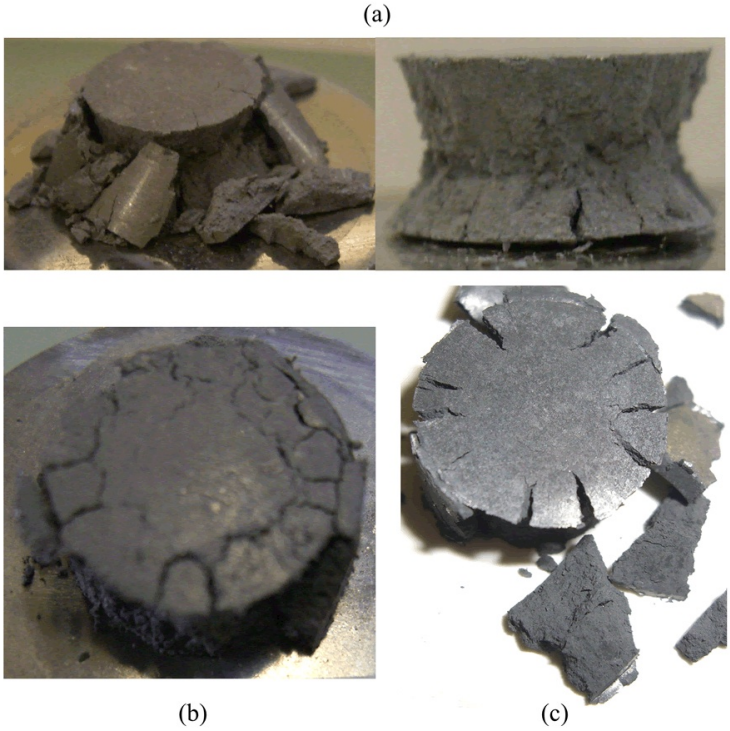

Figure 7.7: (a) Porous sample containing coarse W particles corresponding to curve (1) in Fig. 7.6 (a). (b) Porous sample containing coarse W particles corresponding to curve (2) in Fig. 7.6 (a). (c) Porous sample with fine W particles corresponding to curve (2) in Fig. 7.6 (b).

discs have been used effectively as analogs of energetic materials in the literature (Bardenhagen and Brackbill (1998), Roessig et al. (2002)). The two dimensional metallic particle mesostructure of the composites do not reproduce the coordination number as in three dimensional packings, but numerical modeling can help to estimate the level of influence that the force chains have on the global behavior of the samples. Following the discussion of the two-dimensional simulations, three dimensional simulations of a drop-weight test were also performed using a MM-ALE formulation in LS-Dyna to better understand the role of coordination number on material strength under these specific loading conditions.

Two samples using a randomly distributed mixture of fine (1 μm) W and Al particles (2 μm) (sample 1, Fig. 7.8 (a)) and coarse (10 μm) W and Al particles (2 μm) (sample 2, Fig. 7.8 (b)) of circular shape are used in finite element calculations to investigate the force chain effect. The weight and volume fractions of each the sample constituents were similar in the calculations and experiments (e.g. mass fractions: 20% PTFE, 6% Al, 74% W, and volume fractions: 59% PTFE, 13% Al, 28% W) (Cai et al. (2007)). In the two-dimensional numerical calculations the samples contained about 52 particles of Al, 406 of small W particles or 4 large W particles, respectively. In experiments samples contained about around 50 billion Al particles and 900 billion small W particles or 85000 large particles respectively. It is interesting that despite the many orders difference in the number of particles the considered representative volume of the granular composite with arrangements shown in Fig. 7.8 reflect qualitative difference in behavior detected in experiments as will be shown.

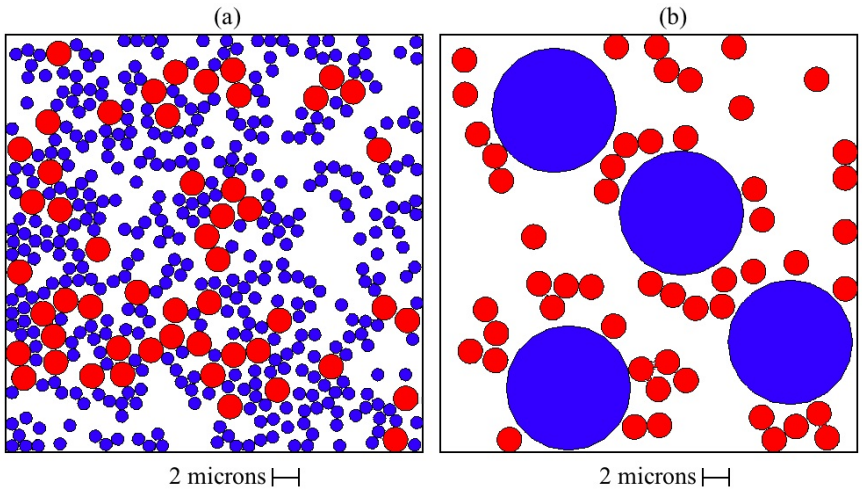

Figure 7.8: (a) PTFE-W-Al sample (sample 1) using 2 μm Al particles and 1 μm W particles. (b) PTFE-W-Al sample (sample 2) using 2 μm diameter Aluminum particles and 10 μm diameter Tungsten particles.

7.3.1 Obtaining the Johnson-Cook parameters for PTFE

A two-dimensional Eulerian Hydrocode [Benson (1992)] is implemented to simulate the behavior of the sample at high strain rates in drop weight tests. Each material in the mixture has a different equation of state, and physical and mechanical properties. The Johnson-Cook constitutive material model Johnson and Cook (1985) will be used in the finite element calculations for the PTFE. Since the parameters for PTFE are not readily available, true total stress and strain data from a series of split Hopkinson pressure bar experiments were used to estimate these values. In Fig.(3) in Zerilli and Armstrong (2001) the experimental data up to a total strain of $\varepsilon = 0.3$ were used and these experimental values are shown as data points in Fig. 7.9. This data will be used to fit the Johnson-Cook material model with failure (Johnson and

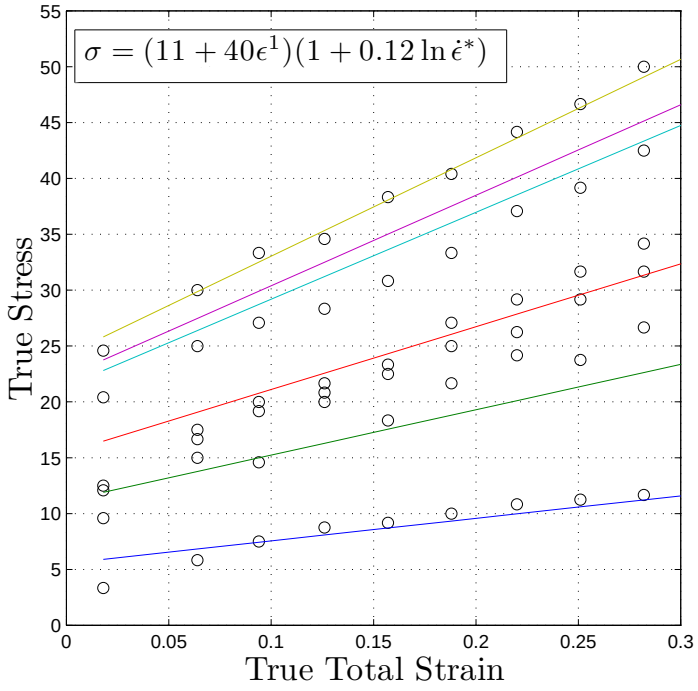

Figure 7.9: Plot of experimental data (denoted by ∘) from Zerilli and Armstrong (2001) and the fitted Johnson-Cook model. The experimental strain rates were: $\dot{\varepsilon} =$ 0.016, 1.14, 29.7, 2650, 5180, and 22600 s^{-1} corresponding to the lowest through the highest slopes of the lines through the experimental data.

Cook (1983)),

$$\sigma_y = \left[A + B\left(\bar{\varepsilon}^p\right)^n\right]\left(1 + C \ln \dot{\varepsilon}^*\right)\left(1 - T^{*m}\right) \tag{7.2}$$

where $\bar{\varepsilon}^p$ is the equivalent plastic strain, $\dot{\varepsilon}^* = \dot{\varepsilon}/\dot{\varepsilon}_0$ is the dimensionless plastic strain rate (taking $\dot{\varepsilon}_0 = 1s^{-1}$), T^* is the homologous temperature, where $T^* = (T - T_{room})/(T_{melt} - T_{room})$, and A, B, C, and n are constants. The data points in Fig. 7.9 were taken at different strain rates but at a constant temperature of $T = 296K$. The experimental strain rates were: $\dot{\varepsilon} =$ 0.016, 1.14, 29.7, 2650, 5180, and 22600

s^{-1}. The best fit of the data points for the range of strain rates corresponded with the following constants: $A = 11$ MPa, $B = 44$ MPa, $n = 1$, C=0.12 and $m = 1$.

The material failure criteria was based upon the equation,

$$\varepsilon_f = [D_1 + D_2 \exp(D_3 \sigma^*)] (1 + D_4 \ln \dot{\varepsilon}^*) (1 + D_5 T^*) \tag{7.3}$$

where D_1=0.05 was obtained from quasistatic and Hopkinson bar experimental data of pure CIPed PTFE samples and D_2,D_3,D_4 and D_5 were set equal to zero as a first approximation. The Gruneisen form of the equation of state was used to define the pressure in compression and tension in PTFE with parameters presented in Steinberg (1996).

The Johnson-Cook material model without failure was used for the tungsten and aluminum particles. The Johnson-Cook parameters for tungsten are $A = 1.51$ GPa, $B = 177$ MPa, $n = 0.12$, $C = 0.016$, and $m = 1$. The Johnson-Cook parameters for aluminum are $A = 265$ MPa, $B = 426$ MPa, $n = 0.34$, $C = 0.015$, and $m = 1.29$ Since the particle deformation or fracture during dynamic loading is minimal in the mixture with PTFE the equation of state used for Tungsten and Aluminum was linear elastic with the bulk and shear moduli equal to $K = 300$ GPa and $G = 160$ GPa for Tungsten and $K = 76$ GPa and $G = 27.1$ GPa for Aluminum.

7.3.2 Numerical Results of a Two-Dimensional Simulation of a Drop Weight Test

In Fig. 7.10, curve 1 the two-dimensional numerical analysis shows that the first compressive stress maxima of sample 1 is 78 MPa; and the corresponding stress of sample 2 at 35 MPa (Fig. 7.10, curve 2) is significantly lower. The level of maximum stress for sample 2 is close to the experimental value (Table 7.1), but is

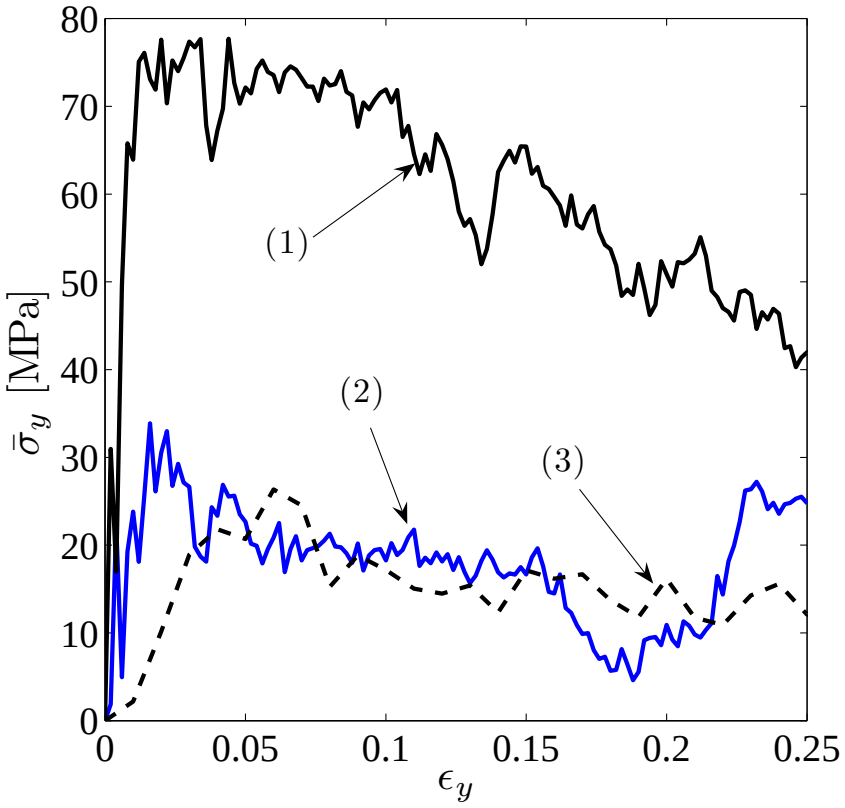

Figure 7.10: Average engineering stress at the top of the numerical sample plotted against the 'global' strain for a sample using small tungsten particles (sample 1, curve 1) and a sample using large tungsten particles (sample 2, curve 2). Note the stress increases in curve 1 after 0.13 global strain while the curve 2 coincides with the results for pure CIPed PTFE (curve 3).

significantly larger than the experimental value for sample 1. The results for a pure, densified PTFE are shown in Fig. 7.10, curve 3 for comparison. The small number of metal particles and their specific configuration used in the calculations may be responsible for this difference. Three dimensional numerical calculations with larger number of particles and higher coordination number may provide better agreement with experiments.

The von Mises stress and equivalent plastic strain distributions for the sample with fine tungsten particles (sample 1) are shown in Fig. 7.11 at 0.022, 0.042 and 0.238 global strain. Several force chains are apparent starting from the top through the bottom of the sample. This can be compared to the sudden increase in the stress-strain plot shown in curve 1 in Fig. 7.10 at the corresponding strain. Upon further deformation, this force chain disintegrates and a macrocrack starts in the matrix at a global strain less than the critical failure strain of matrix material (0.05, from Hopkinson bar experiments), resulting in the decrease in stress in curve 1 (Fig. 7.10). Thus, the maximum global stress attained in compression may occur after the onset of failure in the matrix material.

Force chains propagating through the cracks in the matrix are reactivated upon further deformation (see the stress distribution in Fig. 7.11 (e) corresponding to the global strain 0.238, Fig. 7.11 (f)). This self-organization of metallic particles was accompanied by a macro-crack, which is in qualitative agreement with the observed failure in experiments. The local effective plastic strain in the sample (Fig. 7.11) above this crack shows that the damage in the PTFE matrix material is distributed around the metal particles. It is important to maintain the damage throughout the bulk of the sample to enhance a possible chemical reaction between PTFE and Al.

Several features can be observed from the results for the first sample. The

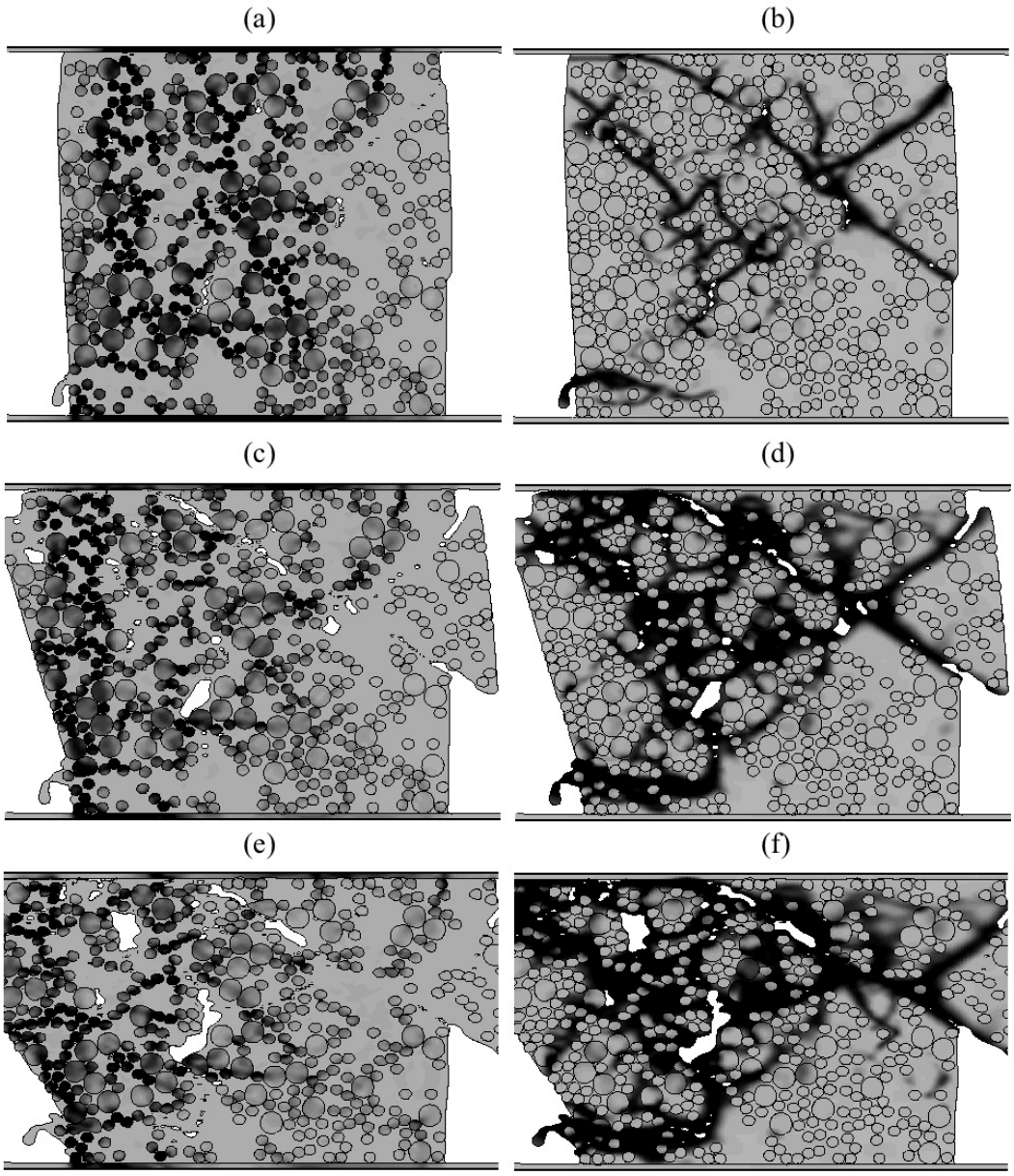

Figure 7.11: The color intensity varies from light gray (0 MPa) to dark gray (500 MPa) for the von Mises stress and 0 to 0.05 plastic strain in sample 1. The von Mises true stress distribution (a) and local effective plastic strain (b) at 0.022 global strain. The von Mises true stress distribution (c) and local effective plastic strain (d) at 0.042 global strain. The von Mises true stress distribution (e) and local effective plastic strain (f) at 0.238 global strain.

vertical and horizontal displacements of the metallic particles, initiated by the vertical displacement of the top boundary, are comparable to their sizes resulting in force chains being created, destroyed and reactivated (with different particles) in the course of sample deformation and fracture. It is interesting that the progressive local fracture of the PTFE matrix material corresponds to the spikes in global stress (compare curve 1 in Fig. 7.10 with Fig. 7.11 (a) and (b)) and the global stress in one of these peaks is observed in the heavily fractured sample (compare curve 1 in Fig. 7.10 with Fig. 7.11 (e) and (f)). This is due to the disintegration of the matrix along with a local dense packing of metal particles resisting further deformation.

The second sample did not have a particle distribution conducive to force chain activation. Through-thickness force chains are not activated as strongly as in the first sample up to 0.25 global strain, though groups of particles have created localized chains. The macro-cracks formed in this sample (Fig. 7.12) prohibited any bulk-distributed damage. Separate calculations (Fig. 7.10 curve 3) with a pure PTFE sample have a stress strain behavior very similar to curve 2 in Fig. 7.10. This suggests that only the matrix material resisted the load.

The vertical and horizontal displacements of the metal particles in the second sample are also comparable to their sizes and to the size of the sample. The calculations also demonstrated that the stress spikes were not related to the activation of force chains propagating from top to bottom, though shorter force chains were activated. The metal particles also initiated shear macro-cracks in the PTFE matrix propagating at 45 degrees (Fig. 7.12 (c)-(f)) from the direction of compression similar to the behavior observed in experiments (see Fig. 7.1 (c), (e) and (f) and Fig. 7.7 (a) and (b)).

The two-dimensional calculations demonstrated that force chains created by

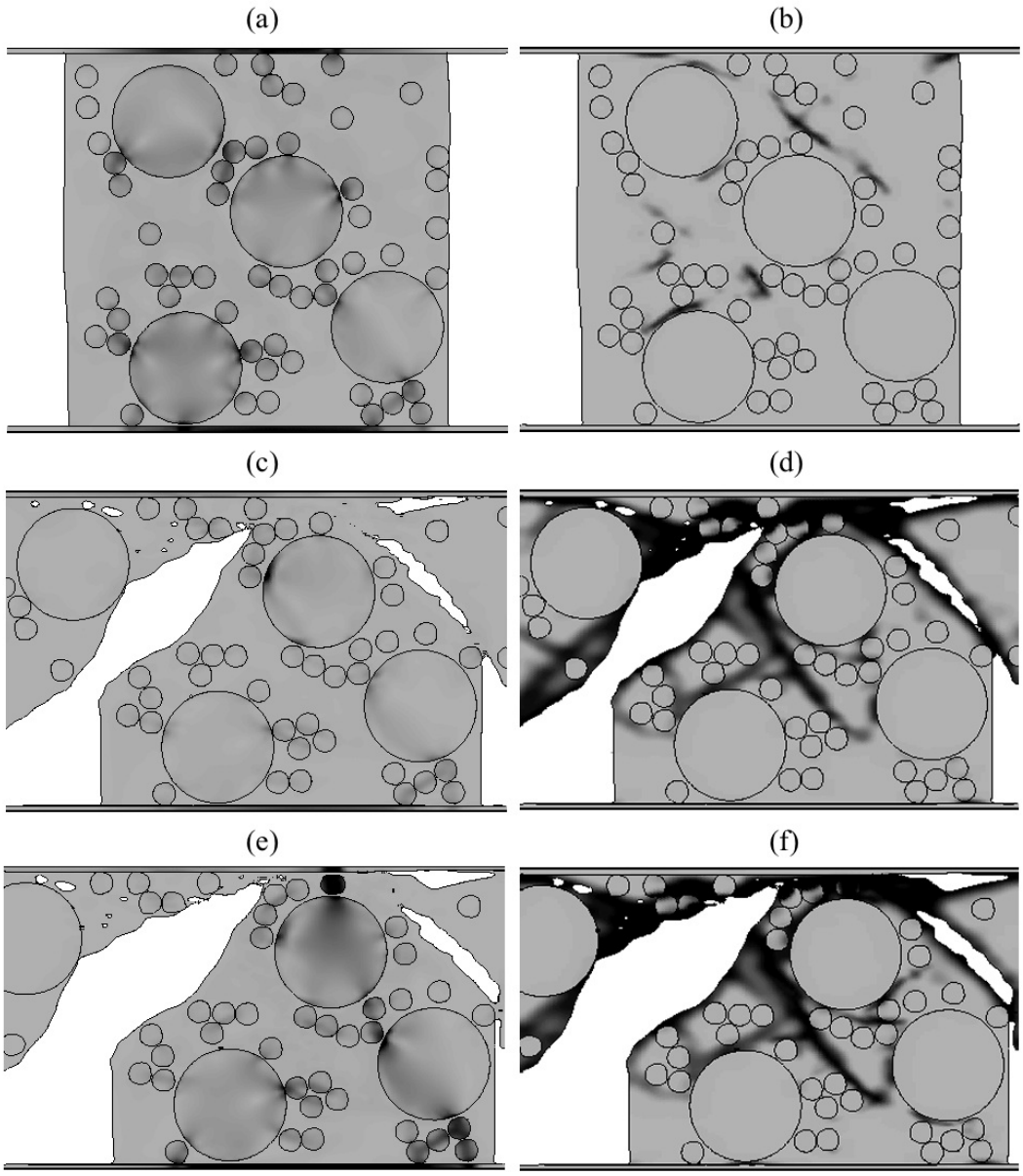

Figure 7.12: The color intensity varies from light gray (0 MPa) to dark gray (500 MPa) for the von Mises stress and 0 to 0.05 plastic strain in sample 2. The von Mises true stress distribution (a) and local effective plastic strain (b) at 0.014 global strain. The von Mises true stress distribution (c) and local effective plastic strain (d) at 0.186 global strain. The von Mises true stress distribution (e) and local effective plastic strain (f) at 0.23 global strain.

circular metallic particles are a probable cause of the higher strength of these mixtures with volume content similar to three-dimensional packing of spherical metallic particles in experiments. It should be emphasized that the dependence of the ultimate sample strength on particle size should be sensitive to particle morphology (for example, particles elongated in one direction can exhibit a different dependence of strength on particle size).

The results presented indicate that the skeleton of small metal particles can significantly affect the strength of this granular composite. At the same time the specific distribution of a three dimensional network of force chains can be more complex than that presented in the two dimensional calculations. For example, in a three-dimensional network, they may be created by the contacts of agglomerated fine particles as schematically shown for example in Fig. 7.13 (b). The same volume of metal particles, when a fraction consists of coarse particles, is less conducive to creating a skeleton that is able to affect the global strength of granular composite (Fig. 7.13 (a)). The correlation of higher strength and stiffness (Fig. 7.2), observed in experiments, suggests that the increase of composite strength is not related to the stronger bonding that is expected between agglomerated fine particles and the matrix material. Numerical calculations demonstrated that forces responsible for particle agglomeration do not significantly contribute to the strength of the granular composite.

These groups of agglomerated particles immediately interact with one another since their interaction was created during the CIPing process (which resulted in arrested compaction and porosity). The alignment of these groups of particles augments the effective elastic modulus as well as the critical failure strength of the sample.

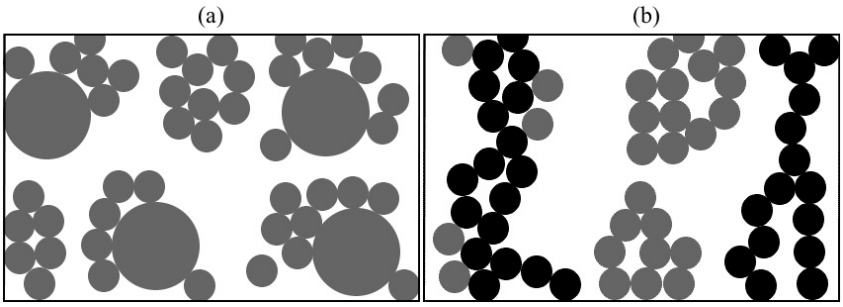

Figure 7.13: Different types of metallic particle agglomerate distributions within the soft PTFE matrix (not to scale). (a) Groups of metallic particles coalesce but do not interact immediately upon loading. The interaction of these groups does not contribute to the effective elastic modulus, but may contribute to the critical failure stress as these groups interact with one another during compression testing. (b) The metallic particle force chains are highlighted by a darker color for distinction.

7.3.3 Numerical Results of a Three-Dimensional Simulation of a Drop Weight Test

In the three dimensional finite element simulations of a drop-weight test, two samples were created using a randomly distributed mixture of fine (0.9 μm) W and Al particles (1.8 μm) (sample 1, Fig. 7.14 (a)) and coarse (9 μm) W and Al particles (1.8 μm) (sample 2, Fig. 7.14 (b)). The drop-weight simulations consist of the sample being compressed between two plates; assuming one is moving at a constant velocity. The weight and volume fractions of each the sample constituents were similar to those in experiments and in the two-dimensional calculations [Cai et al. (2007)]. The prismatic samples are created by randomly placing W and Al particles inside a PTFE matrix [similar to He et al. (1999)]. The two different types

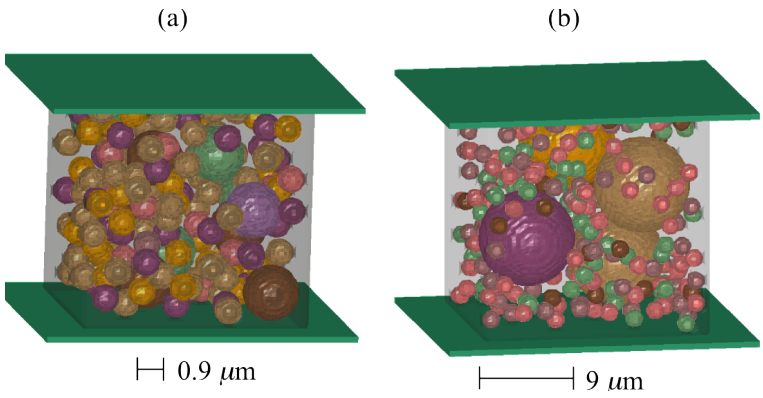

Figure 7.14: The initial geometry of both three-dimensional samples created in LS-PrePost. The Eulerian mesh is not visible and the PTFE matrix is semi-tranparent. (a) The larger particles are Al (1.8 μm diameter) and the smaller are W (0.9 μm diameter). (b) The smaller particles are Al (1.8 μm diameter) and the larger are W (9 μm diameter). The colors correspond to the MM-ALE material number.

of samples are distinguished by the size of the W particles.

The experimental sample size (on the order of millimeters) cannot be modeled with any reasonable fidelity with respect to the micro and mesoscale features created during deformation. This is due to the size constraint of the elements which must be very small between adjacent particles. Thus, the samples considered in this section have typical dimensions of tens of microns (similar to the two-dimensional simulations) on a side for the prismatic samples. The samples and steel plates are depicted in Fig. 7.14.

The Eulerian mesh for the sample with small W particles have the dimensions $L_{Ex} = 10.07\mu m, L_{Ey} = 10.07\mu m, L_{Ez} = 7.57\mu m$ with 75 elements in each direction. Each of the following MMALE parts defined within this mesh were defined using the *INITIAL_VOLUME_ FRACTION_GEOMETRY card in LS-PrePost (see

Appendix A for parameters). Steel plates (Vascomax 250 with properties obtained from Steinberg (1996)) were placed at the top and bottom of the mesh. The plates spanned the entire width and depth of the plate and had a thickness of $0.19\mu m$ (i.e. each plate had a thickness of two elements) as shown in Fig. 7.14. The PTFE matrix material was defined as a rectangular box with the dimensions 7.33 μm in the x and y directions and 7.19 μm in the z direction. In the x and y directions a 2% addition of material was added to prevent boundary grains from protruding through the side surfaces. In this sample, 152 W particles (with a 0.9 μm diameter) and 10 Al particles (with a 1.8 μm diameter) were randomly placed within the matrix material. The initial geometry of the sample is shown in Fig. 7.14. The sample had the following volume fractions: 77.1% PTFE, 7.8% Al and 14.9% W. The corresponding mass fraction are: 38% PTFE, 4.8% Al and 57.2% W.

The Eulerian mesh for the sample with large W particles had the dimensions $L_{Ex} = 29.45\mu$m, $L_{Ey} = 29.45\mu$m, and $L_{Ez} = 22.16\mu$m with 75 elements in each direction. Each of the following MMALE parts defined within this mesh were defined using the *INITIAL_VOLUME_ FRACTION_GEOMETRY card. Steel plates (Vascomax 250 with properties obtained from Steinberg (1996)) were placed at the top and bottom of the mesh. The plates spanned the entire width and depth of the plate and had a thickness of $0.56\mu m$ (i.e. each plate had a thickness of two elements). The PTFE matrix material was defined as a rectangular box with the dimensions 21.45 μm in the x and y directions and 21.04 μm in the z direction. In the x and y directions a 2% addition of material was added to prevent boundary grains from protruding through the side surfaces (unsuccessfully in this case). In this simulation, 4 W particles (with a 0.9 μm diameter) and 243 Al particles (with a 1.8 μm diameter) were randomly placed within the matrix material. The initial geometry of the sample is shown in Fig. 7.15. The sample had the following similar volume fractions

to the previous sample: 76.57% PTFE, 7.66% Al and 15.76% W. The corresponding mass fraction are: 36.8% PTFE, 4.5% Al and 58.7% W.

The bottom plane of nodes of the Eulerian mesh were fixed in all directions in translation and rotation. The top plane of nodes of the mesh were given a velocity boundary condition of -4.43 m/s. This resulted in material (in this case steel) entering into the mesh from the top at a constant velocity. The steel contacting the sample was free to deform.

The calculation was terminated once the sample has deformed in the z direction by 25%. Once the calculation terminates, there are 52 output states available corresponding to 0.5% sample-strain increments.

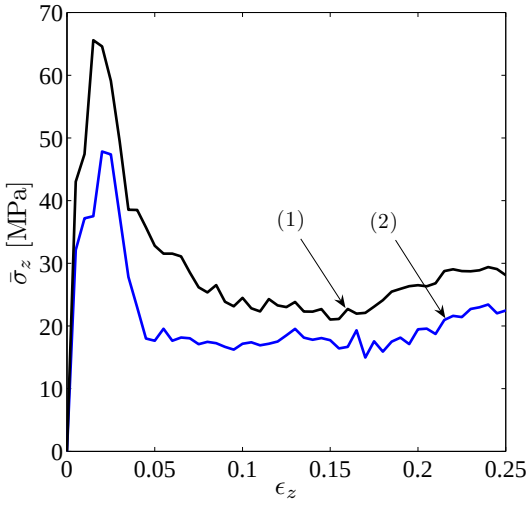

Figure 7.15: The averaged von Mises stress along the top of the sample is plotted against the 'sample' strain ($v_0 t/L_z$). Curve 1 corresponds to the sample with small W particles and curve 2 corresponds to the sample with large W particles.

The averaged von Mises stresses along the top of the sample are desired to

compare the three-dimensional calculations to previous two-dimensional calculations using Raven Benson (1992). At each time-step the nodal-value-average of each element in the top plane of the sample was output into a separate file. These element values were then averaged again to give a single value of stress representing the sample's strength at each time step. The resulting stress-strain plot is shown in Fig. 7.16.

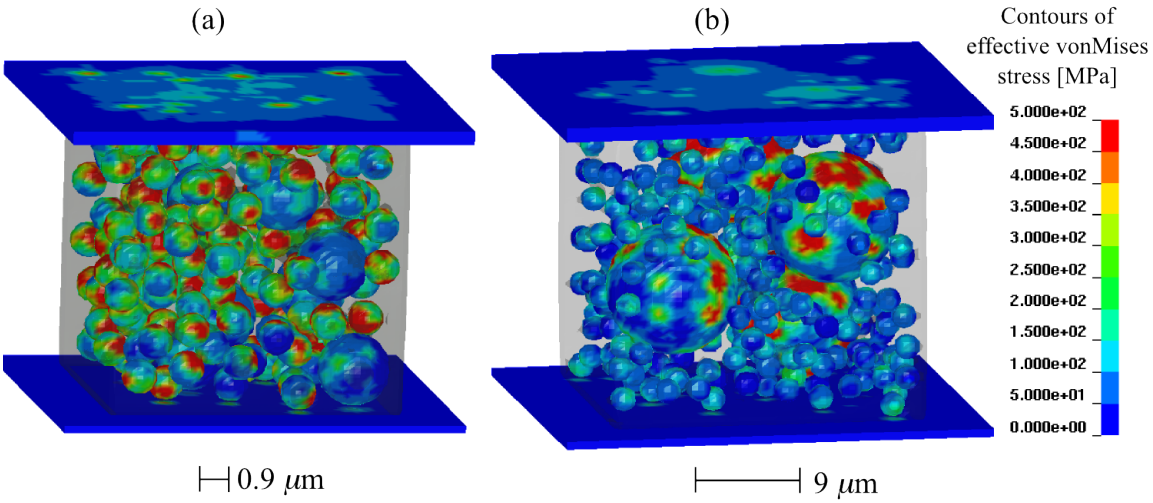

Figure 7.16: The von Mises stress distribution shown in the granular composite samples at a strain of 2%. The PTFE matrix material is semi-transparent so to highlight the metallic granules. The colors correspond to 0 MPa (blue) and 500 MPa (red). (a) Sample with small W particles. (b) Sample with large W particles.

It is clear from Fig. 7.16 that the sample with small W particles exhibits a higher strength as in the two-dimensional calculations. It may be premature to generalize this behavior based upon one calculation of each type of sample. It is important to note that the size of the samples were different but the total number of

elements were the same. This means that the mesh resolution was different for both samples.

The major 'spike' seen in curves (1) and (2) in Fig. 7.15 also occur in two-dimensional calculations when a smaller number of particles is used for the numerical sample. This raises the question of sample behavior based upon the numerical sample size, which is an important factor given the limitations on the speed and capacity of current computers (computer clusters in the case of the three-dimensional calculations). The numerical samples are created by placing the powder grains randomly within the matrix material and given the influence of particle and sample size on material behavior, a statistical average of the sample behavior will be necessary in future numerical studies to determine the statistical behaviors of the granular composite materials.

However, at the present time, the comparisons shown for the two and three dimensional calculations are typical of what was seen in various particle distributions, which were not included in this chapter. The main point stressed here is that small W particles at the same volume fraction in the composite samples is conducive to higher sample strength. In two-dimensional calculations this was verified by observing the mesoscale force chains in the sample as evidenced by the alignment of high stresses in the stress distribution plots. In the three-dimensional calculations, the vonMises stress distributions are shown in Figs. 7.16 and 7.17. In both cases, higher stresses are observed for sample 1 compared to sample 2. This reflects the apparent higher strength in the stress-strain curves shown in Fig. 7.15.

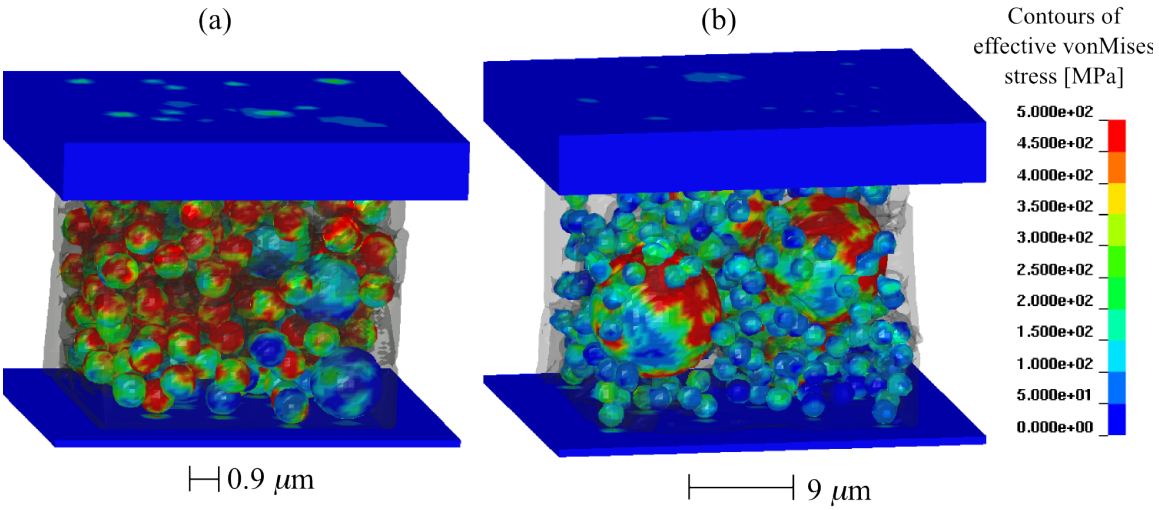

Figure 7.17: The von Mises stress distribution shown in the granular composite samples at a strain of 17%. The PTFE matrix material is semi-transparent so to highlight the metallic granules. The colors correspond to 0 MPa (blue) and 500 MPa (red). (a) Sample with small W particles. (b) Sample with large W particles.

7.3.4 Metallic Particle Packing Studies

In pressed powder composites the groups of agglomerated particles may immediately interact with one another since their interaction was created during the CIPing process, which resulted in arrested compaction and porosity. This is also supported by comparing the volume fraction of metallic particles in CIPed mixtures with PTFE and the volume fraction of them at tapped densities of mixtures of coarse W and fine Al and fine W and fine Al powders taken at the same mass ratio as in the mixture.

Table 7.2: Density and volume fraction of solid components in tapped powders

Powder	Theoretical Density of Solid [g/cm^3]	Tapped Density of Powder [g/cm^3]	Ratio (powder:solid) %
Coarse W	19.3	50.2/5.3=9.5	49
Fine W	19.3	30/7.2=4.2	22
2 μm Al	2.7	5.7/5.3=1.1	40
Coarse W: 2 μm Al 77 wt%:5.5 wt%	13.7	53.1/5.6=9.5	69
Fine W: 2 μm Al 77 wt %:5.5 wt %	13.7	32.2/8.6=3.7	27

Separate metallic particle packing studies were performed using the same constituent mass fractions as in the composite materials with PTFE. The results are given in Table 7.2. The combined volume fraction of fine W and fine Al particles in the mixture with PTFE for a CIPed sample with density 6 g/cm^3 is 0.36. This

is higher than the volume fraction of the granules (0.27) in the tapped mixture of fine W and fine Al taken at the same mass ratio as in the mixture with PTFE. This means that the force chains supporting the mesostructure in this tapped powder will also be present in the CIPed composite sample.

This is not the case with a CIPed composite sample using coarse W and fine Al (density 7.1 g/cm^3). Here the volume fraction of metal particles is significantly smaller (0.425) than the volume fraction of the granules (0.69) in the tapped mixture of coarse W and fine Al powders. This means that the PTFE matrix is dispersing metal particles and preventing them from forming force chains.

Based on this comparison it is reasonable to assume that, given the same constituent mass fractions, the strength of a composite mixture will be higher when the volume fraction of the metallic particles in it are comparable to the corresponding value in tapped powders. This volume fraction can be significantly smaller than the volume fraction in a random packing of spherical particles (0.64) and it should depend on the shape of granules.

7.3.5 Two-Dimensional Numerical Modeling of Shock Waves in Granular Composite Materials

In the previous calculations dynamic behavior of the materials was investigated under impact conditions but without shock wave propagating in the material. For larger impact velocities the propagation of the shock wave will initiate different responses depending on the particle size. For example, if particles of different strengths and sizes are present in the mixture the distribution of internal energy depends on the relative strength of particles and on their relative sizes Nesterenko (1986), Nesterenko (2001).

This can be illustrated based upon the consideration of a coordinate system

moving with the stationary shock front. In the mixture of soft and rigid, heavy particles the latter transform their kinetic energy, which they had before the shock front, into the thermal energy of small, soft particles (or soft matrix) behind the shock front. Thus, a mixture under shock loading works like a natural transformer of the kinetic energy of one component (large, rigid, heavy particles) into the internal energy of another (small, soft, light particles or matrix). This results in dependence in the distribution of internal energy between components on the size of the rigid, heavy particles.

Here, the redistribution of internal energy is investigated where PTFE and the Al particles represent a soft component and tungsten particles represent hard and heavy component with relatively large particle sizes of W. For these calculations the number of particles was increased to ensure that stationary states were achieved behind the shock front in each sample at the end of calculation.

Two samples were prepared for numerical calculations with an impacting plate moving at a constant speed of 500 m/s. These samples have similar microstructures to those shown in Fig. 7.8 except that they are more than three times longer in the direction of the moving boundary so that the properties behind the shock wave may be investigated. The overall sizes of the samples are identical, but in Fig. 7.18 (a) the size of the W particles in the matrix are 1 μm and 10 μm in Fig. 7.18 (b). In the numerical calculations periodic boundary conditions were prescribed for the sides of the samples and a transmitting boundary condition was prescribed along the bottom of each sample to reduce the reflection of the shock front. Portions of the samples are outlined and detailed to the left of Fig. 7.18 (a) and to the right of Fig. 7.18 (b).

The time dependence of ratios of internal energies for each component in the

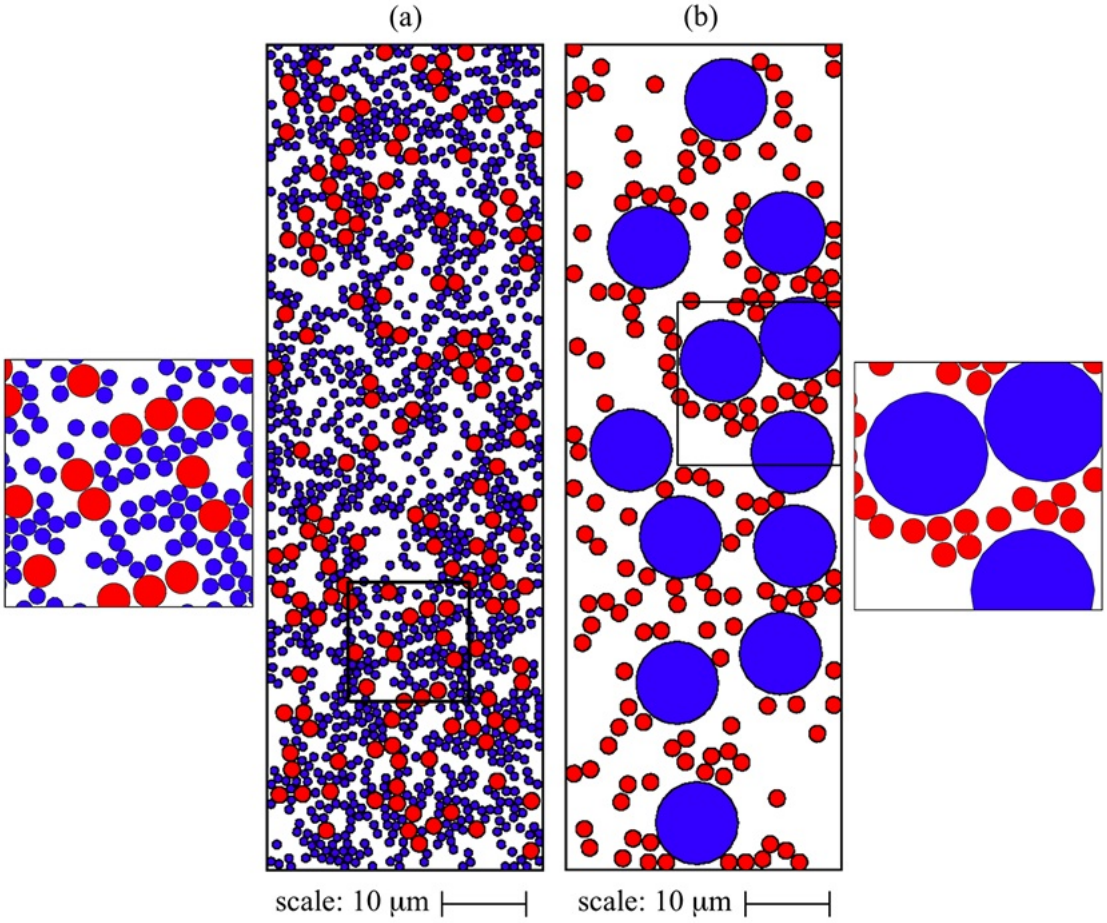

Figure 7.18: Material configuration of the composite samples that will be impacted from the top boundary with a constant velocity $v_0 = 500$ m/s. (a) The sample with small W particles (diameter of 1 μm). The subfigure on the left shows a more detailed view of the microstructure. (b) The sample with large W particles (diameter of 10 μm). The subfigure on the right shows a more detailed view of the microstructure. The Al particles have a 2 μm diameter in both configurations.

sample to the total internal energy in the whole sample is presented in Fig. 7.19 and the ratios of thermal energy increase for each component with respect to total internal energies at the end of calculations in Table 7.3. The internal energy distribution is being approximate constant after some initial period reflecting establishing of approximately stationary shock wave in calculations. The period of nonstationary wave propagation is more extended in the system with large W particles due to their larger inertia, especially with relation to internal energy of PTFE. It should be mentioned that the used boundary conditions provided the energy flow from the impacting plate higher in the sample with small tungsten particles due to their higher resistance to deformation. For this reason the fraction of energies for each component with respect to total internal energies is used in the analysis below.

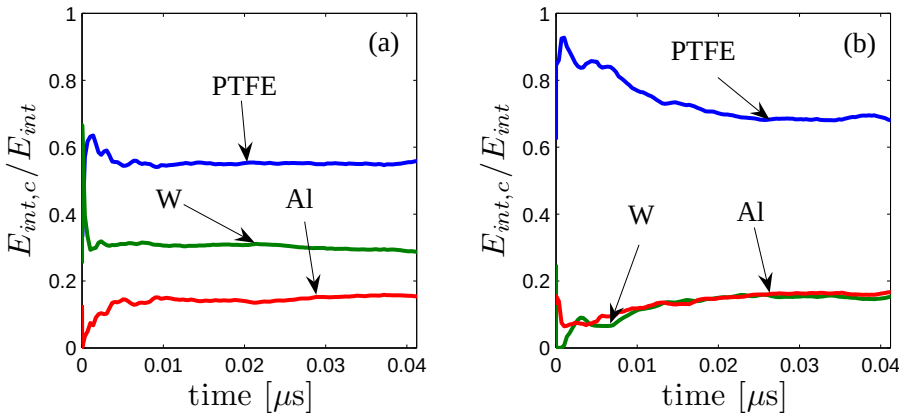

Figure 7.19: (a) Fraction of internal energies in each material during the propagation of a shock wave for the numerical sample with small W particles. (b) Fraction of internal energies in each material during the propagation of a shock wave in the numerical sample with large W particles.

We can see that redistribution of the internal and thermal energy between

components does not follow their mass fraction (0.23, 0.71, and 0.06, correspondingly for PTFE, W, and Al). This means that rigid W particles transform their kinetic energy mainly into the internal energy of PTFE matrix and Al particles. This energy redistribution is more pronounced in the system with large tungsten particles.

Table 7.3: The mass ratio and fractions of increase of thermal energy with respect to total internal energy of composite in samples with large and small W particles.

	Mass Ratio	$E_{int,c}/Eint$	
	-	Sample with small W	Sample with large W
PTFE	0.23	0.18	0.28
W	0.71	0.26	0.13
Al	0.06	0.08	0.10

In Fig. 7.20 the temperature distribution derived from the internal energy distribution is presented for two samples loaded in a similar way. Agglomerated small W and Al particles deform as groups and high temperature regions in the PTFE matrix occur between these groups (see the light gray coloring between these groups in the subfigure on the left of part Fig. 7.20 (a)). It is also apparent that large tungsten particles are less deformed (Fig. 7.20 (b)) than small tungsten particles (Fig. 7.20 (a)). This translates into larger internal energy of PTFE and Al.

In the sample with large W particles high velocity jets (the jets are indicated by arrows in the subfigure to the right of part Fig. 7.20 (b)) of the PTFE matrix flow between the large W particles and the Al particles. The small Al particles moving between the W particles are heavily deformed probably causing the increase

of fraction of thermal energy deposited in Al particles (Table 7.3). In Fig. 7.20 (c) an average velocity profile (in the horizontal direction) of the material starting from the bottom of the samples is shown corresponding to (a) and (b). Curve (1) corresponds to the sample with small W particles and it may be assumed that the material from 20-80 μm above the bottom is stationary. Curve (2) corresponds to the sample with large W particles which demonstrates higher deviations from the average value.

The preferential deposition of internal energy and specifically thermal energy in PTFE and Al can be very important for the increase of temperature of PTFE and Al and their subsequent chemical interaction. The increase of the size of W particles resulted in a significant increase of fraction of thermal energy of PTFE with some increase of thermal energy of Al particles. Large W particles facilitate localized flow in the PTFE matrix. This results in relatively large displacements of Al particles in comparison with large W particles, their shear deformation and coalescence (see insert to Fig. 7.20 (c)) which may be conducive to their chemical interaction with PTFE. This behavior was absent in the granular composite with small W particles (compare inserts to Fig. 7.20 (a) and to Fig. 7.20 (b)).

The relatively large difference in the temperature between different regions in the shock compacted sample (Fig. 7.20 (a) and (b)) and relatively small variations of particle velocity (Fig. 7.20 (c)) reflects the existence of two time scales for equilibration behind shock wave fast scale for establishing equilibration for particle velocity and slow scale for temperature equlibrium.

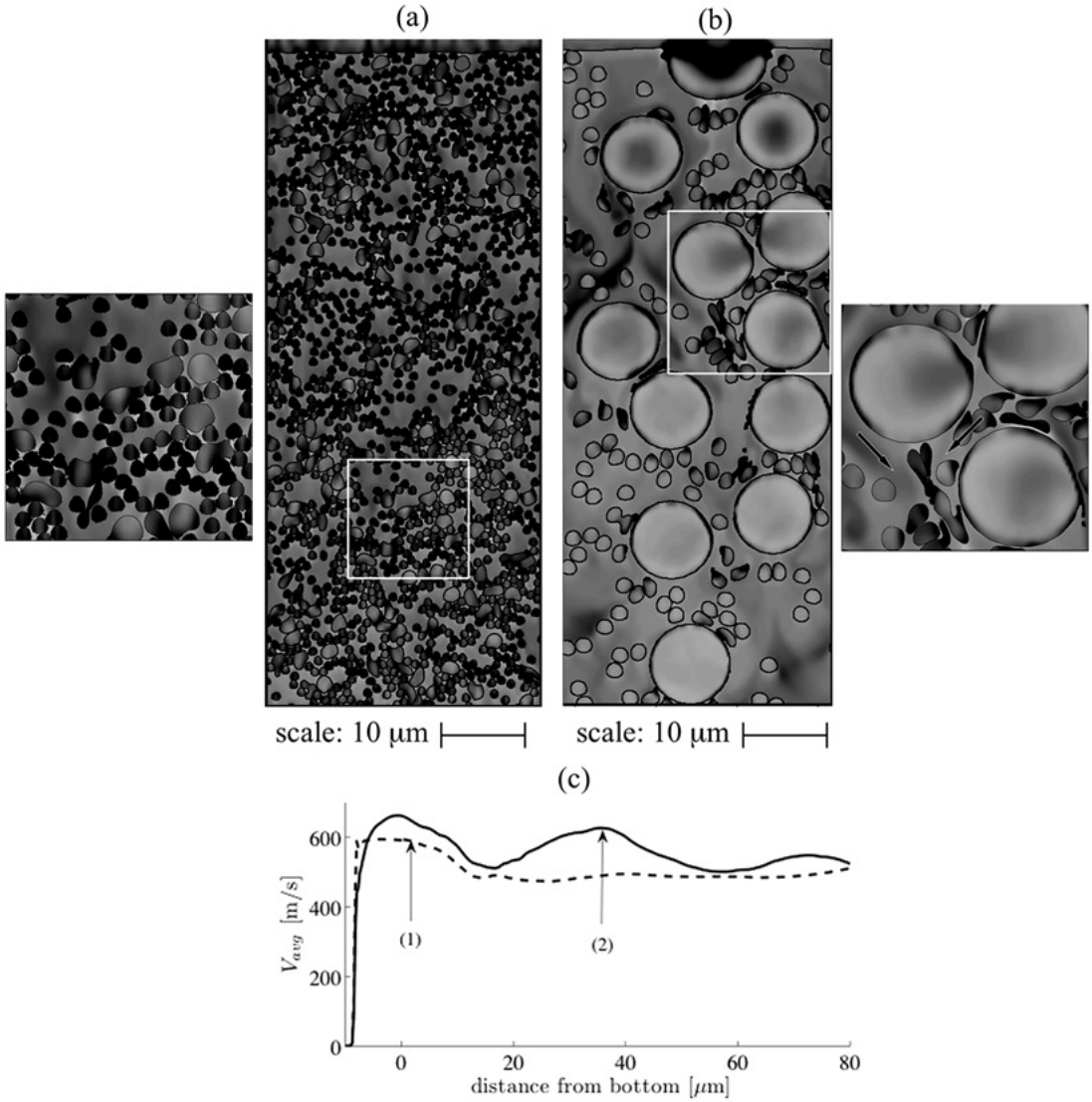

Figure 7.20: Temperature distribution in shocked composite numerical samples at a constant impact velocity of v0 = 500 m/s. The temperature scale ranges from 300 K (light gray) to 550 K (black) for parts (a) and (b). (a) The numerical sample with small W particles at 41.5 ns after impact. (b) The numerical sample with large W particles at 38.3 ns after impact. (c) Velocity profile (averaged in the horizontal direction) of the material starting from the bottom of the numerical samples shown in parts (a) and (b). Curve (1) corresponds to the numerical sample with small W particles. Curve (2) corresponds to the numerical sample with large W particles.

7.4 Conclusions

It was demonstrated that the dynamic mechanical properties of high-density mixtures of PTFE, Al and W powders could be tailored by changing the size of the W particles and porosity of the mixture. A relatively weak PTFE polymer matrix allows the strength and fracture mode of this material to be governed by the granular type behavior of collections of metal particles. Composites with fine metallic particles and a higher porosity exhibited an unusually higher ultimate compressive strength than less porous composites having equivalent mass ratios with coarse W particles. The mesoscale force chains between the fine metallic particles are responsible for this unusual phenomenon as was demonstrated by the numerical calculations. Macrocracks were observed below the critical failure strain for the PTFE matrix material and a competition between densification and fracture in some porous samples in dynamic tests was observed.

Shock loading of this granular composite resulted in an internal energy redistribution between components, which can be tailored by the particle size of W. This resulted in a higher fraction of thermal energy of the soft and light components (PTFE,Al) due to increase of size of the heavy, rigid component (W particles). This may be important for the ignition of a reaction under shock loading in this (PTFE/Al) and similar systems.

Chapter 7 has been submitted to the *Journal of Applied Physics*, E.B. Herbold, V.F. Nesterenko, D.J. Benson, J. Cai, K.S. Vecchio, F. Jiang, J.W. Addiss, S.M. Walley, and W.G. Proud. The dissertation author was the primary investigator and author of this paper.

A

Three Dimensional Drop-Weight Test of Compressed Powder Composites Using an MMALE Formulation with MPPDYNA (and LS-PrePost)

This appendix describes the three-dimensional calculations of a drop-weight simulation of compressed powder composites using LS-Dyna. There were several problems, which will be described throughout these sections that may help one to circumvent these difficulties and save some time. Keyword definitions will be described with as much detail necessary for reproduction of these calculations.

The drop-weight simulation consists of a sample being compressed between two plates; assuming one is moving at a constant velocity. The samples consist of micron sized granules of tungsten and aluminum in a PTFE matrix. This material is reactive under dynamic loading (the PTFE and Al are highly reactive). The macro sized sample (on the order of millimeters) cannot be modeled with any reasonable fidelity due to the size constraint of the elements which must be very small between

adjacent particles. Thus, the samples considered here are have typical dimensions of tens of microns on a side (for prismatic samples).

LS-PrePost will not show a length scale of 10^{-6} or less, so it is advisable to scale the problem appropriately. The nonstandard units used for these simulations are mg, μm, ms and $^{\circ}K$. This (rather unconventional) base gives units of pressure in MPa (i.e. 1 MPa = 1 mg/μm ms^2).

A.1 Problem Details

Thus far, prismatic samples are created by randomly placing W and Al particles inside a PTFE matrix with an algorithm similar to Ref. He et al. (1999). Different types of samples are distinguished by the size of the W particles. In one case, for the model of 'sample 1' from Chapter 7, the diameter of the W particles is 1μm (with 2 μm Al particles) and 10 μm (sample 2) in the second (again with 2 μm Al particles).

Once the geometry of the sample is determined, the positions and particle radii are used in another algorithm that numbers the particles for the MMALE calculation. This is necessary since the interface reconstruction in hydrocodes does not typically distinguish between surfaces of the same type of materials. Thus, it is important to distinguish adjacent particles with different ALE material designations (this prevents the 'bar-bell' effect). One may implement some sort of modified "Map Coloring" algorithm to perform this task.

Before using LS-PrePost to create the keyword file a command file ("file.cfile") may be written to reduce the amount of time spent in LS-PrePost redefining parameters that are used in similar calculations. Keyword definitions may be defined along with tasks such as creating the initial Eulerian mesh for the problem.

A.2 Keywords Used (Summary and Notes)

In the following descriptions, some of the values will be given symbolically to retain some sort of generality. The symbols used are: L_x, L_y, L_z : Characteristic length of the sample, v_0 : Initial velocity in the z-direction, $\varepsilon_{fin.}$: final sample strain (i.e. (initial height - final height)/initial height). The parameter N_{mat} denotes the number of MMALE materials are used in the calculation (see DATABASE_EXTENT_BINARY).

TITLE:

CONTROL:

ALE

$# dct,nadv,meth,afac,bfac,cfac,dfac,efac

3, 1, 2, -1.0

$# start,end,aafac,vfact,prit,ebc,pref,nsidebc

0.0, 1E+20, 0.0, 1E-6, 1.0

TERMINATION

$# endtim

$\varepsilon_{fin.} L_z / v_0$

TIMESTEP

$# dtinit,tssfac

0.0, 0.7

DATABASE:

note: for each DATABASE card (with the exception of EXTENT_BINARY), the only parameter defined was the output time-step (dt = $\varepsilon_{fin.} L_z/(50 v_0)$) such that 50 states were written to the respective output files.

DEFGEO

GLSTAT

MATSUM

BINARY_D3PLOT

BINARY_D3THDT

EXTENT_BINARY

note: 'neiph' stores 7 variables for each MMALE material: 6 stresses and the value of equivalent plastic strain.

$# neiph,neips,maxint,strflg,sigflg,epsflg,rltflg,engflg

$7N_{mat}$,0,0,0,2,1,2,2

$# cmpflg,ieverp,beamip,dcomp,shge,stssz,n3thdt,ialemat

0, 0, 0, 1, 1, 1, 1

$# nintsld,pkp_sen,sclp,unused,msscl,therm

0, 0, 1.0

BOUNDARY:

SPC_SET

$# nsid,cid,dofx,dofy,dofz,dofrx,dofry,dofrz

1, 0, 1, 1, 1, 1, 1, 1

PRESCRIBED_MOTION_SET

$# cid,heading

1, top_motion

$# nsid,dof,vad,lcid,sf,vid,death,birth

2, 3, 0, 1, 1.0, 0, 1.0E+28

HOURGLASS:

$# hgid,ihq,qm,ibq,q1,q2,qb/vdc,qw

1, 1, 0.001, 0, 1.5, 0.06, 0.001, 0.001

DEFINE:

CURVE

$#,lcid,sidr,sfa,sfo,offa,offo,dattyp

1, 0, 1.0,1.0

$# a1,o1

0.000, v_0

1.0, v_0

SECTION:

SOLID_ALE

$# secid,elform,aet

1, 11, 3

$# afac,bfac,cfac,dfac,start,end,aafac

-1.0, 0., 0., 0., 0., 1.0E+20, 1.

MAT:

VACUUM

(air_ale_vacuum)

$# mid,den

1, 1.0000E-12

ELASTIC

(steel_elastic)

$# mid,ro,e,pr,da,db,not used

2, 8.1290E-9, 1.8660E+5, 0.3

JOHNSON_COOK

(ptfe_jc)

$# mid,ro,g,e,pr,dtf,vp

3, 2.1960E-9, 137.0

$# a,b,n,c,m,tm,tr,epso

11.0, 44.0, 1.0, 0.12, 1.0, 600.0, 298.0, 0.001

$# cp,pc,spall,it,d1,d2,d3,d4

1.002E+9, -1.00E+14, 2.00, 1.00, 0.050

(w_jc)

$# mid,ro,g,e,pr,dtf,vp

4, 1.7000E-8, 1.5000E+5

$# a,b,n,c,m,tm,tr,epso

1506, 177.0, 0.12, 0.016, 1.0, 1723, 298, 0.001

$# cp,pc,spall,it,d1,d2,d3,d4

1.32E+8, -1.0E+14, 2.0

(al_jc)

$# mid,ro,g,e,pr,dtf,vp

5, 2.7070E-9, 27100

$# a,b,n,c,m,tm,tr,epso

265, 426, 0.34, 0.015, 1.0, 775, 298, 0.001

$# cp,pc,spall,it,d1,d2,d3,d4

8.7500E+8, -1.000E+14, 2.0

EOS:

GRUNEISEN

(ptfe_eos)

$# eosid,c,s1,s2,s3,gamao,a,e0

1, 1.68E+6, 1.123, 3.983, -5.797, 0.59

(w_eos)

$# eosid,c,s1,s2,s3,gamao,a,e0

2, 4.03E+6, 1.237, 0, 0, 1.67,0.38

(al_eos)

$# eosid,c,s1,s2,s3,gamao,a,e0

3, 5.386E+6, 1.339, 0, 0, 1.97, 0.48

PART:

note: One part should be defined for each MMALE material. This requires separate "pid's" for each and the respective section, material, eos, hourglass, etc. parameters are required. It is not sufficient to simply define a MMALE material and then use INITIAL_VOLUME_FRACTION_GEOMETRY to create parts. Parts are not listed here since each simulation will have unique designations.

ALE_MULTI-MATERIAL_GROUP:

note: This is problem specific.

INITIAL:

VOLUME_FRACTION_GEOMETRY

note: This card is filled by assigning parts, AMMG's, geometry types and values for each part in the calculation. This is specific to each calculation. However, air may be defined as the default background or "fill" material.

A.3 Executing MPPDyna on the Cluster

The keyword files are executed on a Linux (RHE3) cluster with 8 nodes and 4 processors per node for a total of 32 processors. MPICH (Ver. 1.2.6) is used for the message passing interface between processors/nodes. The version of mppdyna is 971 and it is a development version (mpp971_s_R4.43050_Intel_linux86-64_mpich). Before submitting a job one must make a 'machine file' that tells MPICH which processors are available. A typical file will look like the following:

```
‘‘machfile’’
```

```
csm:4
csm1:4
csm2:4
csm3:4
csm4:4
csm5:4
csm6:4
csm7:4
```

where the first line of the file is `csm:4`. To submit a job the command is

```
mpirun -machinefile <file> -np <#> -nodes <#> mppdyna memory=<#>
  i=<keyword.k>
```

where `file` would be `machfile` from above and `keyword.k` would be the keyword file to be executed. There are plenty of other flags for both `mpirun` and `mppdyna`, but this is all that is 'usually' needed. If the run fails due to a memory error, the `memory=<#>` may be used to increase the size of the problem. There is also a `memory2=<#>` command used for allocation on each processor. It has been notes that `memory2` is typically slightly larger than `memory/(np*nodes)`.

B

Various Computer Code for Interfaces with Experimental Apparatus and Numerical Calculations

B.1 Using Matlab to Connect to an Oscilloscope

All of the experiments using the oscilloscope that were performed by the author used a specially developed interface for data processing. The oscilloscope model is a Tektronix TDS2014. The matlab driver for this and other Tektronix models may be found at the manufacturer's website (http://www.tek.com). The driver should be placed within the 'instruments' folder within the Matlab main application folder. The Matlab code below will connect a computer to the oscilloscope and download a waveform from it.

```
% RunExp.m
% written by E. Herbold 5/2/05
% this function connects to the ocsilloscope (tektronix tds2014 only)
% if it is not already connected and then get (download) a waveform
```

```
% from the scope.
clear,clf,clc

Ch.date = date;

% Create a serial port object.
  obj1 = instrfind('Type', 'serial', 'Port', 'COM1', 'Tag', '');

% Create the serial port object if it does not exist
% otherwise use the object that was found.
  if isempty(obj1)
      obj1 = serial('COM1');
  else
      fclose(obj1);
      obj1 = obj1(1);
  end

% Check input buffer size for COM1 **before connecting**
  bfsize = get(obj1,'InputBufferSize');
  if bfsize < 25000
      bfsize = 25000;
      set(obj1,'InputBufferSize',bfsize);
  end

% Connect to instrument object, obj1.
  fopen(obj1);
```

```
% ******************************************************
% Code For Device Object
% ******************************************************

% Create a SERIAL object.
  interfaceObj = instrfind('Type', 'serial', 'Port', ...
                           'COM1', 'Tag', '');

% Create the SERIAL object if it does not exist
% otherwise use the object that was found.
  if isempty(interfaceObj)
      interfaceObj = serial('COM1');
  else
      fclose(interfaceObj);
      interfaceObj = interfaceObj(1);
  end

% Check input buffer size for COM1
  bfsize = get(interfaceObj,'InputBufferSize');
  if bfsize < 250005
      bfsize = 25000;
      set(interfaceObj,'InputBufferSize',bfsize);
  end
  clear bfsize
```

```
% Create a device object.
  deviceObj = icdevice('tektronix_tds2014.mdd', ...
                       interfaceObj);

% Connect device object to hardware.
  connect(deviceObj);

% Execute device object function(s).
  groupObj = get(deviceObj, 'Waveform');
  groupObj = groupObj(1); pause(0.1);

% *****************************************************

% Getting general information
disp('You are about to connect to the Tektronix TDS 2014')
disp('Please make sure your RS-232 cable is plugged into')
disp('your serial port!')
Ch.desc = input('briefly describe setup (one line)','s');
Ch.num = input('How many sensors are used in this experiment? ');
if isempty(Ch.num); Ch.num = 1; end

% get experimental setup data
for cc = 1:Ch.num
    switch cc
        case 1, Ch.nm1 = input('What is the name of the
                        1st sensor? ','s');
```

```
        Ch.pl1 = input('What is the placement of
                 the 1st sensor? ','s');
        Ch.ch(cc) = input('What channel number are
                    you using for the first sensor?');
        if isempty(Ch.ch(cc)); Ch.ch(cc) = 1; end
case 2, Ch.nm2 = input('What is the name of the
                 2nd sensor? ','s');
        Ch.pl2 = input('What is the placement of
                 the 2nd sensor? ','s');
        Ch.ch(cc) = input('What channel number are
                    you using for the second sensor?');
        if isempty(Ch.ch(cc)); Ch.ch(cc) = 1; end
case 3, Ch.nm3 = input('What is the name of the
                 3rd sensor? ','s');
        Ch.pl3 = input('What is the placement of
                 the 3rd sensor? ','s');
        Ch.ch(cc) = input('What channel number are
                    you using for the third sensor? ');
        if isempty(Ch.ch(cc)); Ch.ch(cc) = 1; end
case 4, Ch.nm4 = input('What is the name of the
                 4th sensor? ','s');
        Ch.pl4 = input('What is the placement of
                 the 4th sensor? ','s');
        Ch.ch(cc) = input('What channel number are
                    you using for the fourth sensor? ');
        if isempty(Ch.ch(cc)); Ch.ch(cc) = 1; end
```

```
    end
end
% preallocate Vraw and t
Vraw = zeros(Ch.num,2500); t = zeros(1,2500);
V = zeros(Ch.num,2500);

disp('please run the experiment and then hit return'); pause

for dd = 1:Ch.num
    if Ch.ch(dd) == 1
        set(deviceObj.Cursor(1), 'Source', 'channel1');
        pause(0.05);
        [Vraw(dd,:),t] = invoke(groupObj, 'readwaveform',...
                               'channel1' );
    elseif Ch.ch(dd) == 2
        set(deviceObj.Cursor(1), 'Source', 'channel2');
        pause(0.05);
        [Vraw(dd,:),t] = invoke(groupObj, 'readwaveform',...
                               'channel2' );
    elseif Ch.ch(dd) == 3
        set(deviceObj.Cursor(1), 'Source', 'channel3');
        pause(0.05);
        [Vraw(dd,:),t] = invoke(groupObj, 'readwaveform', ...
                               'channel3' );
    elseif Ch.ch(dd) == 4
        set(deviceObj.Cursor(1), 'Source', 'channel4');
```

```
        pause(0.05);
        [Vraw(dd,:),t] = invoke(groupObj, 'readwaveform', ...
                                'channel4' );
    else
        disp('Channel number must be an integer from 1 to 4');
        break
    end

    % adjust time
    adjust = abs(t(1));
    for i = 1:length(t); t(i) = t(i) + adjust; end
    delt = abs(t(2) - t(1));

    % smooth data
    [V(dd,:)] = data_smooth(Vraw(dd,:),.5,500,2);
end
clear obj1 interfaceObj i deviceObj groupObj delt cc dd adjust
% end RunExp.m

function [Y] = data_smooth(Y,weight,iter,type)
% data_smooth.m
% this function takes in a vector and smoothes the 'noise' by
% weighting the y(i) value to its neighbors value's.
% written by E. Herbold 11/16/04
% Y = the vector to be smoothed
% weight = weight of current value 0<weight<1
```

```
% iter = the number of times to perform the smoothing operation
% type = type of method used if type=1 then this uses
%        type=1 then this uses 3 point weighting
%        type=2 then this uses 5 point weighting
%        if type is anything else nothing will be done
% [Y] returns the modified (overwritten) vector
if type == 1
    if (weight>0) & (weight<1)
        w1 = (1-weight)/2;w2 = weight;w3 = (1-weight)/2;
    else
        disp('weight must be between 0 and 1')
        return
    end
    n = length(Y);
    for i = 1:iter
        yfull = [0; Y; 0];
        Y(1:n-1) = w1*yfull(1:n-1)+w2*yfull(2:n)+w3*yfull(3:n+1);
    end
elseif type == 2
    if (weight>0) & (weight<1)
        w1 = (1-weight)/6;
        w2 = (1-weight)/3;w3 = weight;w4 = w2;w5 = w1;
    else
        disp('weight must be between 0 and 1')
        return
    end
```

```
    n = length(Y);
    for i = 1:iter
        yfull = [0; 0; Y'; 0; 0];
        Y(1:n-1) = w1*yfull(1:n-1)+w2*yfull(2:n)+ ...
        w3*yfull(3:n+1)+w4*yfull(4:n+2)+w5*yfull(5:n+3);
    end
else
    disp('type must be 1 or 2')
    return
end
% end data_smooth.m
```

B.2 Discrete Fourier Transform Examples Using Matlab

Here's a brief explanation of how I am using the discrete fast-fourier transform methods using Matlab. Matlab has an intrinsic `fft(arg1,arg2)` function that takes in two arguments: `arg1` is the data (can be a 1 dim. vector or an n-dimensional array) and `arg2` is the number of data points to be used in the transform. For example, if we have a vector `f` with 200 values we may only want to transform the first 100 values (`f_hat = fft(f,100)`). We may also want to 'pad' the data with zeros, which is useful for comparing discrete transforms of functions to continuous functions that are finite and nonperiodic (the fft function automatically assumes a periodic domain). For example, take a one dimensional vector of data called '`X`'. Any values may be assigned to this vector (or oscilloscope data may be input into the vector, etc).

A simple case is to create this vector with a length of $M = 10$ all with the

same value of 2.5 (i.e. `X(1:10) = 2.5;` or, equivalently, `X = [` 2.5, 2.5, 2.5, 2.5, 2.5, 2.5, 2.5, 2.5, 2.5, 2.5 `]`). In order for these values to take on any meaning in the frequency domain a time domain (or spatial) must be assigned to correspond to '`X`'. The time '`t`' vector must be the same length as the vector it corresponds to; so, a 10 element vector with increasing values may be defined. The intervals between the values in the discrete time domain must be equal since the transformed data depends on multiples of a sampling frequency that will be calculated based on this constant interval. To make matters simple `t` may be defined `t(1:10) = 0:9` or, equivalently, `t = [0, 1, 2, 3, 4, 5, 6, 7, 8, 9]` (the interval is constant and equal to one). In the remainder of this section, M will denote the length of the function `X`, `t` and is also interpreted as the number of discrete time values to compose one period of a function. The `fft` algorithm makes use of the discrete equation

$$\hat{X}(k) = \sum_{j=1}^{N} X(j) \exp\left[-\frac{2\pi i(j-1)(k-1)}{N}\right], \tag{B.1}$$

where $x(j)$ is the sampled function in time, N is the number of data points to be transformed, j corresponds to the sampled function and k corresponds to the transformed function. Note that, regardless of the function, the assumed period is from 0 to 2π (or almost 2π when $j = N$). The `fft` algorithm handles padded zeros in the following way: if the function to be transformed $X(j)$ is has $M = 10$ elements and the user specifies $N > M$, then the algorithm assumes $X(j) = 0$ for $j > M$.

Typically, transformed continuous functions on an infinite domain will have identical units to the original function multiplied by the period T (where $T = t(M) - t(1)$ in the discrete case). In the discrete case the transformed function will be multiplied not by the period T but by M. Thus, one would have to rescale the transformed function by T/M in order to compare discrete transforms to continuous transforms. However, it may be simplest to interpret the magnitude of the

transformed function by the complex coefficients,

$$C(k) = \frac{\hat{X}(k)}{M} = \sum_{j=1}^{N} \frac{X(j)}{M} \exp\left[-\frac{2\pi i(j-1)(k-1)}{N}\right], \tag{B.2}$$

In essence, $C(k)$ is the vector (or array) of complex coeficients of the Fourier series. [NOTE: k and j begin at 1 simply because the first element in any Matlab vector denoted with a 1. In Fortran or C, for example the first element may be denoted with a zero; $X(0)$ instead of $X(1)$ for example. Equations B.1 and B.2 would have to be modified if the elements begin at any other number different from 1.]

For example, the complex Fourier coefficients for a continuous function are

$$C_k = \frac{1}{T} \int_{-T/2}^{T/2} X(t) e^{-2\pi i k t/T} dt, \tag{B.3}$$

which are related to the standard Fourier coefficients a_k and b_k by,

$$C_k = \frac{1}{2}\left(a_k - i b_k\right) for k > 0 \tag{B.4}$$

and $C_k = a_0/2$ for $k = 0$.

The magnitude of $C(1)$ is equal to the mean of the function (typically denoted $a_0/2$ in a Fourier series expansion) and this, in many cases, provides the programmer with a quick check to see if the magnitudes of the coefficients make sense. The mean of the function discrete function $\bar{X}$ may be expressed in many forms

$$\bar{X} \equiv \frac{1}{M} \sum_{j=1}^{N} X(j) \equiv \frac{1}{M} \hat{X}(1) \equiv C(1) \equiv \frac{a_0}{2}. \tag{B.5}$$

The distinction between N and M is that N may denote a large number of points reserved for zeros so that the function may approximate a single pulse in an infinite

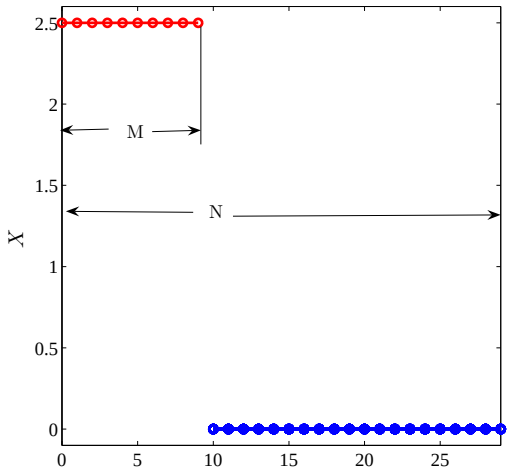

Figure B.1: Constant function of X showing the 'padded' zeros. The definition of M and N are also shown in this figure. M denotes the number of elements in the function X and N denotes the number of elements that will be transformed in the FFT algorithm.

domain. With this notation, $N \geq M$ with equality when one is transforming an harmonic signal. We will use simple examples to see what happens when N and M are different.

In our example of `X` a 10 element vector having 10 values of 2.5, the mean value of this function is obviously 2.5. The fourier series representation of this function should yeild; $C(1) = 5$, $C(k) = 0$ for $k > 1$. Below is the Matlab code of the composition of the vector '`X`' and '`t`'.

```
% fftplot.m
clear,clc,clf
% written by E. Herbold 11/13/07


M = 10;
N = 50*M;
T = [0:M-1];
X(1:M) = 2.5;
[f,C] = NC_fft(X,T,M,N);
```

The constant '`M`' is used to define the length of the vector '`X`' and '`t`' and the constant '`N`' is used to pad the vector with zeros. These definitions of '`M`' and '`N`' are shown in Fig. B.1. The function '`NC_fft`' simply calls the intrinsic fast-fourier-transform subroutine and calculates the frequency scale factor and creates a vector of the frequencies.

```
function [f,C] = NC_fft(X,t,M,N);
% written by E. Herbold 6/14/06
```

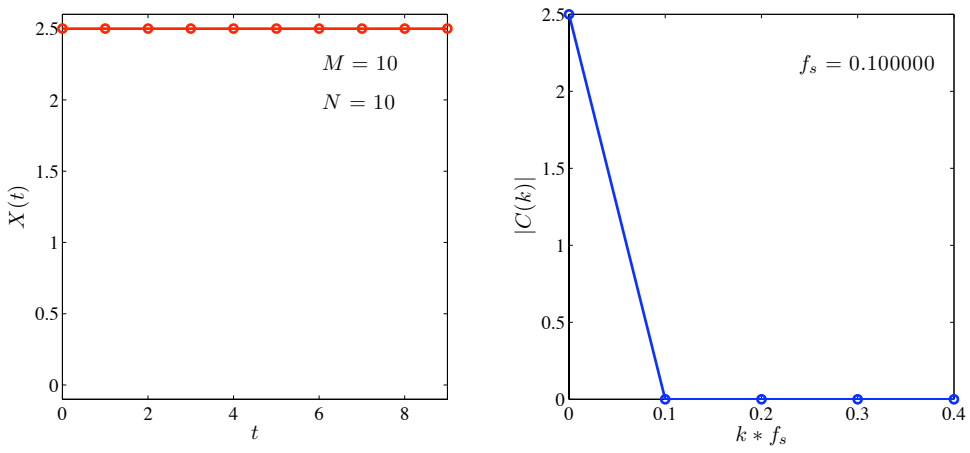

Figure B.2: Constant function of X (left) and the magnitude of the fourier coefficients assuming the function is harmonic (i.e. $M = N$). The value of f_s is calculated by $f_s = M/NT$ where T is the sample time ($t(M) - t(1)$ *which may or may not correspond to the period in numerical examples).

```
xhat  = fft(X,N);        % transform using Matlab's fft function
C = abs(xhat)/M;         % obtain properly scaled coefficients
fs = (M-1)/(t(M)-t(1)); % calculate freq. scale factor
f   = fs*(0:N/2-1)/N;    % determine vector of frequencies

% end NC_fft
```

In Fig. B.2 the constant function is plotted versus time (left) and the corresponding Fourier coefficients are plotted versus frequency (right). In the plot of the coefficients, note that the value when $k = 0$ is 2.5 which is what we predicted

$a_0/2$ to be. The remaining magnitudes of the complex coefficients are zero.

Figure B.3 shows the result of extending the function from $t \in [0, 30]$ with 30 values in the '`X`' and '`t`' vectors. The value of $C(1) = 2.5$ is the same and the remaining coefficients are zero. What we may say about Fig. B.3 compared to Fig. B.2 is that the resolution of the frequency spectrum has been tripled by tripling the number of points that have been 'sampled' for the function '`X`'. The only thing that has changed is the resolution of the frequency spectrum.

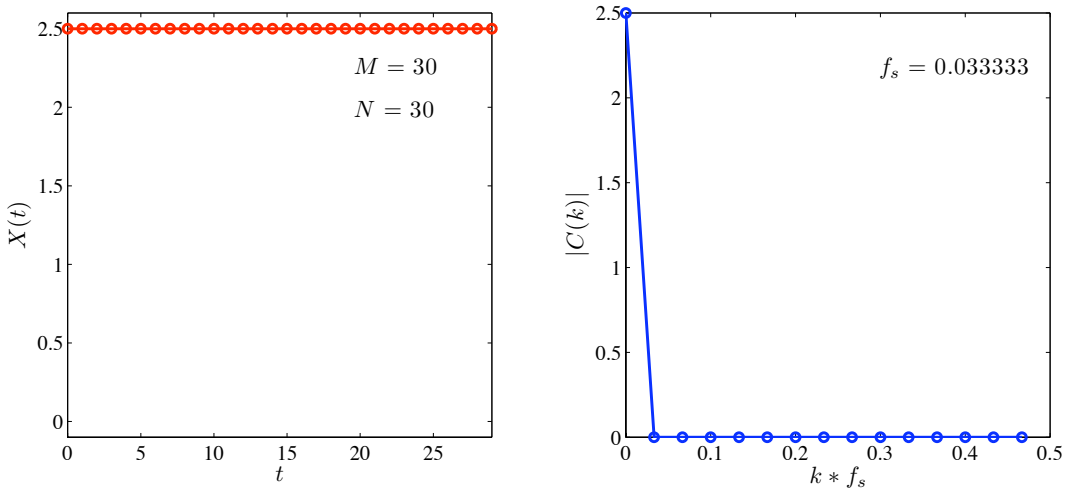

Figure B.3: Triple the number of elements in the X and t vectors (same Δt as in Fig. B.2).

In Fig. B.4 we see the result of taking the same time domain as in Fig. B.2 but tripling the number of sampling points (or vector elements). Note that Fig. B.2 and Fig. B.4 have the same first 5 values of the coefficients at the same frequencies. Thus, by increasing the resolution of the function results in the increased size of the frequency domain.

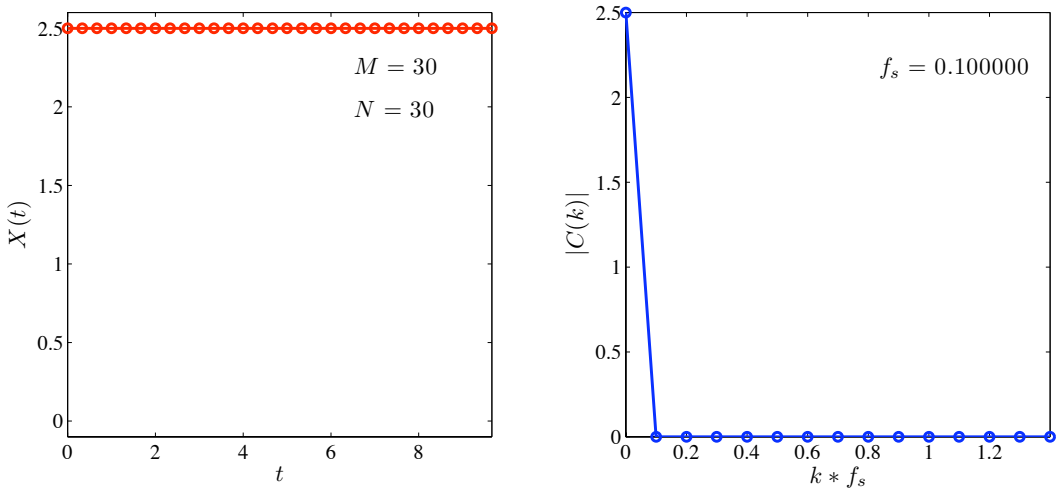

Figure B.4: Increasing the resolution of X by three times. Compare to Fig. B.2.

We just saw what occurs when the time or number of elements in the sample vector '`X`' is altered (i.e. the sampling frequency or the sample time). When sampling frequency increases, this means that the function '`X`' has a higher resolution. Thus, if there were any variation within this function, we would be able to detect higher frequency changes. This results in the increased range of the frequency spectrum. However when the sample time is increased, this leads to an increased resolution in the frequency spectrum.

When the sample function '`X`' is padded with zeros something different happens to the frequency spectrum that we will now discuss. The '`fft`' algorithm assumes the function is an harmonic function and so padding a constant function with zeros only approximates the frequency spectrum of a finite step function on an infinite domain. In Fig. B.5 the number of zeros is equal to the number of points in the funtion. This results in the frequency spectrum of the square wave.

In Fig. B.5 the number of zeros is increased to 2 times the number of

elements in 'X' (i.e. $N = 2M$). Increasing N further results in an increased resolution of the frequency spectrum, which eventually becomes the spectrum for the 'sinc' function as $N \to \infty$ (see Fig. B.6).

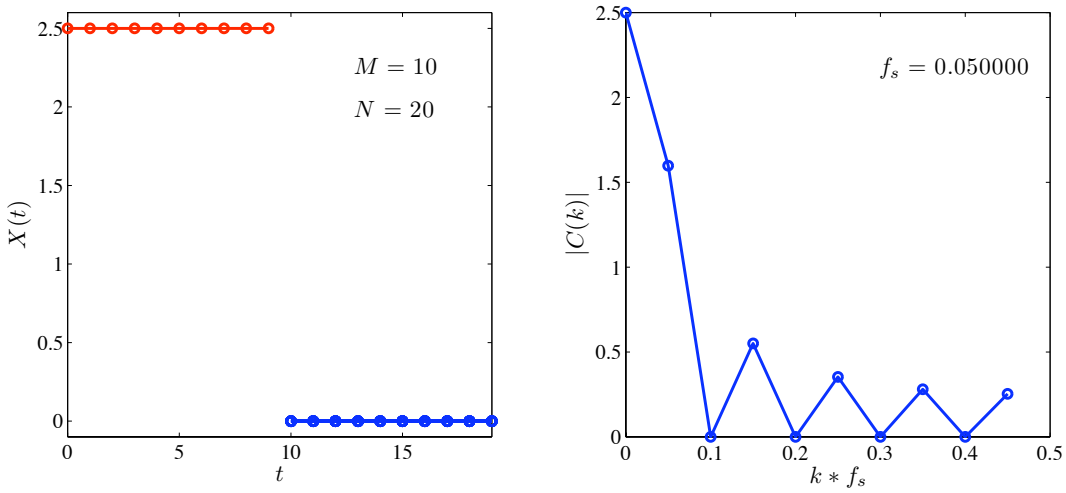

Figure B.5: 'Padding' the vector from Fig B.1 with zeros. The result is the beginnings of the 'sinc' function.

Now that we are equipped with the knowledge of what happens with a simple function, we can look at slightly more difficult frequency spectrums. We may start with a simple 'sin' wave and move on from there. The code for creating the 'sin' function in Matlab is presented below:

```
% fftplot.m
clear,clc,clf
% written by E. Herbold 11/13/07

M = 20;
```

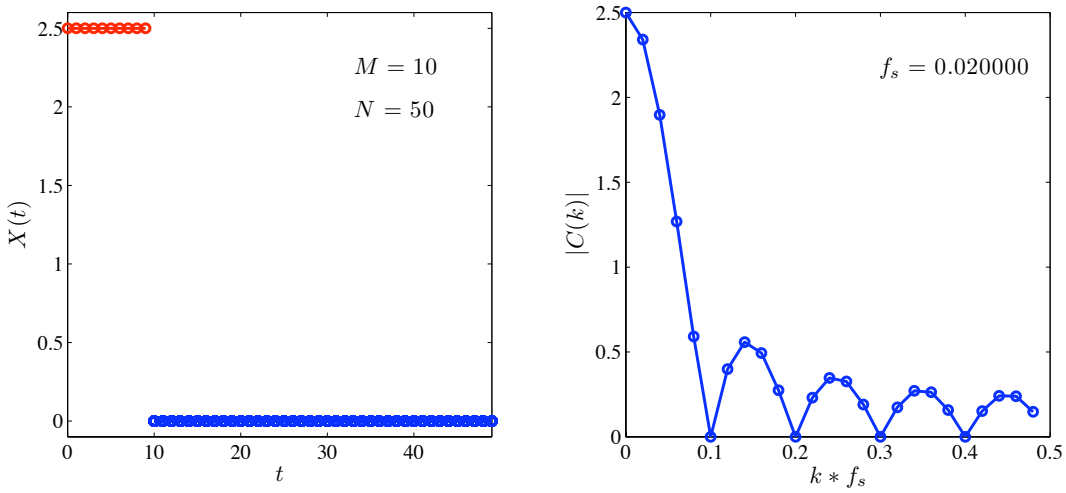

Figure B.6: Increasing the number of zeros to four times the number of points in the X vector. The result is a 'sinc' function with higher resolution.

```
N = 1*M;
T = 2*pi/M*[0:M-1];
X(1:M) = sin(T);
[f,xhat] = NC_fft(X,T,M,N);
```

We are simple letting '`X`' equal to

$$X(t) = A\sin(t). \tag{B.6}$$

Note that the '`sin`' wave does not return to zero such that the next (assumed periodic) wave will again begin at zero at $t = 2\pi$. Thus, we should expect only one nonzero value in the frequency spectrum at $f = 1/2\pi$ and this is indeed the shown in Fig. B.7. Also, note that the frequency spectrum would be identical for the '`cos`' fuction and that the magnitude of the frequency component are directly related to the amplitude A in Eq. (B.6).

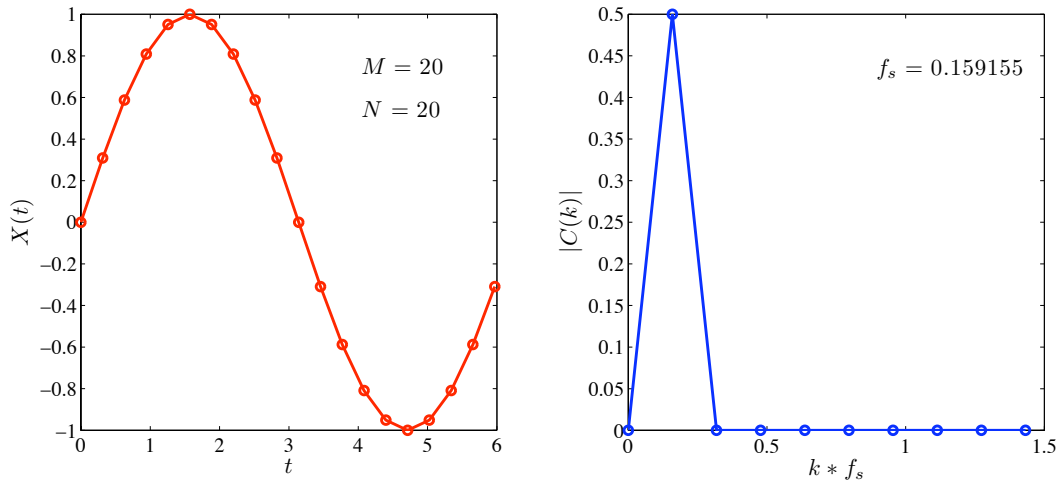

Figure B.7: Fourier spectrum of the sin function. Note that there is only one frequency component at the proper frequency $f = 1/2\pi$.

A slightly more difficult function (with implications to compact solitary waves in 'sonic vacuums') is

$$X(t) = A\cos^4(t) \equiv A\left[\frac{3}{8} + \frac{1}{2}\cos(2t) + \frac{1}{8}\cos(4t)\right] \tag{B.7}$$

with $t \in [-\pi/2, \pi/2]$. In Eq. (B.7) it is clear that this function only has three harmonics at $f_0 = 0$, $f_1 = 1/\pi$ and $f_2 = 2/\pi$ and the period of the each pulse is $T = \pi$. The Matlab code to create this pulse and its spectrum are given below:

```
% fftplot.m
clear,clc,clf
% written by E. Herbold 11/13/07


M = 20;
N = 1*M;
```

```
T = 1*pi*([0:M-1]/M-1/2);
X(1:M) = cos(T).^4;
[f,xhat] = NC_fft(X,T,M,N);
```

Note that, in this code, there is a shift to center the pulses about $t = 0$. This is merely for graphical clarity. The resulting plots of the shape of the pulse and the frequency spectrum are shown in Fig. B.8.

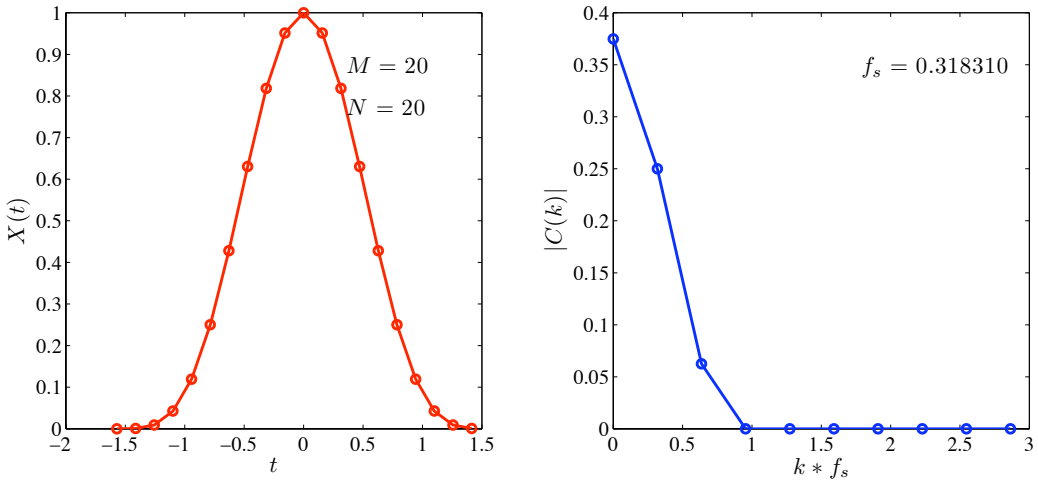

Figure B.8: Fourier spectrum of the function $\cos^4(t)$. There are three nonzero frequency components at $f = 0, 1/\pi$ and $2/\pi$. The average of the function (3/8 from Eq. B.7) is represented at $k = 0$ where is the value is two times the mean of the function ($a_0 = 2\bar{X}(t)$, see Eq. B.5).

However, we are unable to tell whether or not the three nonzero frequency components are zero between these values. Recalling from our previous discussion, we will be able to increase the resolution of the frequency spectrum if we increase the sample time T. The resulting plot is shown in Fig. B.9

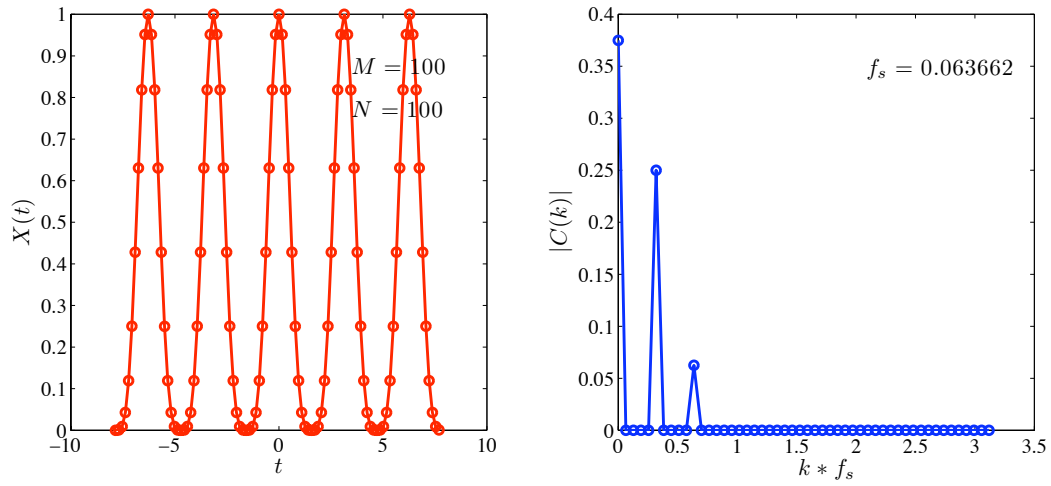

Figure B.9: Fourier spectrum of the function $\cos^4(t)$ with a longer sample period T than in Fig. B.8. Again, there are three nonzero frequency components at $f = 0, 1/\pi$ and $2/\pi$.

From Fig. B.9 we see that there are indeed only 3 nonzero frequency components for the $\cos^4(t)$ function. This is the result assuming the function is harmonic. If we assume that the function is a single pulse what would happen to the frequency spectrum? The results are shown in Fig. B.10.

It appears that the main difference between Fig. B.9 and Fig. B.10 is that all of the frequency components between the first and third harmonic (and beyond) are enhanced. However, if we look at the frequency spectrum on a logarithmic scale in the ordinate axis we see that there may be an infinite number of frequency components with regularly spaced zero components. This logarithmic plot is shown in Fig. B.11.

This is all one needs to use a discrete fft algorithm. We discussed how an

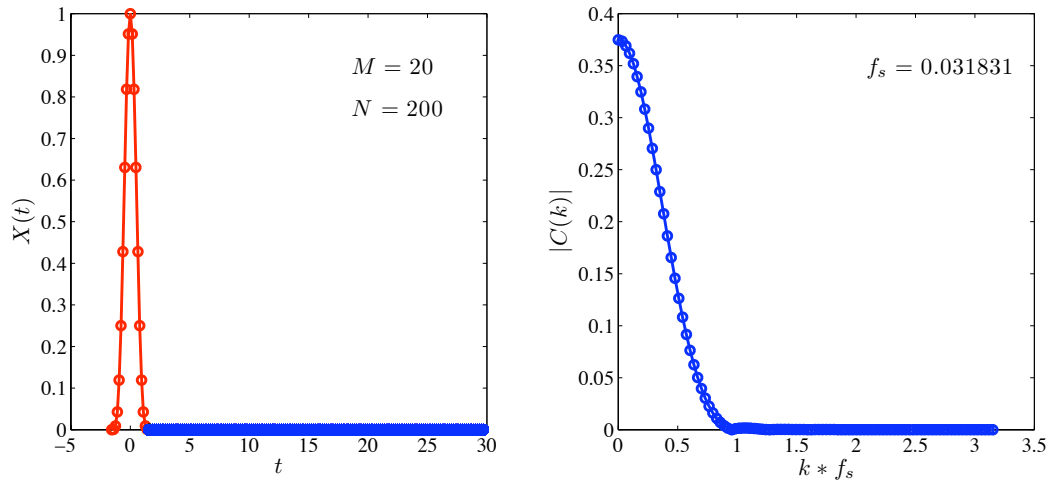

Figure B.10: Fourier spectrum of a single pulse of the function $\cos^4(t)$. There appears to be many nonzero frequency components since the function is approaching the spectrum of a single pulse in an infinite domain. You may note the slight 'bump' around $k * f_s = 1$. This will be shown better in Fig. B.11.

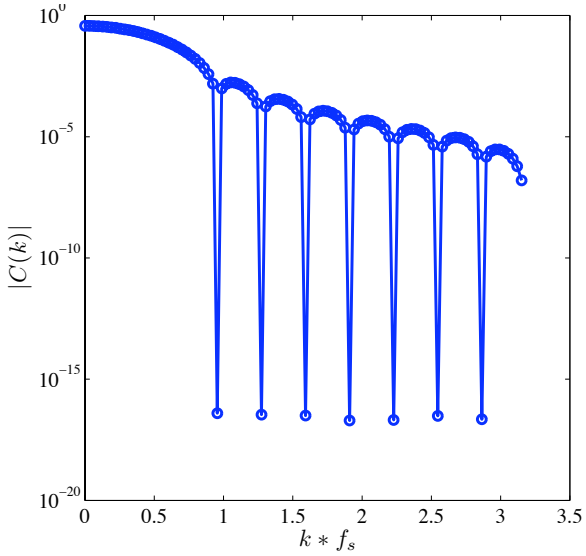

Figure B.11: Fourier spectrum, with a logarithmic ordinate axis, of a single pulse of the function $\cos^4(t)$. There appears to be many nonzero frequency components and regularly spaced 'zero' components (shown near 10^{-16} which is the approximate machine precision).

increased sample time increases the resolution of the frequency spectrum. We also have seen that an increase in sampling frequency results in a larger domain in the frequency spectrum. Lastly, we discussed how 'padding' with zeros affects functions. If the number of zeros is much larger than the number of samples (i.e. the length of the discrete function, or vector '`X`' in this case), then the frequency spectrum will resemble what the function would look like as a non-repeating function on an infinite domain. I did not discuss issues such as the Nyquist frequency or the inner workings of the `fft` algorithm since these discussions are readily found in many undergraduate texts and online. A particularly helpful website (online book actually) is found here: http://research.opt.indiana.edu/Library/FourierBook/toc.html. This book explains

many of the omitted details and derives the discrete transform based on a bottom-up approach. The usefulness of this section is to merely give a guideline for those who wish to use Matlab to perform signal analysis. The plots shown here can be displayed many ways. I thought it best to plot the magnitude of the complex coefficients since this was easily understood by someone who has performed at least one fourier series decomposition by hand.

References

Addiss, J., Cai, J., Walley, S., Proud, W., and Nesterenko, V. F. (2007) High strain and strain rate behaviour of PTFE/Aluminum/Tungsten mixtures. In Elert, M., Furnish, M., Chau, R., Holmes, N., and Nguyen, J., eds., *Shock Compression of Condensed Matter-2007*, vol. 955 of *Shock Compression of Condensed Matter*, American Institute of Physics, American Institute of Physics, pp. 773–776.

Alastalo, A., Kiihamäki, J., and Seppä, H. (2006) Microelectromechanical delay lines with slow signal propagation. *Journal of Micromechanics and Microengineering*, **16**, pp. 1854–1860.

Ames, R. (2006) Energy Release Characteristics of Impact-Initiated Energetic Materials. In Thadhani, N., Armstrong, R., Gash, A., and Wilson, W., eds., *Multifunctional Energetic Materials MRS Proceedings Volume 896*, vol. 896, Materials Research Society, Materials Research Society, pp. 1–10.

Arancibia-Bulnes, C. and Ruiz-Suárez, J. (2002) Broad solitons in homogeneous Hertzian granular chains. *Physica D*, **168**, pp. 159–164.

ASM (1983) ASM Metals Reference Book. In *ASM Metals Reference Book*, ASM, Metals Park, OH, 2nd ed., p. 268.

Ball, R. and Blumenfeld, R. (2002) Stress Field in Granular Systems: Loop Forces and Potential Formulation. *Physical Review Letters*, **88**, no. 11, p. 115505.

Balzer, J., Siviour, C., Walley, S., Proud, W., and Field, J. (2004) Behaviour of ammonium perchlorate-based propellants and a polymer-bonded explosive under impact loading. *Proceedings of the Royal Society of London Ser. A*, **460**, no. 2043, pp. 781–806.

Bardenhagen, S. and Brackbill, J. (1998) Dynamic stress bridging in granular material. *Journal of Applied Physics*, **83**, no. 11, pp. 5732–5740.

Benson, D. (1992) Computational methods in Lagrangian and Eulerian hydrocodes. *Computer Methods in Applied Mechanics and Engineering*, **99**, pp. 235–394.

Benson, D. and Nesterenko, V. (2001) Anomalous decay of shock impulses in laminated composites. *Journal of Applied Physics*, **89**, no. 7, pp. 3622–3626.

Benson, D., Nesterenko, V., Jonsdottir, F., and Meyers, M. (1997) Quasistatic and dynamic regimes of granular material deformation under impulse loading. *Journal of the Mechanics and Physics of Solids*, **45**, no. 11-12, pp. 1955–1999.

Blumenfeld, R. (2004) Stresses in Isostatic Granular Systems and Emergence of Force Chains. *Physical Review Letters*, **93**, no. 10, p. 108301.

Brilliantov, N. and Pöschel, T. (2004) *Kinetic Theory of Granular Gases*. Oxford University Press.

Brilliantov, N. V., Spahn, F., Hertzsch, J.-M., and Pöschel, T. (1996) Model for collisions in granular gases. *Physical Review E*, **53**, no. 5, p. 5382.

Brown, E., Rae, P., Orler, E., G.T. Gray, I., and Dattelbaum, D. (2005) The effect of crystallinity on the fracture of polytetrafluoroethylene (PTFE). *Materials Science and Engineering: C*, **26**, no. 8, pp. 1338–1343.

Brunhuber, C., Mertens, F., and Gaididei, Y. (2006) Envelope Solitons on anharmonic damped atomic chains. *Physical Review E*, **73**, p. 016614.

Büttner, H. and Bilz, H. (1978) *Solitons and Condensed Matter Physics: Proceedings of the Symposium on Nonlinear (Soliton) Structure and Dynamics in Condensed Matter, Oxford, England, June 27-29, 1978*, chap. 3. Springer Series in Solid-State Sciences, Springer Verlag, Heidelberg, pp. 162–165.

Cai, J., Jiang, F., Vecchio, K., Meyers, M., and Nesterenko, V. (2007) Mechanical and microstructural properties of PTFE/Al/W system. In Elert, M., Furnish, M., Chau, R., Holmes, N., and Nguyen, J., eds., *Shock Compression of Condensed Matter-2007*, vol. 955 of *Shock Compression of Condensed Matter*, American Institute of Physics, American Institute of Physics, pp. 723–726.

Cai, J. and Nesterenko, V. (2006) Collapse of Hollow Cylinders of PTFE and Aluminum Particles Mixtures Using Hopkinson Bar. In Furnish, M., Elert, M., Russell, T., and White, C., eds., *Shock Compression of Condensed Matter-2005*, vol. 845 of *Shock Compression of Condensed Matter*, American Institute of Physics, American Institute of Physics, pp. 793–796.

Cai, J., Nesterenko, V., Vecchio, K., Jiang, F., Herbold, E., Benson, D., Addiss, J., Walley, S., and Proud, W. (2008a) The influence of metallic particle size on the mechanical properties of polytetraflouroethylene-Al–W powder composites. *Applied Physics Letters*, **92**, no. 3, p. 031903.

Cai, J., Walley, S., Hunt, R., Proud, W., Nesterenko, V., and Meyers, M. (2008b) High-strain, high-strain-rate flow and failure in PTFE/Al/W granular composites. *Materials Science and Engineering: A*, **472**, no. 1-2, pp. 308–315.

Campbell, C. (1990) Rapid Granular Flows. *Annual Review of Fluid Mechanics*, **22**, pp. 57–92.

Carter, W. and Marsh, S. (1995) Hugoniot Equation of State of Polymers, (unpublished).

Chatterjee, A. (1999) Asymptotic solution for solitary waves in a chain of elastic spheres. *Physical Review E*, **59**, no. 5, p. 5912.

Chubykalo, O., Kovalev, A., and Usatenko, O. (1993) Dynamical solitons in a one-dimensional nonlinear diatomic chain. *Physical Review B*, **47**, no. 6, pp. 3153–3160.

Corwin, E., Jaeger, H., and Nagel, S. (2005) Structural Signature of Jamming in Granular Media. *Nature*, **435**, pp. 1075–1078.

Coste, C., Falcon, E., and Fauve, S. (1997) Solitary waves in a chain of beads under Hertz contact. *Physical Review E*, **56**, p. 6104.

Coste, C. and Gilles, B. (1999) On the validity of Hertz contact law for granular material acoustics. *The European Physical Journal B*, **72**, pp. 155–168.

Coste, C. and Gilles, B. (2008) Sound Propagation in a constrained lattice of beads: High-frequency behavior and dispersion relation. *Physical Review E*, **77**, no. 2, p. 021302.

Daraio, C., Nesterenko, V., and Jin, S. (2004a) Highly nonlinear contact interaction and dynamic energy dissipation by forest of carbon nanotubes. *Applied Physics Letters*, **85**, no. 23, pp. 5724–5726.

Daraio, C., Nesterenko, V., and Jin, S. (2004b) Strongly nonlinear waves in 3D phononic crystals. In Furnish, M., Gupta, Y., and Forbes, J., eds., *Shock Compression of Condensed Matter-2003*, vol. 706 of *Shock Compression of Condensed Matter*, American Institute of Physics, American Institute of Physics, pp. 197–200.

Daraio, C., Nesterenko, V. F., Herbold, E. B., and Jin, S. (2005) Strongly nonlinear waves in a chain of Teflon beads. *Physical Review E (Statistical, Nonlinear, and Soft Matter Physics)*, **72**, no. 1, 016603.

Daraio, C., Nesterenko, V. F., Herbold, E. B., and Jin, S. (2006) Tunability of solitary wave properties in one-dimensional strongly nonlinear phononic crystals. *Physical Review E (Statistical, Nonlinear, and Soft Matter Physics)*, **73**, no. 2, 026610.

Darrigol, O. (2005) *Worlds of Flow: A History of Hydrodynamics from the Bernoullis to Prandtl*. Oxford University Press, Oxford.

Dash, P. and Patnaik, K. (1981) Solitons in Nonlinear Diatomic Lattices. *Progress of Theoretical Physics*, **65**, no. 5, pp. 1526–1541.

Davis, J., Lindfors, A., Miller, P., Finnegan, S., and Woody, D. (1998) Detonation like phenomena in metal-polymer and metal/metal oxide-polymer mixtures. In *11th Detonation Symposium (International)*, pp. 1007–1013.

Davis, R. H., Serayssol, J.-M., and Hinch, E. (1985) The elastohydrodynamic collision of two spheres. *Journal of Fluid Mechanics*, **163**, pp. 479–497.

Denisaev, A., Shteinberg, A., and Berlin, A. (2007) Study of the impact sensitivity of aluminum-polytetrafluoroethylene layered compositions. *Doklady Physical Chemistry*, **414**, no. 2, pp. 139–142.

Dey, T. and Johnson, J. (1998) Shear band formation in plastic bonded explosive (PBX). In Schmidt, S., Forbes, J., and Dandekar, D., eds., *Shock Compression of Condensed Matter-1997*, vol. 429 of *Shock Compression of Condensed Matter*, American Institute of Physics, American Institute of Physics, pp. 285–288.

Dolgoborodov, A., Makhov, M., Kolbanev, I., Streletskii, A., and Fortov, V. (2005) Detonation in an Aluminum-Teflon Mixture. *JETP Letters*, **81**, no. 7, pp. 311–314.

Duvall, G. E., Manvi, R., and Lowell, S. C. (1969) Steady Shock Profile in a One-Dimensional Lattice. *Journal of Applied Physics*, **40**, no. 9, pp. 3771–3775.

Ehrenstein, G. (2001) *Polymeric Materials: Structure, Properties, Applications*. Hanser, Munich.

Fermi, E., Pasta, J., and Ulam, S. (1965) Studies of Non-Linear Prolems (Technical Report). In *Collected Works of E. Fermi*, vol. 2, University of Chicago Press, pp. 978–988.

for Metals, A. S. (1983) *ASM Metals Reference Book*. American Society for Metals, 2nd ed.

Franchini, A., Bortolani, V., and Wallis, R. (1996) Intrinsic localized modes in the bulk and at the surface of anharmonic diatomic chains. *Physical Review B*, **53**, no. 9, pp. 5420–5429.

Freakley, P. K. and Payne, A. R. (1978) *Theory and practice of engineering with rubber*. Applied Science Publishers Ltd., London.

Friesecke, G. and Wattis, J. A. D. (1994) Existence Theorem for Solitary Waves on Lattices. *Communications in Mathematical Physics*, **161**, no. 2, pp. 391–418.

Fung, Y. (1965) *Foundations of Solid Mechanics*. Prentice-Hall, Englewood Cliffs, New Jersey.

Gavrilyuk, S. and Nesterenko, V. (1993) Stability of Periodic Excitations for one model of "Sonic Vacuum". *Prikladnaya Mekhanika i Tekhnicheskaya Fizika*, **34**, pp. 45–48.

Gerritsen, M., Kreiss, G., and Blumenfeld, R. (2008) Stress chain solutions in two-dimensional isostatic granular systems: fabric-dependent paths, leakage, and branching. *Physical Review Letters*, **101**, no. 9, p. 098001.

Goddard, J. (1990) Nonlinear Elasticity and Pressure-Dependent Wave Speeds in Granular Media. *Proceedings: Mathematical and Physical Sciences*, **430**, pp. 105–131.

Goffaux, C. and Vigneron, J. (2001) Theoretical study of a tunable phononic band gap system. *Physical Review B*, **64**, no. 7, pp. 075118–1–5.

Goldenberg, C. and Goldhirsch, I. (2005) Friction enhances elasticity in granular solids. *Nature*, **435**, pp. 188–191.

Gondret, P., Lance, M., and Petit, L. (2001) Bouncing motion of spherical particles in fluids. *Physics of Fluids*, **14**, no. 2, pp. 643–652.

Gorbach, A. and Johansson, M. (2003) Discrete gap breathers in a diatomic Klein-Gordon chain: Stability and mobility. *Physical Review E*, **67**, no. 6, p. 066608.

Gourdin, W. (1983) Energy deposition and microstructural modification in dynamically consolidated metal powders. *Journal of Applied Physics*, **55**, no. 1, pp. 172–181.

Gourdin, W. (1986) Dynamic Consolidation of Metal Powders. *Progress in Materials Science*, **30**, pp. 39–80.

Hamburger (1887) *Tageblatt der Naturforscher Versammlung*.

Hascoët, E. and Herrmann, H. (2000) Shocks in non-loaded bead chains with impurities. *The European Physical Journal B*, **14**, p. 183.

Hascoët, E. and Hinch, E. J. (2002) Linearized impulse wave propagating down a vertical column of heavy particles. *Physical Review E*, **66**, p. 011307.

He, D., Ekere, N., and Cai, L. (1999) Computer simulation of random packing of unequal particles. *Physical Review E*, **60**, no. 6, pp. 7098–7104.

Heimburg, T. and Jackson, A. (2005) On soliton propagation in biomembranes and nerves. *Proceedings of the National Academy of Sciences*, **102**, no. 28, pp. 9790–9795.

Helmholtz, H. (1954) *On the Sensations of Tone*. Dover.

Herbold, E. B. and Nesterenko, V. F. (2007) Shock wave structure in a strongly nonlinear lattice with viscous dissipation. *Physical Review E*, **75**, no. 2, p. 021304.

Herbold, E. B., Nesterenko, V. F., and Daraio, C. (2006) Influence of Controlled Viscous Dissipation on the Propagation of Strongly Nonlinear Waves in Stainless Steel Based Phononic Crystals. In Furnish, M. D., Elert, M., Russell, T. P., and White, C. T., eds., *Shock Compression of Condensed Matter-2005*, vol. 845 of *Shock Compression of Condensed Matter*, American Institute of Physics, AIP, pp. 1523–1526.

Hertz, H. (1881) Über die Beruehrung fester elastiche Koerper. *J. für reine und angewandte Mathematik*, **92**, pp. 156–171.

Hertz, H. (1896) On the contact of elastic solids. In Jones, D. and Schott, G., eds., *Miscellaneous Papers by Heinrich Hertz*, chap. 4, Macmillan, pp. 163–183.

Hinch, E. and Saint-Jean, S. (1999) The fragmentation of a line of balls by an impact. *Proceedings of the Royal Society of London*, **455**, no. 1989, pp. 3201–3220.

Hladky-Hennion, A.-C., Allan, G., and deBilly, M. (2005) Localized modes in a one-dimensional diatomic chain of coupled spheres. *Journal of Applied Physics*, **98**, no. 5, p. 054909.

Hocking, L. M. (1972) The effect of slip on the motion of a sphere close to a wall and of two adjacent spheres. *Journal of Engineering Mathematics*, **7**, no. 3, pp. 207–221.

Holt, W., W. Mock, J., and Santiago, F. (2000) X-ray photoelectron spectroscopy indication of decomposition species in the residue of shocked polytetrafluoroethylene powder. *Journal of Applied Physics*, **88**, no. 9, pp. 5485–5486.

Hong, J. (2005) Universal Power-Law Decay of the impulse Energy in Granular Protectors. *Physical Review Letters*, **94**, p. 108001.

Hong, J., Ji, J.-Y., and Kim, H. (1999) Power Laws in Nonlinear Granular Chain under Gravity. *Physical Review Letters*, **82**, no. 15, pp. 3058–3061.

Hong, J. and Xu, A. (2001) Effects of gravity and nonlinearity on the waves in the granular chain. *Physical Review E*, **63**, p. 061310.

Hong, J. and Xu, A. (2002) Nondestructive identification of impurities in granular medium. *Applied Physics Letters*, **81**, no. 25, pp. 4868–4870.

Jaeger, H. and Nagel, S. (1992) Physics of the Granular State. *Science*, **255**, no. 5051, pp. 1523–1531.

Jaeger, H., Nagel, S., and Behringer, R. (1996) Granular solids, liquids, and gases. *Reviews of Modern Physics*, **68**, no. 4, pp. 1259–1273.

J.C. Foster, J., Glenn, J., and Gunger, M. (2000) Meso-scale origins of the low-pressure equation of state and high rate mechanical properties of plastic bonded explosives. In Furnish, M., Chhabildas, L., and Hixson, R., eds., *Shock Compression of Condensed Matter-1999*, vol. 505 of *Shock Compression of Condensed Matter*, American Institute of Physics, American Institute of Physics, pp. 703–706.

Jia, X., Caroli, C., and Velicky, B. (1999) Ultrasound Propagation in Externally Stressed Granular Media. *Physical Review Letters*, **82**, no. 9, pp. 1863–1866.

Job, S., Melo, F., Sen, S., and Sokolow, A. (2005) How Hertzian solitary waves interact with boundaries in a 1-D granular medium. *Physical Review Letters*, **94**, p. 178002.

Johnson, G. and Cook, W. (1983) A Constitutive Model and Data for Metals Subjected to Large Strains, High Strain Rates and High Temperatures. In *Seventh International Symposium on Ballistics*, pp. 1–7.

Johnson, G. and Cook, W. (1985) Fracture Characteristics of Three Metals Subjected to Various Strains, Strain Rates, Temperatures and Pressures. *Engineering Fracture Mechanics*, **21**, no. 1, pp. 31–48.

Karpman, V. (1975) *Nonlinear Waves in Dispersive Media*. Pergamon Press.

Kastner, M. (2004a) Dimension dependent energy thresholds for discrete breathers. *Nonlinearity*, **17**, p. 1923.

Kastner, M. (2004b) Energy Thresholds for Discrete Breathers. *Physical Review Letters*, **92**, no. 10, p. 104301.

Kittel, C. (2005) *Introduction to solid state physics*. Wiley.

Korteweg, D. and deVries, G. (1895) On the change of form of long waves advancing in a rectangular canal, and on a new type of long stationary waves. *Philosophical Magazine*, **39**, pp. 422–443.

Kunin, I. A. (1975) *Theory of Elastic Media with Microstructure. I - One-dimensional models*, vol. 26. Nauka, Moscow (in Russian).

Kunin, I. A. (1982) *Elastic media with microstructure. I - One-dimensional models*, vol. 26 of *Springer Verlag Springer Series on Solid State Sciences*. Springer Verlag.

Kushwaha, M. (1996) Classical band structure of periodic elastic composites. *International Journal of Modern Physics B*, **10**, no. 9, pp. 977–1094.

Lazaridi, A. and Nesterenko, V. (1985) Observation of a new type of solitary waves in a one-dimensional granular medium. *Zhurnal Prikladnoi Mekhaniki i Tekhnicheskoi Fiziki*, **3**, pp. 115–118.

le Rond d'Alembert, J. (1747) Recherche sur la courbe que forme une corde tendue mise en vibration. *Historical Academy of Sciences Berlin*, **3**, pp. 214–219.

Lindley, P. B. (1966a) Load-Compression relationships of rubber units. *Journal of Strain Analysis*, **1**, no. 3, pp. 190–195.

Lindley, P. B. (1966b) The stiffness of rubber springs. In Allen, P. W., Lindley, P. B., and Payne, A. R., eds., *Use of Rubber in Engineering*, The natural rubber producers' research association, Maclaren and Sons Ltd., London, pp. 1–24.

Liu, Z., Zhang, X., Mao, Y., Zhu, Y., Yang, Z., Chan, C., and Sheng, P. (2000) Locally Resonant Sonic Materials. *Science*, **289**, pp. 1734–1736.

Love, A. (1944) *A Treatise on the Mathematical Theory of Elasticity*. Dover, 4th ed.

Lüerßen, D., Easwar, N., Malhotra, A., Hutchins, L., Schulze, K., and Wilcox, B. (2004) A demonstration of phonons that implements the linear theory. *American Journal of Physics*, **72**, no. 2, pp. 197–202.

Majmudar, T. and Behringer, R. (2005) Contact force measurements and stress-induced anisotropy in granular materials. *Nature*, **435**, pp. 1079–1082.

Makse, H., Gland, N., Johnson, D., and Schwartz, L. (1999) Why Effective Medium Theory Fails in Granular Materials. *Physical Review Letters*, **83**, no. 24, pp. 5070–5073.

Makse, H., Gland, N., Johnson, D., and Schwartz, L. (2004) Granular packings: Nonlinear elasticity, sound propagation, and collective relaxation dynamics. *Physical Review E*, **70**, no. 6, pp. 061302–1–19.

Manacorda, T. (1991) Origin and Development of the Concept of Wave. *Meccanica*, **26**, pp. 1–5.

Manciu, F. and Sen, S. (2002) Secondary solitary wave formation in systems with generalized Hertz interactions. *Physical Review E*, **66**, p. 016616.

Manciu, M., Sen, S., and Hurd, A. (1999a) The propagation and backscattering of soliton-like pulses in a chain of quartz beads and related problems. (I). Backscattering. *Physica A*, **274**, pp. 607–618.

Manciu, M., Sen, S., and Hurd, A. (1999b) The propagation and backscattering of soliton-like pulses in a chain of quartz beads and related problems. (I). Propagation. *Physica A*, **274**, pp. 588–606.

Manciu, M., Sen, S., and Hurd, A. J. (2000) Crossing of identical solitary waves in a chain of elastic beads. *Physical Review E*, **63**, p. 016614.

Manciu, M., Sen, S., and Hurd, A. J. (2001) Impulse propagation in dissipative and disordered chains with power-law repulsive potentials. *Physica D*, **157**, pp. 226–240.

Mann, A., Gavens, A., Reiss, M., Heerden, D. V., Bao, G., and Weihs, T. (1997) Modeling and characterizing the propagation velocity of exothermic reactions in multilayer foils. *Journal of Applied Physics*, **82**, no. 3, pp. 1178–188.

Manziadis, P., Zolotaryuk, A., and Tsironis, G. (2003) Existence and stability of discrete gap breathers in a diatomic β Fermi-Pasta-Ulam chain. *Physical Review E*, **67**, no. 4, p. 046612.

McGregor, N. and Sutherland, G. (2004) Plate impact experiments on a porous teflon-aluminum mixture. In Furnish, M., Gupta, Y., and Forbes, J., eds., *Shock Compression of Condensed Matter-2003*, vol. 706 of *Shock Compression of Condensed Matter*, American Institute of Physics, American Institute of Physics, pp. 1001–1004.

Milne-Thomson, L. M. (1968) *Theoretical Hydrodynamics*. Macmillan Education, London, 5th ed.

Munro, R. (1997) Evaluated material properties for a sintered alpha-alumina. *Journal of the American Ceramic Society*, **80**, no. 8, pp. 1919–1928.

Musienko, A. and Manevich, L. (2004) Classical mechanical analogs of relativistic effects. *Uspekhi*, **47**, no. 8, p. 797.

Nahmad-Molinari, Y., Arancibia-Bulnes, C., and Ruiz-Suárez, J. (1999) Sound in a Magnetorheological Slurry. *Physical Review Letters*, **82**, no. 4, pp. 727–730.

Nesterenko, V. (1986) Potential of shock-wave methods for preparing and compacting rapidly quenched materials. *Combustion, Explosion, and Shock Waves*, **21**, pp. 730–740.

Nesterenko, V. (1992a) *High-Rate Deformation of Heterogeneous Materials*. Nauka, Novosibirsk.

Nesterenko, V. (1992b) A New type of Collective Excitations in a "Sonic Vacuum". In *Akustika neodnorodnykh sred*, Novosibirsk, pp. 228–233.

Nesterenko, V. (1992c) Nonlinear Waves in "Sonic Vacuum". *Fizika Goreniya i Vzrva*, **28**, no. 3, pp. 121–123.

Nesterenko, V. (1992d) Pulse Compression Nature in Strongly Nonlinear Medium. In *Proceedings of Second International Symposium on Intense Dynamic Loading and Its Effects*, Chengu, China, pp. 236–240.

Nesterenko, V. (2003) Shock (Blast) Mitigation by "Soft" Condensed Matter. In Sen, S., Hunt, M., and Hurd, A., eds., *MRS Symposium Proceedings*, vol. 759, Materials Research Society, Materials Research Society, pp. MM4.3.1–12.

Nesterenko, V. F. (1983) Propagation of nonlinear compression pulses in granular media. *Zhurnal Prikladnoi Mekhaniki i Tekhnicheskoi Fiziki*, **24**, no. 5, pp. 136–148.

Nesterenko, V. F. (1993) Examples of "sonic vacuum". *Fizika Goreniya i Vzrva*, **29**, no. 2, pp. 132–134.

Nesterenko, V. F. (1994) Solitary waves in discrete media with anomalous compressibility and similar to "sonic vacuum". *Journal De Physique IV*, **04**, no. C8, pp. 729–734.

Nesterenko, V. F. (2001) *Dynamics of Heterogeneous Materials*. Springer.

Nesterenko, V. F., Daraio, C., Herbold, E. B., and Jin, S. (2005) Anomalous Wave Reflection at the Interface of Two Strongly Nonlinear Granular Media. *Physical Review Letters*, **95**, no. 15, 158702.

Nesterenko, V. F., Lazaridi, A., and Sibiryakov, E. (1995) The decay of soliton at the contact of two "Acoustic Vacuums". *Journal of Applied Mechanics and Technical Physics*, **36**, no. 2, pp. 166–168.

of Naval Research, O. (2005) Naval Research - Science & Technology for America's Readiness. newsletter, http://www.nstarweb.com/enewsletter.html.

Parmley, S., Zobrist, T., Clough, T., Perez-Miller, A., Makela, M., and Yu, R. (1995) Phononic band structure in a mass chain. *Applied Physics Letters*, **67**, no. 6, pp. 777–779.

Pnevmatikos, S., Flyntzanis, N., and Remoissenet, M. (1986) Soliton dynamics of nonlinear diatomic lattices. *Physical Review B*, **33**, no. 4, pp. 2308–2321.

Pnevmatikos, S., Remoissenet, M., and Flyntzanis, N. (1983) Propagation of acoustic and optical solitons in nonlinear diatomic chains. *Journal of Physics C: Solid State Physics*, **16**, pp. L305–L310.

Porter, M. A., Daraio, C., Herbold, E. B., Szelengowicz, I., and Kevrekidis, P. G. (2008) Highly nonlinear solitary waves in periodic dimer granular chains. *Physical Review E*, **77**, no. 1, p. 015601.

Raman, C. (1918) The photographic study of impact at minimal velocities. *Physical Review*, **12**, no. 6, pp. 442–447.

Ramírez, R., Pöschel, T., Brilliantov, N. V., and Schwager, T. (1999) Coefficient of restitution of colliding viscoelastic spheres. *Physical Review E*, **60**, no. 4, p. 4465.

Rayleigh, J. (1976a) *Theory of Sound, Volume One*, vol. 1. Dover.

Rayleigh, J. (1976b) *Theory of Sound, Volume Two*, vol. 2. Dover.

Rayleigh, L. (1906) On the production of vibration by forces of relatively long duration with the applications to the theory of collisions. *Philosophical Magazine*, **11**, p. 283.

Reigada, R., Sarmiento, A., and Lindenberg, K. (2003) Breathers and thermal relaxation in Fermi-Pasta-Ulam arrays. *Chaos*, **13**, no. 2, pp. 646–656.

Remoissenet, M. (1996) *Waves Called Solitons: Concepts and Experiments*. Springer, Berlin, 2nd ed.

Roessig, K., J.C. Foster, J., and Bardenhagen, S. (2002) Dynamic stress chain formation in a two-dimensional particle bed. *Experimental Mechanics*, **42**, no. 3, pp. 329–337.

Rosas, A., ben Avraham, D., and Lindenberg, K. (2005) Velocity distribution in a viscous granular gas. *Physical Review E*, **71**, p. 032301.

Rosas, A. and Lindenberg, K. (2003) Pulse dynamics in a chain of granules with friction. *Physical Review E*, **68**, p. 041304.

Rosas, A. and Lindenberg, K. (2004) Pulse velocity in a granular chain. *Physical Review E*, **69**, p. 037601.

Rosas, A., Romero, A., Nesterenko, V., and Lindenberg, K. (2007) Observation of Two-Wave Structure in Strongly Nonlinear Dissipative Granular Chains. *Physical Review Letters*, **98**, p. 164301.

Russell, J. (1845) Report on Waves. In *Report of the fourteenth meeting of the British Association for the Advancement of Science*, plates 47-62, pp. 311–390.

Sahimi, M. (2003a) *Heterogeneous Materials I: Linear Transport and Optical Properties*, vol. 1. Springer.

Sahimi, M. (2003b) *Heterogeneous Materials II: Nonlinear and Breakdown Properties and Atomistic Modeling*, vol. 1. Springer.

Sander, J. and Hunter, K. (1991) On the development of the theory of the solitary wave. A historical essay. *Acta Mechanica*, **86**, pp. 111–152.

Schneebeli (1885) *Archives des sciences physiques*.

Sen, S., Chakravarti, S., D.P. Visco, J., Wu, D., Nakagawa, M., and J.H. Agui, J. (2003) Impulse propagation in Granular Systems. In Kenkre, V. and Lindenberg, K., eds., *Modern Challenges in Statistical Mechanics*, vol. 658 of *Modern Challenges in Statistical Mechanics*, American Institute of Physics, American Institute of Physics, Melville, NY, pp. 357–379.

Sen, S., Hong, J., Bang, J., Avalos, E., and Doney, R. (2008) Solitary waves in the granular chain. *Physics Reports*, **462**, pp. 21–66.

Sen, S. and Manciu, M. (2001) Solitary wave dynamics in generalized Hertz chains: An improved solution of the equation of motion. *Physical Review E (Statistical, Nonlinear, and Soft Matter Physics)*, **64**, p. 056605.

Sen, S., Manciu, M., and Manciu, F. (1999) Ejection of ferrofluid grains using nonlinear acoustic impulses-A particle dynamical study. *Applied Physics Letters*, **75**, no. 10, pp. 1479–1481.

Sen, S., Manciu, M., Sinkovits, R., and Hurd, A. (2001) Nonlinear acoustics in granular assemblies. *Granular Matter*, **3**, pp. 33–39.

Setchell, R. (1984) Grain-size effects on the shock sensitivity of hexanitrostilbene (HMS) explosive. *Combustion and Flame*, **56**, no. 3, pp. 343–345.

Shen, M. and Cao, W. (1999) Acoustic band-gap engineering using finite-size layered structures of multiple periodicity. *Applied Physics Letters*, **75**, no. 23, pp. 3713–3715.

Shih, C., Nesterenko, V., and Meyers, M. (1998) High-strain-rate deformation and communition of silicon carbide. *Journal of Applied Physics*, **83**, no. 9, pp. 4660–4671.

Shukla, A., Sadd, M., Xu, Y., and Tai, Q. (1993) Influence of loading pulse duration on dynamic load transfer in a simulated granular medium. *Journal of the Mechanics and Physics of Solids*, **41**, no. 11, pp. 1795–1808.

Sigmund, O. and Jensen, J. S. (2003) Systematic design of phononic band-gap materials and structures by topology optimization. *Philosophical Transactions of the Royal Society of London Series A*, **361**, pp. 1001–1019.

Siviour, C., Gifford, M., Walley, S., Proud, W., and Field, J. (2004) Particle size effects on the mechanical properties of a polymer bonded explosive. *Journal of Materials Science*, **39**, no. 4, pp. 1255–1258.

Sokolow, A., Bittle, E., and Sen, S. (2007) Solitary wave train formation in Hertzian chains. *Europhysics Letters*, **77**, p. 24002.

Steinberg, D. (1996) Equation of state and strength properties of selected materials, UCRL-MA-106439, collection of Material Properties.

Stocchino, A. and Guala, M. (2005) Particle-wall collision in shear thinning fluids. *Experiments in Fluids*, **38**, no. 4, pp. 476–484.

Tait, P. (1900) *Scientific Papers*, vol. 2, chap. 87. Cambridge.

Tasi, J. (1976) Initial-value problems for nonlinear diatomic chains. *Physical Review B*, **14**, no. 6, pp. 2358–2370.

Tchawoua, C., Kofane, T., and Bokosah, A. (1993) Dynamics of solitary waves in diatomic chains with long-range Kac-Baker interactions. *Journal of Physics A: Math General*, **26**, pp. 6477–6491.

Timoshenko, S. and Goodier, J. (1987) *Theory of Elasticity*. McGraw-Hill.

Tournat, V., Gusev, V., and Castagnède, B. (2004) Self-demodulation of elastic waves in a one-dimensional granular chain. *Physical Review E*, **70**, p. 056603.

Tyndall, J. (1884) *Sound*. D. Appleton and Co., 3rd ed.

Vergara, L. (2005) Scattering of Solitary Waves from Interfaces in Granular Media. *Physical Review Letters*, **95**, p. 108002.

Viningland, J., Johnsen, O., Flekkoy, E., Toussaint, R., and Maloy, K. (2007) Granular Rayleigh-Taylor Instability: Experiments and Simulations. *Physical Review Letters*, **99**, no. 4, pp. 048001–1–4.

Walley, S., Balzer, J., Proud, W., and Field, J. (2000) Response to Thermites to Dynamic High Pressure and Shear. *Proceedings of the Royal Society of London Ser. A*, **456**, pp. 1483–1503.

Zabusky, N. and Kruskal, M. (1965) Interaction of "Solitons" in a collisionless plasma and the recurrence of initial states. *Physical Review Letters*, **15**, no. 6, pp. 240–243.

Zerilli, F. and Armstrong, R. (2001) Thermal Activation Constitutive Model for Polymers Applied to Polytetraflouroethylene. In Furnish, M., Thadhani, N., and Horie, Y., eds., *Shock Compression of Condensed Matter*, American Institute of Physics, American Institute of Physics, pp. 657–660.

Zhang, J., Fan, L.-S., Zhu, C., Pfeffer, R., and Qi, D. (1999) Dynamic behavior of collision of elastic spheres in viscous fluids. *Powder Technology*, **106**, pp. 98–109.

Zhu, Y., Sienkiewicz, F., Shukla, A., and Sadd, M. (1997) Propagation of explosive pulses in assemblies of disks and spheres. *Journal of Engineering Mechanics*, **123**, no. 10, pp. 1050–1059.